Investigating star-planet properties of different exoplanet populations

A thesis
submitted for the degree of

Doctor of Philosophy

in

The Department of Physics,
Pondicherry University,
Puducherry - 605 014, India

by

C. Swastik
Indian Institute of Astrophysics,
Bangalore - 560 034, India

March 2024

Investigating star-planet properties of different exoplanet populations

C. Swastik
Indian Institute of Astrophysics

Indian Institute of Astrophysics
Bangalore - 560 034, India

Title of the thesis	:	**Investigating star-planet properties of different exoplanet populations**
Name of the author	:	**C. Swastik**
Address	:	Indian Institute of Astrophysics II Block, Koramangala Bangalore - 560 034, India
Email	:	swastik.chowbay@iiap.res.in
Name of the supervisor	:	**Dr. Ravinder K Banyal**
Address	:	Indian Institute of Astrophysics II Block, Koramangala Bangalore - 560 034, India
Email	:	banyal@iiap.res.in

Declaration of Authorship

I hereby declare that the matter contained in this thesis is the result of the investigations carried out by me at the Indian Institute of Astrophysics, Bangalore, under the supervision of Dr. Ravinder K Banyal. This work has not been submitted for the award of any other degree, diploma, associateship, fellowship, etc. of any other university or institute.

Signed:

Date:

Certificate

This is to certify that the thesis entitled **‘Investigating star-planet properties of different exoplanet populations’** submitted to the Pondicherry University by Mr. Swastik Chowbay for the award of the degree of Doctor of Philosophy, is based on the results of the investigations carried out by him under my supervision and guidance, at the Indian Institute of Astrophysics. This thesis has not been submitted for the award of any other degree, diploma, associateship, fellowship, etc. of any other university or institute.

Signed: ________________________________

Date: ________________________________

List of Publications

1. **Host-star metallicity of directly imaged wide-orbit planets: implications for planet formation**
   C. Swastik, R. K. Banyal, M. Narang, P. Manoj, T. Sivarani, B. E. Reddy, S. P. Rajaguru, *Astronomical Journal, 161, 114 (2021).*

2. **Galactic chemical evolution of exoplanet host-stars: Are high-mass planetary systems young?**
   C. Swastik, R. K. Banyal, M. Narang, P. Manoj, T. Sivarani, S. P. Rajaguru, A. Unni, B. Banerjee, *Astronomical Journal, 164, 60 (2022).*

3. **Carbon abundance of stars in the LAMOST-Kepler field**
   A. Unni, M. Narang, T. Sivarani, P. Manoj, R. K. Banyal, A. Surya, S. P. Rajaguru, **C. Swastik**, *Astronomical Journal, 164, 181 (2022).*

4. **Age Distribution of Exoplanet host-stars: Chemical and Kinematic Age Proxies from GAIA DR3**
   C. Swastik, R. K. Banyal, M. Narang, A. Unni, B. Banerjee, P. Manoj, T. Sivarani, *Astronomical Journal, 166, 91 (2023).*

5. **Protoplanetary disks in K_s-band total intensity and polarized light.**
   B. B. Ren, M. Benisty, C. Ginski, R. Tazaki, N. L. Wallack, J. Milli, A. Garufi, J. Bae, S. Facchini, F. Ménard, P. Pinilla, **C. Swastik**, R. Teague, and Z. Wahhaj, *A & A, 680, A114 (2023).*

6. **Age analysis of exoplanet hosting stars from isochrone models**
   C. Swastik, R. K. Banyal, M. Narang, A. Unni, and T. Sivarani, *Astronomical Journal, 167, 270 (2024).*

7. **PDS 70 unveiled by star-hopping**
   Z. Wahhaj, M. Benisty, C. Ginski, S. Arora, **C. Swastik**, R. G. van Holstein, Rob de Rosa, B. Yang, J. Bae, and B. Ren, *A & A, 687, A257 (2024).*

8. **Artefact-free total intensity and polarimetric imaging of the LkCa 15 system**
   C. Swastik, Z. Wahhaj, M. Benisty, S. Arora, C. Ginski, B. B. Ren, R. G. van Holstein, Rob de Rosa, and R. K. Banyal, *Under rev in A & A.*

Oral Presentations

1. Presented a talk titled **"Galactic chemical evolution of planet-hosting stars"** in the *ICPEH , 5–9 February 2024*, Physical Research Laboratory (PRL), Ahmedabad, India.

2. Presented a talk titled **"The Search for Planet around LkCa 15 protoplanetary disk"** in the *Star Formation Studies in India , 8–11 January 2024*, SNBSCS, Kolkata, India.

3. Presented a talk titled **"Timeline of planet formation: Trends evidence from stellar isochrone models"** in the *Exoplanet Conference at IISER Pune , 17–19 August 2023*, IISER Pune, India.

4. Presented a talk titled **"Are giant planet-hosting stars young? Kinematics and chemical properties of exoplanet host stars from GAIA DR3"** in the *41st meeting of the Astronomical Society of India, 1–5 March 2023*, IIT Indore, India.

5. Presented a talk titled **"Did giant planets form late in the galaxy? Insights from the GAIA DR3 data"** in the *Alive Universe - from Planets to Galaxies, 12–14 October 2022*, Shamakhi, Azerbaijan.

6. Presented a talk titled **"Galactic chemical evolution of exoplanet hosting stars: Are high-mass planetary systems young?"** in the *NCTS-ASIAA Workshop: Stars, Planets, and Formosa , 15–19 August 2022*, NTU, Taiwan.

7. Presented a talk titled **"Are giant planet-hosting stars young? Evidence from galactic chemical evolution"** in the *21st National Space Science Symposium , 6–11 December 2021*, Kolkata, India.

8. Presented a talk titled **"Host-star Metallicity of Directly Imaged Planets"** in the *39th meeting of the Astronomical Society of India , 18–23 February 2021*, ICTS - TIFR Bengaluru, IISER Mohali, IIT Indore and IUCAA Pune, India.

Poster Presentations

1. Presented a poster titled **"The Search for Planet around LkCa 15 protoplanetary disk "** in the *42nd meeting of the Astronomical Society of India, 31 Jan – 4 Feb 2023*, IISc, ISRO and JNP, Bengaluru, India.
2. Presented a poster titled **"Did planet formation happen recently ?"** in the *Towards Other Earths III , 17 – 21 July 2023*, Porto, Portugal.
3. Presented a poster titled **"Galactic chemical evolution of planet-hosting stars."** in the *Protostar and Planets VII, 10 - 15 April 2023*, Kyoto, Japan.
4. Presented a poster titled **"Did planet formation occur only recently? Evidences from kinematics and chemical properties of exoplanet host stars from GAIA DR3."** in the *Planet-Eslab-2023, 20 - 24 March 2023*, Leiden, Netherlands.
5. Presented a poster titled **"Chemical analysis of exoplanet host stars: Are high-mass planetary systems young?"** in the *(Exo)Planet Diversity, 12 - 16 Sept 2022*, Berlin, Germany.
6. Presented a poster titled **"Are giant planet-hosting stars young? Evidence from spectroscopic & kinematic analysis of GAIA DR3"** in the *Sagan Exoplanet Summer Hybrid Workshop, 25 - 29 July 2022*, NExSci, Pasadena, CA, USA.
7. Presented a poster titled **"Exoplanet and its host star in the era of GAIA DR3"** in the *Gaia Symposium: DR3 And Beyond, 11 - 15 July 2022*, Indian Institute of Astrophysics, Bengaluru, India.
8. Presented a poster titled **"Galactic chemical evolution of exoplanet hosting stars: Are high-mass planetary systems young?"** in the *Rocky Worlds II, 4 - 8 July 2022*, University of Oxford, Oxford, United Kingdom.
9. Presented a poster titled **"Artifact Free Protoplanetary Disk Imaging with Starhopping RDI. "** in the *40th meeting of the Astronomical Society of India, 31 Jan – 4 Feb 2023*, IIT Roorkee and ARIES Nainital, India.

Acknowledgements

Firstly, I would like to thank my supervisor Dr. Ravinder K. Banyal, whose guidance was important during my research tenure at the Indian Institute of Astrophysics, Bangalore. Dr. Banyal's mentorship was not just about supervision; it was a journey of growth, learning, and overcoming challenges. His relentless support and insightful feedback were pivotal and transformed both my personal and professional life, steering me towards the successful completion of my thesis. His influence extended beyond academic guidance, shaping me into the researcher and person I am today. I would also like to take this opportunity to thank my lead collaborator, Dr. Zahed Wahhaj. Without his help and support, I would not have been able to expand my scope of research in protoplanetary disks. His collaboration was a key element in exploring new dimensions within the realm of protoplanetary disks. Although we have never met in person, his impact on my PhD journey has been profound. His belief in my capabilities and his assistance at various stages of my research have been invaluable. I am eternally grateful for his faith in me and his unwavering support.

Next, I would like to thank my collaborators Prof. Sivarani Thirupathi, Dr. Myriam Benisty, Dr. Athira Unni, Dr. Christian Ginski, Dr. Bin Ren, Mr. Saksham Arora, Dr. Rob de Rosa, Dr. Mayank Narang, Dr. S.P Rajuguru, Mr. Bihan Banerjee, Prof. Eshwar Reddy, Dr. Manoj Puravankara, and Dr. Rob Van Holstein. I would also like to extend my thanks to the chair of BGS and my Doctoral committee member Dr. Gopinathan Maheswar, who constantly pushed me to finish my thesis on time. I would also like to thank our Dean, Prof. Eshwar Reddy and our Director, Prof. Annapurini Subramaniam, for allowing me to work at this institute and providing all the resources necessary for my research. I also would like to thank my Doctoral committee member from Pondicherry University, Dr. Ramesh Naidu, for all the support and suggestions.

My gratitude extends to the Department of Science and Technology of India, whose financial support has facilitated my PhD without hindrance. Also, the project presented in Chapter 6 has received funding from the European Research Council (ERC) under the European Union's Horizon 2020 research and innovation programme (PROTOPLANETS, grant agreement No.101002188) and ESO's visitor program.

I thank Dr. Arumugam Pitchai and the entire library staff for their unwavering support in guiding me to the books and journals necessary for my research. Furthermore, I extend my heartfelt thanks to Ashok, Fayaz, Anish, and the team at the Data Center for their assistance. I cannot express enough gratitude towards Mr. Sankaranarayan, Mrs. Vijayalakshmi, Miss. Sandhya and the entire administrative team, including the administrative officer, the personnel officer, and the accounts officer. Their efficiency and readiness to help with administrative tasks ensured a seamless research process.

The warmth and care provided by the Bhaskara staff, including Manjunath, Chandrasekhar, Narayana, and the housekeeping team, have made Bhaskara more than a place of stay; it has been my home away from home. Their kindness and dedication have made every day here a little easier. Finally, my sincere appreciation goes to the supportive staff at the Indian Astronomical Observatory (IAO) in Hanle, the Centre for Research and Education in Science and Technology (CREST) in Hosakote and the Vainu Bappu Observatory (VBO) in Kavalur. To all of you, I offer my deepest gratitude for making this journey not just possible but truly meaningful.

I am immensely grateful to my seniors—Prasanta, Sandeep, Priyanka, Rubinur, Panini, Avinash, Samrat, Snehalata, Chayan, Avrajit, Dipanweeta, Akanksha, Sireesha, Anshu, Prerna, Sreekant, Bhoomika, Megha, Pavna, Amit, Tridib, Ekta, Anirban, Raghubar, Aritra, Priya, Piyali, Annu, Vikrant, Partha, Sharmila, Ankit, Ritesh, Shejeelammal, Bibhuti, Kshitij, Sahel, Soumya, and Manika—for their indispensable guidance and insightful suggestions. Their wisdom and encouragement have been a beacon of support throughout my journey. A special note of appreciation goes to my current batchmates — Sioree, Deepthi, Indrani, Anirban, Pallavi, Jyoti, Fazlu, Sonith, Samriddhi, and Bharat. Since I joined IIA, their friendship and valuable insights have enriched my experience, fostering a nurturing and collaborative environment. I also extend my heartfelt thanks to my juniors—Ayushi, Abishek, Ameya, Amlan, Amrutha, Anisha, Anjali, Annu, Anohita, Aratrika, Arav, Ajay, Chandan, Devang, Dhanush, Guruwinder, Hrishav, Judhajeet, Kajol, Kanan, Khushbu, Lupamudra, Manjunath, Masoor, Neeraj, Nitish, Parvathy, Payel, Puja, Rakshit, Rachana, Radhika, Raveena, Ravi, Reena, Renu, Rishab, Rupesh, Saraswathi, Shashank, Shatakshi, Shubham Jha, Saikhom, Saili, Sambit, Sankalp, Saurabh, Savitha, Sayuf, Satabdwa, Shivani, Shubhangi, Sipra, Soumyaranjan, Sriram, Sujit, Sunit, Sushant, Swagata, Vishnu, and in particular, my roommate Shubham—for their unwavering company and support. Their presence has made every challenge more manageable and every success more enjoyable.

Most significantly, I am forever indebted to my parents, grandparents, and relatives, whose unwavering support and belief in me have shaped the course of my life. Their faith in my decisions, especially my parents' encouragement to chase my dreams, has been the bedrock of my journey. Equally, I am deeply grateful to my partner, Sanghita, and her family, whose support and inspiration have been a constant source of strength, enabling me to pursue my career goals ambitiously. I extend my heartfelt thanks to Mahitosh and Ashok Rakshit for providing me with a taste of home through their homely meals and nurturing care over the last five years, making my academic pursuit feel less daunting. Finally, in moments of solitude, my pet cat Sonkuri (Chinu) provided an unexpected yet vital form of mental support, making the arduous path of my PhD journey less lonely. Without my pet cat, my PhD journey would have been much harder.

Dedicated to

My parents for their love and sacrifices.

My teachers & the people I've encountered at various stages of my life, who have each contributed a unique brushstroke to the canvas of my personal life. Their wisdom, encouragement, and insights have been instrumental in shaping the person I am today.

Abstract

Numerous groundbreaking discoveries have been made in exoplanet science over the past decade. Recent exoplanet search surveys have provided compelling evidence that planets are exceedingly common, with the majority of stars in our Milky Way galaxy hosting one or more planets. The census has also revealed a rich diversity of exoplanetary systems and raised many fundamental and challenging questions. Answers to some of the questions would partly depend on understating the complexity of planet formation and evolution processes and accurately determining host-star and planet properties. In this thesis work, I have studied the different exoplanet populations in terms of their host-star properties and key planetary characteristics. Specifically, I have investigated the mass-metallicity relationship for directly imaged young and massive gas giant planets found at large orbital separations (> 5 AU). The metallicity scatter found in these studies indicates that the formation mechanism of gas giants at large orbital distances is different from the Jupiter analogs found in closer orbits. The age analysis of star-hosting planets, which also forms a part of this thesis, was carried out using elemental abundances, isochrone fitting, and the space velocity of stars determined from GAIA DR3. Combining various pieces of evidence, we were able to show that the formation timeline of small planets precedes the formation of giant planets. That is to say, the stars hosting giant planets are statistically younger compared to those hosting smaller planets. Furthermore, these results are shown to be consistent with planet formation by the core-accretion process and galactic chemical evolution. Finally, using high-contrast imaging data from SPHERE/VLT, I studied the young (~ 3 Myr old) planetary system Lkca 15 and modeled the properties of dust grains and the morphology of the protoplanetary disk in this system with the goal of understanding the influence of grain properties (size and composition) on the formation of giant planets on such short timescales.

“There are an infinite number of worlds, some like this world, other unlike it.”

Epircurus - letter to Herodotus (300 BC)

Contents

List of Figures

List of Tables

Abbreviations

AU	**A**stronomical **U**nit
CARMENES	**C**alar **A**lto high-**R**esolution search for **M**-dwarfs with **E**xoearths with **N**ear-infrared and optical **É**chelle **S**pectrographs
CKS	**C**alifornia-**K**epler **S**urvery
CPS	**C**alifornia-**P**lanet **S**urvery
CoRoT	**Co**nvection, **Ro**tation and planetary **T**ransits
ESPRESSO	**E**chelle **SP**ectrograph for **R**ocky **E**xoplanet- and **S**table **S**pectroscopic **O**bservations
EXPRESS	**EX**treme **PRE**cision **S**pectrograph
GAIA	**G**lobal **A**strometric **I**nterferometer for **A**strophysics
GCE	**G**alactic **C**hemical **E**volution
HARPS	**H**igh **A**ccuracy **R**adial velocity **P**lanet **S**earcher
HATNet	**H**ungarian-made **A**utomated **T**elescope **Net**work
HCT	**H**imalayan **C**handra **T**elescope
HD	**H**enry **D**raper
HESP	**Hanle Echelle SPectrogrpsh**
HFOSC	**H**imalayan **F**aint **O**bject **S**pectrograph
HIRES	**HI**gh **R**esolution **E**chelle **S**pectrograph
HMI	**H**elioseismic and **M**agnetic **I**mager
HST	**H**ubble **S**pace **T**elescope
IAO	**I**ndian **A**stronomical **O**bservatory
IRAF	**I**mage **R**eduction and **A**nalysis **F**acility

JWST	**J**ames **W**eb **S**pace for **T**elescope
KELT	**K**ilodegree **E**xtremely **L**ittle **T**elescope
LAMOST	**L**arge **A**rea **M**ulti **O**bject **S**pectroscopic **T**elescope
MCMC	**M**arkov **C**hain **M**onte **C**arlo
NASA	**N**ational **A**eronautics and **S**pace **A**dministration
NIST	**N**ational **I**nstitute of **S**tandards and **T**echnology
SDO	**S**olar **D**ynamics **O**bservatory
SNR	**S**ignal to **N**oise **R**atio
TESS	**T**ransiting **E**xoplanet **S**urvey **S**atellite
VALD	**V**ienna **A**tomic **L**ine **D**atabase
WASP	**W**ide **A**ngle **S**earch for **P**lanets

Chapter 1

Introduction and Motivation

1.1 Background and Historical Context

The search for the exoplanets beyond our Solar System is the synthesis of humanity's curiosity, advanced technology, and unyielding determination to understand our place in the Universe. Although the concept of other worlds has been a subject of human imagination and philosophy for thousands of years; only in the last ~ 30 years, we have developed the technology to progress from speculation to observation and discovery.

In ancient times, the Greeks debated the possibility of other worlds; for example, the philosopher Epicurus speculated on the existence of infinite worlds, a notion that was more philosophical than scientific. However, it was in the 16th century that fundamentally changed our understanding of the universe, with Nicolaus Copernicus positing that the Earth and other planets orbited the Sun. This heliocentric model laid the groundwork for considering the existence of planets around other stars. Building on the heliocentric model proposed by Copernicus, Giordano Bruno, an Italian philosopher and astronomer, proposed an idea that was ahead of its time: he suggested that the stars we see at night are similar to our own Sun and could have planets of their own, possibly even harbouring life. This expansion of Copernican theory challenged the existing geocentric model of the universe, which held Earth at the centre of a finite cosmos. Unfortunately, Bruno's radical ideas, along with his criticism of certain religious doctrines, led to his persecution by the Roman Catholic Church. He was eventually tried for heresy and burned at the stake in 1600. In the late 17th century, Christiaan Huygens, a prominent astronomer, and Isaac Newton, with his laws of motion and gravitation, furthered the idea that the laws governing celestial bodies were universal. By the 18th and 19th centuries, astronomers like William Herschel, who discovered Uranus, began to contemplate the possibility of other planetary systems seriously. In the late 19th and early 20th centuries, there were a few alleged detections of exoplanets, but these were later debunked as observational errors or misinterpretations. Only in the latter half of the 20th century, with the advent of more sophisticated telescopes and detection methods, it was scientifically possible to detect exoplanets. The real turning point, however, came in the 1990s. The first planet was detected around a pulsar PSR B1257+12 which was observed by Wolszczan & Frail (1992) in 1992. This was soon followed by the discovery of 51 Pegasi b in 1995, a Jupiter-like planet orbiting very close to its host star (~ 4.2 days) by Mayor & Queloz (1995). These first findings not only validated the presence of exoplanets but also challenged pre-existing theories of planet formation, which were primarily based on our solar system.

The early 21st century witnessed a massive surge in exoplanet discoveries, primarily attributed to advancements in detection techniques and instrumentation. Further, the discoveries made by NASA's Kepler Space Telescope in 2009 revolutionized our understanding of exoplanetary systems. Kepler's primary mission was to determine the frequency of Earth-like planets in the habitable zone, areas where conditions might be suitable for life as we understand it*. By its retirement in 2018, Kepler had identified over 2,600 confirmed exoplanets, revealing that multi-planet systems are common and that rocky, potentially habitable worlds might be more prevalent than previously thought.

With the launch of the James Webb Space Telescope (JWST) in 2021 and the continued efforts of ground-based observatories using techniques like direct imaging and gravitational microlensing, the frontier of exoplanetary research promises to investigate deeper into the atmospheres, compositions, and potential biosignatures of these distant worlds. These advances remind us that our quest to understand the universe and our role within it is a continuous journey, driven by a long-standing passion for exploration and enhanced by today's advanced technologies.

1.2 Exoplanets Detection Techniques

Different methods, both direct and indirect, are used to find exoplanets. These methods require high-precision observational techniques, critical analysis of observed data, and comprehensive models of planetary kinematics and structure. So far, except for the direct imaging technique, all these methods depend on some perturbation of the light from the host stars created by the orbiting planets. Some key techniques used to detect these planets are briefly explained below.

---

[*] https://www.jpl.nasa.gov/missions/kepler

1.2.1 Radial velocity

One of the earliest and most successful methods of detecting exoplanets is the radial velocity or Doppler method. So far, it has detected over$\sim$1070 exoplanets. The method is based on the gravitational pull a planet exerts on the star it orbits, as illustrated in Fig. 1.1. As the planet orbits, it causes the star to wobble around a circular or elliptical orbit around the centre of mass. The Doppler effect, observed as shifts in a star's spectral lines, can indicate the presence of orbiting planets due to their gravitational influence on the star's motion. This wobble has a radial component, which brings periodic shifts to the absorption lines of the star's spectra relative to standard lab wavelength (Mayor & Queloz 1995; Butler & Marcy 1996; Butler et al. 2000, 2004). For exact measurements of these line shifts, especially around FGK-type stars, which are located in the visible wavelength area, high-resolution and stable spectroscopic observations are necessary. Subsequent studies in the Near Infrared region (NIR), especially around M-type stars, have been done, and there is ongoing research for planet detection against late M-type stars to brown dwarfs, using radial velocity at the infrared region (Sabotta et al. 2021; Ribas et al. 2023). The method, however, has certain limitations as it is most sensitive to giant planets within $\leq$ 10 au. Further, due to high RV jitter around young stars, this method works well only for older stars ($\geq$ 2.5 Gyrs). Also, detections from the RV method only give a minimum value for a planet's mass and cannot be determined accurately without knowing the inclination of a planet's orbit. The radial velocity technique measures the parameter $M_P.sin\, i$, where M_P is the true mass of the planet, and i is the angle of inclination. The first giant planet 51 Peg b, around a sun-like star, was detected using this method in 1995 (Mayor & Queloz 1995).

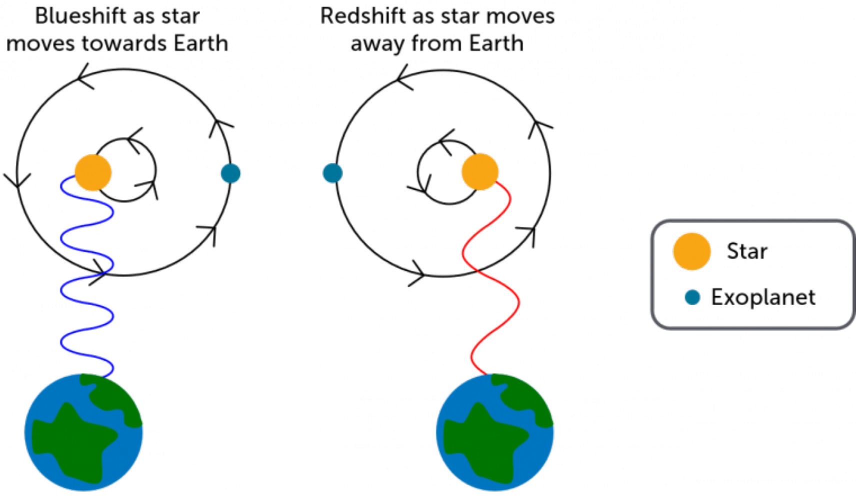

FIGURE 1.1: The radial velocity technique for discovering exoplanets relies on identifying changes in the velocity of a star caused by the shifting gravitational force exerted by an unseen exoplanet as it revolves around the star. Credits: Priceton instruments.

1.2.2 Transit photometry

The transit method of exoplanet detection involves observing for the dip in the star's light when a planet crosses in front of it. The depth of this dimming provides some of the key information about the planet's size in relation to its host star (Charbonneau et al. 2000). So far, the transit has detected over ~ 4146 exoplanets (NASA Exoplanet Science Institute 2024). However, to observe a transit, the planet's orbit must lie at a small angle close to edge-on along our line of sight. It also does not provide any information regarding the planet's mass and is more favourable in detecting giant planets orbiting very close to their host star ($\lesssim 1$au). Transit photometry has been mainly successful due to the space-based Kepler and TESS missions since transit detection from ground-based observations has been less fruitful. Fig. 1.2 shows a schematic diagram for the transit method detection of an exoplanet. The first exoplanet detected using transit photometry is HD 209458b by Henry et al. (2000). Upcoming missions Plato (PLAnetary Transits and Oscillations of stars) and Ariel (Atmospheric Remote-Sensing Infrared Exoplanet Large-survey) will be launched in 2026 and 2029, respectively. These

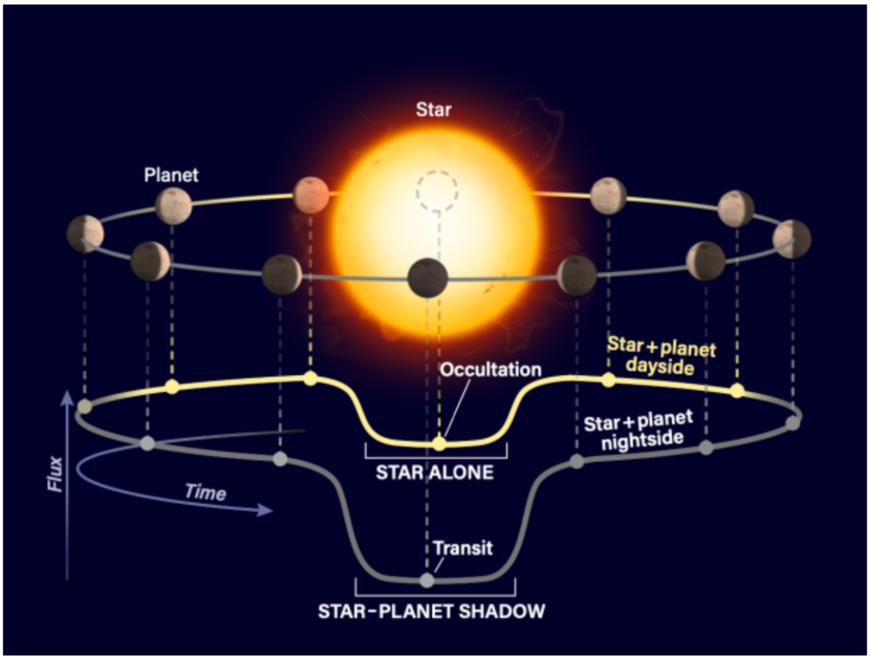

FIGURE 1.2: The transit method detects planets by observing dip in starlight when a planet crosses between Earth and its host star. This technique is effective only when the alignment of the star and planet coincides with our viewpoint from Earth. Credit: Astronomy: Roen Kelly

two missions are expected to characterize known exoplanets and also detect new exoplanets.

1.2.3 Direct imaging

Direct imaging of exoplanets is a challenging yet increasingly viable method due to advancements in adaptive optics and coronagraphs. This technique is particularly effective for young, giant exoplanets that are in far-away orbit from their host stars (Luhman et al. 2006; Marois et al. 2008a). These young planets, typically less than 100 million years old, emit thermal radiation in the mid and far-infrared range, where the emissions from their host stars are less intense. Coronagraphs are used in direct imaging to block the light of the host stars, to improve the contrast ratio between the host star and the planet, allowing the fainter light of the planets to be observed. Direct imaging not only captures images of these exoplanets but also opens the door for studying their atmospheres through spectroscopy. This can reveal critical information about the planet's composition and weather patterns. To date, around 69 planets have been discovered using this method (NASA Exoplanet Science Institute 2024). 2M1207b is the first exoplanet detected using direct imaging by Chauvin et al. (2004). Future large segmented mirror telescopes such as the thirty-meter telescope (NFIRAOS+IRIS) and extremely large telescope (METIS+HARMONY) will be able to detect even smaller planets and much closer to their host star (≤ 0.1") by high-contrast imaging.

1.2.4 Gravitational microlensing

Based on Einstein's theory of general relativity, massive objects can bend and magnify the light of background objects. In the context of exoplanet detection, if a star (acting as a lens) passes in front of a more distant star (source), the gravitational field of the lensing star can magnify the light of the background star (Beaulieu et al. 2006; Kains et al. 2013). If the lens star harbours a planetary system, then those planets can also act as lenses, each one producing a short deviation in the brightness of the source. Gravitational microlensing is particularly sensitive to planets that are at a distance of 1 to 5 au from their host stars, making it complementary to other methods. To date, $\sim$ 204 exoplanets have been detected using microlensing. The only major challenge in microlensing is that the system can be observed once and no repeated observation is possible as the alignment for the two stars to act as lens is mostly not repetitive in our time scales. OGLE 2003–BLG–235b is the first planet detected using microlensing by (Bond et al. 2004). Nancy Grace Roman Space Telescope expected to launch in 2027 will be able to detect every type of solar‘ analogue except Mercury.

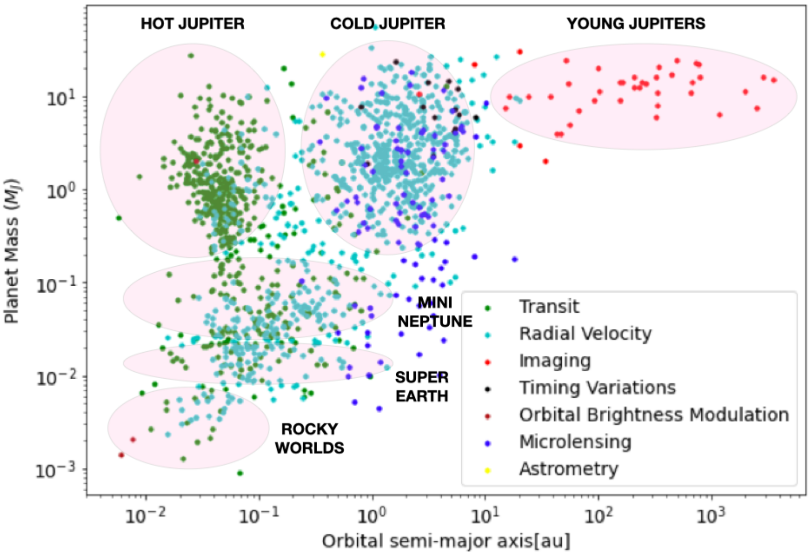

FIGURE 1.3: Distribution of confirmed exoplanets in mass orbital-distance plane. Symbols are color-coded according to discovery methods.

1.2.5 Astrometry

This method involves the precise measurement of a star's position in the sky. As a planet orbits a star, it induces a wobble in the star's position (Sahlmann et al. 2011; Benedict et al. 2017; Gaia Collaboration et al. 2018). By measuring this wobble over time, astronomers can infer the presence of a planet. Astrometry has the potential to detect planets at further distances from their stars when compared to the transit or radial velocity method. However, the method requires very precise measurements, making it challenging with current technology. To date, three planets have been detected using astrometry. However, with the release of GAIA DR4 data in 2025, the expected number of planets detected by astrometry using GAIA will surpass other detection techniques. DENIS-P J082303.1-491201b is the first planet detected using astrometry by Sahlmann et al. (2013).

1.3 Exoplanet Demographics

1.3.1 Detection methods and their influence on demographics

The field of exoplanet demographics is deeply influenced by the different detection techniques, each with its own set of sensitivities and biases. The transit method, used extensively by missions like Kepler, has not only detected giant planets, orbiting close to the star but also detected thousands of smaller planets, including Earth-sized and super-Earths, thanks to its ability to detect slight dimmings in starlight caused by planetary transits. On the other hand, the RV is more biased toward detecting giant planets in mainly close to moderate orbits around older stars as shown in Figure 1.3. The radial velocity method has been important in detecting many of the earlier exoplanets but tends to find Jupiter-like planets, skewing our perception towards a universe abundant in such planets, while smaller terrestrial ones might be less detected. In the case of directly imaged planets, this technique is mainly effective for young giant planets orbiting far 10s to 100s of au from their host stars. Thus, direct imaging introduces a bias toward detecting bright, young gas giants at wide separations from their host stars. For gravitational lensing, it is sensitive to a larger range of planets, including those in habitable zones. This method offers a broader view of exoplanet demographics, including the detection of low-mass planets at large distances from their stars. Finally, astrometry, which measures tiny motions of a star in the sky due to the gravitational tug of an orbiting planet, is also sensitive to giant planets in close to moderate orbits.

Overall, each detection method contributes uniquely to our understanding of exoplanet demographics, but they also introduce specific detection and selection biases. Thus, no single method can span the entire parameter space of exoplanets.

These biases highlight the necessity of using a multi-method approach in order to gain a more comprehensive understanding of the different types of exoplanets in our galaxy.

1.3.2 Different exoplanet populations

Exoplanets come in different shapes and sizes as shown in Figure 1.3. Here I provide a brief description of the primary types of exoplanets:

- **Hot-Jupiters:** These are gas giants similar to Jupiter in mass (0.3 to 5 M_J), but they orbit very close to their parent star ($P < 10$ days), which results in very high surface temperatures. These are mainly detected by Transits.
- **Cold-Jupiters:** Similar to hot Jupiters in mass, they orbit at a moderate distance from their parent star ($10 < P < 200$ days). These are mainly detected by Radial velocity.
- **Young-Jupiters:** These are similar in mass to that of hot and cool Jupiters, but orbit at a very large separation ($P \geq 1000$ days) or more. They are young and emit light of their own. They are mainly detected by direct imaging.
- **Super-Earths:** These planets have a mass greater than Earth's but significantly less than that of Uranus or Neptune ($0.8 < R_\oplus < 1.2$). Depending on the mass these planets are mostly rocky, like Earth, or can be ice giants if they possess significant amounts of gas.
- **Mini-Neptunes:** Slightly bigger than super-Earths ($2 < R_\oplus < 4$), these planets have a thick atmosphere and are thought to be composed largely of gas. They have a rocky core surrounded by an envelope of hydrogen and helium.
- **Terrestrial:** These are rocky, Earth-like planets with solid surfaces, smaller and denser than gas giants, and usually within 2 AU of their star. Composed

mainly of silicate rocks or metals, they have masses from 0.5 to 1.5 $M_\oplus$ and short orbital periods. These are mainly detected by the transit method.

1.3.3 Exoplanet population statistics and trends

Given that we have detected > 5500 planets, it becomes important and statistically feasible to analyse the different exoplanet populations and the trends in order to understand how the populations of small and giant exoplanets differ statistically. Below, I discuss some of the important exoplanet statistics and trends from literature, that are well established.

- **Frequency and distribution of exoplanet types:** Statistical analyses have revealed a diverse range of exoplanet types, including gas giants, ice giants, terrestrial planets, and super-Earths. One notable trend is the surprisingly high frequency of super-Earths and mini-Neptunes, which don't have any analogues in our solar system. Further planets like hot Jupiter are absent in our solar system (Akeson et al. 2013). Further, it is also found that the giant planets are most common at distances of 1–10 au, with a significant fourfold increase in occurrence around 1 au. Beyond this range, the occurrence of giant planets declines, particularly at distances greater than 8 au (Fulton et al. 2021). These findings indicate that our solar system architecture can be somewhat unique when compared to the current population of exoplanets.
- **Radius valley/Fulton gap:** The Radius valley, also known as the Fulton gap, is observed in the radius histogram of exoplanets, specifically a scarcity of planets with radii between $1.5R_\oplus$ and $2R_\oplus$ in the close-in orbits (~ 3 to 30 days). It highlights two main types of low-mass exo-planets: larger super-Earths and smaller mini-Neptunes. This gap is thought to result from

processes like photoevaporation, which strips gaseous layers from planets near their stars, leaving rocky cores (Fulton et al. 2017).

- **Star-Planet correlations:** The correlations between the chemical composition of a star and its planets have been a major field of investigation since the detection of early exoplanets (Santos et al. 2000; Fischer et al. 2002; Fischer & Valenti 2005). For instance, it has been observed that stars with planets have higher metallicity than stars without planets. This correlation supports the core accretion theory of planet formation. Further studies have found that stellar metallicity increases as a function of planet mass (Narang et al. 2018). Moreover, it has also been shown that giant planets are on average hosted by young stars (Swastik et al. 2022, 2023).
- **Multi-planet systems:** Almost one in five exoplanet-hosting stars have more than one detected planet. These systems, where several planets orbit the same star, offer valuable insights into the dynamics and evolution of planetary systems.

1.4 Star-planet Connection and its Link to Protoplanetary Disk

The study of exoplanets, their host stars, and their protoplanetary disks from which they form requires an accurate and uniform determination of stellar parameters, including the composition of the host-star and the circumstellar environment. This is important as the stellar and disk properties, such as its mass, temperature, and chemical composition, directly influence the formation and evolution of its companion planet. Thus, a homogeneous approach is necessary to investigate the properties of exoplanet-hosting stars for drawing meaningful conclusions about exoplanet demographics. Since stars, protoplanetary disks and planets form from the same molecular cloud, their compositions are intricately connected. This connection can be observed through the chemical imprint left by various processes such as dust removal, planet accretion and disk accretion. By studying these imprints, we can gain insights into the formation, migration, and evolution mechanisms of planetary systems. For instance, (Meléndez et al. 2009) found peculiar chemical signatures in the Sun when compared to solar twins, suggesting the influence of planet formation processes on stellar composition. Further, several studies such as e.g (Fischer et al. 2002; Fischer & Valenti 2005; Narang et al. 2018; Desrochers et al. 2018) have shown that the stellar abundance is intrinsically linked to the type of planet it hosts. Thus, it is important to study the host star and/or its protoplanetary disk to shed light on how planets form.

1.5 Techniques to Study Planet Hosting Stars

1.5.1 Chemical analysis

Chemical analysis of host stars primarily involves spectroscopy. By examining the spectral lines, we can identify the chemical elements present in the star's photosphere and determine their abundances. High-resolution spectroscopy is particularly crucial for this purpose as it allows us to determine the exact composition of the stellar photosphere using radiative transfer models. Chemical analysis of stars is also important as it helps us to understand the star's formation timeline and the potential for planet formation in its system. Chapter 2 and Chapter 3 of this thesis detail how studying the chemical composition of the host-star can provide insights about planet formation.

1.5.2 Kinematic analysis

Kinematic analysis of host stars involves tracking the past motions of a group of stars to determine when they were physically closest, which is thought to be the period of their formation. This is done by measuring the star's radial velocity, proper motion (the star's apparent motion across the sky), and parallaxes. Together, these measurements help in understanding the dynamic history and future trajectory of the star within its galactic environment. With the release of GAIA DR3 data in July 2022, it was made possible to investigate the kinematic properties and the stellar orbital parameters for a large number of exoplanet-hosting stars which is detailed in Chapter 4.

1.5.3 Age analysis

Since the age of a star is not a direct measurable quantity, determining the age of host stars is quite challenging. One common technique is asteroseismology, which involves studying sound waves that travel through the star's interior. These waves affect the star's brightness and provide clues about its internal structure and age. However, it requires longer time-series data, which is only accessible for a limited sample of stars. Additionally, it only applies to stars hotter than about spectral type K, as cooler stars do not typically exhibit the oscillations required for estimating ages using asteroseismology (Silva Aguirre et al. 2015; Christensen-Dalsgaard & Aguirre 2018). Another method is to compare the star's characteristics, such as luminosity and temperature, with stellar evolution models. This comparison can estimate the star's age based on its position on the Hertzsprung-Russell diagram. One can also estimate the stellar ages from the star's kinematic properties or its membership in stellar clusters, whose ages can be more easily determined.

Chapter 4 and Chapter 5 of this thesis discuss the estimation of stellar ages of the planet-hosting stars using the isochrone method.

1.5.4 Direct imaging of circumstellar disks

For the nearby star forming regions, direct imaging stands as a crucial technique for observing circumstellar disks and their embedded planets. Recent breakthroughs, particularly with instruments like the ALMA, VLT and the JWST, have captured the images of these disks, shedding light on their structure, composition, and the processes of planet formation within them. Studies such as those by Andrews et al. (2018) and Avenhaus et al. (2018) have provided critical insights into disk morphology and dust distribution, offering clues about the early stages of planetary system development. Thus, direct imaging not only enhances our understanding of individual systems but also contributes to the broader knowledge of planetary formation and evolution. Chapter 6 of this thesis investigates the LkCa 15 system and its proto-planetary disk compositions in order to understand the role of the circumstellar disk in planet formation.

Each of these techniques contributes to a comprehensive understanding of host stars, their properties, and their circumstellar environments. They are often used together to provide a more holistic picture of the host-stars and their role in planet formation.

1.6 Challenges in Investigating Star-Planet Connection

Investigating the properties of host stars is a complex task, fraught with various challenges that come from observational limitations, intrinsic stellar properties, and data processing techniques. These challenges can be categorized into several key areas:

- **Signal-to-Noise Ratio and instrumental limitations:** High-quality observations are essential for studying host star properties, but achieving a sufficient signal-to-noise ratio (SNR) can be challenging. This is particularly true for faint or distant stars. Additionally, instrumental limitations, such as the resolution of spectrographs or the sensitivity of detectors, can constrain the accuracy of the observed data, impacting the precision of measurements like stellar composition, temperature, and luminosity.
- **Stellar activity and variability:** Stars, including the planet-hosting stars, often exhibit various forms of activity, such as flares, spots, and magnetic cycles, which can complicate the analysis of their properties. This variability can introduce noise into the data and mask or mimic certain stellar properties, making it difficult to obtain accurate measurements. Disentangling these effects to study the inherent properties of the star requires modeling and data analysis techniques.
- **Availability of homogeneous datasets:** A significant challenge in stellar astrophysics is the lack of homogeneous datasets. Different telescopes and instruments often have varying sensitivities, calibration methods, and data processing techniques, leading to inconsistencies in the data. This heterogeneity can introduce systematic errors and make it difficult to compare

results or combine datasets from different sources, hindering a comprehensive understanding of host star properties.

- **Complexity of stellar atmospheres:** Stellar atmospheres are complex and dynamic, with various layers and processes that are not fully understood. Modeling these atmospheres accurately is challenging due to factors like convection, magnetic fields, and radiation processes. This complexity makes it difficult to interpret observational data and to understand the physical conditions within the star.
- **Data processing and analysis:** The vast amounts of data collected from stellar observations require advanced data processing and analysis techniques. Extracting meaningful information from this data involves dealing with noise reduction, signal extraction, and the application of complex algorithms, often requiring significant computational resources and expertise in data science.

1.7 Scope of the Thesis

My thesis endeavors to understand the intricate role played by the chemical composition of the cloud from which the stellar hosts and their protoplanetary disks have formed and how their composition plays a key role in the process of planet formation. The journey of my investigation started with a focus on young giant planets that are observed through direct imaging. The main goal of this work was to investigate the influence of the metallicity of host stars of Jupiter ($1M_J \leq M_P \leq 4M_J$) and super-Jupiters ($4M_J < M_P \leq 25M_J$). We find that metallicity plays an important role in the formation of Jupiters, but we don't see any correlation between the planet's size and its metallicity for super Jupiters. These findings hint at distinct planet formation mechanisms: core accretion for Jupiter-like planets and disk instability for the super-Jupiters. This is discussed in detail in chapter 2.

Investigating deeper, we probed whether the chemical composition of host stars, which is a tracer of the initial molecular cloud from which the star and planet have formed, offers any clues to planet formation. Most of the previous studies involving exoplanet host stars' chemical abundances were mainly focused on [Fe/H] (e.g. Gonzalez 1997; Santos et al. 2001; Fischer & Valenti 2005; Udry & Santos 2007). Although Fe is an essential element believed to play a key role in planet formation, the formation mechanism of different elements is vastly different; we expect their signatures to show up in the star's chemical composition. Since my main research interest is understanding planet formation, I decided to study the elemental composition of exoplanet-hosting stars to investigate any significant differences in the abundances between stars hosting small and giant planets. Upon investigation, we find that the host stars of small planets are α-rich when compared to host stars of giant planets. This is because to form a giant planet, the core of 10-15$M_\oplus$ must be formed before the gas in the proto-planetary disk dissipates. Since at the early stages of the Milky Way, the ISM was enriched mainly with α elements (Mg, Si, Ca, Ti, etc.) from Type II supernovae; the formation was much slower compared to the gas dissipation rate and thus ended as forming small planets. As the ISM enrichment increased over time and with the subsequent enrichment of ISM with Fe-peak elements (Fe, Ni, Co, Mn, etc.) from Type Ia supernova, the core began to form much faster. It thus began the onset of giant planet formation. This work has been explained in detail in Chapter 3.

To verify our findings from the chemical analysis of exoplanet-hosting stars, we turned to the GAIA DR3 dataset, analyzing spectroscopic, photometric, and astrometric data to deduce fundamental stellar parameters like velocity dispersion, Z_{max}, and eccentricity. These parameters serve as proxies for stellar ages in a group of stars, revealing distinct age differences between hosts of small and giant planets. Our analysis of galactic space velocities and orbital parameters further supports the notion that stars with giant planets are statistically younger than those hosting smaller planets. This conclusion was corroborated by an in-depth examination using isochrone fitting methods, accounting for various parameter and model uncertainties. I have detailed the findings in chapter 4.

The next phase of my research investigates newborn planetary systems, with a keen focus on LkCa 15, a pre-mainsequence star around $\sim$ 1 to 3 Myrs old. This period marks a critical stage in planet formation, presenting an unparalleled opportunity to observe the formation of these planetary systems. LkCa 15 is suspected to host two planets (Sallum et al. 2015) in the inner part of the disk. However, subsequent studies by Carrera et al. (2019) have suggested it to be inner disk signals. Nevertheless, the advent of advanced instruments like VLT-SPHERE has now bridged the gap, enabling us to probe these previously inaccessible young systems within Star Formation Regions (SFRs) $\sim$ 1-5 Myrs. At such young ages, both planets and disks emit brighter signals, enhancing detectability and potentially unveiling a significant number of new planets, thereby enriching our statistical understanding of planetary prevalence. Moreover, I have investigated the correlations between disk properties and planet formation. Using K band images from SPHERE/VLT obtained using RDI star-hopping technique (Wahhaj et al. 2021) and using radiative transfer modelling, we've managed to a) measure disk properties with remarkable precision, b) remove the disk to isolate and detect any planets that might be hidden on top of the disk. This capability allows us to refine our constraints on disk morphology significantly. Through modeling with the radiative transfer code RADMC-3D, we aim to understand the influence of disk properties, such as flaring and presence of cavity, on the formation of massive planets within these short timescales. Such models not only facilitate comparisons with observed disk properties but also help us in predicting disk behaviors that are critical during planetary formation. The combination of dynamical models and observational data helps our understanding of disk-planet interactions. By aligning model predictions with observed disk morphologies, we can validate the conditions necessary for planet formation, potentially aligning theoretical frameworks with empirical evidence. My work represents a step towards unraveling the complexities of planet formation,

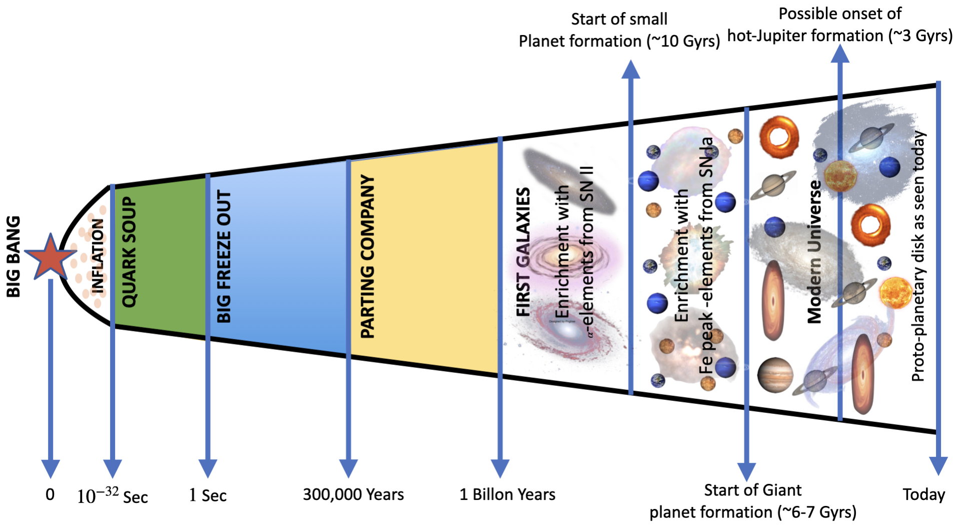

Figure 1.4: The galactic formation timeline of planets as suggested from different analyses from my PhD thesis.

leveraging cutting-edge technology and innovative methodologies to peep into the cradle of planets.

In summary, my thesis provides a comprehensive exploration of how stars and their surrounding environments play a key role in planet formation (Figure 1.4). Using different observation techniques like direct imaging, spectroscopy, photometry, polarimetry and astrometric data analysis, I have sought to trace the evolutionary trajectory of planets from their nascent stages in protoplanetary disks to several billion years into their existence. The goal is to piece together a detailed narrative of planet formation, shedding light on the influences that shape these celestial bodies.

1.8 Outline of the Thesis

- **Introduction :** This chapter introduces the journey of exoplanet discovery, outlining the historical context, various detection techniques, and the significance of understanding the star-planet connection. It highlights the evolution of exoplanet research from speculative philosophy to the sophisticated technology-driven field it is today, marking significant milestones such as the first confirmed detections in the 1990s. The chapter details the different methods used to detect exoplanets, including radial velocity, transit photometry, direct imaging, gravitational microlensing, and astrometry, each with its strengths and limitations. It also addresses the demographics of exoplanets, revealing a universe filled with a wide variety of planets, from hot Jupiters to Earth-like worlds, and the statistical trends that hint at our solar system's uniqueness. A deep dive into the chemical, kinematic, and age analysis of planet-hosting stars offers insights into their formation and evolution, emphasizing the interconnectedness of stars, their planets, and the circumstellar disks from which they emerge (refer to Chapter 1).

- **Spectroscopic analysis of host stars of directly imaged planets:** In this chapter, I analysed the high-resolution spectra of 18 young stars that host directly imaged planets. I used archival high-resolution spectroscopic data from HARPS, FEROS, UVES and HIRES. By using iSpec, a radiative transfer code to model stellar spectra, together with the Bayesian Monte Carlo Markov Chain (MCMC) technique, I estimated the stellar atmospheric parameters and metallicities of these stars. My analysis shows that metal-rich stars tend to have Jupiter-sized planets (with a mass up to 5 times that of Jupiter), which supports the core accretion theory of planet formation. On the other hand, for planets larger than 5 Jupiter masses, known as super Jupiter, we found a more scattered distribution of the stellar metallicities, indicating that gravitational instability might be the process by which these planets formed (refer to Chapter 2).

- **Galactic chemical evolution of exoplanet hosting stars:** In this chapter, I investigated the chemical composition of 968 stars with exoplanets from the HARPS-GTO, CKS and CPS samples. I analysed the abundance of 17 elements to understand their role in planet formation. A significant part of my findings is the inverse relationship between the abundance of alpha elements relative to iron and the mass of planets, showing that stars with smaller planets have more alpha elements than those with giant planets. This suggests that systems with smaller planets came into being earlier in the galaxy's history. In contrast, systems with giant planets developed later, only when the ISM was enriched with Fe-peak elements. Multi-planetary systems with low and high-mass planets didn't show a clear trend, which might indicate they were younger. Overall, my study links the process of forming planets with the chemical enrichment in the galaxy, indicating that low-mass planets were forming at all stages of the galaxy, while the formation of giant planets happened around younger stars that were chemically Fe-rich (refer to Chapter 3).

- **Kinematics age analysis of planet-hosting stars from GAIA DR3:** In this chapter, I analyzed the GAIA DR3 data to look into the chemical composition, kinematics, and ages of stars that have planets around them. My findings suggest that stars with giant planets are metal-rich but are low in alpha elements, which means they likely formed later in the galaxy's history after the ISM enrichment with Fe-peak elements. I found that most of these stars with planets are part of what's called the thin disk, which is a younger population of stars. The study also finds differences in galactic space velocities and orbital parameters between stars hosting small and Jupiter-like planets. Small planet-hosting stars exhibit higher Z_{max} and eccentricities, trends of older stars, compared to their giant planet-hosting counterparts. These observations back up the idea that the giant planets formed later, at a time when there were enough Fe and Fe-peak elements in ISM, which is important for how planets grow according to the core-accretion theory (refer to Chapter 4).

- **Age analysis of extra-solar planets from stellar isochrone models:** In this chapter, I determined the ages of over 2336 stars with planets orbiting them by using a method known as isochrone fitting. I found a significant link between the mass of the planets and their host stars. Even though there are some differences in the age estimates due to the models used, the results consistently showed that most of the planets (between 70% and 85%) orbit stars that are younger than 7 Gyrs. This suggests that the majority of planet formation took place after there was enough material in ISM. These findings also support the core-accretion theory of planet formation. My study indicates that small planets began forming around 6-7 billion years ago, while the formation of giant planets is a more recent event, mainly in the last 4-5 billion years (refer to Chapter 5).

- **Understanding planet formation in LkCa 15 proto-planetary disk:** In this chapter, I present the images of the LkCa 15 protoplanetary disk using Ks-band in both total intensity and polarized light, using the star-hopping RDI technique to address the issue of self-subtraction seen in earlier ADI observations. The goal was to detect new planets and to study the disk's shape and morphology. By using RADMC-3D, a radiative transfer code to model proto-planetary disks, I can accurately reproduce most of the disk morphologies, which includes identifying a variety of grain sizes in the disk: submicron grains within the 21-52 au region, micron-sized grains from 26 to 90 au, and millimetre-sized grains spanning 46 to 131 au. The disk shows significant flaring and a radial layout of dust grains, with finer grains located nearer to the star and coarser grains found further away. Although new planets were not detected, I could put upper mass limits for any possible planets inside the disk (refer to Chapter 6).

- **Conclusion :** In the concluding chapter of this thesis, I have presented a detailed summary of all the findings and results obtained in this thesis. Also, I have listed the scientific problems that I plan to investigate in the future (refer to Chapter 7).

Chapter 2

Spectroscopy of Stellar Hosts of Directly Imaged Planets [*]

2.1 Introduction

Existing planetary search methods are constrained by severe selection effects and detection biases (e.g. Cumming 2004; Zakamska et al. 2011; Kipping & Sandford 2016). However, multiple detection techniques sample different regions of the star-planet parameter space, thus providing useful insights about the rich diversity and underlying population of the planetary systems. While the transit and radial velocity methods have been successful in unraveling planet population spanning extremely close-in (∼0.1 AU) to moderate orbits (∼10 AU), the direct imaging is

---

[*] Part of this work have been published in Swastik et al. (2021).

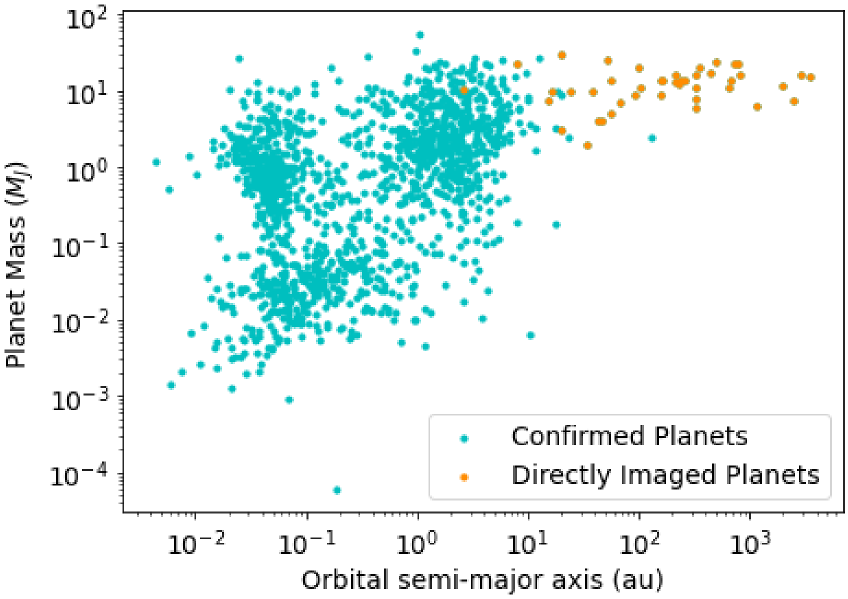

FIGURE 2.1: Distribution of confirmed exoplanets in mass orbital-distance plane. The orange dots represent planets discovered by the direct imaging technique, and the blue dots are planets discovered by other detection methods. The data points are taken from the NASA Exoplanet Science Institute (2024).

most useful for probing the planetary architecture in the outermost regions (10s-1000s AU) of stars (Winn & Fabrycky 2015; Bowler 2016; Baron et al. 2019). The planet population discovered by the transit technique and radial velocity largely belongs to main-sequence and post-main sequence stars. In contrast, the direct imaging method has been most effective in uncovering newly formed warm and massive planets in wider orbits around nearby young stars in the solar neighborhood (e.g. Lagrange 2014; Bowler 2016; Meshkat et al. 2017; Baron et al. 2019).

Following the success of the Kepler space mission, a wealth of new information has emerged about the planet population associated with main-sequence and evolved stars (Borucki et al. 2011a; Howard et al. 2012; Mulders et al. 2016; Batalha 2014; Johnson et al. 2017; Petigura et al. 2017; Narang et al. 2018; Fulton & Petigura 2018; Petigura et al. 2018). The growing number of exoplanets from space discoveries and their follow-up studies from the ground is making planetary statistics more robust and significant. Because of their large number, the statistical properties of close-in planets (≤ 1 AU) and their host stars are relatively better studied. A great deal of research effort has been devoted to understanding the diversity of planets and the characteristics of their primary hosts. Many useful insights have been gained by studying the interdependence of planetary properties and stellar parameters (Gonzalez 1997; Santos et al. 2000, 2004; Fischer & Valenti 2005; Udry & Santos 2007; Johnson et al. 2010b; Ghezzi et al. 2010; Mulders et al. 2016; Mulders 2018; Narang et al. 2018; Adibekyan 2019). Stellar metallicity and planet occurrence rate, for example, is one such important correlation for testing the veracity of various planet formation mechanisms under different conditions (e.g. Udry & Santos 2007; Mulders 2018; Santos et al. 2017; Narang et al. 2018; Banerjee et al. 2024). However, these results have been demonstrated only for stars with close-in (≤ 1 AU) planets that have been detected primarily by radial velocity and transit methods.

Directly imaged planets (DIP) are located at relatively large orbital distances from their host stars ($2.6 - 3500$ AU), which provides a unique window to probe an entirely different planetary population. While there is a general consensus that giant planets are common around high-metallicity stars compared to their low-metallicity counterparts, a clear picture is still lacking about the role of metallicity and the exact mechanism of giant planet formation at larger distances.

The majority of the 69 planetary companions discovered so far by direct imaging technique are massive planets at larger orbital distances from the host stars NASA Exoplanet Science Institute (2024). Figure 2.2(a) shows the confirmed exoplanets in a mass - orbital distance plane, where the segregation of planets into different populations is evident. Treating DIPs as a separate population and studying their hosts' properties can provide vital clues about the dominant mechanism of planet formation at large orbital distances from the star. The parameter space of massive planets at long orbital periods occupied by DIPs is relatively unexplored for the correlation studies of host star-planet properties. Also, the high-mass limit

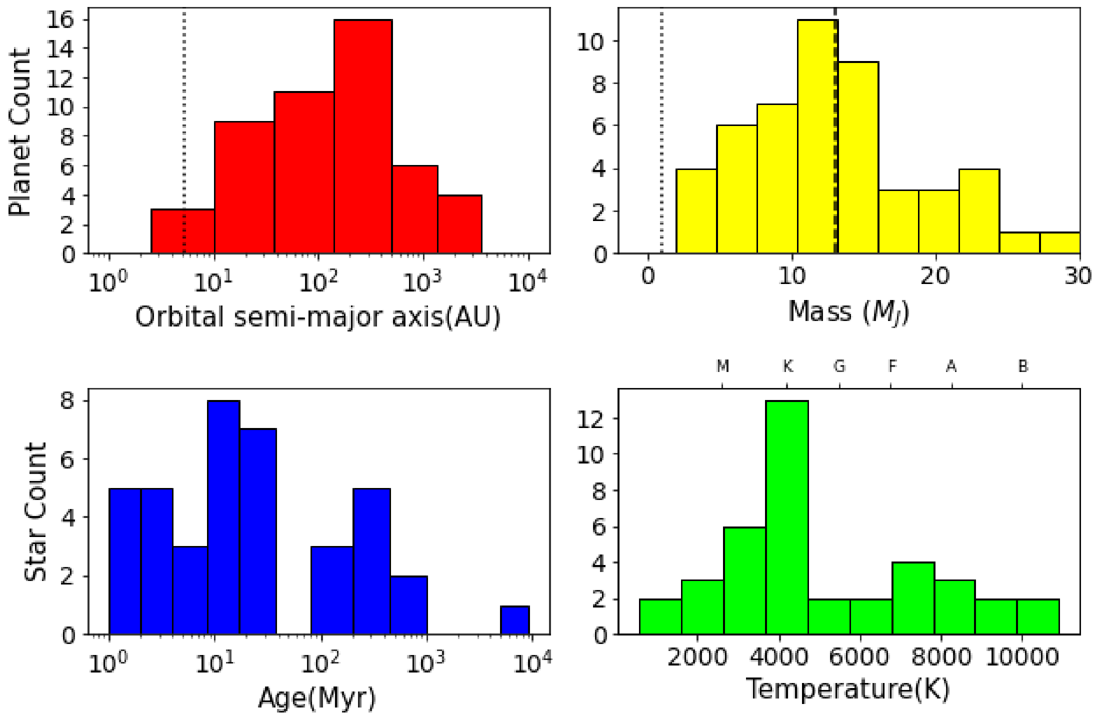

FIGURE 2.2: Histograms of orbital distance and mass of directly imaged systems (top panel) with age and temperature distribution of their stellar hosts (bottom-panel). The dotted lines in the top panel represent Jupiter's orbital distance and mass, while the dashed line at 13 $M_{\rm J}$ is the minimum deuterium-burning mass limit.

of wide-orbit planets overlaps with the low-mass tail of brown dwarfs and sub-stellar companions. Therefore, in certain cases, the limitation of low-number DIP statistics can be partly overcome by a complementary study of known brown-dwarf companions sharing the same parameter space (Ma & Ge 2014; Vigan et al. 2017; Nielsen et al. 2019). Therefore, it is essential to investigate the role, if any, of the host-star metallicity in influencing the process of the giant planet and brown dwarf formation over a wide range of astrophysical conditions.

We have examined the confirmed list of DIP hosted on NASA's Exoplanet archive (Akeson et al. 2013)[†]. The available stellar and planetary parameters are compiled from the composite planet data table for known exoplanets and published

---

[†] https://exoplanetarchive.ipac.caltech.edu/index.html

literature. Each of these systems has been studied and discussed in depth by individual discovery and follow-up chapters. However, there are limited instances where the DIP distribution and stellar properties are studied as separate ensemble (Neuhäuser & Schmidt 2012; Bowler 2016).

At the time when the work was done in 2020, 45 stars hosting DIPs were listed in Table 2.1 are taken from the NASA Exoplanet archive. The atmospheric properties of the stars hosting these wide orbit companions are not very well studied, and most notably, the metallicity is known only for 14 such systems.

In general, previous studies (Buchhave et al. 2014; Santos et al. 2017; Narang et al. 2018; Schlaufman 2018) have shown that the average metallicity of the host star increases as a function of planetary mass. However, the trend reverses for most planetary mass above 4-5 M_J (Narang et al. 2018; Santos et al. 2017; Schlaufman 2018; Maldonado et al. 2019). These results suggest the possibility of two planet formation scenarios with the Jupiter-like planets ($0.3 - 5M_J$) likely formed by the core-accretion process(e.g. Mizuno 1980; Pollack et al. 1996; Ida & Lin 2004; Mordasini et al. 2012) and the massive super-Jupiters ($> 5M_J$) via the disk instability mechanism (e.g. Boss 1997; Mayer et al. 2002; Boss 2002; Matsuo et al. 2007; Santos et al. 2017; Narang et al. 2018; Goda & Matsuo 2019). These findings, backed by large statistics, truly reflect the underlying metallicity-mass distribution of compact planetary systems (orbital period $\leq$ 1 yr). This raises another important question whether or not such trends hold for planets formed at vast orbital distances from the central star. Since DIPs are found at large distances from their host stars, this planet population motivates us to explore the mass-metallicity relationship for giant planet populations at large distances in light of various planet formation scenarios. This chapter has used high-resolution spectra available from various public archives to determine the stellar parameters and metallicity of 18 stars hosting DIPs in a consistent and homogeneous way to study the various correlations among stellar and planetary properties.

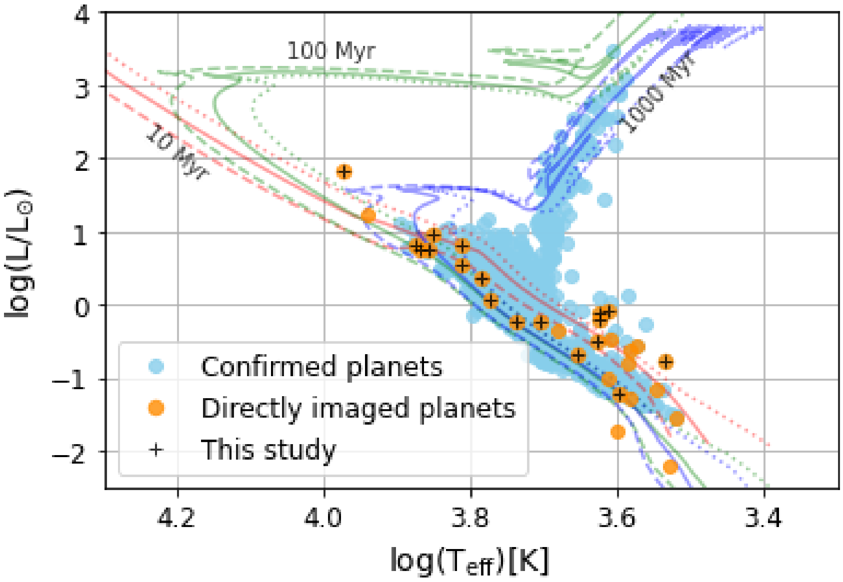

FIGURE 2.3: The location of confirmed exoplanet hosting stars in the HR diagram. The $T_{\rm eff}$ and luminosity L are compiled for 2831 confirmed planet hosts that are cross-matched with *Gaia* DR2 catalog. The sky-blue circular symbols represent the host stars of planets discovered by indirect methods. The orange circles show the stellar companions of directly imaged planets. A subset of 18 DIP host stars used in the present study is indicated by orange circles with the '+' symbol in the middle. Isochrones computed using Choi et al. (2016) are shown for three age groups (red-line: 10 Myr, green-line: 100 Myr and blue-line: 1000 Myr) and metallicity range: solid-line [Fe/H]=0 dex, dotted-line [Fe/H]=0.5 dex and dashed-line [Fe/H]=-0.6 dex.

The rest of the chapter is structured as follows. In section 2.2, we give a brief overview of directly imaged planetary systems. We describe our sample and give the selection criteria in section 2.3. Our methodology and Bayesian approach used for the estimation of various stellar parameters is discussed in section 2.4. In section 2.5 and section 2.6, we discuss our results and compare them with previous findings. Finally, we give our summary and conclusions in section 2.7.

2.2 Directly Imaged Systems

Of the 5500+ confirmed planets, the direct imaging technique accounts for the discovery of 69 planetary-mass objects around 61 stars. Among these, 55 are in a single planetary system, and five are in multi-planetary systems -LkCa 15 (Sallum et al. 2015), TYC 8998-760-1 (Bohn et al. 2020), HD 206893 (Hinkley et al. 2023), bet Pic (Lagrange et al. 2010), and PDS70 (Keppler et al. 2018) with two planets each, and HR8799 (Marois et al. 2008b) with four. The majority of them are discovered from deep imaging surveys of nearby star-forming regions. These planet search programs largely target young pre-main sequence stars that belong to nearby stellar associations and moving groups, all within 200 pc of the Sun (Bowler 2016). The high luminosity of planets at the early formation stage makes them amenable to direct imaging. Further, the high-resolution and high-contrast imaging of planets is facilitated by adaptive optics technology and stellar coronagraphy. With advanced differential imaging and psf extraction techniques, the new generation of instruments, e.g. Gemini Planet Imager (GPI) (Macintosh et al. 2008), ScExAO on Subaru (Jovanovic et al. 2015), and SPHERE/ERIS (Davies et al. 2018; Beuzit et al. 2019) on VLT are capable of probing Jupiter-mass planetary companions within a few mas separation from the central star.

Masses of self-luminous planets are inferred from hot-star evolutionary tracks and infrared fluxes, but in some cases, they are well constrained by precise astrometric measurements (Baraffe et al. 2003; Wang et al. 2018; Snellen & Brown 2018; Nielsen et al. 2019; Wagner et al. 2019). The onset of deuterium burning limit ($\sim 13 M_\mathrm{J}$) is a commonly used criterion to separate a planet from a brown-dwarf (Burrows et al. 1997; Saumon & Marley 2008; Spiegel et al. 2011). However, by taking different composition and formation scenarios into account, the upper cut-off range could be as high as $25 - 30\ M_\mathrm{J}$ (Baraffe et al. 2010; Schneider et al. 2011). We acknowledge this ambiguity of overlapping mass range, but we clump all directly imaged objects up to $\sim 30 M_\mathrm{J}$ in the DIP category for the present work.

The histogram shown in Figure 2.2(b) reveals that except for one case[‡], the projected semi-major axis distance of all DIPs is larger than Jupiter's orbital distance. The distribution peaks at an orbital distance of 150-500 AU and extends up to ≈ 3500 AU. The lower limit of the distribution is set by the inner working angle of the coronagraph, while the drop beyond a few thousand AU is influenced by the limited sensitivity to detect the positional change of planets in long-period orbits.

The median mass of the DIP population is about $\approx 12.5\,M_{\rm J}$ with lowest mass object $2\,M_{\rm J}$ and about half the number more massive than $13\,M_{\rm J}$. Most stellar hosts of these planets are also relatively young, i.e., $\approx 75\%$ below the age of ~ 100 Myr and more than two-thirds of the total belonging to the late spectral types with $T_{\rm eff} \leqslant 4500$ K. From the literature, we also find evidence of circumstellar disks around 22 such systems [§].

The equilibrium temperature of imaged planets ranges from $300 - 2800$ K, though most of them are above 1600 K. The projected angular separation between the host star and planet varies by four orders of magnitude ranging from $\approx 10^{-2} - 10^{2}$ arc-sec. A large angular separation from the central star and inherent brightness due to their high temperature make this giant planet population ideal for direct detection (Traub & Oppenheimer 2010).

We note that the current DIP sample is not a true representative of the underlying population of planets in outer orbits. It is heavily biased towards young, hot, more massive ($\geqslant 4 M_{\rm J}$) companions of young stars. The complexity of high-contrast instruments and the limitation of observing a single object at a time also make the discovery rate slow. Studying DIP hosts spectroscopically is a major challenge because of their wide spectral range and complexities (veiling, extinction, etc) associated with young and pre-main sequence stars. Therefore, it is also difficult

---

[‡] CFBDSIR J145829+101343b is the closest planet at orbital distance 2.6 AU from the central star that is resolved by the direct imaging.

[§] https://www.circumstellardisks.org/

to apply a strictly uniform and homogeneous methodology for the whole sample's characterization.

2.3 Sample Selection

At the time when this work was done in March 2020, the NASA Exoplanet Archive had 3185 stars with confirmed planets found by various discovery methods. We found 2831 out of stars cross-matched with the GAIA DR2 catalog, which has the most accurate parallaxes and precise multi-band photometry of all-sky stellar sources down to magnitude $G \approx 21$. Figure 2.3 shows the location of these stars in the HR diagram with T_{eff}, and stellar luminosity is taken from the GAIA catalog. The archive also contains the list of 45 host stars of directly imaged planets given in Table 2.1. Of these, 42 are found in the GAIA DR2 catalog, and their position in the HR diagram is also shown in Figure 2.3. The summary of astrophysical parameters of the DIP host stars listed in Table 2.1 and our selection criteria for spectroscopic analysis is as follows:

- We searched various public archives for the availability of high-resolution optical spectra for individual DIP hosts and also surveyed the literature on their metallicity. Based on these findings, we separated the 45 DIP host stars in Table 2.1 into three distinct groups demarcated by horizontal lines.
- The first 18 stars in Table 2.1 is a subsample of DIP host stars analyzed in this chapter for which the spectra are available from public archives, but literature metallicity is known only for ten targets. These stars have an effective temperature range between 4059-10690 K and a G-band magnitude smaller than ~ 13. For this subsample, we determined the atmospheric parameters and metallicity [Fe/H] homogeneously for the first time. We obtained high-resolution, high-SNR spectra for 14 targets from the ESO science archive

facility[¶] and for four targets from Keck[‖] archive. The ESO's Science Portal provides access to the already reduced and wavelength-calibrated data. Details of original spectra, e.g., telescope/instrument, resolution, wavelength coverage, and SNR, are listed in Table 2.2.

- In the 2nd group of Table 2.1, there are 4 DIP host stars for which the metallicity is taken from the literature. The last 23 DIP hosts belonging to the 3rd group in Table 2.1 are not analyzed in this chapter because the majority of them are fainter ($m_v > 13$). For these stars either the spectra were not available in the public domain or the quality of the data was poor (low-SNR). This group also includes some of the hot and very rapidly rotating stars ($v \cdot \sin i > 160$ Km/s), which do not have clear spectral features and reliable atmospheric models for parameter estimation.

- Most stellar parameters listed in Table 2.1 are taken from the NASA Exoplanet Archive. Furthermore, we cross-checked the accuracy of these parameters and replaced the missing values with those from the discovery and relevant follow-up chapters. The $\log g$ values marked by '*' symbols are not listed in the standard archives(such as the Nasa exoplanet archive), and we have calculated them from stellar mass and radius values available from the literature.

2.4 Estimation of Stellar Parameters

Spectral synthesis and equivalent width (EW) method are two commonly used techniques to derive the stellar parameter of interest from a high-resolution spectra of stars (Gray & Corbally 1994; Erspamer & North 2002; Nissen & Gustafsson 2018; Blanco-Cuaresma 2019; Jofré et al. 2019). Despite intrinsic differences,

---

[¶] http://archive.eso.org/scienceportal/

[‖] https://koa.ipac.caltech.edu/cgi-bin/KOA/nph-KOAlogin each method requires the proper prescription of a stellar atmospheric model, a well-characterized atomic line list, reference solar abundance, and the radiative transfer code. Most notably, the relevant model parameters in both methods are allowed to vary, and a least-squares minimization is performed to reach the convergence. For example, in the EW case, the desired parameters are those for which the correlation between abundances and equivalent widths (excitation equilibrium and ionization balance) is minimized to zero. In spectral synthesis, theoretical spectra are iteratively generated from the model atmosphere and compared with the observed spectra of the star until the best match is found. The parameters of the best-matched spectra are the closest that describe the properties of the real star. The spectral synthesis method, which we adopted for our Bayesian model, is also suitable for analyzing young and fast-rotating stars present in our sample.

2.4.1 Generation of model spectra

We adopted the Bayesian approach to infer the stellar parameters from the model spectra generated using iSpec –an integrated open-source software (Blanco-Cuaresma et al. 2014b). iSpec is a Python wrapper that incorporates various radiative transfer codes, stellar atmospheric models, and many ready-to-use tools to derive stellar parameters and abundances (Blanco-Cuaresma et al. 2014b,a). As explained in the next section, we use iSpec only as a back-end module to generate synthetic spectrum on the fly to navigate the stellar parameter space for determining the posterior distribution of T_{eff}, $\log g$, [Fe/H] and $v \cdot \sin i$ for our 18 target stars. For generating the model spectra in iSpec, we selected the radiative transfer code SPECTRUM (R.O Grey) because of its faster performance compared to other codes (Blanco-Cuaresma et al. 2014a). This code assumes the local thermodynamic equilibrium condition and requires a grid of plane-parallel model atmosphere as input. We chose ATLAS9 model atmosphere that has grid sampling of

250 K in $T_{\rm eff}$, 0.5 dex in log g and the metallicity sampled over 0.4,0.2,0.0,-0.5,1,-1.5,-2,-2.5,-3,-4 grid points (Castelli & Kurucz 2003). To generate model spectra for intermediate values, iSpec uses interpolation. The solar abundances are taken from Asplund et al. (2009) and the atomic line list from the VALD database Piskunov et al. (1995) that also comes bundled with iSpec. We also adjusted the oscillator strengths and broadening parameters for some of the lines in our line list to improve our ability to model the stellar spectrum in the 600-620 nm wavelength regions, following the procedure given by (Stempels et al. 2007). The microturbulence and macro turbulence velocities were internally calculated by iSpec using empirical relations (Blanco-Cuaresma et al. 2014a).

2.4.2 Data preparation

Doing Bayesian analysis on the whole spectrum is computationally prohibitive. To reduce the computational load, we considered three distinct wavelength regions of the spectrum. These regions are free from telluric lines and also serve as good proxies for different stellar parameters without any degeneracy (Petigura et al. 2018).

The first region is the Mg-I triplet (5150-5200 Å), which is sensitive to log g. The second region (6000-6200 Å) includes a significant number of well-isolated and unresolved spectral lines that are sensitive to $v \cdot \sin i$ and [Fe/H], and the third region (6540-6590 Å) covers the H_α line whose outer wings are sensitive to $T_{\rm eff}$. We have used all three regions for most targets except for HIP 78530, which shows severe line blending due to fast rotation. In that case, we have used only Mg-I triplet and H_α segments.

TABLE 2.1: Stellar parameters of directly imaged planet host stars.

	Literature values							**This work**			
Star	Age [Myrs]	M_P [M_J]	$T_{\rm eff}$ [K]	$\log g$ [cms^{-2}]	[Fe/H] [dex]	$v \cdot \sin i$ [kms^{-1}]	Ref	$T_{\rm eff}$ [K]	$\log g$ [cms^{-2}]	[Fe/H] [dex]	$v \cdot \sin i$ [kms^{-1}]
DIP host stars analyzed in this chapter											
HD 106906	13	11 ± 2	6516^{+165}_{-165}	–	–	$55^{+4.0}_{-4.0}$	1 2 A	6798^{+20}_{-40}	$4.23^{+0.02}_{-0.05}$	$0.04^{+0.01}_{-0.02}$	$49.12^{+0.22}_{-0.17}$
AB PIC	17.5	13.5 ± 0.5	5378^{+55}_{-55}	4.44 ± 0.21	-0.05 ± 0.04	$11.5^{+0.1}_{-0.1}$	3 4 5 6 A	5285^{+10}_{-9}	$4.53^{+0.01}_{-0.01}$	0.04 ± 0.02	$10.35^{+0.06}_{-0.04}$
GJ 504	160	$4.0^{+4.5}_{-1.0}$	6234^{+25}_{-25}	4.33 ± 0.10	0.28 ± 0.03	$7.4^{+0.5}_{-0.5}$	7 8 B	6291^{+14}_{-16}	$4.34^{+0.01}_{-0.02}$	$0.27^{+0.02}_{-0.03}$	$5.47^{+0.12}_{-0.17}$
HN Peg	237	21.99 ± 9.43	6034	4.48	-0.02 ± 0.02	$10.6^{+0.5}_{-0.5}$	9 10 11 A	6186^{+14}_{-7}	$4.48^{+0.03}_{-0.02}$	$0.00^{+0.01}_{-0.02}$	$8.73^{+0.06}_{-0.05}$
51 Eri	20	2.0	7146	3.99 ± 0.24	$0.24^{+0.35}_{-0.35}$	$71.8^{+3.6}_{-3.6}$	12 13 A	7276^{+11}_{-9}	$4.08^{+0.03}_{-0.02}$	$0.13^{+0.03}_{-0.02}$	$65.19^{+0.14}_{-0.17}$
HR 2562	600	30 ± 15	6534	$4.18^{+0.04}_{-0.05}$	0.08	14 15 16	16 17 18 C	6785^{+29}_{-27}	$4.40^{+0.04}_{-0.05}$	$0.21^{+0.02}_{-0.03}$	$43.51^{+0.15}_{-0.17}$
Fomalhaut	440	2.6 ± 0.9	8689	$4.11^{+0.85}_{-0.85}$	$0.27^{+0.19}_{-0.19}$	$91.06^{+0.5}_{-0.5}$	17 18A	8508^{+43}_{-12}	$4.02^{+0.01}_{-0.02}$	$0.13^{+0.05}_{-0.03}$	$75.31^{+0.57}_{-0.14}$
HR 8799	30	7^{+4}_{-2} 10^{+3}_{-3} 10^{+7}_{-4}	7376^{+218}_{-217}	4.22	-0.5	–	19 20 21 22 A	7339^{+4}_{-5}	$4.19^{+0.01}_{-0.02}$	$-0.65^{+0.02}_{-0.01}$	$34.79^{+0.24}_{-0.13}$
HD 203030	220	$24.09^{+8.38}_{-11.52}$	5472^{+84}_{-61}	$4.50^{+0.05}_{-0.05}$	$0.06^{+0.07}_{-0.07}$	$6.3^{+0.3}_{-0.3}$	15 21 23 24 D	5603^{+10}_{-8}	$4.64^{+0.03}_{-0.01}$	$0.30^{+0.02}_{-0.01}$	$5.62^{+0.13}_{-0.14}$
HD 95086	17	5 ± 2	7750 ± 250	4.0 ± 0.5	-0.25 ± 0.5	20 ± 10	25 26 27 A	7883^{+43}_{-65}	$4.58^{+0.02}_{-0.06}$	$0.14^{+0.05}_{-0.04}$	$17.14^{+1.31}_{-0.52}$
bet Pic	12.5	11 ± 2	8052	4.15	-0.1 ± 0.2	122.0	3 28 29 A	7890^{+13}_{-17}	$3.83^{+0.03}_{-0.02}$	$-0.21^{+0.03}_{-0.02}$	$116.41^{+2.32}_{-2.05}$
HIP 78530	11	23 ± 1	10500	–	–	–	30 31 A	10690^{+24}_{-10}	$4.68^{+0.02}_{-0.01}$	$-0.50^{+0.03}_{-0.01}$	$144.74^{+0.55}_{-3.14}$
LkCa 15	1	–	4210^{+185}_{-199}	–	–	$13.90^{+1.20}_{-1.20}$	23 32 33 D	4589^{+7}_{-7}	$3.65^{+0.01}_{-0.01}$	$0.26^{+0.01}_{-0.01}$	$16.82^{+0.1}_{-0.2}$
PDS70	5	8 ± 6 8 ± 4	4225^{+242}_{-71}	–	–	–	23 34 35 36 A	4152^{+5}_{-9}	$3.68^{+0.01}_{-0.01}$	$-0.11^{+0.01}_{-0.01}$	$17.27^{+0.1}_{-0.1}$
CT CHA	2	17 ± 6	4200^{+211}_{-115}	–	–	$12.80^{+1.7}_{-1.7}$	8 23 37 38 B	4403^{+6}_{-10}	$3.66^{+0.01}_{-0.01}$	$-0.56^{+0.01}_{-0.01}$	$13.97^{+0.10}_{-0.15}$
GQ LUP	1	20	4092^{+211}_{-165}	–	–	–	23 39A	4416^{+3}_{-5}	$3.65^{+0.01}_{-0.04}$	$-0.35^{+0.01}_{-0.01}$	$6.33^{+0.03}_{-0.07}$
ROXs 12	6	16 ± 4	3850^{+100}_{-70}	–	–	–	40 41 D	4059^{+3}_{-4}	$3.71^{+0.01}_{-0.01}$	$0.14^{+0.01}_{-0.01}$	$7.20^{+0.03}_{-0.04}$
GSC 06214-00210	11	16 ± 1	4200^{+150}_{-150}	–	–	–	3 4 D	4119^{+6}_{-13}	$3.70^{+0.01}_{-0.04}$	$-0.06^{+0.01}_{-0.01}$	$4.24^{+0.04}_{-0.05}$

Note – The instrument listed in the reference column are as follows – A: HARPS; B :UVES ; C : FEROS ; D :HIRES. The entire table is published in Swastik et al. (2021). For the sake of simplicity, only a few rows are shown.

Table 2.2: Properties of archival spectra and instrument used.

Instrument	**Spectral Range (in nm)**	**Resolution**	**SNR**
HARPS	378.2-691.3	115000	174
UVES	472.7-683.5	74450	218
FEROS	352.8-921.7	48000	305
HIRES	336.0-810.0	85000	60

Note – The SNR quoted in the above table is the median SNR of all the stellar spectrums for a given instrument. The last column refers to the median SNR of all DIP host stars spectra observed with each instrument.

Additionally, some of the stars in our sample (S.No 13-18 in Table 2.1) have emission features that indicate the presence of an accretion disk around the star. The characteristic veiling ** dominated H_α emission for these stars is shown in Figure 2.4. This accretion shocked region on the stellar surface generates the veiling continuum and decreases the depth of the stellar absorption lines (Calvet & Gullbring 1998). Since we don't have reliable models for emission lines (such as the H_α), we chose less contaminated and emission-free regions 5900-5965Å for deducing the stellar parameters (Stempels & Piskunov 2002, 2003). In addition, we included the 6100-6200Å segment for Lkca15, Ross12, PDS 70, and GSC 06214-00210 together with 5900-5965Å for determining stellar parameters since this region also lacks emission lines. In the Bayesian analysis discussed in the next section, we considered veiling as a free parameter to account for the excessive line filling due to the accretion, following the procedure by Stempels & Piskunov (2002, 2003).

Individual spectra of stars come from single-object spectroscopic observations from the different instruments. The FITS files contain a 1D spectrum with the specification of wavelength, flux, and flux errors. If the flux error was not specified, we

---

[**] Stellar veiling is a phenomenon that occurs when the excess continuum emission from a star's hot surrounding material, such as an accretion disk, reduces the contrast of spectral lines in the observed spectrum of the star. As a result, the lines appear "veiled" or weaker than their actual strength, which complicates the analysis of the star's surface properties and composition.

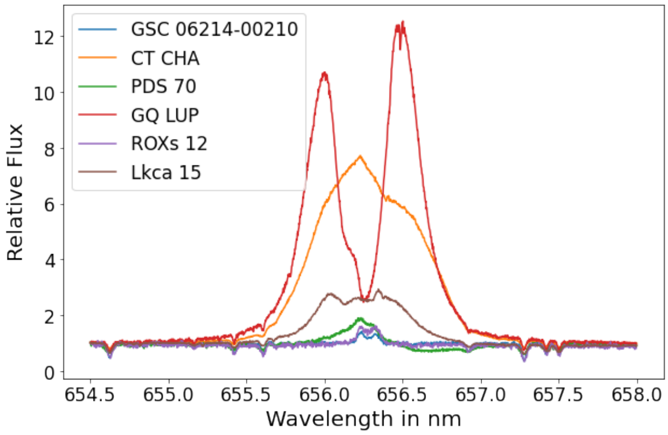

FIGURE 2.4: The presence of veiling inferred from H_α emission line seen in the spectra of stars 13-18 in Table 2.1.

assumed the errors to be limited by the photon noise. A certain amount of preprocessing was needed to prepare the data for further analysis. We used standard packages in IRAF [††] for continuum normalization and the radial velocity correction in the spectra. The model spectrum was generated at the same wavelength grid as the observed spectrum.

2.4.3 Bayesian inference and MCMC sampler

We chose the Bayesian approach for probabilistic inference because it eliminates the dependence of derived stellar parameters on the initial guess values and also places realistic constraints on the errors (Shkedy et al. 2007). We denote our minimal set of model parameters as $\theta \equiv \{T_{\text{eff}}, \log g, [\text{Fe/H}], v.\sin i\}$ and observed stellar spectrum as $D \equiv \{y_{\text{data}}, y_{\text{err}}, \lambda\}$, where y_{data} is the measured flux at wavelength λ and associated uncertainty y_{err}. The model predicted normalized flux $y_{\text{mod}}(\theta, \lambda)$ is calculated from first principles using radiative transfer code and appropriate model of the stellar atmosphere. The goal is to find *posterior* $p(\theta|D)$

[††] IRAF is distributed by the National Optical Astronomy Observatories, which is operated by the Association of Universities for Research in Astronomy, Inc., under contract to the National Science Foundation.

which is the most likely distribution of the model parameters θ conditioned on the observed data D. We know, from Bayes's theorem

$$p(\theta|D) = \frac{p(\theta)p(D|\theta)}{p(D)} \tag{2.1}$$

where $p(D|\theta)$ is the *likelihood* of observing spectra D, given the set of model parameters θ, $p(\theta)$ is *prior function*. The term $p(D)$ in the denominator of eq. 4.1 is a normalization constant, also called *evidence*, which is hard to compute, but not required when we use a sampler. Note that each term in eq. 4.1 is a probability density function whose analytical form is rarely known in practice. The Markov-Chain Monte-Carlo (MCMC) process allows us to numerically estimate the parameters by randomly drawing a sequence of samples from the posterior distribution of model parameters constrained by the data (Hogg & Foreman-Mackey 2018). We used *emcee* implementation of MCMC[‡‡] in python. The flowchart of our algorithm is shown in Figure 2.5. First, we initialize the starting parameters θ_s of the model from our prior knowledge of the star, e.g. spectral type, luminosity class etc. Using θ_s as seed we generate an ensemble of $\{\theta_1, \theta_2, ...\theta_k\}$ called walkers drawn from a physically realistic range of uniform priors, i.e. ±200 K for $T_{\rm eff}$, ±0.5 dex for log g, ±0.25 dex for [Fe/H] and ±2 to ±20 for $v \cdot \sin i$ depending on the star.

Each walker is a random realization of θ which relies on algorithm(e.g., Metropolis-Hastings) for sampling the parameter space. A function call to iSpec generates the model spectrum for the proposal parameter from the MCMC sampler. We define a simple log likelihood function $lnP(D|\theta)$ to compares the observed spectrum $y_{\rm data}$ with the model spectrum $y_{\rm mod}$ as:

[‡‡] https://emcee.readthedocs.io/en/stable/

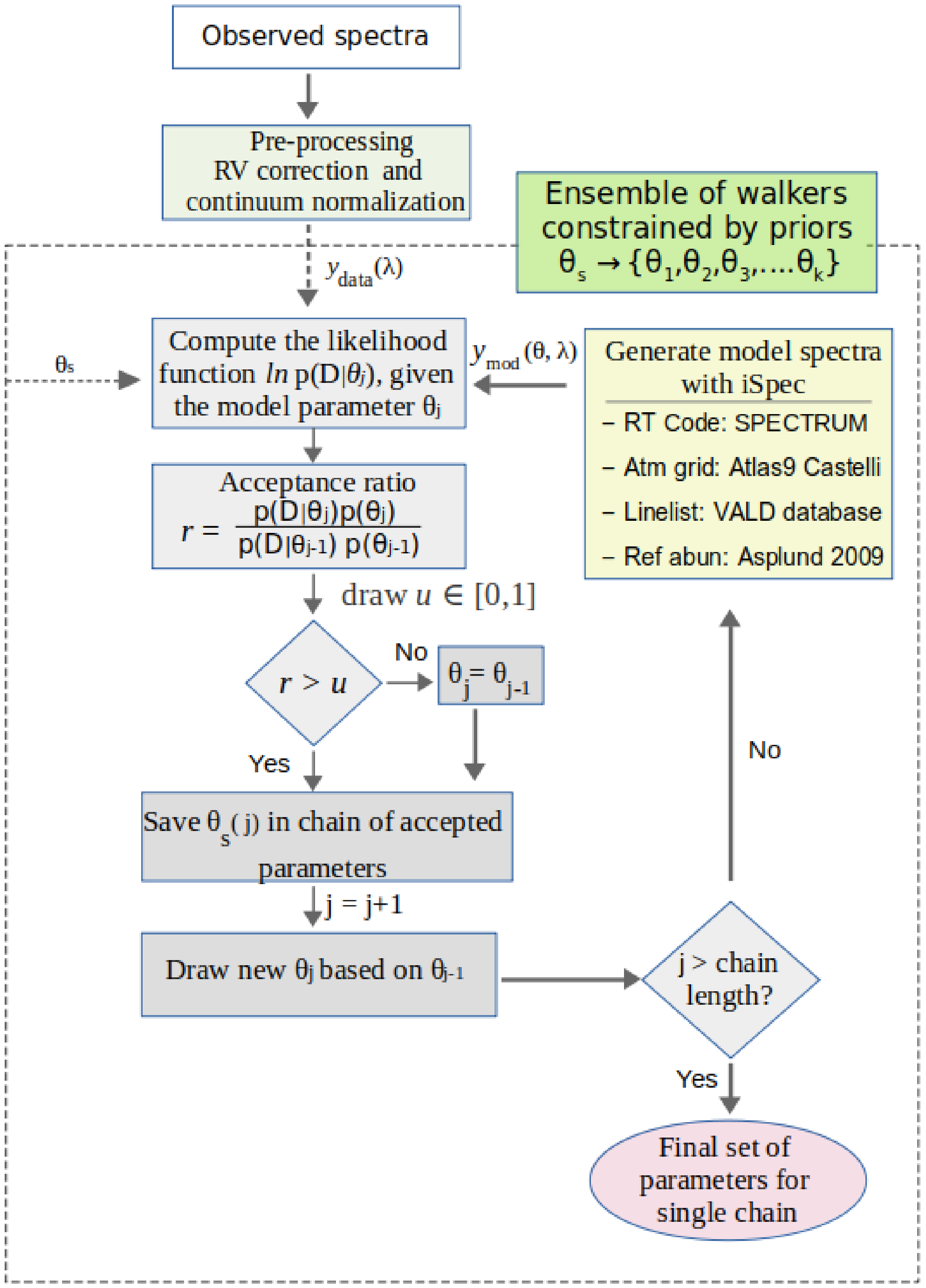

FIGURE 2.5: Workflow diagram of iSpec along with *emcee*. For a requested set of stellar parameters, iSpec generates the synthetic spectrum and compares it with the original spectrum. The most likely posterior distribution of the stellar parameters is obtained using Bayesian inference.

$$lnP(D|\theta) = -\frac{1}{2}\sum\left(\frac{y_{\text{data}} - y_{\text{mod}}(D|\theta)}{y_{\text{err}}}\right)^2 \tag{2.2}$$

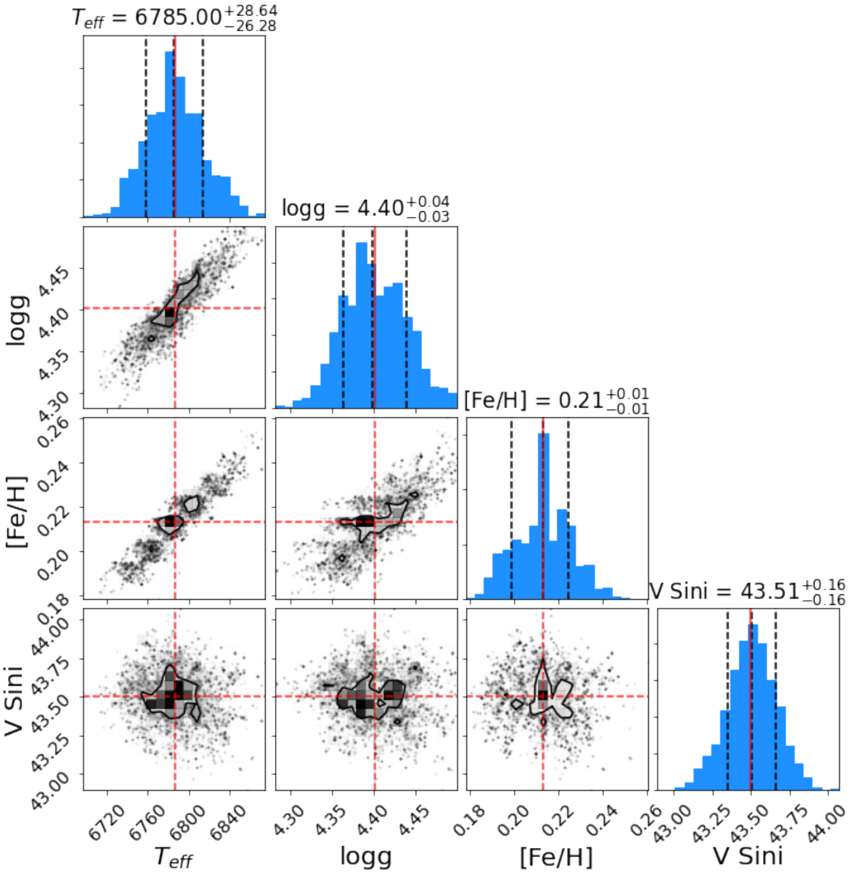

Figure 2.6: Posterior distributions of stellar parameters for HR2562, obtained from MCMC analysis (40 chains, 300 steps, a burn-in limit at 140 steps). The diagonal panel shows 1-D projections of the probability density, while the off-diagonals show 2-D projections of the correlations between parameters. The mean of each parameter is shown by the red dashed lines, while the 1σ spread is indicated by black dashed lines.

Every walker numerically explores the parameter space by taking a “step” to a new value θ_{j+1} that is drawn from a normal proposal distribution centered on θ_j. The new proposal θ_{j+1} is accepted if it has a higher posterior value than the current sample, θ_j. If the new proposal value has a lower posterior, then the choice to accept or reject a new proposal with a certain probability is made randomly.

The walker, thus, guided by Markov’s process, iteratively converges towards the target distribution by producing a chain of accepted parameters, as illustrated in Figure 2.5. We discard some of the early samples in each chain as they are likely to lie outside the target distribution. This is termed as “burn-in”. Finally, after the burn-in, we obtain a posterior distribution of our stellar parameters.

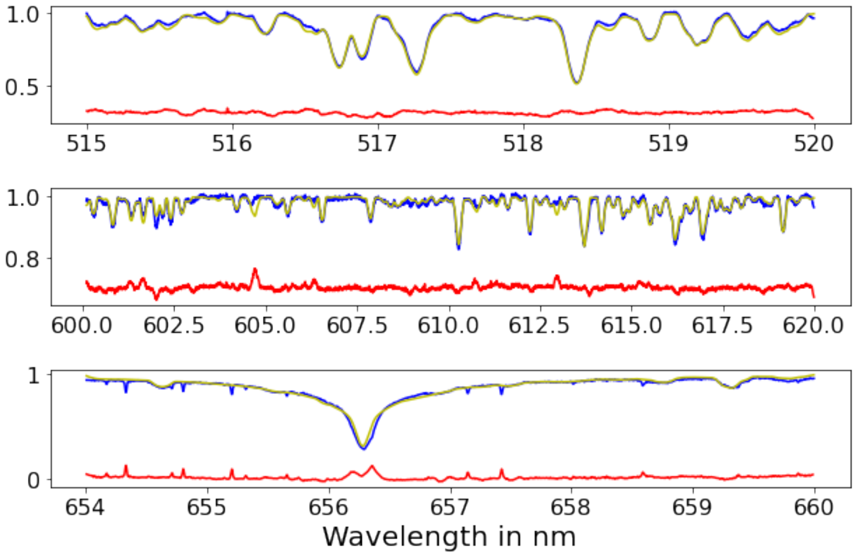

FIGURE 2.7: Comparison between observed spectra (blue) and synthetic spectra (yellow) for HR2562 in three distinct wavelength regions. The synthetic spectra were generated from stellar parameters obtained using Bayesian analysis. Note that offset is added to the residuals (red) for clarity.

After some experimentation, we found that by using 300 steps following a burn-in limit of 140 steps for 40 test chains, we get a reasonable posterior distribution to determine the statistics of stellar parameters. For illustration, the final distribution of $T_{\rm eff}$, log g, [Fe/H] and $v \cdot \sin i$ for HR2562 is shown in the Figure 2.6. Since our posterior distribution is multivariate, some of the model parameters are likely to correlate. The shape of the contour plots in Figure 2.6 reflects the degree of correlation between different stellar parameters, e.g., expected correlation can be seen between log g, and $T_{\rm eff}$ while for others; the scatter is uniform, implying no correlation. As a representative example, we show the synthetic spectra for HR 2562 generated using Bayesian inferred model parameters in Figure 2.7, which matches reasonably well with the observed spectra.

For the stars with veiling (S.No 13-18 in Table 2.1), the estimation of stellar parameters was done in parallel with determining of veiling. This was possible because the line shapes and relative absorption line depths are affected by the stellar parameters and are independent of the presence of veiling. We followed a similar procedure as described in Stempels & Piskunov (2002, 2003), where veiling was modeled as free parameter $V(\lambda)$ in the log-likelihood function in **Eq. 2.2**. We used the modified log-likelihood function to obtain the stellar parameters by the same procedure as described above.

The final stellar parameters for our selected stars with mean values and $\pm 1\sigma$ uncertainty are listed in Table 2.1. The errors associated with the stellar parameters are the Bayesian error bars that are related to the sampling of the model spectra. The intrinsic uncertainty associated with the model generating the spectrum is not taken into account. Typical standard errors associated with metallicity (±0.15) are discussed in details by Blanco-Cuaresma et al. (2014b) and Jofré et al. (2019).

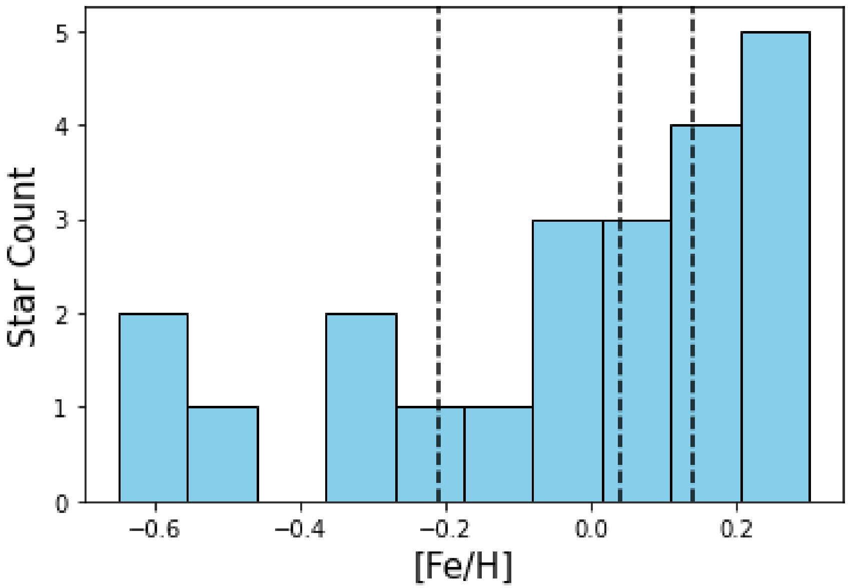

FIGURE 2.8: The observed metallicity ([Fe/H]) distribution of a subset of stars (S.No. 1-22 in Table 2.1.) known to host directly imaged planets. The dashed lines represent the median and the 1st and 3rd quartiles of the distribution.

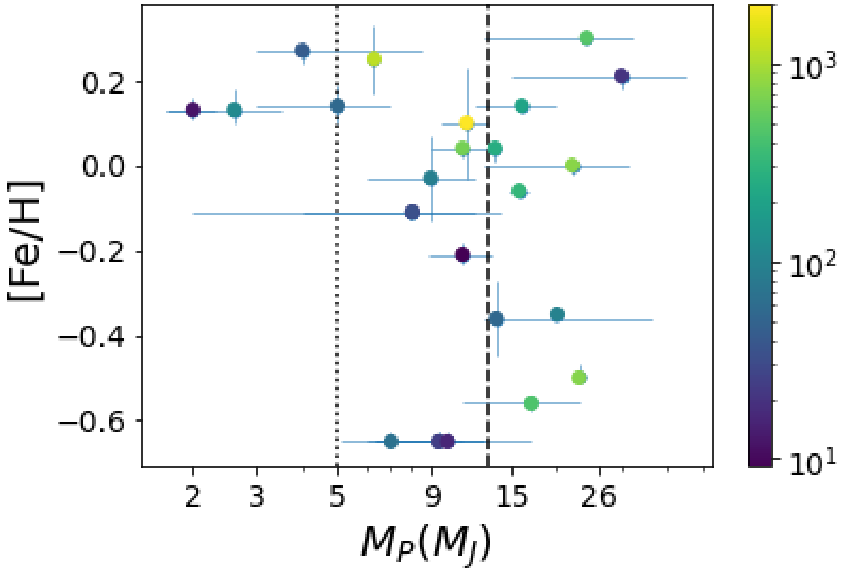

FIGURE 2.9: The distribution of mass of directly imaged planets and the host-star metallicity. The dotted line indicates $5M_J$ and dashed line indicates $13M_J$ boundary. The color bar to the right represents the orbital distance in AU

2.5 Results

2.5.1 Metallicity of DIP host stars

We have estimated the stellar parameters for a subset of stars harboring directly imaged planets listed in Table 2.1. Figure 2.8 shows the distribution of observed metallicity for 22 stars, 18 of which are analyzed in the present work, and the metallicity value for four stars is taken from previous studies. The metallicity of these targets do not show any trend or clustering but widely varies from +0.30 dex (HD 203030) to -0.65 dex (HR 8977) with a median centered at 0.04 dex, which is closer to the solar value. The first and third quartiles are -0.21 and 0.14 dex, respectively, with 12 of them having metallicity higher than the solar value. The large scatter seen in [Fe/H] is not very surprising as it likely reflects the heterogeneity of the DIP host stars associated with different star-forming regions, parent clusters, or moving groups.

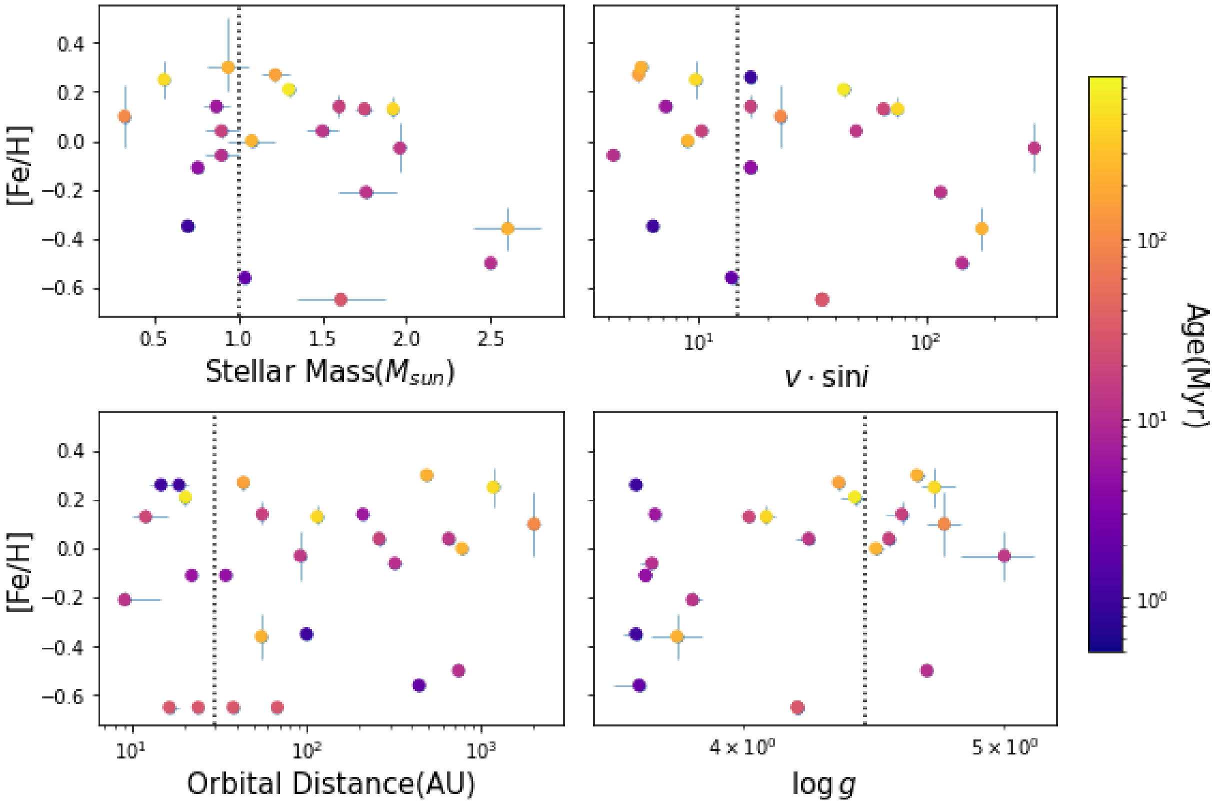

FIGURE 2.10: Correlation of host-star metallicity with other stellar parameters. The dotted line in the bottom-left plot represents the orbital distance of Neptune, in the top-right it represents the limit where equivalent-width method can estimate the metallicity of the star while in other plots it refers to the corresponding parameters of the Sun.

2.5.2 Metallicity and planet mass

To study the relationship between host-star metallicity and planet mass, we used the planetary mass data from the NASA Exoplanet Database from the composite planet list. We divided our DIP sample into three mass bins: $1M_J < M_p \leqslant 5M_J$, $5M_J < M_p \leqslant 13M_J$ and $M_p > 13M_J$ as shown in Figure 2.9. The average metallicity is 0.17±0.07 dex for four stars in the 1st bin, −0.08±0.29 dex for seven stars in the 2nd bin, and -0.11 ± 0.30 dex for ten stars in the 3rd bin. The mean metallicity in each bin shows a declining trend with increasing planetary mass. We also note that regardless of their orbital distance, directly imaged planets with $M_p \leqslant 5M_J$ have mostly metal-rich hosts.

2.5.3 Metallicity and other stellar parameters

Figure 2.10 shows the distribution of metallicity as a function of orbital distance, stellar mass, $\log g$ and $v \cdot \sin i$. For low-mass stars, $M_\star \leq 1 M_\odot$, we find that average metallicity is near-solar with standard deviation 0.21 dex. Stars with $M_\star > 1 M_\odot$ are found to be slightly metal-poor with average metallicity to be -0.10 dex and standard deviation 0.30 dex.

We also find that the average metallicity of fast rotating stars ($v \cdot \sin i > 15$ km/s) is -0.1 dex with a standard deviation of 0.29 dex, while for slow rotators ($v \cdot \sin i < 15$ km/s) it is solar, 0.02 dex with a standard deviation of 0.28 dex. The Spearman's rank correlation coefficient between the stellar metallicity and projected rotational velocity of the star $v \cdot \sin i$ is -0.42 with a p-value of 0.05, which suggests a weak negative correlation. Furthermore, there is no noticeable dependence of host star metallicity on orbital distance and $\log g$

2.5.4 Comparison with literature

To compare our results in Table.2.1, we have included the stellar parameters of DIP host stars from the literature. For each stellar parameter, we computed the sample mean difference and the maximum deviation between our values and those reported in the literature. For effective temperature, we find the sample mean difference to be +103K and the maximum deviation to be 380K for Lkca 15. We note that $T_{\rm eff}$ for most hosts stars in literature is determined photometrically, which could account for the observed differences. For surface gravity, the sample mean difference is -0.06 dex and the maximum difference is 0.58 dex for the HD 95086. Likewise, for metallicity, the sample mean difference is found to be -0.035 dex and the maximum difference, seen again for HD 95086, is 0.39 dex. For rotation velocity, we find a good match between the literature and our values for slowly rotating DIP hosts ($v \cdot \sin i < 20$), whereas the maximum difference is found to be about 16 km/s for the fast rotating star Fomalhaut. By and large, our values for [Fe/H] and $\log g$ determined uniformly using the spectroscopic method are within the error margin of those quoted in the literature. However, for such a heterogeneous sample, the observed differences in stellar parameters obtained by different analysis methods, atmospheric models, radiative transfer codes and line lists, etc., are not entirely unexpected (Jofré et al. 2014, 2019; Blanco-Cuaresma 2019).

2.6 Discussion

In the standard paradigm for the formation of a Jupiter-like planet via core nucleated accretion (e.g. D'Angelo & Lissauer 2018), a rocky protoplanetary core forms first, which then accretes gas and dust from the surrounding disk to become a gas giant (Boss 1997; Bodenheimer & Pollack 1986; Pollack et al. 1996; Ikoma et al. 2001). The critical (or minimum) core mass required to form a gas giant depends on various factors (e.g., location on the protoplanetary disk, accretion rate of solids, etc.) and generally decreases with increasing disk radius: minimum core mass drops from $\sim 8.5\ M_{\oplus}$ at 5 AU to $\sim 3.5\ M_{\oplus}$ at 100 AU (Piso & Youdin 2014; Piso et al. 2015). If the protoplanetary disk is rich in solids, i.e., higher metallicity, then the rocky core can grow faster and reach the critical mass for gas accretion well before the disk is depleted of gas. Therefore, it is easier to form Jupiter-like gas giants in disks around higher metallicity stars (e.g., Ida & Lin 2004; Kornet et al. 2005; Wyatt et al. 2007; Boss 2010; Mordasini et al. 2012). Indeed, observations have shown that the frequency of Jupiter-like planets is higher around higher metallicity stars (e.g. Gonzalez 1997; Santos et al. 2001; Fischer &

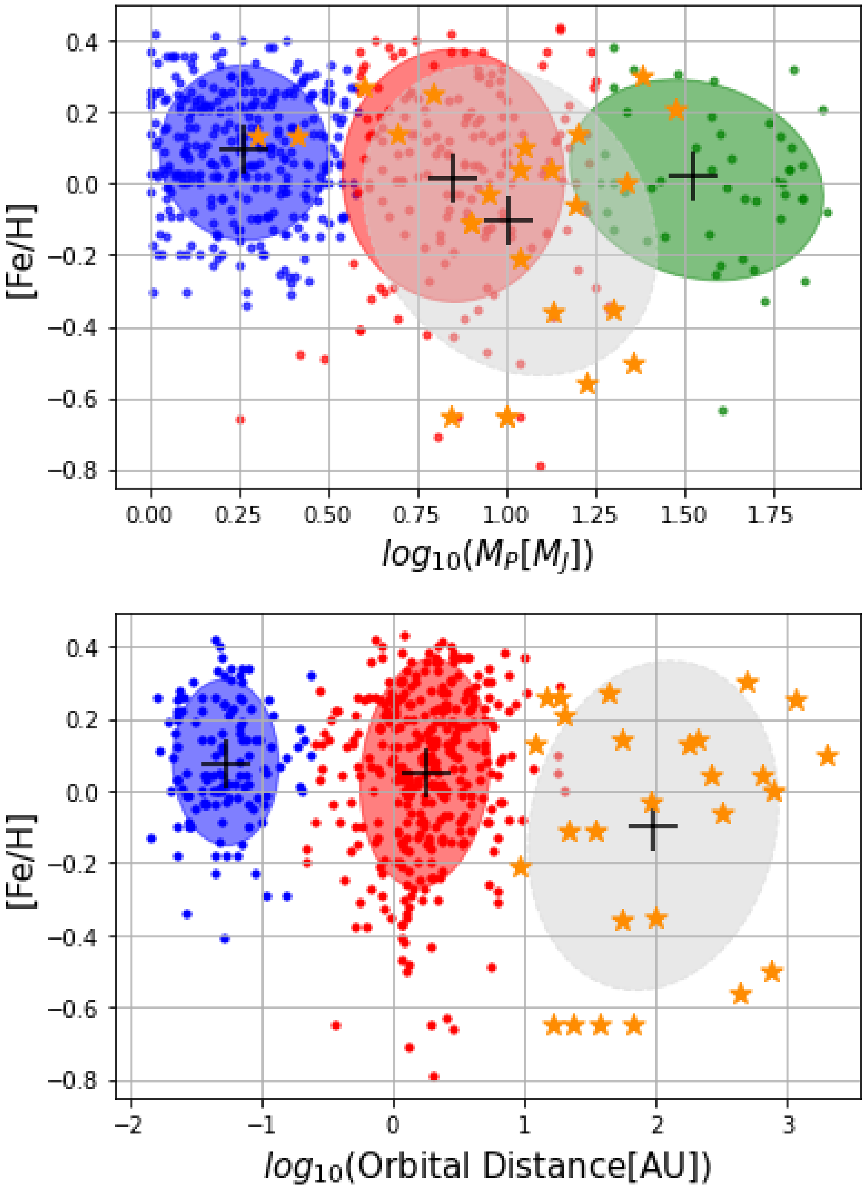

FIGURE 2.11: Top panel: A Gaussian mixture analysis of the combined sample of giant planets and brown dwarf in *metallicity-planetary mass* plane. Three separate clusters correspond to Jupiter-type (blue), super-Jupiters (red), and brown dwarfs (green). Bottom panel: Two populations resulting from the Gaussian mixture analysis in *metallicity-orbital distance* plane (red and blue). The DIP population (orange ⋆ with a gray ellipse) analyzed in this work is interspersed between super-Jupiters and brown dwarfs, as shown in the top panel in the metallicity-planetary mass plane, whereas it occupies a separate region in the metallicity- orbital distance plane. The centroid of each cluster is indicated by '+' symbols.

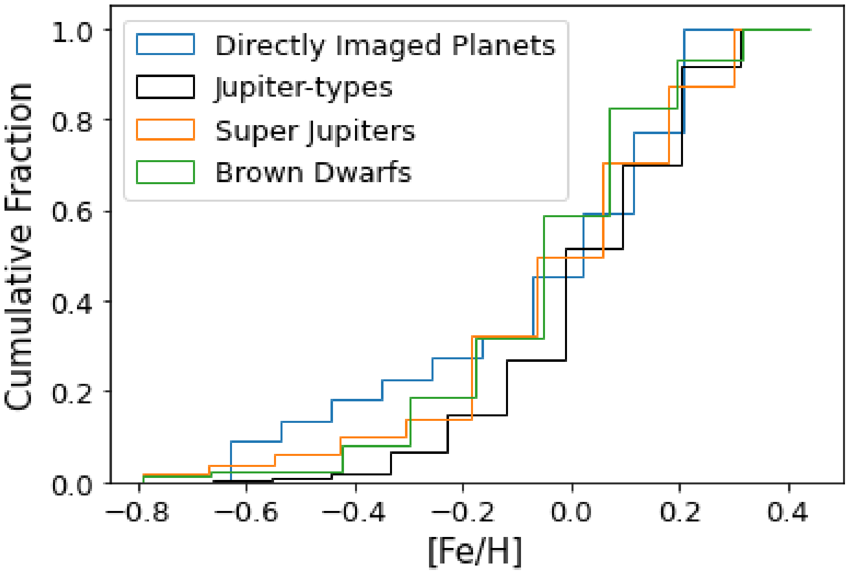

FIGURE 2.12: Cumulative metallicity distribution of DIP host stars from the present studied (blue). The green curve represents cumulative metallicity distribution of brown-dwarf companions while the black and orange curve represents the Jupiter-type and super Jupiter's respectively.

Valenti 2005; Udry & Santos 2007). While not as strong as that seen for gas giants, smaller planets also show a weaker tendency to occur more frequently around relatively higher metallicity stars, even though their host stars appear to have a larger spread in the metallicity (e.g., Wang & Fischer 2015; Buchhave et al. 2014; Mulders et al. 2016). It has now been adequately established that the host star metallicity ([Fe/H]), on average, increases with increasing planet mass or radius (e.g. Buchhave et al. 2014; Petigura et al. 2018; Narang et al. 2018; Mulders 2018). Thus the observed strong dependence of the planet mass/radius on the host star metallicity supports the core accretion model for planet formation. However, the observed correlation of increasing host star metallicity with increasing planet mass turns over at about 4-5 M_J. For planet masses higher than this (super-Jupiters), the correlation reverses, and the average host star metallicity decreases as the mass of the planet increases (Santos et al. 2017; Narang et al. 2018). This suggests that stars hosting super-Jupiters are not necessarily metal-rich, unlike stars hosting Jupiters. This trend appears to continue for more massive companions: the average metallicity of stars with a brown-dwarf secondary is also close to solar to sub-solar, and not super-solar like stars hosting Jupiter. (Ma & Ge 2014; Narang et al. 2018; Schlaufman 2018).

Our sample of directly imaged planets occupies a mass range similar to that of super-Jupiters and brown dwarfs. The fact that the average host star metallicities of brown dwarfs and super-Jupiters are similar and that they differ from that of Jupiter-hosts perhaps indicates a similar formation scenario for them that is different from that of Jupiters. It has been suggested that massive planets and low-mass brown dwarfs can form via gravitational fragmentation of the disk rather than core accretion (e.g. Boss 1997; Mayer et al. 2002). The model of planet formation based on gravitational instability predicts that there is no correlation between the mass of a planet and the metallicity of its host star (e.g., Boss 2002; Cai et al. 2006; Matsuo et al. 2007; Boss 2010). This leads to a wide range of metallicities among host stars. On the other hand, the core accretion model predicts a relationship between these factors, resulting in a much narrower range of metallicities compared to disk instability.

We further compare the directly imaged planets with the large population of giant planets and brown dwarfs around main-sequence stars discovered by techniques other than direct imaging. To this end, we found 637 stars hosting 746 giant planets and massive objects with mass range $1-55M_{\rm J}$ listed in NASA's exoplanet archive. We also searched the above sample in the SWEET-CATALOG (Santos et al. 2013; Sousa et al. 2018), which provides the metallicity information for 459 stellar hosts having 494 companions. Additionally, a catalog of 58 brown dwarfs and their stellar companions was chosen from Ma & Ge (2014). A joint sample of 552 objects was formed by combining the giant planets and brown dwarfs. This combined sample has a mass range from $1-80M_{\rm J}$ and orbital distance spanning 0.02-20 AU. Since objects in the combined sample come from RV, transits, TTV, astrometry, and microlensing observations, we have used the minimum mass $(M \cdot \sin i)$ wherever the true mass was not available.

We then ran a clustering analysis on the 2D-data set of combined samples of giant planets and brown dwarfs with host star metallicity as one parameter and orbital distance and companion mass as another. For clustering analysis, we considered a Gaussian mixture model and implemented using a Python library *scikit-learn* package (Pedregosa et al. 2011). The Gaussian mixture model optimally segregated the combined sample into three clusters in *metallicity* - *planet mass* plane, as shown in the top panel of Figure 2.11 and into two clusters in *metallicity* - *orbital distance* plane as shown in the bottom panel of the Figure 2.11.

The clustering analysis in Figure 2.11 at the top clearly divides the combined sample into three mass and metallicity bins. The mass boundaries roughly located at $\approx 4M_\mathrm{J}$ and $\approx 14M_\mathrm{J}$ are consistent with multiple populations of giant planets (i.e., Jupiters and super-Jupiters) and brown-dwarfs, pointing to their different physical origin. Further on, the declining centroid metallicity of each group in Figure 2.11 at the top, i.e., 0.089 ± 0.02, 0.023 ± 0.002 to 0.013 ± 0.009 dex, is also consistent with previous results. The DIP population studied in this work is also shown for comparison in Figure 2.11. The DIP population falls between the super-Jupiters and brown dwarfs populations, both in mass and metallicity.

The analysis of orbital distance and stellar metallicity shows that the combined population of close-in objects separates into two distinct groups, as shown in the bottom panel of the Figure 2.11. Again, the DIP sample analyzed in this work is added to the plot for comparison. In *metallicity* – *orbital distance* plane, three populations again clearly separate out. On comparing the centroid values of the metallicity, which are 0.076, 0.042, and -0.097 dex, (standard deviation in each case $\leq 10^{-6}$), we find a decreasing metallicity trend with increasing orbital distance. A similar metallicity dependence with orbital distance is also reported for the Jupiter analogs (Mulders et al. 2016; Buchhave et al. 2018; Mulders 2018).

In Figure 2.12, we compare the cumulative metallicity distribution of DIP host stars with stellar companions of brown-dwarfs Ma & Ge (2014), and giant planets –both Jupiter-type and super-Jupiters. We note that the cumulative distribution of DIP host stars at the lower metallicity region clearly differs from the stellar hosts of Jupiter-type planets, whereas the distribution for super-Jupiters and brown-dwarf hosts falls in between the two. However, there is no marked difference in the higher metallicity side beyond [Fe/H]> 0.

Although the specific factors that influence planet formation are still not fully understood, metallicity seems to be one of the major contributing factors that determine the type of planets likely to be formed around a star. Using synthetic planet population models Mordasini et al. (2012) showed that a high-metallicity environment determines whether or not a giant planet in the mass range $1 - 4M_{\rm J}$ can form. But metallicity alone is not the only parameter in determining the final mass of the planet except for the very massive planets ($\geq 10M_{\rm J}$), as the critical core must form very fast before the dissipation of the gas in the disk by accretion onto the star (Hayashi et al. 1985; Matsuo et al. 2007). The prediction of Mordasini et al. (2012) that the very massive planets ($\geq 10M_{\rm J}$) can form only at very high metallicity conditions is contrary to our findings. Our results are indicative of the possibility of two planet formation pathways: one in which the giant planets up to $4 - 5M_J$ might be formed by the core accretion process, and the other where the massive super-Jupiters and brown-dwarfs are formed via gravitational fragmentation of the protoplanetary disk.

Our results for wide-orbit (10s-1000s AU) planets are also consistent with the mass-metallicity trend observed for super-Jupiters and brown-dwarfs in close-in (≤ 1 AU) orbits around main-sequence stars. The formation mechanism of planets in wider orbits is still unclear. However, the mixed metallicity of our DIP host star sample and its close resemblance with the commutative metallicity distribution of brown dwarf hosts make it likely that massive and young planets in wider-orbits too formed via gravitational instability. However, a larger sample is required to further validate such conclusions.

2.7 Summary and Conclusions

We have used high-resolution spectra to measure the atmospheric parameters of young stars that are confirmed host stars of planets detected by direct imaging technique. Our sample consists of 22 such stars selected from NASA's Exoplanet Archive. For 18 of these targets, the stellar parameters and metallicity are determined in a uniform and consistent way. The summary of our results is as follows:

1. We used the Bayesian analysis to estimate the atmospheric parameters and metallicity for 18 DIP host stars. The MCMC technique was used to obtain the posterior distribution of stellar using model spectra generated using the iSpec. The computed metallicity [Fe/H] of these stars spans a wide range from between $+0.3$ and -0.65 dex.
2. We investigated the trend between the average host star metallicity and mass of the planet, which shows that directly imaged planets with $M_P \leqslant 5M_J$ tend to have metal-rich hosts. This is in line with the predictions of planet formation via core accretion. However, as the planet's mass increases, the average metallicity of the host stars shows a declining trend, suggesting that these planets are likely formed by gravitational instability. These findings seem consistent with the results reported by Santos et al. (2017) and Narang et al. (2018). Since the metallicity of a star doesn't change during evolution, we do not expect these trends to change significantly for the currently undetected population of cool and massive giant planets in the outstretched regions of the main sequence stars. Moreover, main sequence host stars, in general, show a trend of decreasing metallicity with increasing orbital distance of the

planet (e.g., Mulders et al. (2016), Buchhave et al. (2018), Mulders (2018), Narang et al. (2018)).

3. From clustering analysis, as discussed above in section 6, we find that the DIP host stars separate as a different class of celestial objects in stellar metallicity–orbital distance plane. Furthermore, we can see a decreasing trend in the centroids of the host-star metallicity as the star-planet separation increases.

4. In the planetary mass-stellar metallicity plane, it is found that the Jupiter-like planets are more likely to form around a metal-rich star. It also shows a decreasing trend in average stellar metallicity as the planetary mass increases. The DIP population clusters lie in between the super-Jupiters and brown dwarf populations.

It is also important to recognize that the composition of circumstellar material from which the planets are formed needn't necessarily be the same as the composition of the parent star. The degree of similarity or difference would depend on how and where planets are formed, what stage of evolution they are in, the disk mass, and planet multiplicity. The number of directly imaged planets detected still remain less ∼69. Further, most of the directly imaged planets are either Herbig Ae/Be stars or T-Tauri stars and thus it makes it difficult to characterise them as their model atmosphere are complicated unlike the FGK stars and thus makes parameter estimation unreliable. A clear picture is expected to emerge from the ongoing high-contrast imaging surveys and future experiments aimed at searching planets in wider orbits.

Chapter 3

Galactic Chemical Evolution of Exoplanet Hosting Stars [*]

3.1 Introduction

When, where, and how planets are formed is an actively pursued area in exoplanet science. With the planetary census already reaching the 5500 mark, it becomes statistically feasible to study the properties of the planets and their host stars to address various scientific goals. At a broader level, one such goal is to understand how fundamental properties (e.g. age, mass, chemical composition, T_{eff}, $\log g$, etc.) of stars hosting planets differ from stars without planets (SWP). Further insights can be gained by correlating various astrophysical properties of stellar hosts with the orbital and physical properties of the exoplanets occupying a wide parameter space.

---

[*] Part of this work have been published in Swastik et al. (2022)

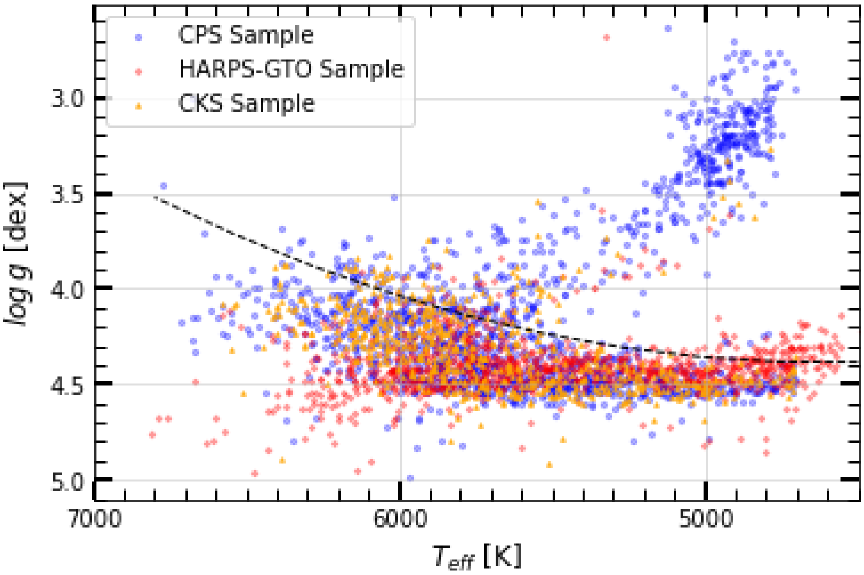

FIGURE 3.1: Exoplanet host stars from the HARPS-GTO (red), CPS (blue) and CKS (yellow) surveys. The dashed black line separates the main-sequence stars lying below the line from the evolved stars lying above (Brewer & Fischer 2018). In this chapter, we study only the main sequence stars.

The early detections using radial velocity techniques have shown that the occurrence of Jupiter's is higher around metal-rich stars (e.g. Gonzalez 1997; Fischer & Valenti 2005; Udry & Santos 2007). Subsequently, an extensive spectroscopic survey of planet hosts (e.g. Bruntt et al. 2012; Buchhave et al. 2012; Everett et al. 2013; Fleming et al. 2015; Johnson et al. 2017; Buchhave et al. 2014; Petigura et al. 2018; Mulders 2018; Narang et al. 2018; Swastik et al. 2021) have shown that (a) host star metallicity ([Fe/H]) increases as a function of planet mass, peaking around $M_P \approx 4M_J$ and showing large scatter for the massive giant planets and brown dwarf hosts (Narang et al. 2018) (b) overall, stars with planets seem to have higher metallicity compared to the stars without planets. Two main theories have been put forward to explain this metallicity excess (Ecuvillon et al. 2004). The "primordial" hypothesis suggested that the initial protoplanetary cloud was metal-rich, which resulted in such metal-rich hosts (Santos et al. 2004; Valenti & Fischer 2008; Johnson et al. 2010b). Conversely, the "self-enrichment" hypothesis suggests that the elevated metallicity observed in stars with planets results from the accretion of a significant number of rocky, metal-rich planets (Lin et al. 1996;

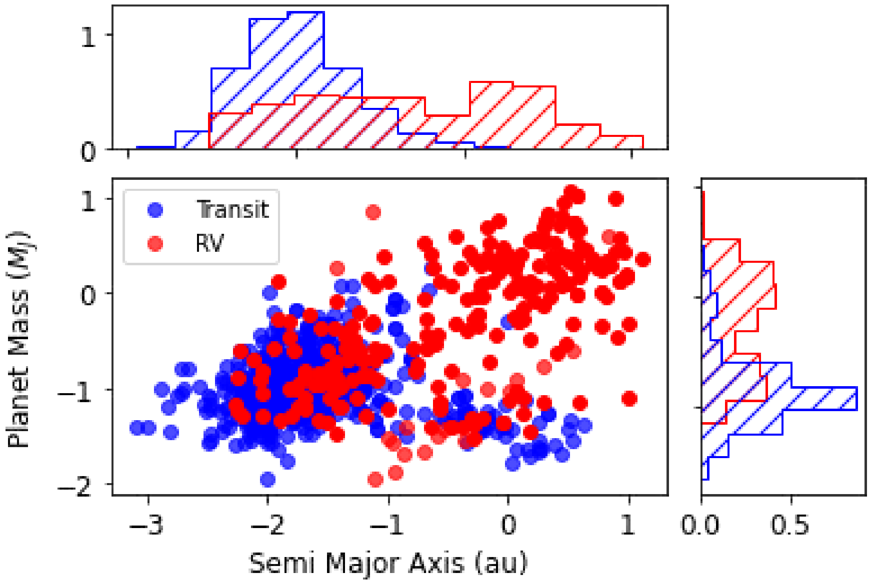

FIGURE 3.2: Distribution of planet mass and semi-major axis (on the log scale) for the RV and transit planets used in this study. The corresponding histogram is also shown at the top and right corner of the figure.

Laughlin & Adams 1997; Gonzalez 1997; Murray et al. 2001; Pinsonneault et al. 2001). Regardless of the validity of one theory or another, the growing consensus is that a metal-rich environment plays a vital role in forming planetary systems. Particularly, the gas giants are believed to be formed from the core-accretion process, which requires a fast build-up of the planetary core up to 10-15$M_\oplus$. The core has to be formed quickly within a few Myr before the gas dissipation takes place. The metal-rich protoplanetary material aids the formation of the cores, followed by the accretion of the gas to form the outer envelope.

In the context of planet formation, most of the aforementioned studies have mainly focused on iron abundance ([Fe/H]). It is also because estimating the abundances of all the elements for a given star is not always straightforward. Although iron is not the most abundant metal in the Universe, the optical spectra for the solar-type stars contain many prominent iron lines, making the abundance determination easier (Blanco-Cuaresma et al. 2014b; Adibekyan 2019). The iron abundance is also traditionally used as a proxy for the overall metallicity of the star with

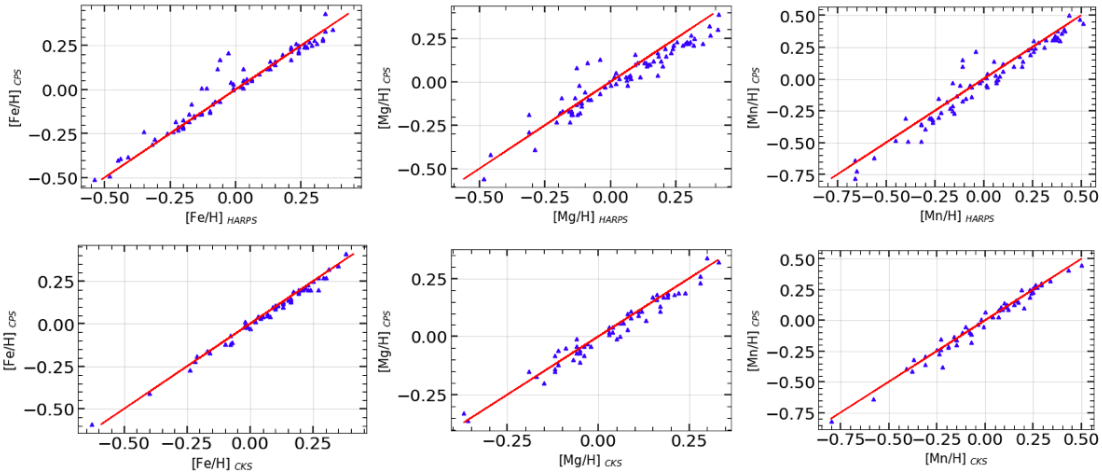

FIGURE 3.3: **Top row :** Comparison of elemental abundances of Fe, Mg and Mn for stars that are common between the CPS and the HARPS-GTO sample. **Bottom row :** Comparison of Fe, Mg and Mn abundance for stars that are common between the CPS and the CKS sample. The solid red curve represents x = y line.

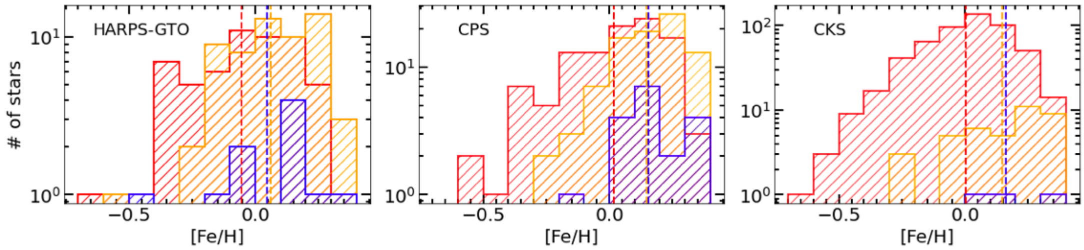

FIGURE 3.4: Metallicity distribution for the HARPS-GTO, CKS and CPS sample. The colors red, yellow, and blue represent small planets, giant planets, and super-Jupiters, respectively. The vertical lines represent the mean of the distribution.

the assumption that the composition of the metals changes proportionally to the iron content. However, the formation mechanism for different elements is vastly different, and their signatures do show up in the chemical composition of stars. Therefore, studying stars' detailed abundance patterns could provide further clues to the observed planet morphology and architecture.

In the past, there have been limited studies of elemental abundances, i.e., [X/Fe]

[†]for a larger sample of planet-hosting stars. For example, Brugamyer et al. (2011); Adibekyan et al. (2012a); Hinkel et al. (2014); Brewer et al. (2016); Brewer & Fischer (2018), analyzed the spectra of known planetary hosts and found an overabundance of α-elements (Mg, Si, S, Ca, Ti) for the planet-hosting stars (PHS). Similarly, Delgado Mena et al. (2017) and Delgado Mena et al. (2018) investigated the abundances of heavy elements of planet-hosting stars and found that stars with planets show an overabundance of elements such as Zn for [Fe/H] $<$ -0.1 dex. They also found most s-process elements to be under-abundant in planet-hosting stars. These studies clearly show that knowing the iron content of stars alone is not sufficient, and a detailed abundance analysis is required to understand the complete picture of planet formation. The limited studies that focused on the [X/Fe] were mainly based on specific elements (such as only on $\alpha-$ or iron-peak elements). Similarly, studies such as Wilson et al. (2021) investigated the correlation between occurrence rate and chemical abundances for 10 elements for the host stars of Kepler planets. They also studied the correlation between planet radius (R_P) and abundances and detected a significant correlation between [Mn/Fe] and R_P. However, these results are highly skewed towards shorter orbital period planets. A recent investigation by Tautvaišienė et al. (2022) which focused on 25 RV detected PHS and found that main-sequence giant planet-hosting stars are metal-rich compared to the low-mass planet hosting. They also found that PHS is systematically higher in α-content than the non-hosting counterparts at the lower metallicity regime ([Fe/H]$\leq$-0.2). These studies provide a scientific motivation for us to investigate how the planet mass M_P varies as a function of the abundances of different classes of elements and for a diverse sample of PHS detected both by transit and RV. Studying the [X/Fe] pattern with M_P can also give clues about the preferred formation route for planets belonging to different mass ranges.

In the context of the standard galactic chemical evolution (GCE), core-collapse

---

[†] [X/Fe] = [X/H]-[Fe/H]

TABLE 3.1: Table listing the samples from different surveys used in this chapter.

Sample	Instrument	Stars observed	Small planets	Giant planets	Super-jupiters
HARPS-GTO	ESO/HARPS	1111	119	81	17
CKS	Keck/HIRES	1127	934	65	9
CPS	Keck/HIRES	1615	215	117	29

Note: We didn't consider the planets hosted by sub-giant stars in our sample. The final curated sample consists of only main sequence stars.

supernovae, mostly the Type II (SNe II), enriched the early universe with α-elements, which also occurred on a faster time scale than Type Ia supernovae (SNe Ia) (Matteucci & Francois 1989; Alibés et al. 2001; Matteucci et al. 2009; Kobayashi et al. 2020). According to the classical view, SNe II occurs when a massive star collapses ($8M_\odot < M_\star$) rapidly after the completion of its stellar burning process, which ends in an explosion. On the other hand, the most accepted model of SNe Ia involves a binary system in which at least one of the stars is a white-dwarf. The white dwarf accretes mass from its binary companion and reaches the critical mass (also known as Chandrasekhar limit), which results in thermal runaway, followed by an explosion. The SNe II produce a large amount of α-elements and fewer iron-peak elements. The SNe Ia, on the other hand, is the major producer of iron-peak elements (Edvardsson et al. 1993; Costa Silva et al. 2020; Kobayashi et al. 2020). As a consequence of staggered progression, iron-peak elements enriched the interstellar medium (ISM) at much later stage compared to the α-elements. Therefore, at population level, the α to iron-peak ratio, [α/Fe], in stars is a good proxy for age to probe the history of galactic chemical evolution (Haywood et al. 2013; Costa Silva et al. 2020; Delgado Mena et al. 2019; Kobayashi et al. 2020).

In this chapter, we study the elemental abundances of a large sample of over 900 planet-hosting stars with the goal of examining the role of GCE in the context of exoplanetary systems. We infer that the majority of the high-mass planetary systems ($M_P > 0.3M_J$) are likely formed at later stages of the GCE, mainly after

SNe Ia have sufficiently enriched the Galactic ISM with iron-peak elements. Our premise is based on the fact that the production of most elements is dictated by GCE and a heavy elements-driven core-accretion mechanism is a favored pathway for the formation of giant planets.

For this work, we use the spectroscopic abundances of planet-hosting stars obtained from three previous studies, namely, HARPS-GTO (Mayor et al. 2003; Lo Curto et al. 2010; Santos et al. 2011), California Kepler survey (CKS) (Brewer & Fischer 2018) and California planet survey (CPS) (Brewer et al. 2016). We measured the correlation between [X/Fe] and planet mass to statistically examine if stars hosting giant planets are younger than the small planet hosts. We interpret our results in terms of GCE and mainly focus on the α and iron-peak elements since their formation timeline is evidently different. In our findings, α-elements and Eu show a strong negative correlation with planet mass, but not so significant correlation was found for the iron-peak and s-process elements.

The rest of the chapter is organized as follows. In Section 3.2, we describe our sample. In Section 3.3, we discuss the various [X/Fe] trends as a function of planet mass. Further in Section 3.4, we compare the trends obtained in Section 3.3 and interpret our results. Finally, we give our summary and conclusions in Section 3.5.

3.2 Sample Preparation

To study the elemental abundances of the α, iron-peak and other elements (mainly the s-process and the r-process elements) of the exoplanet host stars, we used the data-set from three different surveys, namely, HARPS-GTO (Mayor et al. 2003; Lo Curto et al. 2010; Santos et al. 2011), California Planet survey (CPS) (Brewer et al. 2016), and California Kepler survey (CKS) (Brewer & Fischer 2018). The plot between T_{eff} and $\log g$ for the stars combined from the above three samples is shown in Figure 3.1. In this work, we analyze the main sequence stars which lie below the dashed black line shown in Figure 3.1. We divided the planet masses taken from NASA's exoplanet archive into three mass bins, namely, small planets (SP) [$M_P \leq 0.3\ M_J$], giant planets (GP) [$0.3\ M_J < M_P \leq 4\ M_J$] and super-jupiters (SJ) [$4\ M_J < M_P \leq 13\ M_J$]. In this section, we briefly describe the original samples and how it was curated to obtain the final sample for our analysis.

3.2.1 HARPS-GTO sample

The HARPS-GTO stars used in this study come from three HARPS subsamples: Mayor et al. (2003); Lo Curto et al. (2010); Santos et al. (2011). The sample consists of 1111 F, G, and K main-sequence stars (Adibekyan et al. 2012b) observed with HARPS, a high-resolution spectrograph (R$\sim$ 115000) at the La Silla observatory (ESO, Chile). The HARPS-GTO sample has 163 stars with at least one companion[‡] and 948 stars without any companion. The stars were extensively studied and their chemical abundances are published in a series of papers (Mayor et al. 2011; Adibekyan et al. 2011, 2012b; Suárez-Andrés et al. 2017; Bertran de Lis et al. 2015; Suárez-Andrés et al. 2016; Delgado Mena et al. 2018, 2019, 2017, 2021; Costa Silva et al. 2020). The technique employed to obtain the elemental abundances is mostly the equivalent width method. An initial study for the HARPS sample was done for elements with A $<$ 29 by Adibekyan et al. (2012b) which focused mainly on the chemical separation of thin and thick disk stars. The study also showed an overabundance of all the elements ([X/H]) for the giant planet hosts. However, no trends for [X/Fe] with planet mass were studied. We took the elemental abundance of eight elements (Mg, Si, Ca, Ti, Cr, Ni, Co, Mn) from Adibekyan et al. (2012b) for our analysis.

[‡] Data from https://exoplanetarchive.ipac.caltech.edu/

For the neutron-capture elements, a separate study was conducted for the HARPS-GTO sample by Delgado Mena et al. (2017) and Delgado Mena et al. (2018). For the s-processes such as Ba, Sr, Ce, and Zr, it is found that planet-hosting stars are under-abundant compared to stars without planetary companions. These results are significant as they throw light on how s-process elemental abundances play a role in distinguishing stars with and without planets. However, the stellar abundance as a function of planet mass was not studied in detail in these papers. Thus, we took the elemental abundances ([X/Fe]) for two iron-peak elements (Cu, Zn) and seven neutron-capture elements (Sr, Y, Zr, Ba, Ce, Nd and Eu) from Delgado Mena et al. (2017) and combined it with the eight elements from Adibekyan et al. (2012b) to study the trends of α, iron-peak, s, and r-process elements as a function of planet mass.

3.2.2 California Planet Survey (CPS)

The abundance of stars in CPS is taken from Brewer et al. (2016). The sample consists of 1615 F, G, K and M stars which were observed using HIRES spectrograph ($R \sim 70000$) on the KECK I telescope as a part of radial velocity planet search program (Johnson et al. 2010a; Howard et al. 2010; Wright et al. 2011; Brewer et al. 2016). These stars were observed in the red configuration of HIRES without iodine cells in the beam path. We used the abundances of nine elements (Mg, Si, Ca, Ti, Cr, Mn, Fe, Ni, and Y) for our analysis from the CPS sample, which was obtained using the synthetic spectral fitting (Brewer et al. 2016) (SME; Piskunov & Valenti (2017)). To extract the planet-hosting stars from the sample, we cross-matched the CPS catalog with NASA exoplanet archive (Akeson et al. 2013; NASA Exoplanet Science Institute 2024) with a search radius of 3" (see Viswanath et al. (2020) for details)[§] and found that 227 stars are hosting 361

[§] We used a larger search radius initially but found that search radius of 3" was sufficient in this case to extract all the planet-hosting stars. We also double-checked them with other parameters such as Simbard's0 name to verify if they are truly planet-hosting stars.

Table 3.2: Key parameters of exoplanet host stars used in this study.

Star ID	Planet name	RA	DEC	Survey	$M_P(M_J)$	[Fe/H]	[Mg/Fe]	[Si/Fe]
HD 100777	HD 100777 b	173.9646761	-4.7556922	HARPS-GTO	1.03	0.25	0.04	0.05
HD 10180	HD 10180 c	24.4732364	-60.5115264	HARPS-GTO	0.04122	0.08	0.04	0.02
HD 10180	HD 10180 d	24.4732364	-60.5115264	HARPS-GTO	0.03697	0.08	0.04	0.02
...								

Note: The entire table is available in machine-readable format. For brevity, the first 3 rows and 10 columns are only shown here.

planets.

3.2.3 California Kepler Survey (CKS)

The CKS sample used in this study comes from Brewer & Fischer (2018). It consists of 1127 stars which are Kepler objects of interest (KOI). The CKS sample primarily consists of KOIs with the magnitude in the Kepler band $K_P \leqslant 14.2$ (Borucki et al. 2011b; Johnson et al. 2017; Petigura et al. 2017). The CKS KOIs used in this study were observed using the same instrumental configuration as that of the CPS host stars described in Section 3.2.2. For our analysis, we took the elemental abundances for nine elements (Mg, Si, Ca, Ti, Cr, Mn, Fe, Ni, and Y) for the KOIs from Brewer & Fischer (2018), which used synthetic spectral fitting similar to the CPS host stars. We crossmatched the CKS data used in this study with NASA exoplanet archive (Akeson et al. 2013; NASA Exoplanet Science Institute 2024) with a search radius of 3” (same as done for CPS) and found a total of 600 stars hosting at least one planet. The remainder of the sample consists of planetary candidates, false positives, and stars without planets (see the kepler false-positive table for details). For our analysis, we have only considered the main sequence stars from the CKS sample, which hosts confirmed planets.

3.2.4 Planet mass

The data for the planet mass was mostly obtained from the NASA exoplanet archive (Akeson et al. 2013; NASA Exoplanet Science Institute 2024). For 24 planets, the masses were taken from the exoplanet.eu catalog for which the mass was not available in the NASA exoplanet archive. For the transiting planets in the CKS sample, the mass is derived from the *mass-radius* relation given by Chen & Kipping (2017). For planets detected by radial velocity (RV) in the HARPS-GTO and CPS, the minimum mass (M_P) was used. For the giant planets in the CKS sample for which the RV follow-up observations were done, the actual mass derived from the RV analysis was used. The distribution of planet mass and orbital distance for our sample is shown in Figure 3.2.

3.2.5 Abundance comparison

The elemental abundances derived by different techniques suffer from systematic biases (Blanco-Cuaresma 2019). The abundances for the host stars of CPS and CKS are derived by synthetic spectral fitting using spectroscopy made easy (SME; Piskunov & Valenti (2017)). On the other hand, the abundances of the HARPS-GTO sample were primarily determined using the equivalent width method using MOOG (Sneden 1973). We wanted to compare if the elemental abundances obtained by the two different groups have any significant offset or scatter amongst them. We found 79 stars common between HARPS-GTO and CPS samples while 56 stars common between CPS and CKS samples. Figure 3.3 shows the abundance comparison between the HARPS-GTO vs CPS and CKS vs CPS sample for three different elements; Fe, which is used as a proxy for overall metallicity; Mg, which is an α-peak element and Mn, which is a iron-peak element. Most stars in CPS and CKS samples were not only observed using the same telescope and instrumental setup but also analyzed using the same techniques and thus show a less spread about x = y line in Figure 3.3. Barring few outliers, our analysis indicates that overall abundances determined in three samples using different methods are largely consistent. Since we didn't find any significant offset or scatter between our samples, no correction was made for further study.

3.2.6 Final sample

The distribution of T_{eff} and $\log g$ for the original HARPS-GTO, CPS and CKS samples is shown in Figure 3.1. The original sample includes many evolved stars, mostly sub-giants. In this study, we have restricted our analysis to the main sequence stars, since, for the sub-giants, it is difficult to account for Non-Local Thermodynamic Equilibrium (NLTE) and evolutionary effects which can cause mixing in the photospheric abundances. Following the procedure of Brewer & Fischer (2018), we selected stars below the black dashed line (see Figure 3.1), which represents the main sequence stars. Thus, our final data consists of 217 planets hosted by 141 stars from the HARPS-GTO sample, 600 stars hosting 1008 planets from the CKS sample, and 227 stars hosting 361 planets in the CPS sample. A detailed description of our final sample is given in Table 3.1.

3.3 Analysis and Results

One of the goals of this work is to examine the correlation between the abundance of the host stars with their planet mass and how it relates to the chemical evolution of elements in the galaxy. The knowledge of different elements produced in various stages of GCE can help us understand the observed trends between

[X/Fe] and planet mass. In fact, such trends would be indicative of timescales when planets of different masses were formed. We used regression analysis and Spearman's coefficients to study the correlation between planet mass and chemical abundances [X/Fe] of the stellar hosts. In standard linear regression, the presence of outliers can significantly influence the least-squares fit which approximates the underlying trends between the parameters of interest. We, therefore, used the Huber regression model, which is a robust approach to produce a 'weighted' regression line that is less sensitive to outliers. Furthermore, to keep our regression analysis simple, we have not included stars hosting multiple planets belonging to SP, GP, and/or SJ categories. The list of multi-planetary systems comprises: 14 stars hosting 34 planets in HARPS-GTO; 24 stars hosting 70 planets in CKS; and 16 stars hosting 42 planets in the CPS sample. The selected planet-hosting stars and associated stellar and planetary parameters are given in Table 3.2. Figure 3.4 shows the histogram of the metallicity distribution of our sample. Clearly, the massive planets ($> 0.3M_J$) are mainly hosted by metal-rich stars, while for the smaller planets ($< 0.3M_J$) there is no specific preference in terms of the metallicity of the host stars. The regression trends for various elements are presented in the following subsections.

3.3.1 α-elements

The α-element abundances of the planet-hosting stars can be a proxy to the age of the stars (Delgado Mena et al. 2019). A significant contribution of α-elements comes from SNe II. In this chapter, we examine the abundance pattern for four common α-elements (Mg, Si, Ca and Ti) that were studied in the HARPS, CPS, and CKS samples. Figure 3.5 shows the variation of α-abundances of host stars with the mass of their planetary companions. The last row in Figure 3.5 represents the mean abundance of all four α-elements in each sample. The uncertainties associated with the individual abundance measurements are about 0.02-0.05 dex.

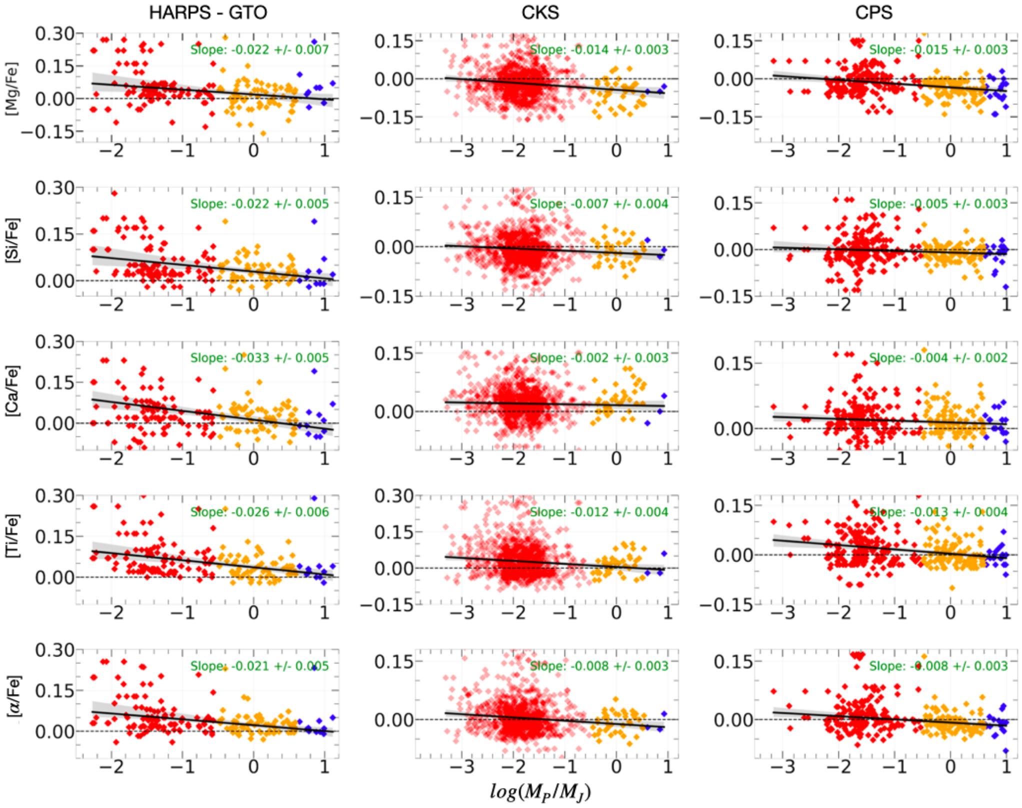

FIGURE 3.5: Observed trends for α-element abundances of host stars and planet mass for the HARPS-GTO, CKS, and CPS samples. The colors are red, yellow, and blue represent small planets, giant planets, and super-Jupiters, respectively. The black line shows the Huber regression fit and the grey shaded region represents the 95 percentile confidence interval. The slope value for the best-fit line is shown in each panel. The last row is the arithmetic mean, of the α-element abundance from the above four rows.

In the HARPS-GTO case, we find a clear negative correlation for all the α-element abundances with the planet's mass. In the case of the CKS sample, which is dominated by small planets, the correlation is weaker compared to the HARPS-GTO sample. The CPS sample also shows a significant negative correlation for all the elements. A strong (weak) correlation implies a large (small) Spearman's rank coefficient and small (large) p-value as shown in Table 3.3.

Clearly, there is an overall decline of [α/Fe] with increasing planet mass in all three samples. This can be understood as the gradual enrichment of ISM with iron produced in SN Ia, and not necessarily the decline of [α/H], which can also

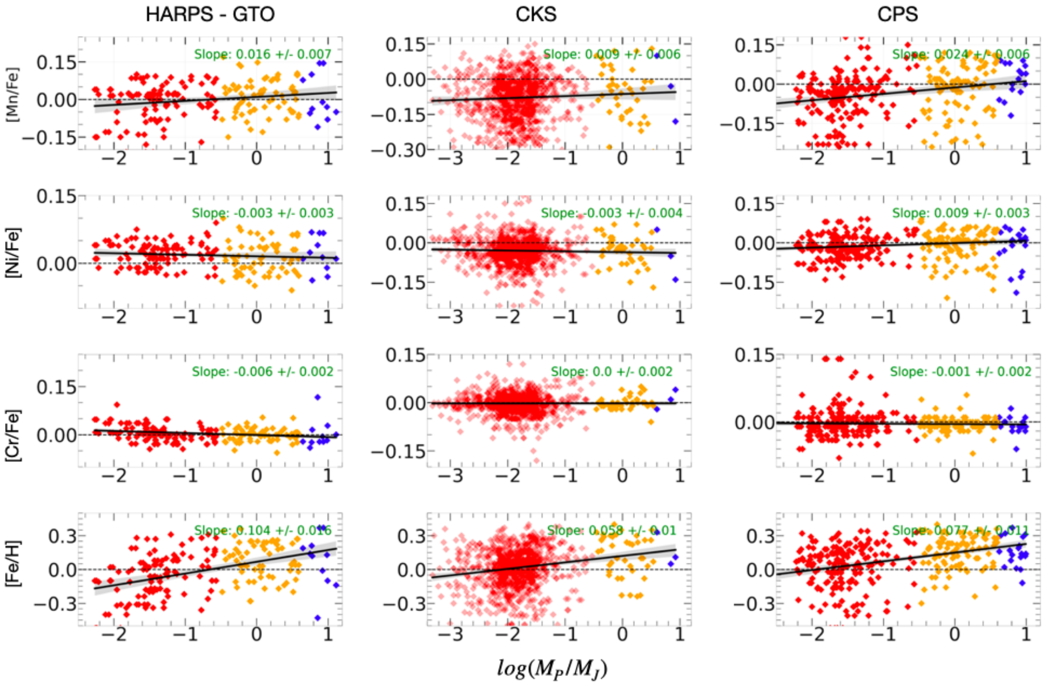

FIGURE 3.6: Host star chemical abundances for iron-peak (Mn, Cr, and Ni) elements and metallicity ([Fe/H]) as a function of planet mass for the HARPS-GTO, CKS, and CPS sample. Symbols and the colors are same as that of Figure 3.5.

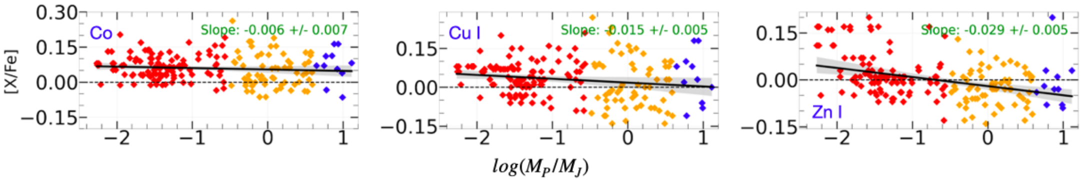

FIGURE 3.7: Stellar abundances for iron-peak elements (Co, Cu and Zn) as a function of planet mass exclusively for HARPS-GTO sample. The Co, Cu, and Zn abundances were not available for CKS and CPS samples. Once again, the color scheme and the black line representation are the same as that of Figure 3.5.

be seen in Figure 3.3.4, Figure 3.10. Interestingly, the regression analysis done separately for multi-planetary systems (Figure 3.3.5, Figure 3.13) does not show any significant correlation of [α/Fe] with the planet mass. Additionally, the overall α-element abundances for this sample are also found to be lower across three mass bins.

3.3.2 Iron-peak elements

The significant contribution of iron-peak elements comes from the Type-Ia supernovae, which occurred at the later stages of GCE compared to SNe II. Again, we analyzed the iron-peak abundance trends for three elements (Cr, Mn, Ni) common for HARPS-GTO, CKS and CPS samples and three elements (Co, Cu, Zn) exclusively from HARPS-GTO samples. Figure 3.6 (except the last row) and 3.7 show the iron-peak abundances trends as a function of planet mass. We also find a positive correlation between the Mn abundance and planet mass for all three samples. On the other hand, the abundance of Zn shows behaviour similar to α-peak elements (a strong decreasing trend). This is likely because Zn is also synthesized in core-collapse supernovae. Therefore, we see the same effect of GCE in Zn as we see in the α-elements (Kobayashi et al. 2020). For Co, Ni and Cu, we don't see any significant abundance trends with planet mass. In the case of Cr, we see a negative trend for the HARPS-GTO sample, but we don't see any trend for the CKS and CPS samples. The last row of Figure 3.6 shows the increasing trend of stellar metalicity ([Fe/H]) with planet mass, which is a well-established result reported in many similar studies (Fischer & Valenti 2005; Narang et al. 2018).

Overall, the iron-peak elements don't show any significant correlation with planet mass (as listed in Table 3.3) except for Mn and Zn. Also, the enrichment of Fe-peak elements with Fe is either increasing (for Mn, Co, Ni and Cu I) or zero (Cr), as seen in Figure 3.11 which is in sharp contrast to the trends for α elements.

3.3.3 Heavy-elements

Stellar fusion alone cannot produce elements heavier than iron. Most of the heavy elements (A>30) are formed by the neutron capture process which can be broadly

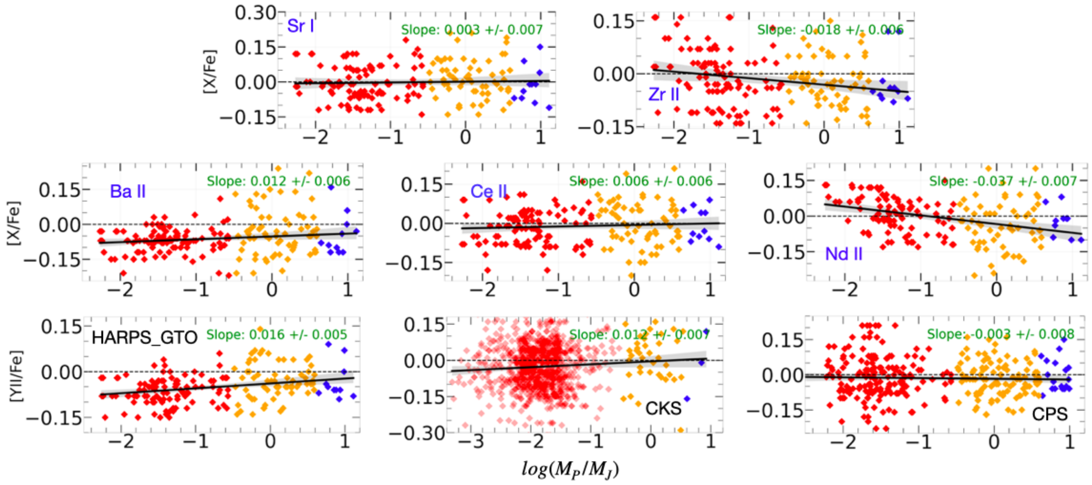

FIGURE 3.8: **Top row :** Host star chemical abundances for light s-process elements as a function of planet mass for the HARPS-GTO sample. **Middle row :** Host star chemical abundances for heavy s-process elements as a function of planet mass for the HARPS-GTO sample. The color scheme is the same as that of Figure 3.5. **Bottom row :** Light s-process element (Y) abundances as a function of planet mass for HARPS-GTO, CKS, and CPS sample.

classified into slow- and rapid- processes. The slow-process (s-process) takes place when the density of neutrons is low ($n_n \sim 10^8$ cm^{-3}), and the successive captures of neutrons happen at a longer time scale ($\sim 10^3 - 10^4$ years) (Herwig 2005; Karakas & Lattanzio 2014; Frebel 2018; Kobayashi et al. 2020). If the nuclei are unstable, then a β-decay will occur, transforming neutron to protons (thus increasing atomic number). In the case of rapid-process (r-process), the density of neutrons is higher ($n_n > 10^{22}$ cm^{-3}), therefore, the time scale is much shorter ($\sim$few milliseconds to seconds) between the subsequent neutron captures compared to s-process ($\sim 10^3 - 10^4$ years). Also since the r-process time scale is much shorter than the β-decay time scales (Baraffe et al. 1992; Cowan et al. 2021; Saraf et al. 2023; Saraf & Sivarani 2023, 2024), the r-process happens much faster. The GCE trends for the various heavy elements with Fe are shown in Figure 3.12. For all the heavy elements, in the region [Fe/H]>-0.5, we find a gradual decrease in [heavy elements/Fe] abundances with Fe-enrichment.

TABLE 3.3: Spearman's rank correlation coefficient ρ values obtained between elemental abundance [X/Fe] and planet mass for HARPS-GTO, CKS, and CPS samples. The values in the parenthesis represent the p-values associated with the correlation.

Category	Element	Atomic number	HARPS	CKS	CPS
α-elements	Mg	12	-0.27 (1.93×10^{-4})	-0.10 (2.3×10^{-3})	-0.28 (5.71×10^{-7})
	Si	14	-0.39 (4.02×10^{-8})	-0.10 (3.05×10^{-3})	-0.10 (4.01×10^{-2})
	Ca	20	-0.42 (1.14×10^{-9})	-0.06 (8.02×10^{-2})	-0.13 (1.23×10^{-2})
	Ti	22	-0.45 (1.69×10^{-10})	-0.13 (7.18×10^{-5})	-0.25 (2.84×10^{-6})
	α-avg	–	-0.45 (5.92×10^{-9})	-0.13 (5.661×10^{-5})	-0.25 (6.42×10^{-6})
Iron-peak	Cr	24	-0.22 (2.91×10^{-4})	-0.01 (5.55×10^{-1})	0.00 (9.72×10^{-1})
	Mn	25	0.17 (2.28×10^{-2})	0.08 (3.52×10^{-2})	0.26 (9.37×10^{-7})
	Co	27	-0.08 (1.37×10^{-1})	–	–
	Ni	28	-0.08 (2.08×10^{-1})	-0.01 (6.47×10^{-1})	0.12 (4.44×10^{-3})
	Cu	29	-0.14 (4.03×10^{-2})	–	–
	Zn	30	-0.39 (3.21×10^{-8})	–	–
Light s-process	Sr I	38	0.03 (0.63)	–	–
	Y II	39	0.27 (6.99×10^{-5})	0.01 (5.63×10^{-1})	-0.04 (3.11×10^{-1})
	Zr II	40	-0.21 (3.97×10^{-3})	–	–
Heavy s-process	Ba II	56	0.17 (2.68×10^{-2})	–	–
	Ce II	58	0.06 (3.16×10^{-1})	–	–
	Nd II	60	-0.36 (1.09×10^{-6})	–	–
r-process	Eu II	63	-0.37 (1.07×10^{-6})	–	–

3.3.3.1 Light s-process elements

The major production site for the s-process elements is in the He intershell of the asymptotic giant branch (AGB) stars (Baraffe et al. 1992; Goswami et al. 2021; Goswami & Goswami 2022). The s-process elements are further categorized based on their atomic masses. Here, we studied the abundances for three light s-process elements (Y, Sr, Zr). The top row and bottom row in Figure 3.8 show the light s-process abundances trends as a function of planet mass. For YII and SrI we don't see any significant correlation in our samples, whereas for ZrII, we find a negative trend with planet mass as pointed out in Table 3.3.

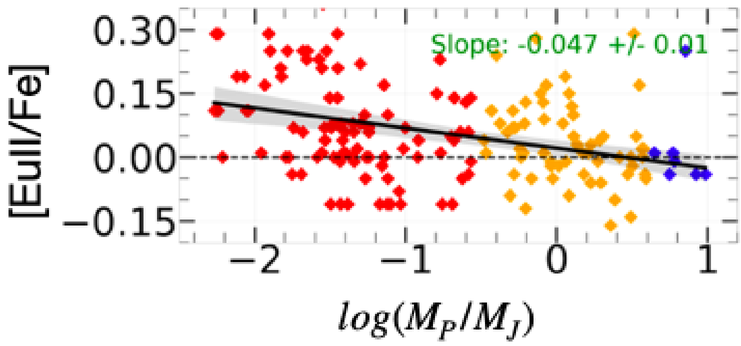

FIGURE 3.9: Variation of Eu abundance (r-process element) as a function of planet mass for the HARPS-GTO sample. The color scheme is the same as that of Figure 3.5.

3.3.3.2 Heavy s-process elements

The three heavy s-process elements analyzed in this work are Ba, Ce, and Nd. The middle row of Figure 3.8 shows the heavy s-process abundance trends as a function of planet mass. We find that the correlation between BaII and CeII abundances and planet mass is weak. On the other hand, Nd shows a strong negative trend as planet mass increases. The behavior of Nd resembles α-elements.

3.3.3.3 r-process elements

Although the formation mechanism of r-process elements is a field of active research, with the recent observations of kilonova GW170817, it is possible to explain the Eu abundances solely from neutron star merger models (van Oirschot et al. 2019). The only pure r-process element known and studied here is Eu from the HARPS-GTO sample. Figure 3.9 shows the strong negative trend of Eu with planet mass which looks similar to the α-elements.

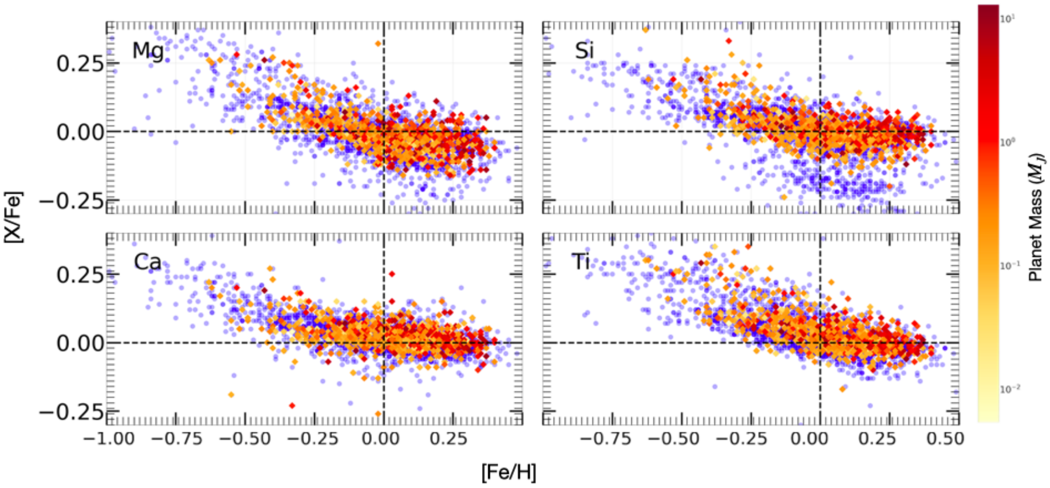

FIGURE 3.10: Abundance ratios [X/Fe] vs [Fe/H] for α-elements for stars belonging to all the three samples: HARPS-GTO, CKS, and CPS. The blue dots represent stars without planets while the color bar represents stars hosting planets of different masses.

3.3.4 Elemental abundances [X/Fe] as a function of [Fe/H]

In the case of α-elements, we see the [X/Fe] trend to be decreasing with [Fe/H], while for iron-peak elements, we see a variety of trends with [Fe/H]. The overall trends seen in these figures are consistent with the standard GCE model. The planet-hosting stars primarily lie in the metal-rich regime, as seen in Figures 3.10, 3.11 and 3.12.

3.3.5 α-element abundance for the multi-planetary systems.

For the subsample of multi-planetary systems excluded from the analysis in Section 3.3, we do not find a noticeable correlation between the α-element abundance and the planet mass (see Figure 3.13). This indicates the multi-planetary systems that host at least one giant or a super-giant, are also recently formed.

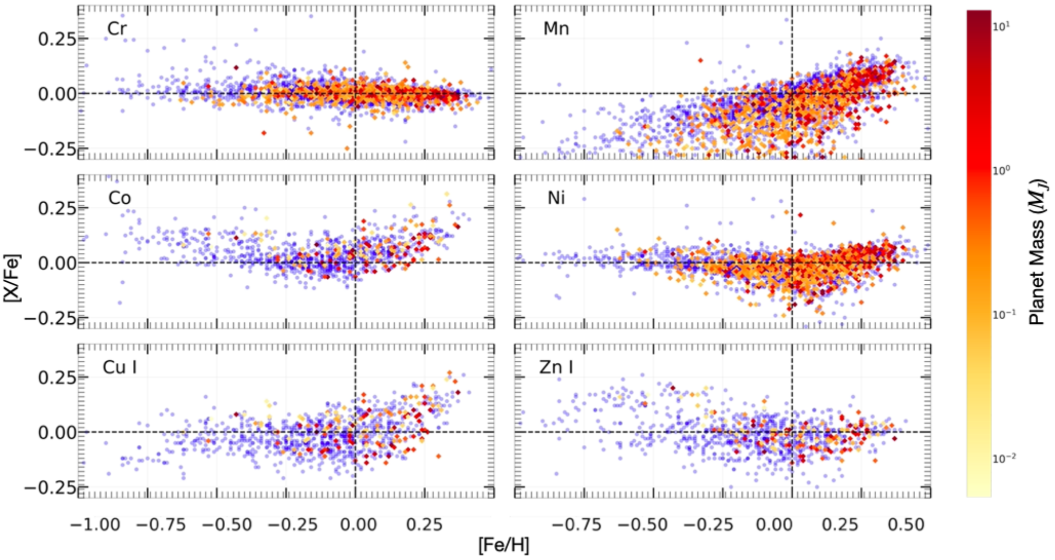

FIGURE 3.11: Abundance ratios [X/Fe] vs [Fe/H] for iron-peak elements for stars belonging to all three samples: HARPS-GTO, CKS and CPS. The blue dots represent stars without planets while the color bar represents stars hosting planets of different masses.

3.4 Discussion

3.4.1 α-elements: proxy to planet mass and age

The *alpha* elements are primarily formed by SNe II, which happened at the earlier stages of the GCE, while the iron-peak elements are believed to have formed during the SNe Ia, occurring at the later stages of GCE. Relative to iron, the abundances of α-elements and those formed mostly by SNe II in general increases with the age of the star (Nissen 2015; Bedell et al. 2018; Anders et al. 2018; Feuillet et al. 2018; Buder et al. 2019; Delgado Mena et al. 2019). From Figure 3.5, we see that [α/Fe] and planet mass have negative slope. In addition, the low-mass planets hosts show larger [α/Fe] dispersion compared to the parent stars of Jupiter and super-jupiters (see Section 3.4.2 for further discussion). One plausible interpretation of such trends is that the low-mass rocky planets have been forming around all generations of stars (old as well as young), while the high-mass giant planets likely

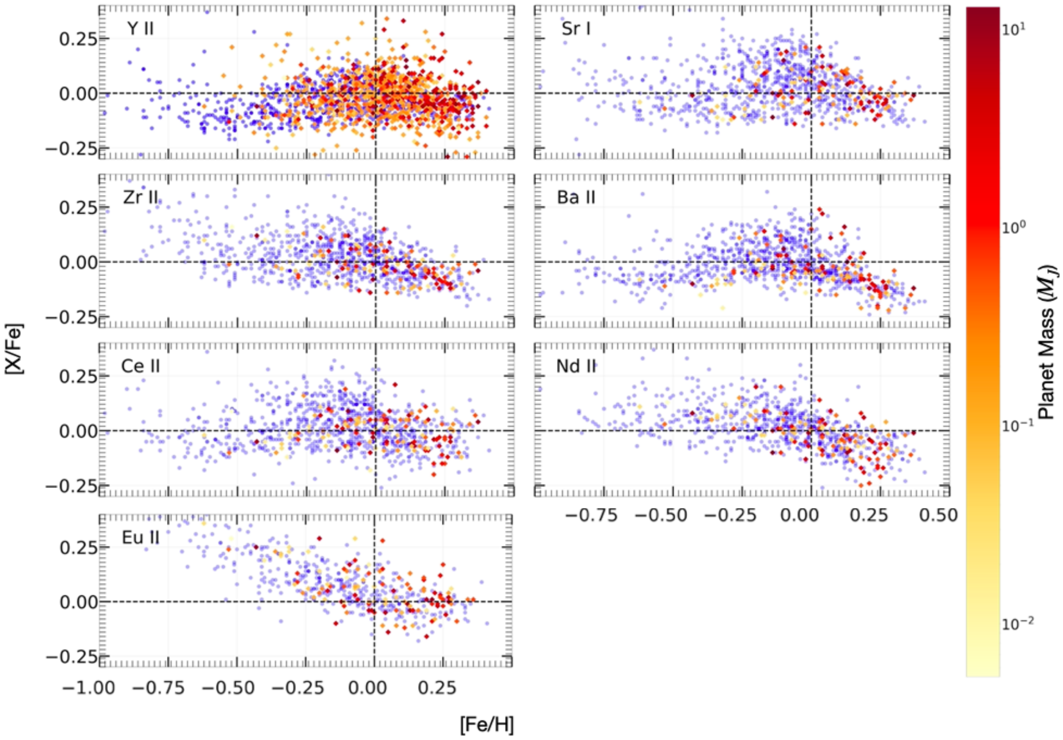

FIGURE 3.12: Abundance ratios [X/Fe] vs [Fe/H] for heavy elements (A>30) for stars belonging to all the three samples: HARPS-GTO, CKS and CPS. The blue dots represent stars without planets while the color bar represents stars hosting planets of different masses.

formed around younger stars when ISM was sufficiently enriched with iron-peak elements. The same reasoning must apply to the multi-planetary systems hosting at least one low-mass and one high-mass planet such as Jupiter or super-Jupiters. As shown in Figure 3.3.5, Figure 3.13, the slope between α-element abundance and planet mass is nearly an order of magnitude smaller compared to the corresponding slopes in Figure 3.5. This implies, that multiplanetary systems accompanying at least one high-mass planet are clearly α-deficient and therefore, younger. This wouldn't be the case for multi-planetary systems hosting only the small planets.

Since the iron-peak elements are formed at later stages of GCE, it suggests a similar formation timeline for the hosts of giant planets and possibly super-Jupiters, if core accretion was the dominant mechanism. Moreover, the abundance of iron-peak elements scales in same way as the abundance of iron [Fe/H]. Thus, the trends for

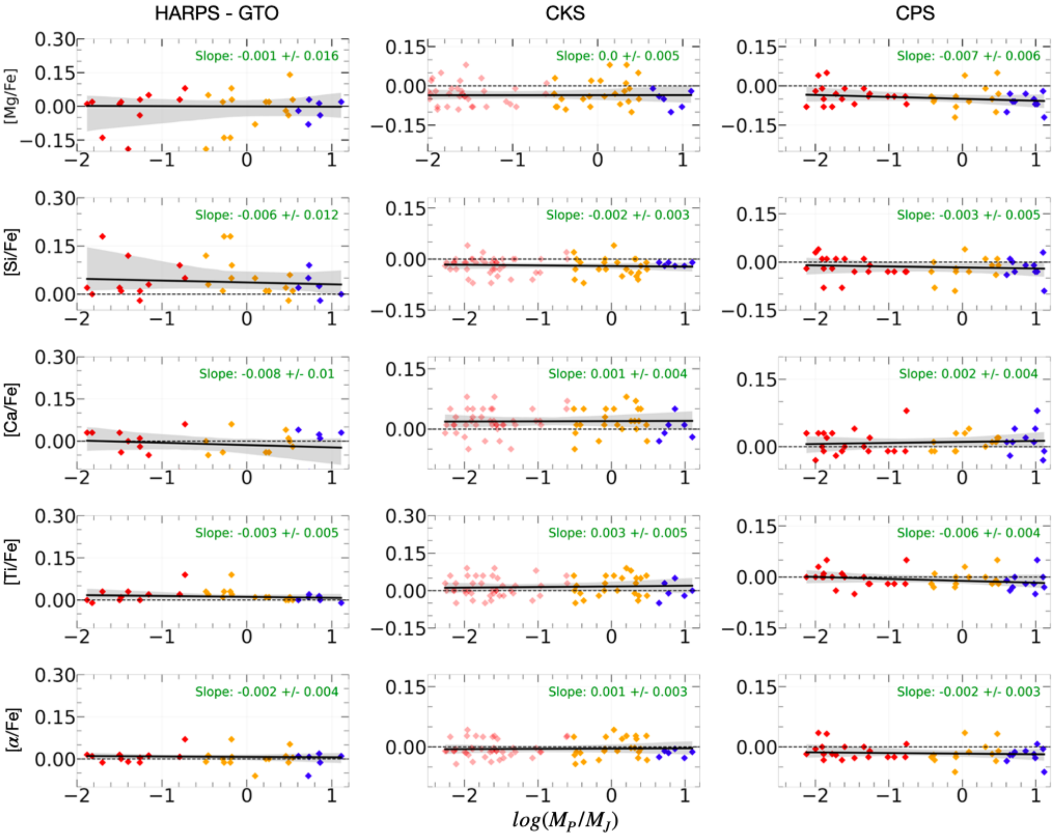

FIGURE 3.13: α-element abundances as a function of planet mass for the multi-planetary systems which host at least one planet each in low-mass and Jupiter and/or super-Jupiter mass regimes. The last row is the arithmetic mean of the α-element abundance from the above four rows.

iron-peak elements with planet mass is nearly positive or zero, as expected except Zn, which shows a strong negative trend similar to α-elements. The anomalous behavior of Zn is also seen in several studies (e.g. Bisterzo et al. 2004; Mikolaitis et al. 2017; Delgado Mena et al. 2019). Zn is found to increase with age, as it is also synthesized in core-collapse supernovae, and thus follows the GCE trends similar to α-elements (Kobayashi et al. 2020). We also see a positive trend for Mn as planet mass increases. Mn is produced mostly in SNe Ia (Nomoto et al. 1997; Kobayashi et al. 2006) and this trend indicates that statistically massive planet hosts are Mn-rich, and the presence of Mn in the host star may be crucial in the formation of giant planets. Interestingly, the GCE effect is also strong for [Mn/Fe] even for the field stars as evident from Figure 3.11. However, that alone cannot explain a relatively large slope of [Mn/Fe] versus planet mass among iron-peak elements seen in Figure 3.6. The yield for Ni is quite similar during SNe Ia and SNe II (Nomoto et al. 2013; Mikolaitis et al. 2017), thus, we expect a flat trend with planet mass which is also seen observationally. In line with GCE, the absence of any significant trend in iron-peak elements with planet mass independently suggests that the production of most iron-peak elements co-evolved with Fe. But more importantly, the later enrichment of the ISM with Fe and iron-peak elements, as the trends indicate, could be an important ingredient for the formation of high-mass planets.

For the heavy elements, the trends with planet mass can also be explained by the hypothesis discussed above. In the case of Eu, which is a r-process element, is largely formed through neutron-star mergers (Drout et al. 2017; Côté et al. 2018). These merger events predate the time scales of SNe Ia (Skúladóttir & Salvadori 2020; Reggiani et al. 2021). Further, studies have also shown that Eu abundance increases with age (Snaith et al. 2015; Delgado Mena et al. 2019) similar to α-elements. In our analysis, we find that Eu elemental abundance decreases as a planet's mass increases, a behavior similar to that of α-elements. The decrease of [Eu/Fe] with planet mass further strengthens our results and supports our hypothesis that exoplanet host stars with planet mass $>0.3 M_J$ could indeed be younger than SP hosts.

The s-process elements are primarily produced in low-mass AGB stars; thus, their contribution is expected to increase with time. The light s-process (Sr, Y, Zr) elements also show trends similar to iron-peak elements. Their trends for chemical abundances have a negative correlation with age ($\leq 8\,Gyr$) as shown by other studies (e.g. Battistini & Bensby 2016; Delgado Mena et al. 2019), which is expected as their production timeline is similar to the iron-peak elements. For heavy s-process element Ba, we see a positive slope with planet mass, but the trends are

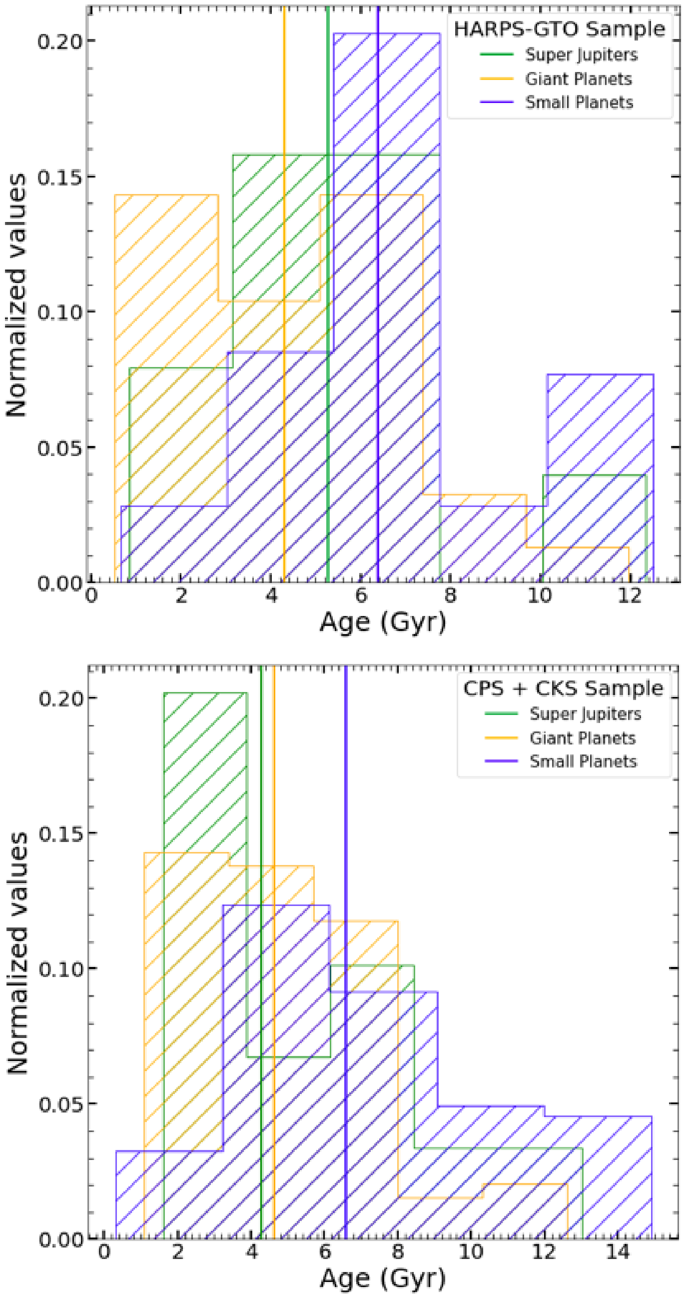

FIGURE 3.14: Age distribution of planet-hosting stars derived using isochrone fitting. The vertical lines represent the median for each of the distribution.

opposite for Nd, with Nd showing a strong negative trend with planet mass similar to Eu. This is because even though Nd is considered as a heavy s-process element, only about 56 percent of it is formed via the s-process (Arlandini et al.

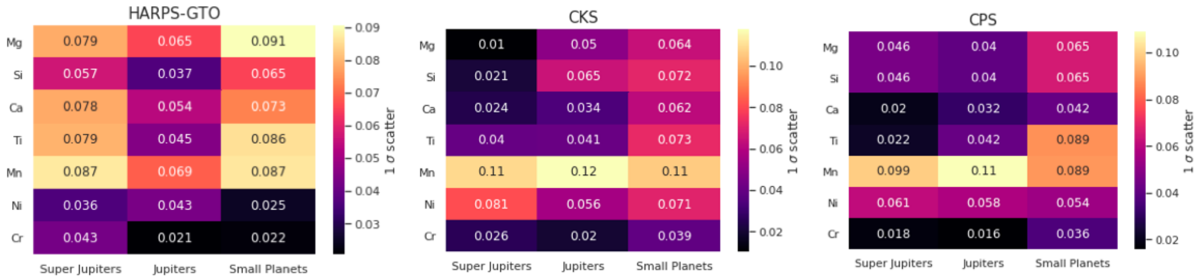

Figure 3.15: Heat-map of 1σ scatter from Figure 3.5 and Figure 3.6 for the abundance dispersion of the host stars of small planets, Jupiters, and super-Jupiters. A linear de-trend was applied to the original abundance data to compute the 1σ scatter for each mass bin.

1999; Bisterzo et al. 2016). The remaining Nd is produced by the r-process, predating the timescale scales of the s-process. Thus, in light of GCE, the α-element abundance seems as a good proxy for the planet's mass. One possible implication of this finding could be that stars hosting small planets have been forming through all epochs while the formation of stars hosting giant planets and super-Jupiters happened in later epochs when the ISM was sufficiently enriched by the iron and iron-peak elements.

3.4.2 Independent age analysis

The negative correlation between α-elements and planet mass presented in Section 3.3 indicates that stellar hosts of giant planets are probably younger. To corroborate our result, we took the independent age estimates of the HARPS-GTO, CPS and CKS sample from Delgado Mena et al. (2019), Brewer et al. (2016) and Brewer & Fischer (2018), respectively. In these studies, the stellar ages were determined using the isochrone fitting technique requiring effective temperature (T_{eff}) and luminosity (L) which were obtained from photometric and spectroscopic studies. For the HARPS-GTO sample, the ages were estimated using DR2 parallaxes and PARSEC isochrones (Bressan et al. 2012), while for the CPS and CKS sample the ages were determined by Yonsei - Yale isochrones (Demarque et al. 2004) and Dartmouth Stellar Evolution isochrones (Dotter et al. 2008). Although the individual age estimates will vary depending on the choice of model, it will not impact the underlying statistical trends, as these models do not have any significant systematic (Delgado Mena et al. 2019).

The age distribution of our samples divided into three mass bins is shown in Figure 3.14. We see that the host stars of giant planets ($M_P > 0.3 M_J$) and super Jupiters are younger compared to stars hosting smaller planets. For example, the median age (in Gyr) of SP, GP, and SJ hosts is 6.40, 4.30, and 5.23 for the HARPS-GTO sample and 6.58, 4.62, and 4.3 for the CPS and CKS samples. For planet-hosting stars in the HARPS-GTO sample, (see Figure 7 of Delgado Mena et al. (2019)) have found a positive correlation between [α/Fe] abundances and stellar age. This combined with the decrease of negative slope between [α/Fe] and planet mass found in this work, further lends independent support to our inference that stellar systems harboring massive planets could be younger. Further, when GAIA DR3 data was released later in July 2022, we did another independent study using stellar kinematics and isochrone models and arrived at similar conclusions. This is discussed in detail in chapter 4 and chapter 5.

Further, within the giant planet population, there is an observed paucity of hot Jupiters around old stars. To explain the dearth of old stars hosting massive and hot planets, Hamer & Schlaufman (2019) have argued that the tidal interaction between the host star and the planet can cause the planet to spiral into the star. Older stars will lose their hot Jupiters if this tidal infall timescale is relatively short. However, the tidal infall timescale (based on Equation 4 in Hamer & Schlaufman 2019) for a Jupiter-like planet around a Sun-like star for orbital periods $>\sim 7$ days can be as long as the main-sequence lifetime of these stars. The tidal infall timescales are even longer for planets less massive than Jupiter. Only giant planets with $M_P > 2\ M_J$ and orbital period < 5 days have tidal infall timescale much shorter than 1 Gyr. Hence tidal infall might be playing a key role, but it alone cannot explain the lack of hot giant planets around older stars.

Abundance scatter or dispersion is another measure of implicit spread in stellar ages. With the chemical evolution of the galaxy, the dispersion in elemental abundance, especially the [α/Fe] is expected to increase. We refer to the abundance spread seen in Figure 3.5 and Figure 3.6. This spread is further quantified in Figure 3.15 where we show the heat maps for the 1σ scatter in the abundance distribution of the stellar hosts. From Figure 3.15, the 1σ scatter for α-element abundances is much more pronounced for the small planet-hosting stars than the Jupiter and super-Jupiter hosts. Also, the scatter in the iron-peak elements, except for Mn, is relatively smaller than α-elements in all three samples. The large scatter in the α-element abundances implies a large dispersion in the ages of stars hosting small planets. This means small planets started forming early in our galaxy when [α/Fe] was high and continued to form in later generations of stars when [α/Fe] declined. On the contrary, the abundance distribution of stars hosting Jupiter-analogs and super-Jupiters has a small scatter and hence similar age, indicating the massive planets belong to a later generation of stars, represented by overall low [α/Fe] and increased iron-peak element abundance. Note that the overall scatter seen in Figure 3.5 and Figure 3.6 is much larger than the error in abundance determination of individual stars which is typically, 0.02-0.05 dex.

3.4.3 GCE and formation of giant planets

Results from Section 3.3 clearly establish a link between the abundance of iron and iron-peak elements and the giant planets. Among existing theories, gravitational instability has been highlighted as a favoured mechanism for the formation of giant planets beyond the snow line (Boss 1997; Mayer et al. 2002). Furthermore, Kratter

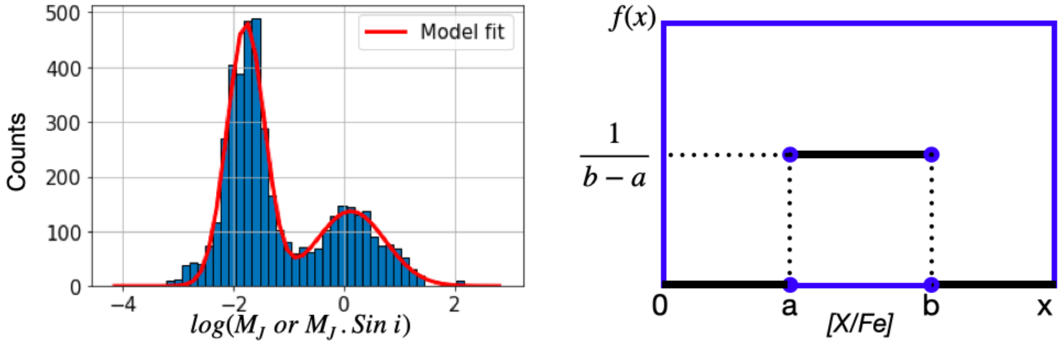

FIGURE 3.16: **left**: The observed distribution of exoplanet mass (in log scale) taken from NASA exoplanet archive. **Right**: A uniform distribution assumed for α-element abundances of planet hosting stars.

et al. (2010) demonstrated that a disk must have a gas-cooling time shorter than the Keplerian shearing timescale for runaway gravitational instability to occur. It is conceivable that, at significant distances (∼10s AU) from the star, radiative losses from metals in the protoplanetary disk may aid in cooling the gas during its early stages. However, scores of directly imaged planets and brown dwarfs in wider orbits have not shown any marked dependence on the stellar metallicity (Swastik et al. 2021).

The close-by gas giants detected by transit and RV surveys are expected to form via core accretion process (Pollack et al. 1996; Matsuo et al. 2007; Birnstiel et al. 2016; Owen & Murray-Clay 2018; Drazkowska et al. 2022). The galactic chemical evolution trends for α and iron-peak elements in Figure 3.3.4 (Figure 3.10-3.12) shows that in the region [Fe/H] $>$ -0.5, [α/Fe] decreases with the enrichment of [Fe/H], but for iron-peak elements, the trends are mostly flat or increasing with [Fe/H]. Therefore, with the enrichment of Fe in ISM, the content of iron-peak elements scales much faster with Fe compared to the α-peak abundances. The fact that the gas giants are known to be formed from a metal-rich protoplanetary disk is a natural consequence of the large addition of iron-peak elements.

To form a gas giant through the core accretion model, two critical processes are essential. Initially, a solid core or embryo must be formed, typically around $\sim 10M_\oplus$, within the protoplanetary disk. This formation occurs through a series of collisions and the amalgamation of planetesimals (for a more detailed explanation, see Drazkowska et al. (2022)). Following this, there must be a rapid accumulation of gas from the surrounding protoplanetary disk, occurring before the complete depletion of gas and dust (Rice & Armitage 2003; Birnstiel et al. 2016; Drazkowska et al. 2022). For the core to successfully attract a gaseous envelope, it must form at a relatively rapid pace, within $\sim$ 3-10 Myr. (Matsuo et al. 2007; Ayliffe & Bate 2012; Emsenhuber et al. 2021). Whether a proto-planet will end up like a rocky planet or a gas giant will depend on the amount of material present in the proto-planetary disk (Alibert et al. 2005). The gas-giant planet formation requires the core to build faster to outdo the gas dissipation rate so that the gas is not entirely depleted by the time the massive core ($\sim 10M_\oplus$) is formed. Although protoplanetary disks were massive during the early phase of GCE, the refractory *alpha* elements alone would have contributed to the formation of the core. By the time the core formed, most of the gas in the disk would dissipate, leading to a preferential formation of rocky planets. However, as the galaxy chemically evolved, the ISM was enriched in both α and iron-peak elements coming from the SNe Ia. This additional enrichment would propel the growth of grains, pebbles, planetesimals and finally, the core (Drazkowska et al. 2022). Since the chemically enriched material fuels the growth of the core quickly reaching the critical mass, the disk will have sufficient gas left to accrete onto the surface of the core to form the gas giants (Matsuo et al. 2007; Ayliffe & Bate 2012; Drazkowska et al. 2022). Thus, the delayed enrichment of ISM by SNe Ia created pathways for the formation of gas giants, which seems consistent with the core accretion process.

3.4.4 Biases and statistical validity of our results

Exoplanet host stars selected from various transits and RV surveys could suffer from different detection and selection biases. The transit method, for example, is primarily sensitive to planets orbiting close to the star with near-edge on configuration. The radial velocity method, on the other hand, is suitable for detecting giant planets at large orbital distances (see e.g., Figure 3.2). Since the RV precision is adversely affected by stellar activity and line-broadening mechanisms, the highly active and fast-rotating stars are usually excluded from the RV surveys, keeping the focus largely on the main sequence dwarfs. However, to our knowledge, no study exists that links the chemical composition of stars to stellar activity and/or rotation. Therefore, it is very unlikely that possible biases in RV/transit search would impact the chemical analysis of the exoplanet-hosting stars. As reported in section 3.3, the stellar abundance trends with planet mass are similar and consistent with GCE for all three samples, regardless of the search method.

Further to ensure our results are not biased due to low-number statistics or random correlations in the abundances, a Monte Carlo test was carried out. We attempted to reproduce the correlations obtained in Section 3.3 by using simulated planet mass and abundances. Since the trends for α-elements were most robust, we used them as a case study for this analysis. For our simulations, we constructed a bimodal function describing the observed planet mass distribution as shown in the left panel of Figure 3.16. The apparent mass distribution of confirmed exoplanets has two peaks, - one near 0.01 M_J and another at 1 M_J. The intrinsic mass distribution of exoplanets could be different from the apparent mass distribution, but we discount any selection effects since they are hard to quantify (Malhotra 2015).

For abundances, we assumed a uniform distribution, bound by a rectangular window function shown in the right panel of Figure 3.16. The lower and upper bounds

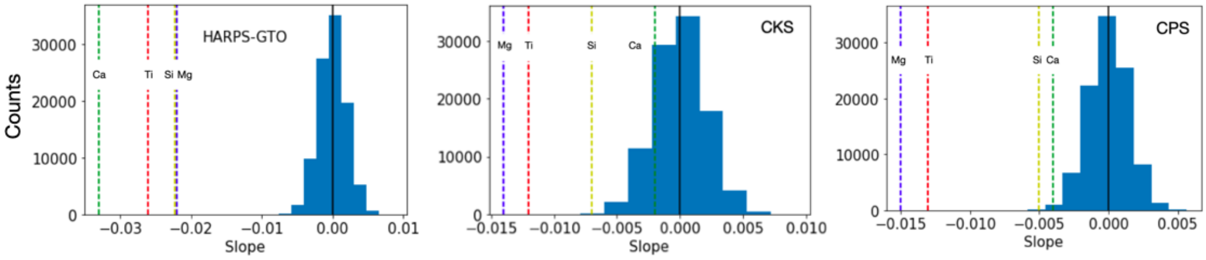

Figure 3.17: The distribution of numerical slope (between α-element abundances of host star versus planet mass) generated from Monte-Carlo simulations for the HARPS-GTO, CKS, and CPS samples. The solid black line represents the mean of the distribution and color dotted lines represent the measured slope from Figure 3.5.

for the abundance distributions in each sample are taken at 3σ cutoff on either side of the observed distribution mean of the averaged α-abundances plotted in the last row of Figure 3.5.

For each simulation run, we randomly draw 500 samples from the assumed distributions of planet mass and abundance. We then calculate the slope of the best-fit line between the planet's mass and abundance. The goal is to check how often the observed slope is reproduced in a reasonably large numerical experiment, with the underlying abundance distribution assumed to be uniform. The simulation was repeated 100,000 times, and the final histograms of slopes are shown in Figure 3.17. For the HARPS-GTO sample, the observed slopes for all the elements are significantly far from the mean of the numerical slopes, suggesting that observed trends are highly improbable due to chance outcomes. In fact, none of the trials produced results that matched the observed slopes, thus rendering the probability of observed trends arising from random occurrence extremely low ($\leqslant 10^{-5}$). Similarly, for the CKS and CPS samples, the observed slopes for Mg, Si, and Ti are also significantly away from the mean of the numerical distribution, with Ca as an exception which is only about 1 σ (CKS) and 3 σ (CPS) away. Generally, this analysis suggests that the observed α-element trends obtained in Section 3.3 cannot be generated by simple randomness, and these trends are also not due to low-number statistics. Therefore, *planet-abundance* pattern observed in a finite sample of exoplanet host stars must be a correct manifestation of the underlying population.

3.5 Summary and Conclusions

Exoplanet properties are intimately connected to the properties of their stellar hosts. In this study, we examined the chemical compositions of stars with orbiting planets, focusing on planets within various mass categories. We analyzed the abundances of 17 elements belonging to different classes based on their formation mechanism and evolution of the chemical history of the galaxy. We used data from well-known exoplanet search programs, namely, HARPS-GTO, CKS, and CPS, and planetary mass from the NASA exoplanet catalog. Our analysis includes 968 planet-hosting stars, which are discovered by both transit and radial velocity methods. Here, we present a summary of our results :

1. We find that for all the α-elements, which are mainly produced in SNe II, there is an unambiguous negative slope with planet mass for all the three samples used in this study, showing that stars hosting small planets are clearly α-rich compared to stars harboring giant planets and super-Jupiters.
2. We observe a positive correlation for manganese and almost no correlation for iron-peak elements in relation to planet mass in most cases. Given that iron-peak elements predominantly originate from Type Ia supernovae and scale similarly to iron, their surface composition, denoted as [X/Fe], in stars hosting planets remains largely unchanged, irrespective of the planetary mass.
3. For the r-process element Europium (Eu), primarily formed in neutron star mergers occurring at earlier stages of Galactic Chemical Evolution (earlier

than Type Ia supernovae), the trend of [Eu/Fe] in relation to planet mass is akin to that of -elements.

4. The s-process elements are primarily produced in AGB stars and are formed at much later stages of the GCE (after SNe Ia enrichment). We expected their trends to follow iron-peak elements. However, we find that Nd shows a significant negative trend with planet mass. This could be because a significant amount of Nd is produced by r-process.

5. Our abundance analysis of exoplanet host stars shows two specific trends with planet mass; a distinct negative slope for alpha-elements including Eu and a near-zero slope for most iron-peak elements. Seen in the context of GCE, these results imply that stellar systems with small planets may have started forming early in the evolutionary history of our galaxy, whereas, the emergence of high-mass planetary systems had to wait until the ISM was sufficiently enriched.

6. To validate our findings, we compare the stellar ages estimated from the isochrone fitting. Our independent age analysis also shows that the stars of massive gas giant planets are indeed statistically younger than the stars hosting low-mass planets.

7. Compared to their low-mass counterparts, we also find a relatively small scatter in the abundance distribution of stellar hosts of high-mass planets. This is compatible with the younger age and temporal offset in the formation scenario of Jupiters and super-Jupiters.

8. Our sample of multi-planetary systems hosting at least one low-mass and one high-mass planetary companion, do not show any correlation between [α/Fe] and planet mass. In addition, their overall [α/Fe] abundance across all three mass bins is also lower. This too, suggests the possibility that such multiplanetary systems are younger.

In summary, our analysis of the elemental abundances in a substantial sample of 968 stars hosting planets links the process of planet formation to the chemical enrichment evolution of the Interstellar Medium (ISM). The comprehensive abundance profiles of stars with exoplanets align well with the broader trends of galactic chemical evolution. Based on the patterns observed between stellar elemental abundances and planetary mass, we infer that low-mass planets likely formed throughout various star formation epochs, whereas giant planets tend to form around chemically enriched, relatively younger stars.

To substantiate these conclusions, upcoming high-resolution spectroscopic surveys should focus on a larger sample of stars hosting exoplanets, ensuring uniform and consistent determination of their chemical abundances. Additionally, further theoretical and experimental research is necessary to deepen our understanding of the significance of chemical abundance, particularly the influence of iron-peak elements in the formation and growth of dust grains, pebbles, and planetesimals within astrophysical environments.

Chapter 4

Kinematics Age Analysis of Planet-hosting Stars from GAIA DR3 [*]

4.1 Introduction

The GAIA space mission is driving unparalleled progress in the fields of astronomy and astrophysics, a feat made possible by the extensive and high-quality dataset gathered from its onboard high-precision spectroscopic, astrometric, and photometric tools (Gaia Collaboration et al. 2018, 2022). Similarly, the influence of GAIA on the study of exoplanets is remarkably significant. The potential of the GAIA mission for discovering planets was initially explored by Perryman et al.

---

[*] Part of this work have been published in Swastik et al. (2023)

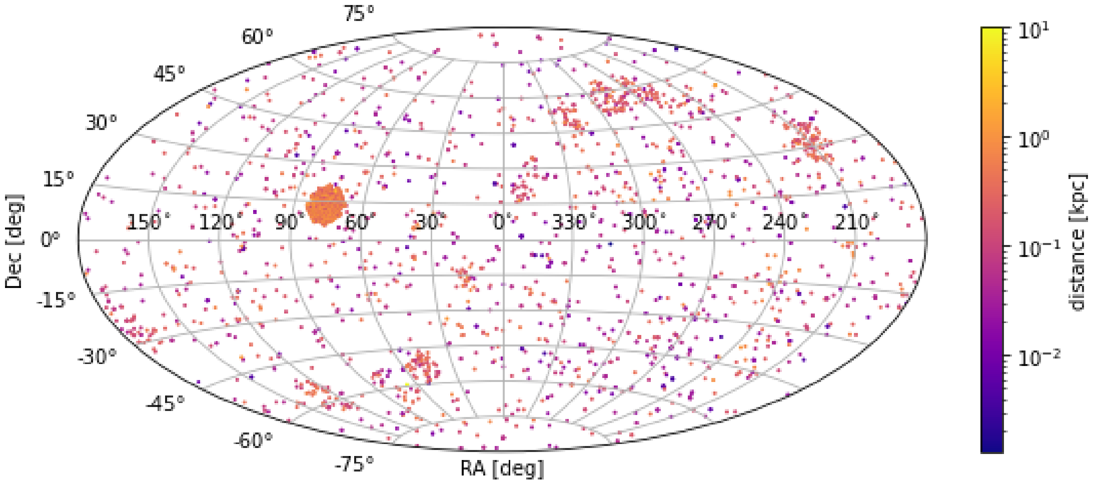

FIGURE 4.1: Exoplanet hosting stars for which Gaia parameters are available. The colorbar represents the distance in kpc from the sun. Also, note the blob of the planet above the galactic plane, which represents the Kepler field.

(2014). Given its role as a crucial method for detection, astrometry enables the determination of both the mass and the orbital period of exoplanets. With the forthcoming data release, GAIA is poised to uncover several thousand new exoplanets, benefiting from an astrometric precision that is 30 times greater than that of its forerunner, HIPPARCOS (van Leeuwen 1997). However, the contributions of GAIA to exoplanet research extend beyond mere planet detection through astrometry.

The GAIA mission has facilitated the determination of stellar and planetary radii with unparalleled precision, achieving an accuracy of ∼5% through the use of the most accurate parallaxes available (Berger et al. 2018, 2020b). Consequently, the precise measurement of stellar and planetary radii has reinforced correlations between stars and their planets, such as the relationship between planet radius and stellar metallicity (Buchhave et al. 2014; Schlaufman 2018; Narang et al. 2018). Further, the existence of the "radius valley" a gap in the distribution of exoplanet radii that separates the super-earths ($R \sim 1.4 R_\oplus$) and mini Neptunes ($R \sim 2.4 R_\oplus$), with a clear paucity around $R \sim 1.8 R_\oplus$, is now well established from observational results (Fulton et al. 2017; Armstrong et al. 2019; Petigura

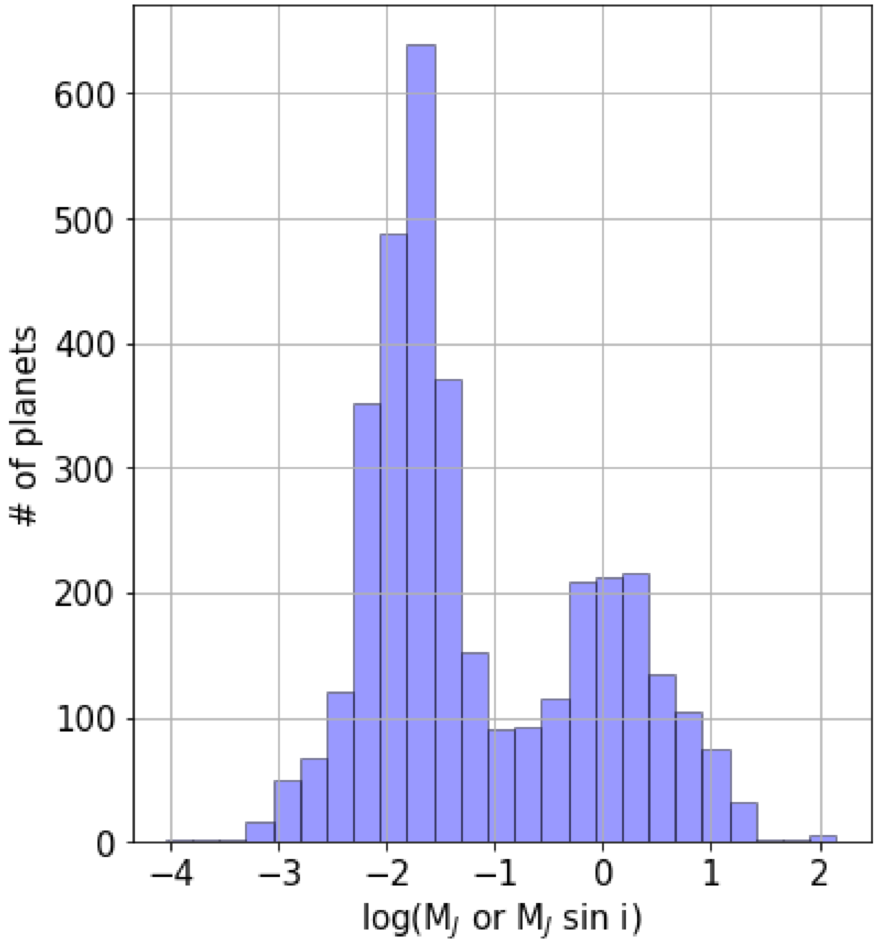

FIGURE 4.2: Planet Mass Distribution for the Sample with Host Stars Listed in GAIA Archive.

et al. 2022).

Significant research effort is also devoted to exploring star-planet connections, showing how the fundamental properties of stars determine the orbital and physical characteristics of the planetary systems. For example, spectroscopic studies have shown that the metallicity distribution for stars with small (M_P <$0.3M_J$) and giant planets ($0.3M_J \leq M_P \leq 13M_J$) is different, indicating that they likely belong to different populations and also metallicity plays a key role in giant planet formation (Gonzalez 1997; Santos et al. 2001; Fischer & Valenti 2005; Udry & Santos 2007; Buchhave et al. 2012, 2014; Dong et al. 2014; Fleming et al. 2015; Johnson et al. 2017; Petigura et al. 2018; Mulders 2018; Narang et al. 2018; Swastik et al. 2019, 2021). Further, a detailed abundance analysis shows that the chemical composition of stars hosting small and giant planets is different, with the latter being α-poor (Swastik et al. 2022; Unni et al. 2022). Using [α/Fe] ratio as a proxy for the age, these studies suggest that the small planetary systems may have started forming early in the Milky Way history compared to the late formation onset of the giant planets (Delgado Mena et al. 2019). Estimating the ages from isochrone fittings for a sub-sample of exoplanet hosting stars have also arrived at similar conclusions (Bonfanti et al. 2015; Swastik et al. 2022). Such age differences are also reported based on the position and kinematics studies of the confirmed population of planet-hosting stars.

Important as they are, the majority of these studies used mixed samples of stars originally observed in different planet search and follow-up surveys (Santos et al. 2011; Brewer et al. 2016; Brewer & Fischer 2018). In most cases, the stellar properties themselves are determined using different observing strategies, instrument settings, and analysis methods. This results in various systemic and offsets, making the interpretation and comparison more difficult across different studies. Ideally, to make the findings more robust and universal, a sufficiently large sample of stars should be observed with the same equipment under similar conditions, and a uniform methodology must be applied to determine the parameters of interest. With the latest release of the GAIA DR3 data, it is possible to study a much larger and uniform sample of planet-hosting stars whose properties have been determined homogeneously.

The General Stellar Parametriser (GSP) module uses spectra from a medium resolution (R $\sim$ 11,500) radial velocity spectrograph (Recio-Blanco et al. 2022). The GSP-Spec module computes the stellar atmospheric parameters (T_{eff}, logg, metallicity ([M/H])) and abundances ([X/Fe]) for thirteen different species for each star, including three Fe-peak elements, Cr, Ni and Fe. Additionally, it provides the mean abundances of eight α-elements (O, Ne, Mg, Si, S, Ar, Ca, and Ti) in the

TABLE 4.1: Key parameters of exoplanet hosting stars used or estimated in this study.

TIC ID	hostname	Method	Planet	Pl- Mass(M_J)	RA
TIC 328465904	CD Cet	Radial Velocity	CD Cet b	0.01243	48.3530155
TIC 380966347	HD 14787	Radial Velocity	HD 14787 b	1.121	35.8085099
TIC 435339847	K2-77	Transit	K2-77 b	1.9	55.228521
TIC 435339558	K2-79	Transit	K2-79 b	0.0415	55.2559307
TIC 242961495	K2-80	Transit	K2-80 b	0.0148	59.037486
TIC 242961495	K2-80	Transit	K2-80 c	0.00869	59.037486
...					

Note – The entire table is available in machine-readable format. For simplicity, only the first 6 rows and 6 columns are shown here.

catalog. Other than spectroscopic parameters, GAIA also provides homogeneous and accurate astrometric and photometric parameters for nearly two billion stars, the largest to date.

In this chapter, we investigate a sample of 2611 planet-hosting stars whose parameters have been determined homogeneously. We used the Gaia DR3 data and analyzed the spectroscopic and kinematic parameters of stars hosting small and giant planets. The outline of this chapter is as follows: We describe our sample in Section 4.2. We report the results of the spectroscopic, kinematic, and isochrone age analyses in Section 4.3. In Section 4.4, we briefly discuss our results in the context of planet formation theories and also elude to possible biases and systematic effects of our findings. Finally, in Section 4.5, we conclude and summarise the results.

4.2 The Sample

4.2.1 Sample selection

For this study, we used the confirmed list of exoplanetary systems from NASA exoplanet archive (Akeson et al. 2013; NASA Exoplanet Science Institute 2024) and cross-matched it with the latest Gaia data release DR3 to obtain the stellar data for the planet-hosting stars. We first employed the Astronomical Data Query Language (ADQL) to identify the GAIA DR3 source IDs associated with our exoplanet-hosting stars. Subsequently, we utilized ADQL to extract the corresponding data from the Astrophysical parameters table. In cases where multiple matches were found, we manually verified the G-Band magnitude quoted in the NASA exoplanet archive and selected the closest match to the search result in the GAIA DR3 dataset. Additionally, for the purpose of validation, we used TOPCAT to perform Ra-Dec cross-matching with a search radius[†] of $3''$ and obtained identical results to those extracted using ADQL.

In the case of GAIA, the spectroscopic data is obtained from the Radial Velocity Spectrometer(RVS) instrument on board GAIA, which is a medium-resolution spectrograph. The data products from the RVS spectra are listed in the *Astrophysical parameters* table. Further, each parameter is associated with a *quality flag*[‡] indicating quality of the data. For the analysis presented in this chapter, most of our samples are associated with the best-quality flag (0 in this case) and we excluded the stars with low-quality data flags (9 in this case). Our primary sample, therefore, consists of 2611 planet-hosting stars (accounting for 3553 planetary companions) for which the radial velocity data was available from the GAIA

[†] Initially, we used a larger search radius and found that most of the planet-hosting stars can be extracted with a search radius of $3''$. For cases where we were not able to obtain the matches, we increased the search radius up to $15''$ and also checked for the G-band magnitude to confirm if the target is indeed a planet-hosting star.

[‡] For more details on *quality flag*, see Table 2 of Recio-Blanco et al. (2022)

archive. The sample extracted from GAIA as well as the important parameters derived in this chapter are listed in Table 4.1. Figure 4.1 shows the distribution of these stars in Mollweide projection, while Figure 4.2 shows the distribution of planet mass whose sources are listed in the GAIA archive.

Since the original sample contained many evolved stars, notably giants and subgiants, we restricted our analysis to the main sequence stars. The reason is that it is difficult to account for the Non-Local Thermodynamic Equilibrium (NLTE) and other evolutionary effects that can alter the surface abundances of the evolved stars (Swastik et al. 2022). We followed the procedure of Brewer & Fischer (2018) to exclude the evolved stars using T_{eff} and $\log g$ cutoff. Further, we included only those host stars where the companion mass $< 13M_J$ and also to avoid biases from possible mixing, we also excluded stars with multi-planetary systems containing a combination of small and giant planets. After applying these filters, our final sample was trimmed to 971 stars with 1309 planets for which the spectroscopy data is available and 2130 stars with 2861 planets for which astrometric data is available. Also, we excluded the lower main-sequence stars from our age sample (T_{eff} <4400K), as the isochrone ages for the lower main-sequence stars are not very accurate given the large uncertainties. Thus after curation, we analysed the ages of 806 stars hosting 1071 planets. In the sample described above, about $\sim$ 83% of stars in the astrometrically curated sample belong to transit surveys (mostly Kepler) and $\sim$ 17% belong to different RV surveys. In the spectroscopic sample, $\sim$ 64% stars are from transit discoveries while the remaining come from the RV detections. Additionally, the spectroscopic sample is a subset of the astrometric sample, meaning the astrometric data is available for all stars belonging to the spectroscopic sample.

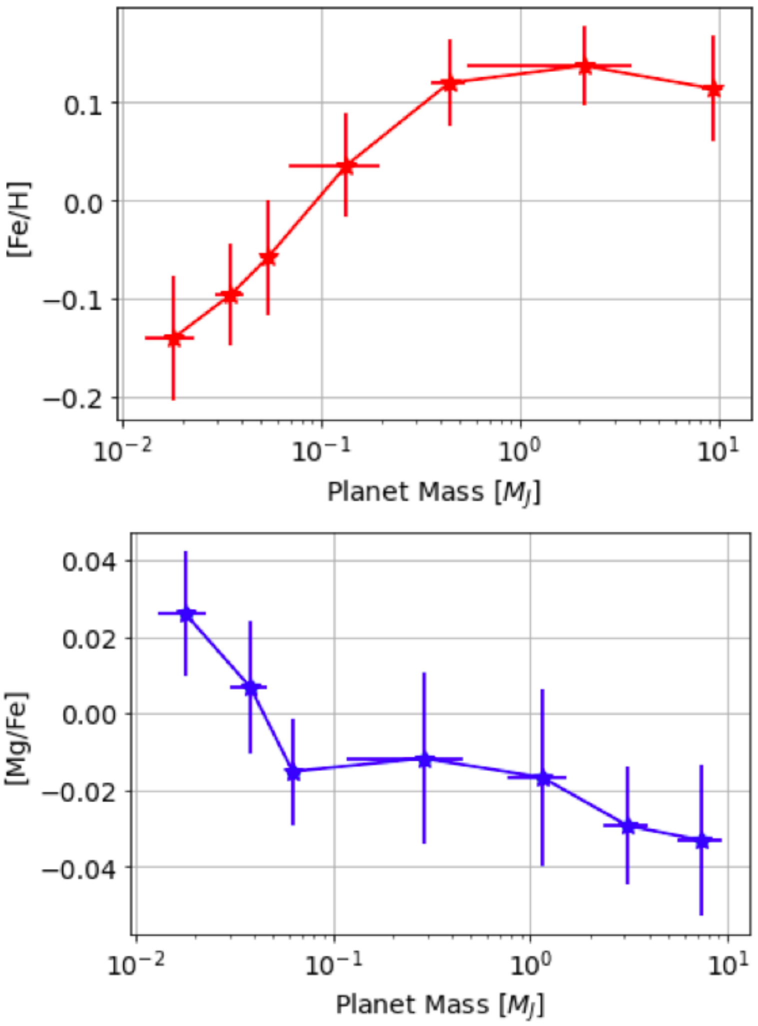

FIGURE 4.3: **Top :** Host star metallicity as a function of planet mass. **Bottom :** [Mg/Fe] of planet-hosting stars as a function of planet mass. The errors in metallicity and Mg abundances are represented by the standard error of the mean, whereas the errors in planet mass are represented by the standard deviation in each bin.

4.2.2 Calibration

4.2.2.1 Calibration of Metallicities and abundances

Although GAIA-DR3 provides the homogeneous estimation of stellar parameters for the largest number of stars to date, it requires several calibrations and filtering for any rigorous scientific study. For instance, the data from the GAIA-GSP spec module suffers from systematic errors(Recio-Blanco et al. 2022) and hence one needs to account for such biases to perform any meaningful analysis on the data. Although some calibrations have been already been proposed for GAIA data using three major ground-based surveys: APOGEE-DR17 (Abdurro'uf et al. 2022), RAVE-DR6 (Steinmetz et al. 2020), and GALAH-DR3 (Buder et al. 2021), we still find a significant offset and scatter in the calibrated data as shown in Table 4.2 (last two rows) when compared to high-resolution and high SNR spectroscopic data from the HARPS-GTO sample (Mayor et al. 2003; Lo Curto et al. 2010; Santos et al. 2011). Also, the calibration polynomials are established for stars with a wide range of atmospheric parameters in $\log g$, and T_{eff}, and thus, we decided to use our own tailored calibration for our sample of planet-hosting stars. Therefore, we use the HARPS-GTO sample (Mayor et al. 2003; Lo Curto et al. 2010; Santos et al. 2011), which is a survey of 1111 stars that were chosen to detect planets by radial velocity and also have a similar range of atmospheric parameters as that of the planet-hosting stars used in this chapter. Although the wavelength coverage of HARPS (378-691 nm) and GAIA (846-870 nm) is different, it will not affect

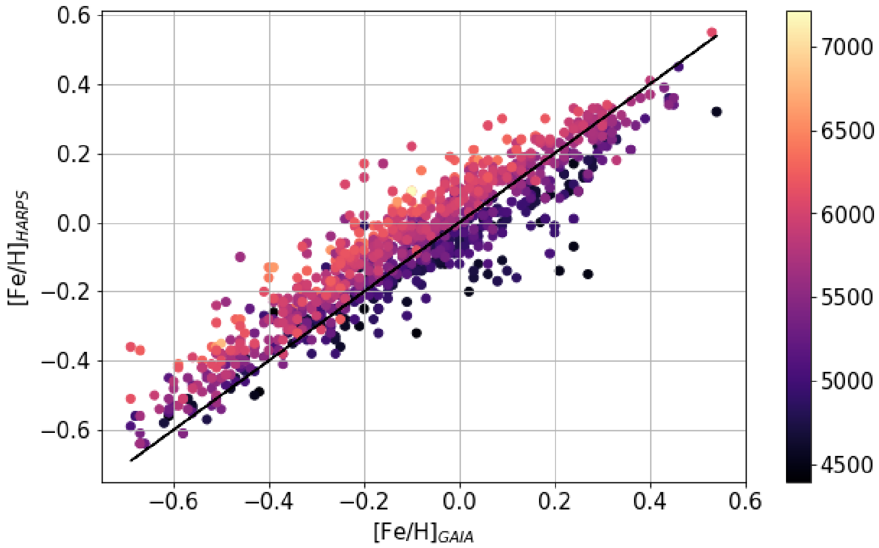

Figure 4.4: Comparison of the [Fe/H] values from GAIA GSP-Spec module and the HARPS sample. The black line is the x=y line and the color bar on the right represents the effective temperature of the star.

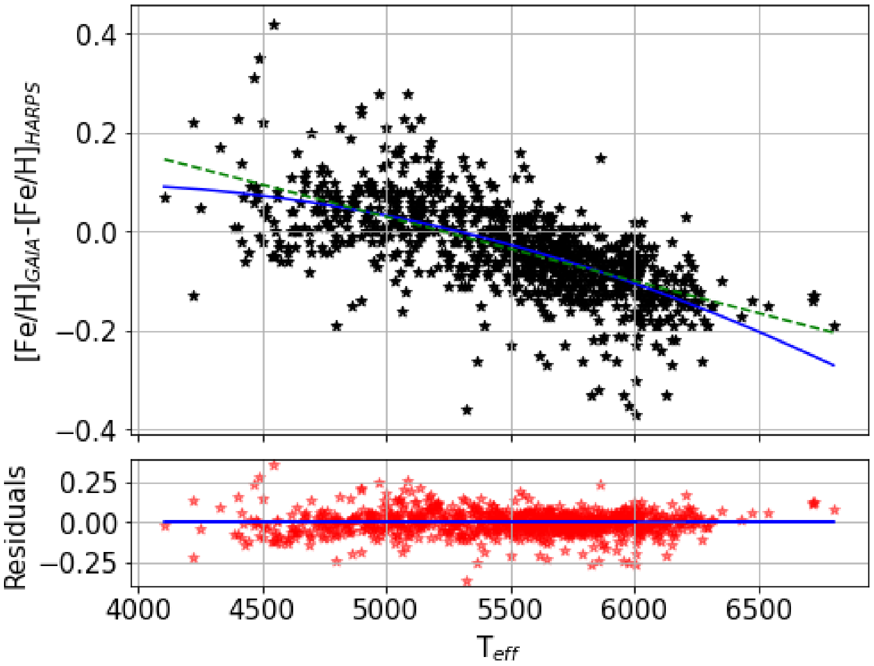

FIGURE 4.5: Comparison of δ[Fe/H] = [Fe/H]$_{GAIA}$-[Fe/H]$_{HARPS}$ as a function of T$_{eff}$. A quadratic polynomial best describes the trends of δ[Fe/H] with T$_{eff}$. The blue is the best-fit polynomial with the coefficients (p0, p1, p2) = (-3.96e-08, 2.97e-04, -4.57e-01) for the top figure, while the bottom figure shows the residuals in the approximation of the trend by the above polynomial. The green dashed line shows the linear fit for the data.

the estimate of stellar atmospheric parameters as there are sufficient Fe-lines to estimate the metallicities. We cross-matched our sample and found 932 common stars between the HARPS and the GAIA samples. Upon comparing the metallicities of the stars from GAIA and HARPS, as shown in Figure 4.4, we find that the distribution about the $x = y$ line is not symmetric. In addition, we also find a temperature gradient with [Fe/H], where the [Fe/H] is underestimated for hotter stars ($\geq$ 5500K) and overestimated for cooler stars ($\leq$ 5500K). Therefore, to account for the temperature dependence, we analyzed the δ[Fe/H] = [Fe/H]$_{GAIA}$-[Fe/H]$_{HARPS}$ as a function of T$_{eff}$. The relationship between the δ[Fe/H] and T_{eff} can be best described by a quadratic polynomial (Figure 4.5) given below:

$$\delta[\mathrm{Fe/H}] = [\mathrm{Fe/H}]_{GAIA} - [\mathrm{Fe/H}]_{HARPS} = \sum_{i=0}^{2} p_i.T_{eff}^{i} \tag{4.1}$$

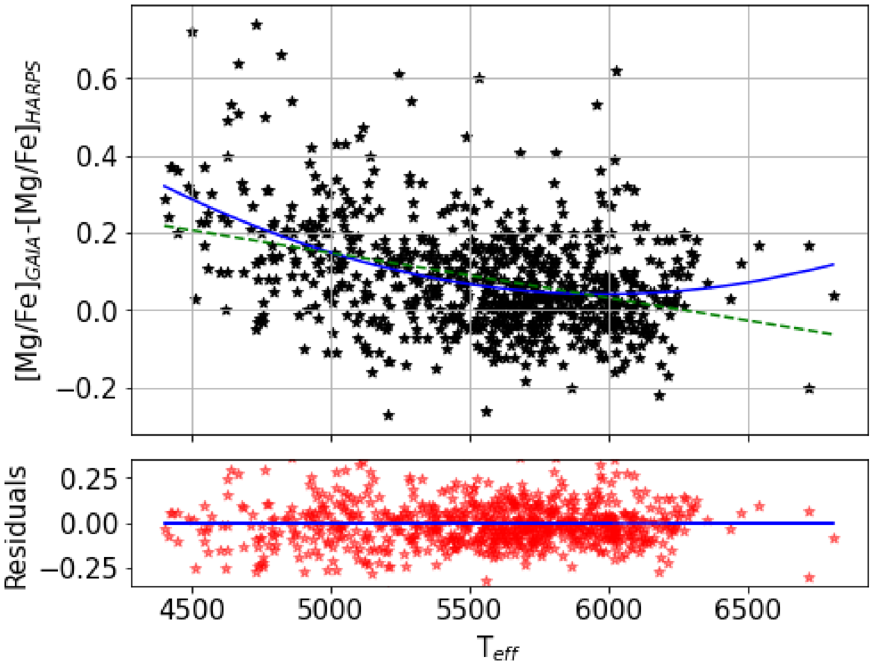

FIGURE 4.6: Variation of δ[Mg/Fe] = [Mg/Fe]$_{GAIA}$-[Mg/Fe]$_{HARPS}$ as a function of effective temperature. A quadratic polynomial best describes the trends of δ[Mg/Fe] with T$_{eff}$. The best-fit polynomial is represented by the blue line in the top figure, by the coefficients (p0, p1, p2) = (1.12e-07, -1.34e-03, 4.05), while the figure at the bottom shows the residuals in the approximation of the trend by the above polynomial. The green dashed line shows the linear fit for the data.

Thus, for a given T_{eff} we compute the δ[Fe/H] using Eq. 4.1 to estimate the offset in [Fe/H]. We then calibrated our data using Eq. 4.1 and then checked for any remaining offset in the HARPS-GTO and GAIA calibrated data using our calibrations. We find no significant offset between GAIA calibrated and HARPS-GTO data as listed in Table 4.2. We then applied the same correction to the sample of planet-hosting stars to correct the estimation bias and then used those calibration values to study the correlation trends.

We performed a similar calibration for alpha-elements and found a temperature gradient with a difference of α- abundances. Since Mg is the strongest tracer for α abundances (Kobayashi et al. 2020; Swastik et al. 2022), we analyse the [Mg/Fe] from the HARPS and the GAIA sample. The Figure 4.6 shows the δ[Mg/Fe] as a function of T_{eff}. We used the calibration procedure, similar to [Fe/H], and then applied the suitable corrections for the planet-hosting stars.

4.3 Results

We used different proxies of stellar ages from spectroscopic, photometric and astrometric data from the GAIA DR3 to analyze the confirmed exoplanet population. Below, we present our results obtained from the GAIA DR3 data in the context of planet formation.

4.3.1 Spectroscopic analysis of the planet hosts stars

Although we have already analyzed the chemical composition of the exoplanet-hosting stars in chapter 3, the analysis was done for a small sample of planet-hosting stars. The Gaia DR3 provides a significantly large sample of stars whose spectroscopic parameters are determined homogeneously. The GSP-Spec module (Recio-Blanco et al. 2022) does the spectroscopic processing using the combined Radial Velocity Spectrometer (RVS) spectra of single stars to calculate stellar chemo-physical characteristics. The RVS covers a spectral range of 846-870 nm and has a resolution of R $\sim$ 11500 (Cropper et al. 2018). The GSP-Spec module estimates the stellar atmospheric parameters (T_{eff}, $\log g$, [M/H][§]) and the abundances of 13 chemical species (N, Mg, Si, S, Ca, Ti, Cr, Fe I, Fe II, Ni, Zr, Ce and Nd). The stellar atmospheric parameters are estimated using the Matisse GAUGUIN algorithm and artificial neural network (ANN) (Recio-Blanco et al. 2016, 2022). However, the abundances are obtained solely from the Matisse GAUGUIN algorithm using Gaussian fitting methods (Zhao et al. 2021; Recio-Blanco et al.

[§] Here [M/H] is defined as the total metal content of the star.

2022). For the analysis presented in this chapter, we used the stellar parameters and abundances from the Matisse GAUGUIN algorithm.

Since GAIA spectroscopic data from the GSP-Spec module suffers from estimation biases (Recio-Blanco et al. 2022), we used the HARPS-GTO sample (a high-resolution sample of 1111 stars targeted mainly with the goal of detecting planets by radial velocity) for calibration (Mayor et al. 2003; Lo Curto et al. 2010; Santos et al. 2011). After taking care of the calibration and possible estimation biases, as discussed in section 4.2.2, we investigated the host star metallicities and [Mg/Fe] (a proxy for overall α abundances) in the GAIA archive as a function of planet mass. We chose [Mg/Fe], since we wanted to investigate the ratio of the abundances of elements produced from Type II supernovae (Mg) to Type I supernovae (Fe) and since the major production site for Mg is Type II supernovae, it is the strongest tracer for the overall α abundance in a star (Kobayashi et al. 2020). We used the planet mass from the NASA exoplanet archive (Akeson et al. 2013; NASA Exoplanet Science Institute 2024)¶ and binned the data appropriately in terms of planet mass depending on the number of stars in each bin, with four bins for small planet-hosting stars (M_P <$0.3M_J$), two for giants ($0.3M_J \leq M_P \leq 4M_J$), and one for super-Jupiters ($M_P > 4\ M_J$). We found that the host star metallicity increases as a function of planet mass with a turn-around after $\sim 4\ M_J$ as seen in Figure 4.3. Although several studies have shown similar results (Fischer & Valenti 2005; Valenti & Fischer 2008; Narang et al. 2018; Swastik et al. 2021), they were mostly limited to either small samples or inhomogeneous measurements of metallicities. Here, in this chapter, we could reproduce these results for a large number of exoplanet-hosting stars using the data from the RVS spectra from the GAIA DR3.

We also find that, for the α-element abundances ([Mg/Fe]), there is a decreasing

---

[¶] For the planets detected by transits, we used the planet mass-radius relationship from (Chen & Kipping 2017). For the planets detected by RV, we used the minimum mass (M.sini) as listed in the NASA exoplanet archive.

trend with planet mass, as seen in Figure 4.3. For comparison with α element, we used only Fe abundances, as abundances of only two other Fe-peak elements (Ni and Cr) were available and Fe is estimated with much better precision compared to Ni and Cr in the GAIA GSP-Spec module. Since [Fe/H] and α-enhancement are proxies for ages for a population of stars (Swastik et al. 2022; Delgado Mena et al. 2019), the decline in α-abundances, together with enhancement of [Fe/H] indicate that giant planets are preferentially hosted by younger stars while the stars having small planetary companions have a wider spread in the age.

4.3.2 Kinematic analysis of exoplanet hosting stars

The kinematic analysis of stars entails tracking the past motions of a group of stars to determine when they were physically closest, which is thought to be the period of their formation. In this case, stellar parameter estimation such as the galactic space velocities (U, V, W) and orbital parameters (eccentricity and Z_{max}[‖]) is based on minimal assumptions and does not need stellar modelling but high-quality astrometry and radial velocities measurements. In our case, we used the radial velocity and proper motion data from the GAIA DR3 data to compute the galactic space velocities (Johnson & Soderblom 1987; Ujjwal et al. 2020). Further, we used galpy (Bovy 2015) to compute the stellar orbital parameters (eccentricity and Z_{max}) and used the solar motion $(U_{\odot}, V_{\odot}, W_{\odot}) = (11.1, 12.24, 7.25)$ kms^{-1}from Schönrich et al. (2010) as a reference. We analyzed a sample of 2130 stars and found that the stars hosting small planets have higher median eccentricity and Z_{max} compared to giant planet-hosting stars, as seen clearly in Figure 4.7.

Further, peculiar velocity (ν_{pec})[**] and total velocity dispersion (σ_{tot})[††] distribution

---

[‖] Z_{max} is integral of motion that tells us the maximum height above or below the galactic plane on the disk that a star travels.

[**] $\nu_{pec}^2 = U_{LSR}^2 + V_{LSR}^2 + W_{LSR}^2$; It is represented by the radius drawn from the origin in the Toomre diagram

[††] $\sigma_{tot}^2 = \sigma_U^2 + \sigma_V^2 + \sigma_W^2$

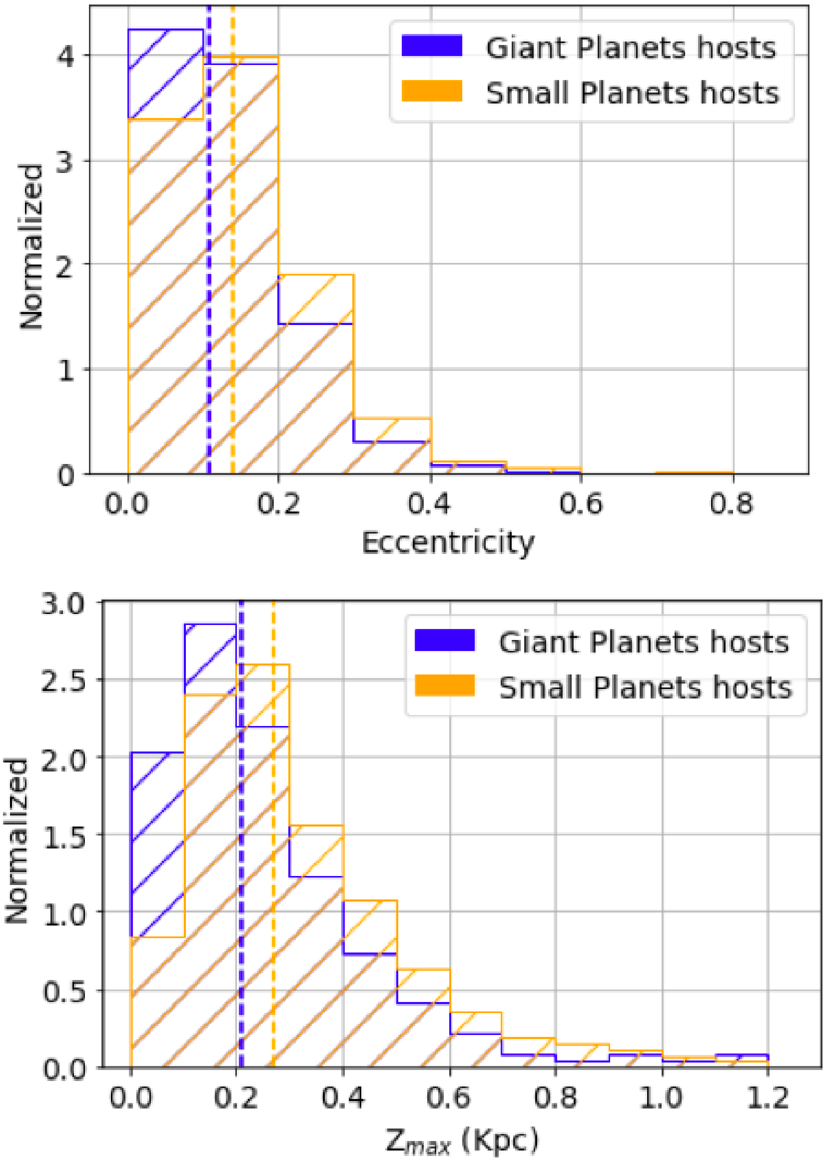

FIGURE 4.7: Galactic orbital parameters for the small and giant planet-hosting stars. **Top:** Eccentricity distribution for the planet-hosting stars (binned at 0.1 dex). **Bottom:** Z_{max} distribution for the different population of exoplanet hosting stars (**binned at 0.1 Kpc**). The vertical lines represent the median of the distribution for the small and giant planet hosts.

have notable difference for small and giant planet-hosting stars as shown by the red and blue circles in Figure 4.8. We find that the scatter in the ν_{pec} is much more significant for small planet hosts than for giant planet-hosting stars. In the case of small planet hosts, e.g., 50 and 80 percent of the population lies at the velocity

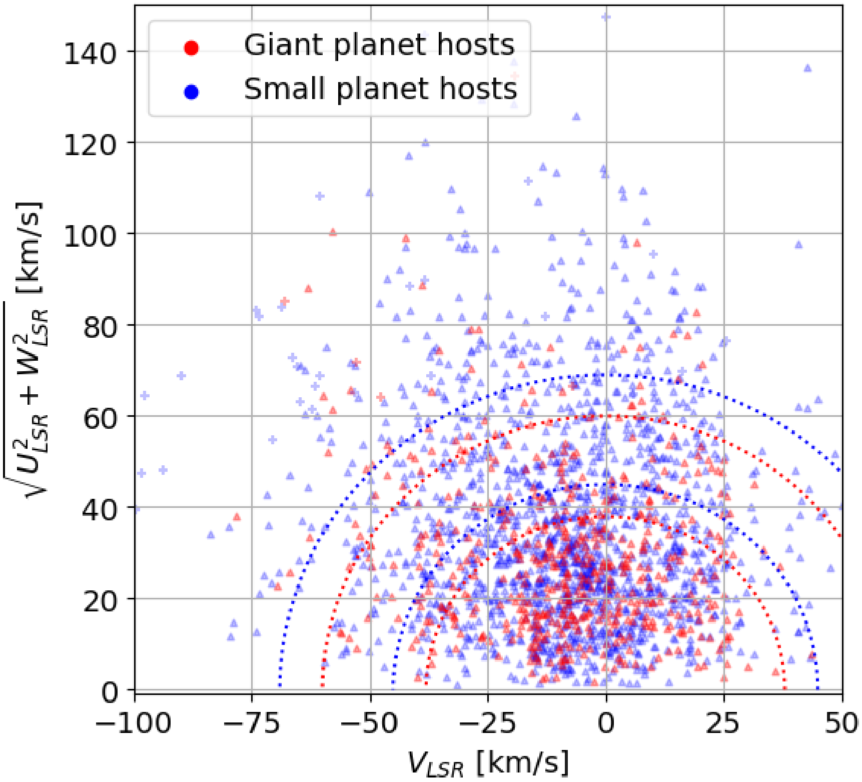

FIGURE 4.8: Toomre diagram for the current sample of planet-hosting stars. The blue and red circles represent the locus of ν_{pec} for the small and giant planet hosts. The area enclosed by inner circles has ∼ 50% of stars population while the outer circles capture ∼ 80% of the population in each category.

radius of 46 km/s and 69 km/s, compared to 38 km/s and 60 km/s for giant planet hosts. Since the age for an ensemble of stars increases radially from the origin, with the thin disk (younger population) stars having low ν_{pec} and extending to thick disk and halo stars (older population) having higher ν_{pec} (Reddy et al. 2006; Casagrande et al. 2011). The clustering of the giant planet hosts around the origin of the Toomre diagram (Figure 4.8) indicates that they belong to a statistically younger population of stars compared to stars hosting small planets, which show a larger spread in ν_{pec} (and σ_{tot}). Considering the uncertainties associated with Gaia proper motion, RV (radial velocity), and parallaxes, we conducted an additional assessment to investigate the impact of these uncertainties on the estimation of ν_{pec} and σ_{tot}. To account for uncertainties in the space motion of stars, we calculated the error in U, V, and W using the relationships described in equation 2 of Johnson

& Soderblom (1987). The median uncertainties in U, V, and W were found to be 0.16, 0.49, and 0.17 km/s, respectively. To determine if these uncertainties affect the analysis presented in this chapter, we performed a Monte Carlo simulation where each space velocity component U, V, and W of a star is randomly generated from a Gaussian distribution with the mean and standard deviation obtained as described above. We then calculated ν_{pec} using these random realizations of U, V, and W for both small and giant planet-hosting stars. This process was repeated 100,000 times and we find that the 1σ spread in ν_{pec} for small and giant planet hosts is 0.35 and 0.18 km/s, which is relatively small (Figure 4.9, top row) compared to the absolute difference in the ν_{pec} between small and giant planets ($\sim$ 10 km/s), suggesting that the uncertainties in the Gaia astrometric parameters do not significantly affect the analysis presented in this chapter. We also conducted a similar analysis for σ_{tot} as shown in the bottom row of Figure 4.9. We have also noted the median and spread obtained from the Monte Carlo analysis for ν_{pec} and σ_{tot} in Table 4.2.

Further, we classified the likelihood of each star belonging to the thin disk, thick disk, or halo using the approach adopted by Reddy et al. (2006). Therein, the parent sample is considered to be a mixture of the three populations, and it is assumed that every population has a Gaussian random distribution of velocities for each component (Reddy et al. 2006; Adibekyan et al. 2011). By assigning a probability threshold of 70% for a star to belong to a particular population, we find $\sim$ 98% of the planet-hosting stars belong to a thin disk population (Table 4.3). We also find that the sample of stars hosting small and giant planets cannot be manifested in terms of thin vs thick disk population. In terms of galactic orbital parameters, we find that on average, stars hosting small planets have higher median eccentricity and Z_{max} compared to giant planet-hosting stars. We also performed an Anderson-Darling test (AD) and found that the difference is significant for both galactic space velocities and orbital parameters (Table 4.3), suggesting that small and giant planet-hosting stars likely belong to different populations.

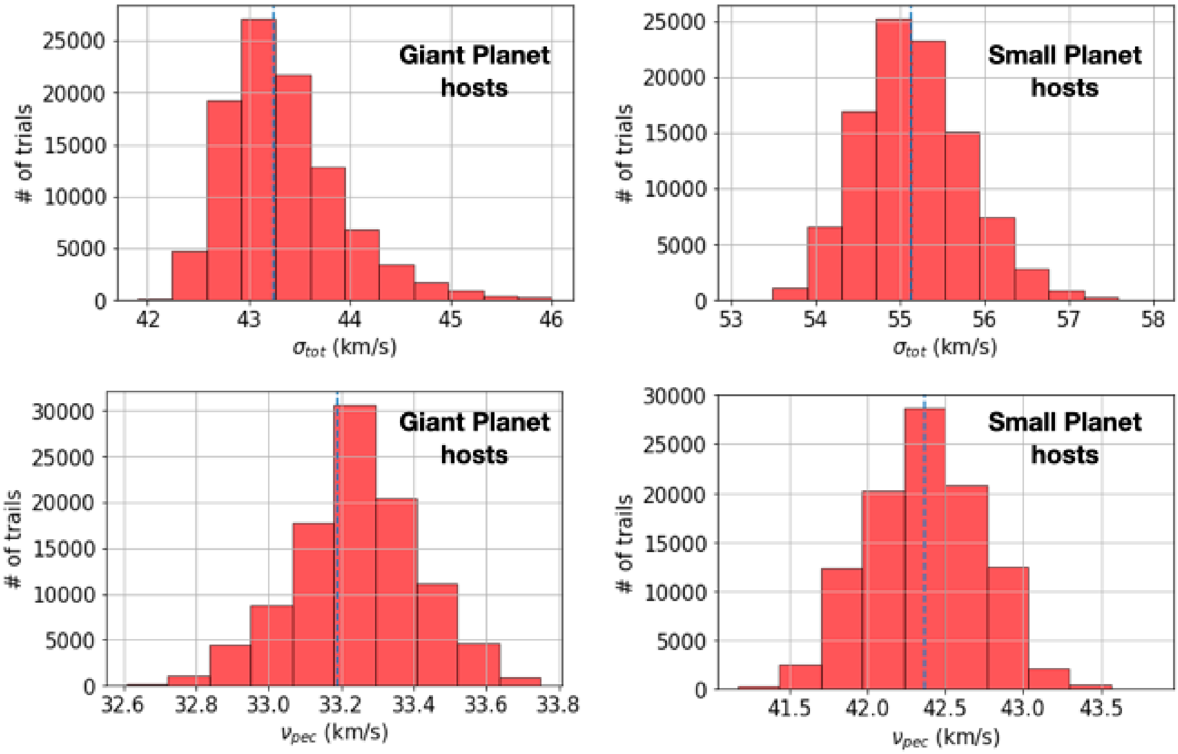

FIGURE 4.9: Distribution of ν_{pec} and σ_{tot} for the planet-hosting stars obtained from Monte Carlo simulation. The vertical dashed lines represent the median of the distribution.

Several studies (e.g. Chen 2003; Casagrande et al. 2011; Wojno et al. 2018; Ness et al. 2019; Bashi & Zucker 2022) have indicated that the higher values of Z_{max}, eccentricity and σ_{tot} are a proxy for older stars. For instance, Wojno et al. (2018) found that eccentricity differ by ~ 0.05 and z_{max} by ~ 0.04 for the young (≤ 3Gyr) and the old (≥ 8 Gyr) stars. For exoplanet hosting stars, using a limited sample (135 stars) of Neptune, super-earth and Jupiter hosts, Adibekyan et al. (2012a) have also shown that Jupiter hosting stars have lower median eccentricities and Z_{max} compared to stars hosting Neptunes (see table 3 of Adibekyan et al. (2012a)). In our study, this is validated for a larger sample of exoplanet-hosting stars using the astrometric and radial velocity data from GAIA. We note that the distribution of Z_{max}, eccentricity, ν_{pec} and σ_{tot} are statistically different for stars hosting small and giant planets. For comparison, these parameters along with the p-value are listed in Table 4.3.

4.4 Discussions

Several galactic orbital (σ_{tot}, eccentricity and Z_{max}) and spectroscopic ([Fe/H] and [α/Fe]) parameters are proxy to stellar ages. To study different exoplanet populations and their formation timeline, we investigated the ages of their host stars. Our analysis shows that small planet-hosting stars have higher σ_{tot}, eccentricity, Z_{max} and [α/Fe] and lower [Fe/H] compared to stars hosting giant planets. Since higher σ_{tot}, eccentricity, Z_{max} and [α/Fe] are indicators of older population (Chen 2003; Casagrande et al. 2011; Wojno et al. 2018; Ness et al. 2019; Bashi & Zucker 2022), we find that the small planet-hosting stars are statistically older compared to their giant planet hosts. While the majority of our planet-hosting stars primarily belong to the thin disk population and exhibit a predominance of higher metallicity (refer to Figure A1 of Swastik et al. (2022)), we conducted additional investigations to determine what extent the stars hosting small and giant planets are younger. This analysis involved controlling for the correlation between planet mass and stellar metallicity, considering that stellar ages are directly influenced by various stellar properties, including mass and radius. For instance, for a controlled stellar sample with the criteria of -0.2<[Fe/H]<0.4 and $0.7\mathrm{R}_{sun} < \mathrm{R}_{star} < 1.3\mathrm{R}_{sun}$, we examined the extent to which the histogram offsets persisted. Notably, although the offsets were still observable, they exhibited a decrease and the histogram peaks shifted towards younger ages. This is expected since we selectively removed stars from specific age groups (older in this case) within the sample. We also repeated this analysis for other combinations as well and found similar trends. The fact that young, metal-rich stars have a preference for hosting giant planets aligns with the natural progression of the chemical evolution of the galaxy and it is more challenging for giant planets to form around older, metal-poor stars.

Radial velocity (RV) and transit detection are two of the most popular techniques used to detect exoplanets. However, these techniques have inherent biases that can impact our understanding of exoplanet populations (Swastik et al. 2022). The radial velocity technique, e.g., can detect massive planets that are close to their host star and have intermediate orbital periods (up to $\sim$ 10 AU). However stellar activity and line-broadening mechanisms reduce RV precision, and therefore very active and fast-rotating stars are usually excluded from the RV surveys. The transit method on the other hand is more sensitive to short orbital period planets (mostly below $\sim$ 1 AU) whose orbits are favourably aligned along the observer's line of sight. Both of these methods have their own detection biases and therefore lead to a non-representative sample of the true exoplanet population in the galaxy. For instance, younger stars have large variability, therefore, finding smaller planets around stars is more challenging (Vanderburg et al. 2016).

It is possible that some small planets might have missed detection around young stars due to sensitivity limitations. However, different age proxies used in this work indicate that older stars have fewer giant planets compared to younger stars. The fact that giant planets are easier to detect irrespective of detection technique or the age of the star indicates that the overall occurrence rate of giant planets is much lesser around old stars and suggests that giant planets may have started forming late in the galaxy.

While the GAIA DR3 dataset provides highly accurate data on stellar parameters and motions, it is important to consider potential biases and uncertainties that could affect the accuracy of age estimates and kinematic analyses. One significant source of systematic errors is the reliance on stellar models for age determination, which can be influenced by factors such as metallicity and interstellar extinction. Additionally, despite the high precision of the kinematic data, it can still be affected by biases resulting from uneven sky coverage and minor inaccuracies in proper motion measurements. Future GAIA DR4 data will be able to provide more accurate data on astrometry given the longer observation time scale compared to GAIA DR3.

Stars and planets both originate from the same molecular cloud within the interstellar medium (ISM), and the metal content in the ISM is a crucial factor in the formation of planets. Our study reveals a significant finding that stars hosting giant planets are statistically associated with a younger population. For the formation of a giant planet, a core of $\sim$10 $M_\oplus$ must be formed within a relatively short timeframe of around 10 million years (Pollack et al. 1996) before the dissipation of gas in the protoplanetary disk. This core primarily consists of refractory elements, including both α-elements (such as Mg, Si, Ca, etc.) and Fe-peak elements (such as Fe, Ni, etc.). During the demise of the first stars as core-collapse supernovae (SNe II), the interstellar medium (ISM) became enriched with α-elements. However, during the early stages of the Milky Way's existence, the ISM lacked sufficient enrichment in heavy elements, particularly Fe-peak elements. This limitation hindered the core-accretion process necessary for the formation of giant planets (Rice & Armitage 2003; Matsuo et al. 2007; Drazkowska et al. 2022). With the gradual enrichment of the ISM through Type Ia supernovae (SNe Ia), the availability of more Fe-peak elements, such as Fe, Ni, Cr, Mn, etc., facilitated the onset of giant planet formation (Matteucci & Francois 1989; Alibés et al. 2001; Matteucci et al. 2009; Kobayashi et al. 2020; Swastik et al. 2022). Therefore, the scarcity of giant planets around older stars and the widely observed planet-mass and stellar-metallicity correlation can be understood as a natural outcome of the galactic chemical evolution of the Milky Way. Seen that way, the temporal offset between the formation of small and giant planets will also be consistent with chemo-kinematic trends of planet-hosting stars and the mass-metallicity relationship.

4.5 Conclusions

The properties of exoplanets are closely related to the traits of their stellar hosts. In this work, we studied planet-hosting stars' chemical abundances and kinematics. We used the GAIA DR3 data, for which the stellar parameters are available for the large number of exoplanet-hosting stars whose parameters have been estimated uniformly. We analyzed the astrometric, photometric, and spectroscopic data from the GAIA DR3. Here, we present a brief summary of our analysis :

- Using the GAIA spectroscopic metallicities and abundances from the RVS spectra, we find that the host stars of giant planets are metal-rich and α-poor compared to small planet-hosting stars. This finding indicates that host stars of giant planets belong to a younger population of stars which started forming in the later stages of the galaxy after the enrichment of ISM with Fe-peak elements.
- We find that most of our planet-hosting stars belong to the thin disk population, indicating that the overall sample of exoplanets-hosting stars belongs to the younger generations. For the galactic space velocities and orbital parameters, we find that host stars of small and Jupiter-like planets belong to a separate population. We also find that small planet-hosting stars have higher Z_{max} and eccentricities (which is a signature for older stars) compared to giant planet-hosting stars.

The present observations using the latest GAIA DR3 data suggest that the giant planets started forming at the later stages of the GCE evolution when the ISM was sufficiently enriched with Fe-peak elements by Type Ia supernovae, which happened around $\lesssim 6$ Gyr. The enrichment of ISM is necessary to form the core of the giant planets faster before the dissipation timescale of the gas in the protoplanetary disk. Our results are also consistent with the core-accretion theory of planet formation (Pollack et al. 1996; Matsuo et al. 2007; Birnstiel et al. 2016; Owen & Murray-Clay 2018; Drazkowska et al. 2022). Future missions consisting of astrometry, photometry and spectroscopic investigations should focus on a larger sample of exoplanet-hosting stars, measuring their chemical abundances and astrometric parameters uniformly and more precisely to support these findings.

Table 4.2: Differences in median offset and robust sigma between GAIA GSP-Spec and individual surveys.

	T_{eff}	log(g)	[M/H]	$\log(g)_{calibration}$	$[M/H]_{calibration}$
RAVE-DR6	(-12; 93)	(-0.28; 0.19)	(-0.05; 0.11)	(-0.003; 0.18)	(-0.05; 0.09)
APOGEE-DR17	(-32; 86)	(-0.32; 0.17)	(0.04; 0.12)	(-0.005; 0.15)	(0.06; 0.12)
GALAH-DR3	(20; 87)	(-0.26; 0.21)	(0.01; 0.10)	(0.003; 0.18)	(-0.001; 0.10)
HARPS-GTO (current work using equation 4.1))	(-12, 97)	(-0.24, 0.30)	(-0.04, 0.08)	(-0.05, 0.25)	(0.001, 0.07)
HARPS-GTO (with GAIA proposed polynomial)				(-0.18, 0.24)	(-0.07, 0.09)

Note – The first three rows are taken from Table D1 of Recio-Blanco et al. (2022). The values in the parenthesis are median offset, followed by robust sigma (standard deviation obtained by removing outliers) computed from the residuals. The last two rows are for HARPS-GTO data with the calibration results from equation 4.1, and GAIA proposed polynomials.

TABLE 4.3: Comparison of small and giant planet-hosting stars in terms of their galactic parameters.

	Small-planet	Giant-planet	p-Value
Thin disk	1464	579	>0.05
Thick disk	29	7	>0.05
Z_{max} (kpc)	0.27±0.12	0.21±0.09	10^{-4}
Eccentricity	0.14±0.07	0.11±0.06	10^{-5}
ν_{pec} (km/s)	42.79± 0.35	33.19±0.18	10^{-6}
σ_{tot} (km/s)	53.70±0.41	42.89±0.41	–

Note – Errors represent the 1σ spread in the corresponding distribution of the parameters, except for ν_{pec} and σ_{tot} where the 1σ spread is obtained from the Monte Carlo method by taking into account for the uncertainties in U, V, and W (see text for more details). The p-value represents the probability of two samples belonging to the same distribution using the Anderson-Darling test.

Chapter 5

Ages from Stellar Isochrone Models [*]

5.1 Introduction

Several correlations connecting the stellar and planetary properties have emerged in the past decade (Santos et al. 2004; Fischer & Valenti 2005; Fischer et al. 2014; Narang et al. 2018; Sousa et al. 2021; Swastik et al. 2021; Unni et al. 2022; Banerjee et al. 2024). One such correlation is the stellar age-planetary mass correlation. The ages of Stars With Planets (SWP) are crucial for investigating numerous aspects of planetary system evolution, such as dynamical interactions among planets (Laughlin & Chambers 2002) and tidal effects generated by SWP (Pätzold et al. 2004; Barker & Ogilvie 2009). Understanding the ages of stars holds significant

---

[*] This work has been submitted for publication in Astrophysical Journal.

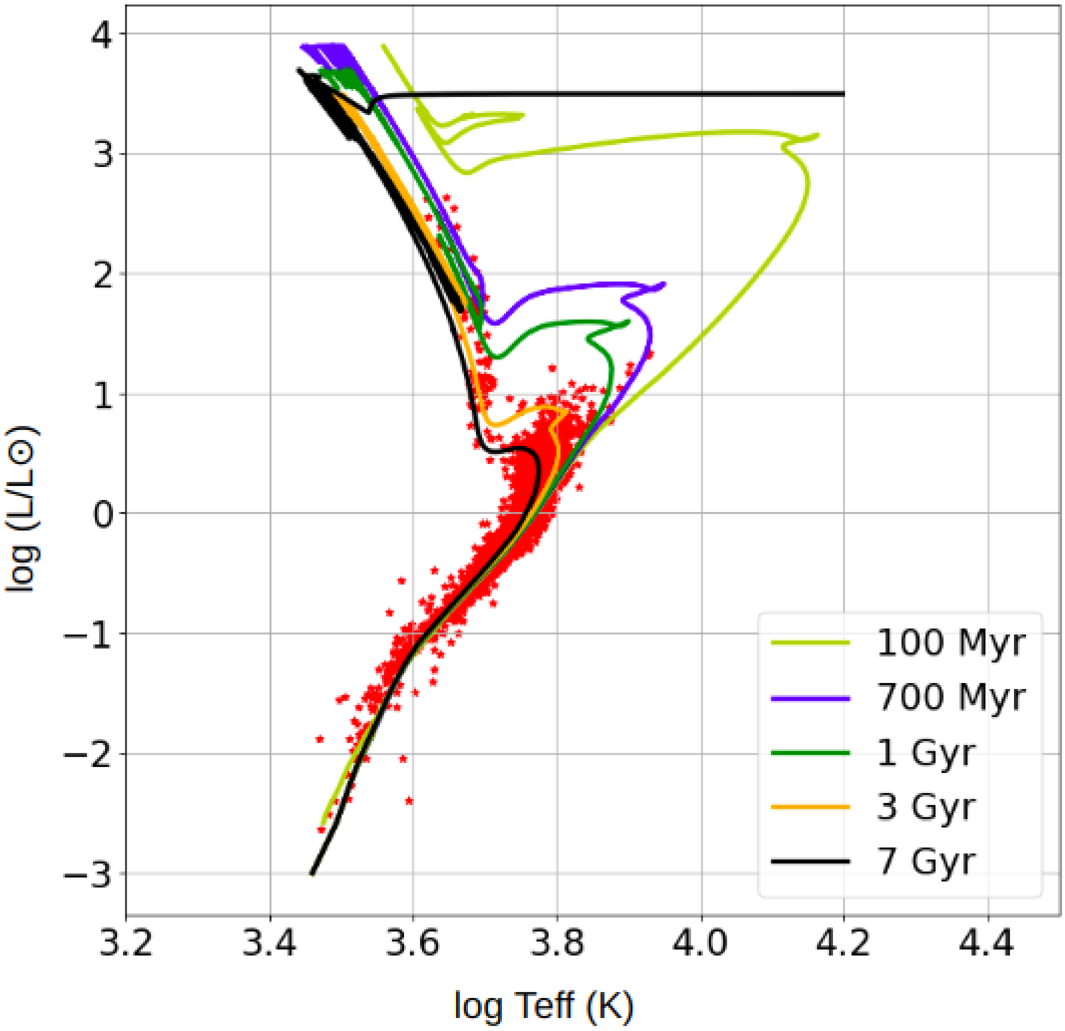

Figure 5.1: Stellar isochrone models generated using MESA. The red symbols represent planet-hosting stars. The isochrones are drawn for the solar-scaled abundances.

importance in the process of selecting stellar candidates for planet detection (Bonfanti et al. 2015) and assessing their potential habitability. The rotation and activity levels of a star which serve as indicators of stellar age, play a crucial role in determining the habitability of planets orbiting around them.

The majority of planets have been detected around main-sequence FGK stars. Due to the degeneracy of parameters and the slow evolution of observable parameters, it is difficult to accurately constrain the ages of these stars. Owing to the ambiguities inherent in estimating age, greater precision is required for these

Table 5.1: Sample distribution of stars hosting small and giant planets used in this chapter.

Count	Stellar-hosts	Planets
Total	2336	3034
Small ($M_P < 0.3M_J$)	1834	2509
Giant ($0.3M_J \leq M_P \leq 5M_J$)	502	526

Note – The above values are listed after the sample curation as described in section 6.2.

investigations. Unlike other stellar properties, such as T_{eff}, log g, and [Fe/H], ages cannot be directly observed or measured. To estimate stellar ages, one uses an indirect model-dependent technique such as isochrone fitting (Valls-Gabaud 2014). Other approaches, such as gyrochronology and activity index, are also used in addition to isochrone fitting from stellar evolutionary models. Chemical analysis (also known as chemiochronology, (Delgado Mena et al. 2019; Swastik et al. 2022)) and stellar kinematics (Binney et al. 2000; Wu et al. 2021) can be used to estimate the ages of an ensemble of stars but cannot be used for individual cases. Asteroseismology stands as the sole method capable of ascertaining the age of a star with an impressive level of precision, reaching uncertainties as low as approximately $\sim 11\%$ (Bellinger et al. 2019). However, it requires longer time-series data, which is only accessible for a few stars. Additionally, it only applies to stars hotter than about spectral type K, as cooler stars do not typically exhibit the oscillations required for estimating ages using asteroseismology (Silva Aguirre et al. 2015; Christensen-Dalsgaard & Aguirre 2018). Each of the aforementioned models requires input parameters derived from various sources. Each input parameter is accompanied by its own uncertainty, which propagates to the ultimate error estimation overages.

Most of the ages for the planet-hosting stars come from individual sources using different techniques and methods. Since each model and the input parameters that go into the model have their uncertainty, it is not possible to tabulate such values for any meaningful statistical analysis. There have been limited homogeneous studies for the ages of the planet-hosting stars. Early studies such as Saffe et al. (2005) have estimated the stellar ages of the 49 planets hosting stars. They mainly observed FGK stars from Complejo Astronomico El Leoncito (CASLEO, San Juan – Argentina) with the REOSC spectrograph attached to the Jorge Sahade 2.15-m telescope. The 49 observed stars have distances ranging from 10 to 94 pc. Since the sample was very small, it was not possible to draw any robust conclusions about different populations of planets. Recent studies for 326 planets hosting stars by Bonfanti et al. (2015) using the Padova and Trieste evolutionary codes (PARSEC) have found that ∼6% of stars have ages lower than 0.5 Gyr, while ∼7% of stars are older than 11 Gyr. Their findings revealed that the majority of their planet-hosting stars fall within the age range of 1.5 to 2 Gyr, indicating a prevalence of younger systems. Using astroseismology data for 33 Kepler exoplanet host stars, Silva Aguirre et al. (2015) have found that the majority of Kepler host stars are older than the Sun. Further study for 335 transiting planets hosting stars by Bonfanti et al. (2016) has shown that the median age of the sample is ∼5 Gyr, which is similar to the solar age. These studies motivated us to look for possible correlations between stellar ages and planet mass. However, the major limitations of these studies are that they are based on a very small sample of stars and that the ages derived in these chapters have a strong dependence on the models as well as input parameters, which makes the estimates less reliable for statistical analysis.

In order to understand how stellar ages are correlated with planetary properties, we need to analyze a large number of planet-hosting stars with minimal errors in their ages. Due to the significant challenges in obtaining accurate age estimates from isochrone models due to substantial uncertainties, our approach involved verifying these estimates using a combination of established isochrone fitting models and input parameters derived from both photometric and spectroscopic data. Our

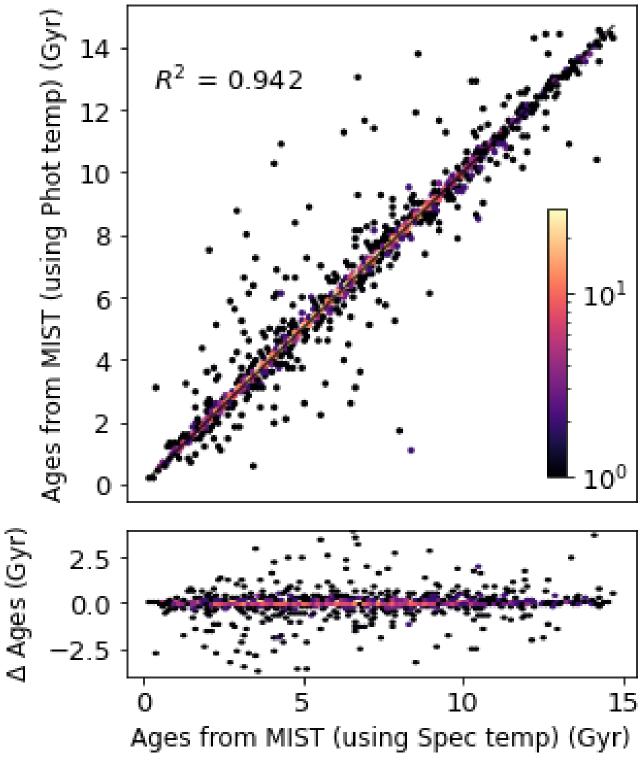

FIGURE 5.2: Comparison of stellar ages computed from photometric $T_{\rm eff}$ from Gaia DR3 and spectroscopic $T_{\rm eff}$ from sweet-cat. The color coding represents the density of points. The R^2 is the coefficient of determination which is a measure used to indicate the proportion of the variance in a dependent variable. A higher value indicates a strong correlation between the variables.

findings indicate that, while slight variations in age estimates may occur based on the specific input parameters or models employed, the overall statistical trends for the extensive star sample remain unchanged. In this study, our objective is to assess the ages of the stars that host planets, aiming to uncover various relationships between stellar ages and planetary properties, including the orbital period and mass of the planets. We used combinations of input parameters from photometry and spectroscopy and three isochrone fitting models (MIST-MESA (Huber et al. 2017; Berger et al. 2020a), PADOVA-PARSEC (Bressan et al. 2012) and q2-Yonsei-Yele (Han et al. 2009; Ramírez et al. 2014)) for the analysis. The chapter is structured as follows. In section 5.2 we describe our sample of stars hosting planets. Section 5.3 discusses the methodology of the age determination techniques using isochrones. In section 5.4 and section 5.5 we discuss the trends

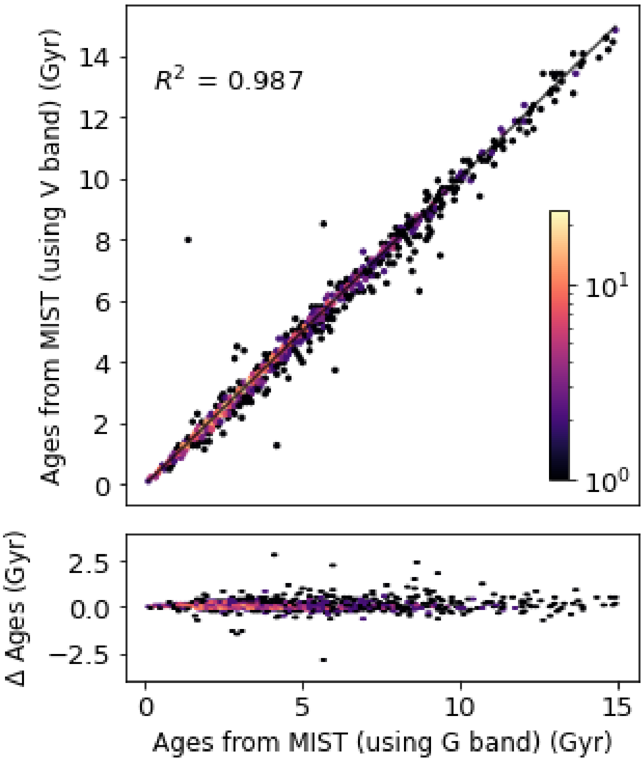

FIGURE 5.3: Comparison of stellar ages computed by V band (Johnson) and G band (Gaia) mag. The color coding represents the density of points.

for stellar ages as a function of planet mass and interpret the results in the context of GCE. Finally, we summarise and conclude our findings in section 5.6.

5.2 Sample Selection

To study the dependence of stellar ages on planetary properties such as planet mass (M_P) and orbital period, we selected an initial sample of 3775 planet-hosting stars from the NASA exoplanet archive (Akeson et al. 2013; NASA Exoplanet Science Institute 2024). In order to estimate the stellar ages from isochrone fitting techniques, we require precise stellar parameters, which come from spectroscopy, photometry, and astrometry. For the photometric and astrometric data, we cross-matched [†] our data with GAIA DR3 data (Gaia Collaboration et al. 2022), while for the spectroscopic data, we used sweet-cat (Andreasen et al. 2017; Sousa et al. 2018, 2021) which is a catalog of stellar parameters for SWP determined homogeneously from spectroscopy. We narrowed down our analysis to main sequence stars due to the complexities associated with accounting for evolutionary effects, such as non-LTE, which can introduce variations in photospheric metallicities (Bergemann et al. 2011; Swastik et al. 2022). Subsequently, we excluded super-Jupiters ($M_P \geq 5M_J$) and multi-planetary systems hosting at least one small planet ($M_P < 0.3M_J$) and a giant planet ($M_P \geq 0.3M_J$), as including such multi-planetary systems would complicate our ability to discern differences in stellar populations between small and giant planets. Furthermore, we selected stars for inclusion based on their estimated ages, only retaining those with uncertainties smaller than their main-sequence lifetime, as recommended by Pont & Eyer (2004). Additionally, we excluded lower main-sequence stars from our age sample (T_{eff} <4400K), since the main-sequence lifetime for these stars is > the age of the universe, and thus the current stellar isochrone models are not reliable to estimate the ages of these stars. Consequently, our final dataset comprised 2336 stars hosting 3034 planets (refer to table 5.1).

5.3 Age Determination from Stellar Isochrones

To determine the ages from isochrone, one places the star on the Hertzsprung−Russell diagram (HRD) with T_{eff} on the x-axis and luminosity L on the y-axis (Figure 5.1). The T_{eff} and L can be obtained by several techniques. In the case of T_{eff}, it can be determined both by spectroscopy and photometry (color-index), while the L is computed from the observed total flux, which is obtained from the photometric

---

[†] Initially, we used a wider search radius, but in this instance, a 3” search radius was adequate to retrieve all planet-hosting stars. We also used other sources, such as the SIMBAD, to confirm that they are actual planet-hosting stars.

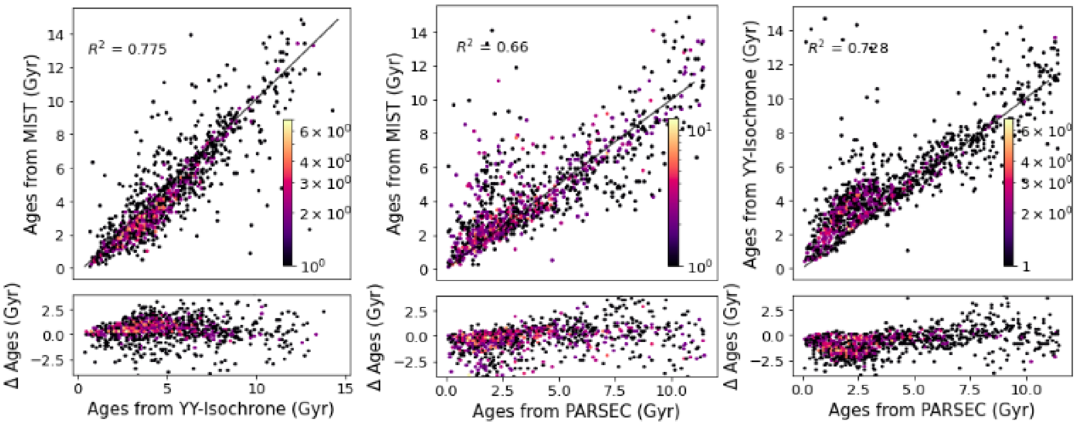

FIGURE 5.4: Comparison of stellar ages from MESA, PARSEC, and Yonsei-Yele isochrone fitting models. The color coding represents the density of points.

magnitude (Rodrigo et al. 2017), and distance from the parallax (π). These observables have their own intrinsic errors and systematics based on the techniques used to obtain them. Thus, the isochrone placement technique becomes challenging to determine the ages of a star with high accuracy. Further, for the lower main-sequence stars (T_{eff} <4400K), the isochrone ages are not reliable as the evolution timescales for these stars are > age of the universe, and thus it becomes challenging to model the evolution of such systems.

Another factor that influences the determination of isochrone ages is the selection of models/grids. While different isochrone models share a common goal of estimating stellar ages, they diverge in their underlying assumptions. For instance, the equation of state (EOS) employed by the PARSEC models primarily relies on the FreeEOS tool [‡]. In contrast, MIST and YY isochrones predominantly use the OPAL (Opacity Project at Livermore) (Iglesias & Rogers 1996) and the SCVH (Stewart, Colwell, Vasil, and Helfand) equation of state (Saumon et al. 1995), respectively. Furthermore, variations in solar abundances among the different isochrone models contribute to discrepancies in their results. For example, YY-isochrones adopt solar abundances from (Grevesse & Sauval 1998), while MIST isochrones employ the values from Asplund et al. (2009). Additionally, the

---

[‡] https://freeeos.sourceforge.net/

TABLE 5.2: Comparison of stellar ages for the small and giant planet-hosting stars using different models and input parameters

	Giant-planet (Gyr)	Small-planet (Gyr)	p-value
MESA G Spec	3.00±2.56	4.69±2.47	10^{-26}
MESA G Phot	3.34±3.12	5.08±2.95	10^{-16}
MESA V Spec	2.38±2.89	4.58±2.37	10^{-16}
MESA V Phot	3.42±3.34	5.03±2.83	10^{-29}
Yonsei Y G Spec	3.45±3.15	5.05±2.48	10^{-36}
PARSEC G Spec	2.63±2.21	3.78±2.01	10^{-13}

Note: The errors quoted are the median 1σ spread in the above distributions. Here, the p-value obtained from the KS test represents the probability that the two samples belong to the same distribution.

choice of atmospheric models, such as ATLAS12, PHOENIX (Bt-stell), SYNTHE, MARCS, and others, in conjunction with the EOS, opacity values and solar abundances, further contributes to systematic differences in the estimation of stellar ages. These differences are critical factors that must be taken into account when determining isochrone ages. They highlight the complexities and uncertainties involved in age estimation and demonstrate the need for careful consideration and comparison of multiple isochrone models to mitigate potential biases.

Statistical inferences drawn for a sample of stars become inherently unreliable due to the dependence of individual star age determinations on both the input parameters and the models used. Therefore, we estimate the ages of the stars using various models and different combinations of input parameters. Our objective is to assess whether consistent statistical conclusions could be drawn across different combinations of models and input parameters. Here, we vary certain input parameters (for instance, we use T_{eff} from photometry and spectroscopy) while keeping the other parameters constant (for instance using G-band magnitude and MESA isochrone models) to demonstrate how the age varies from one case to another and how the overall stellar age for the population of exoplanets varies statistically.

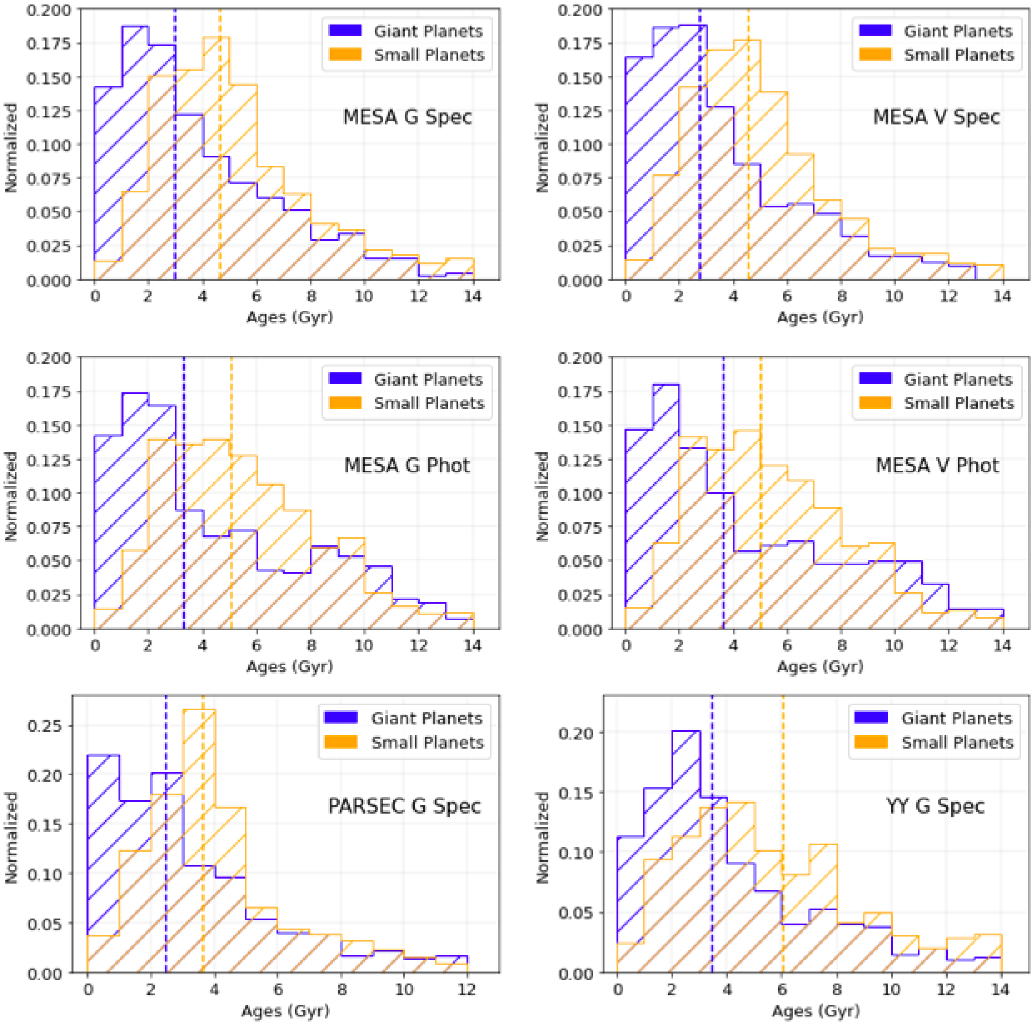

FIGURE 5.5: Histogram for ages of the planets hosting stars for small and giant planets. The label is indicated in the following format: isochrone model-photometric band-temperature from spectroscopy or photometry. The dashed lines represent the median ages corresponding to their color labels in the histograms.

5.3.1 Choice of stellar temperatures

The temperature of a star is mostly obtained by spectroscopy or photometric measurements. Both of these techniques have certain assumptions while obtaining the estimate of the T_{eff} and this leads to a systematic difference in the estimation of ages (Wing & Yorka 1979). To verify how the input ages affect the stellar age estimates from isochrone fitting we took the T_{eff} from two sources: sweet-cat (Sousa

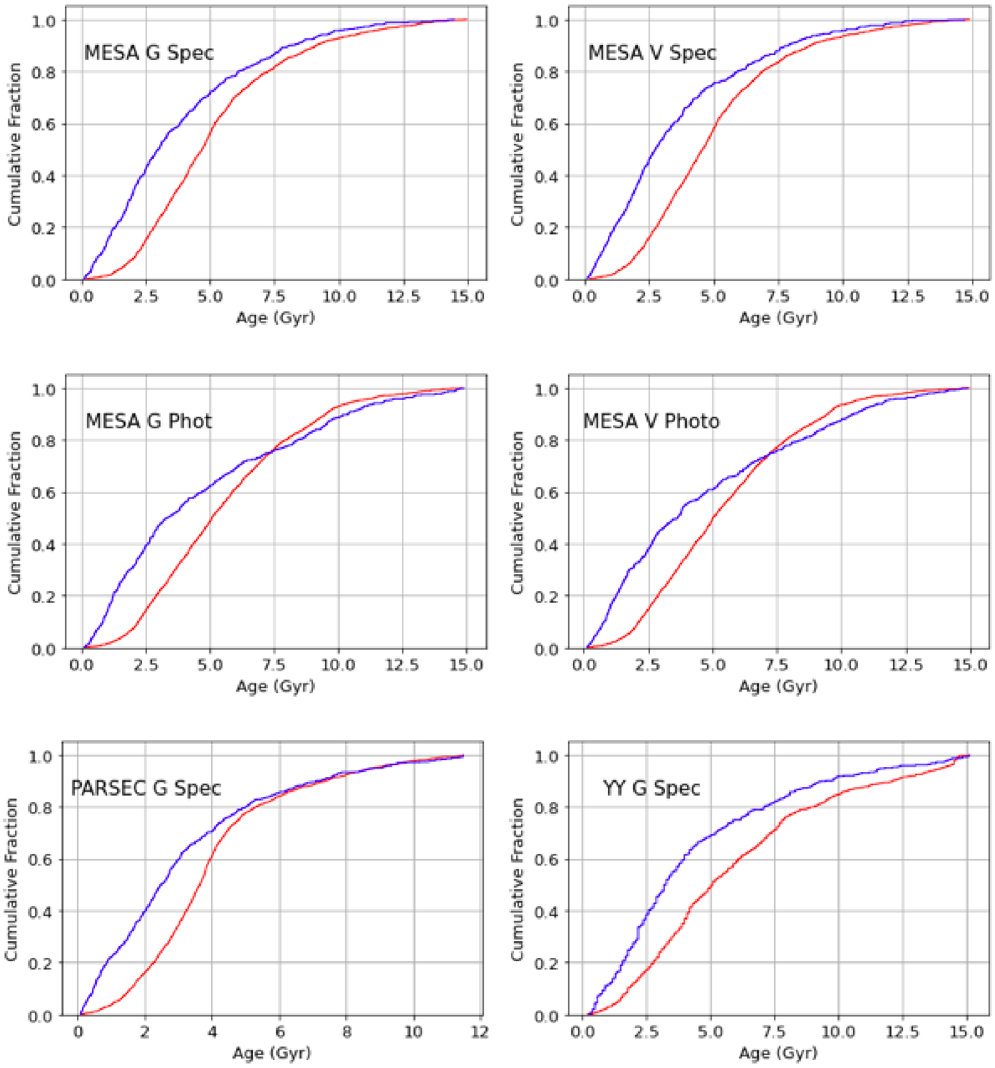

FIGURE 5.6: Cumulative distribution for the stellar ages of small (red) and giant (blue) planet-hosting stars obtained using different isochrone models and input parameters.

et al. 2021) (spectroscopic) and GAIA DR3 (Gaia Collaboration et al. 2022) (photometric). Figure 5.2 shows the spread in age using photometric and spectroscopic temperatures using PARSEC isochrone models (Bressan et al. 2012) and GAIA parallaxes (Lindegren et al. 2021). We find a small scatter but no systematics in the age estimates from the spectroscopic and photometric temperatures. We also used other stellar isochrone fitting models to verify this and obtained similar spreads in all the cases.

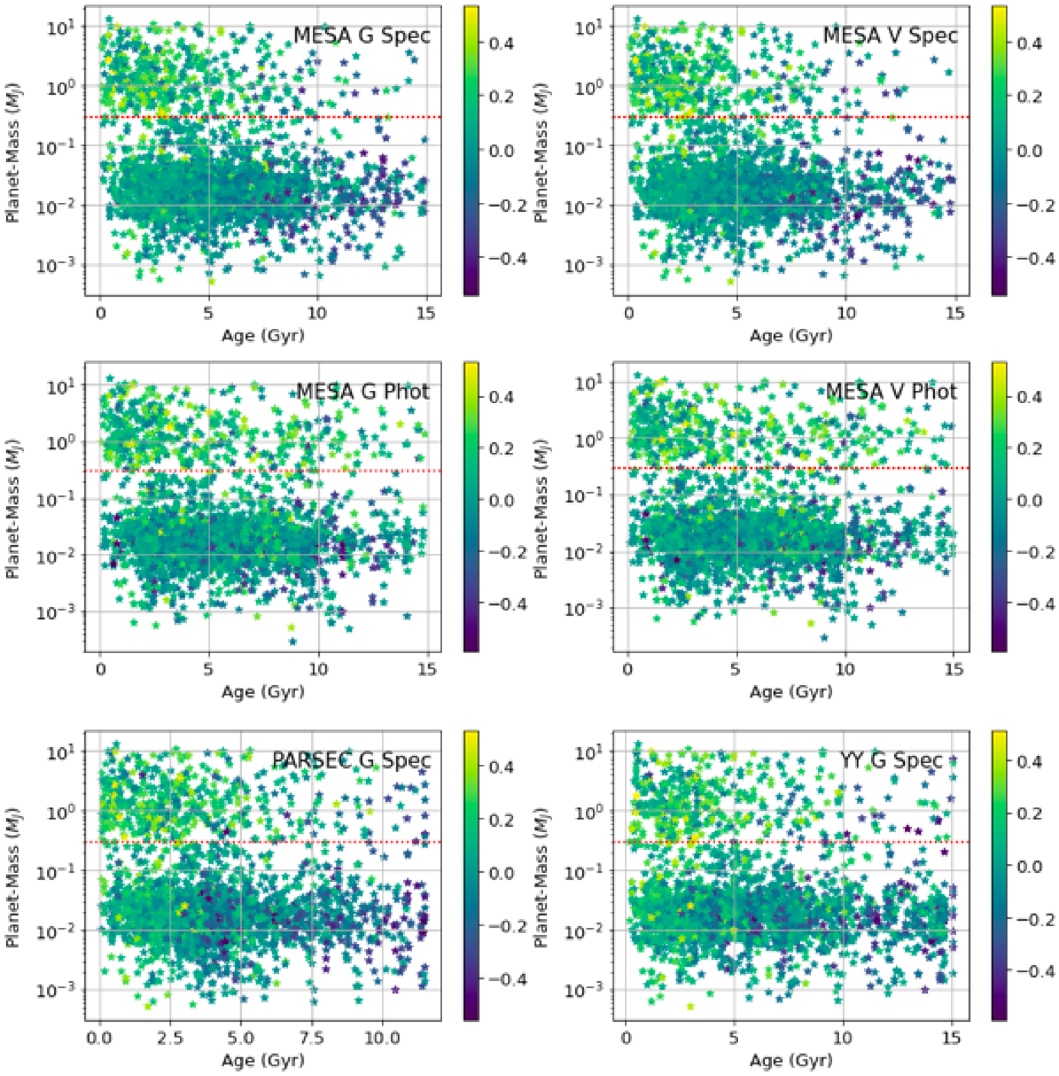

Figure 5.7: Planet mass as a function of stellar age. The color bar on the right represents the stellar metallicity values obtained from the literature. The dashed red line ($M_P = 0.3M_J$) separates the small and giant planet-hosting stars.

5.3.2 Choice of photometric band magnitude

Since the luminosity estimate for our model is dependent on the total flux (f), which is again estimated from the given band magnitude, we decided to investigate if the choice of the photometric band magnitudes plays any significant role in the estimation of stellar ages. We decided to use the Johnsons V-band and Gaia G-band magnitudes to estimate the ages of the exoplanet host star. Stars for which V-band magnitude was not available, we used the relationship as described in GAIA archive [§] and used G, G_{bp} and G_{rp} magnitudes to obtain the V-band magnitude. We also tested the above relation for the stars whose both G-band and V-band were available and we found the V-band obtained from the empirical relation matches with the observed ones. Figure 5.3 shows the correlation between the ages determined from V- and G-band magnitudes using spectroscopic temperatures and MESA-ISO-Classify code. We find that the ages obtained from G-band and V-band are strongly correlated and do not show any significant systematic differences. We also performed this analysis with several other combinations of input parameters (for instance, using photometric and spectroscopic T_{eff}) and did not find any considerable dispersion in any case.

5.3.3 Choice of models

Most of the stellar ages obtained using isochrone use a standard stellar evolutionary isochrone fitting model to estimate the age of stars. However, the choice of the model plays an equally important role as that of the other input parameters (Delgado Mena et al. 2019). Here we choose three widely used stellar isochrone model: MIST-MESA (Huber et al. 2017; Berger et al. 2020a), PADOVA-PARSEC (Bressan et al. 2012) and q2-Yonsei-Yele (Han et al. 2009; Ramírez et al. 2014) to estimate the age of our exoplanet hosting stars. Figure 5.4 shows the scatter plot in the stellar ages obtained using various isochrone fitting models using spectroscopic temperatures and G magnitude. We find that the ages estimated using MESA and YY are well in agreement, with a moderate spread but no significant systematic differences. For the stellar ages obtained using PARSEC models, we find a large scatter for stars with ages > 6 Gyr, when comparing with the ages obtained using MESA and YY. We also find a notable systematic difference in the

---

[§] https://gea.esac.esa.int/archive/documentation/GEDR3

Table 5.3: Distribution of Jupiter hosting stars in terms of their stellar ages and orbital period.

	Young hot Jup (Count)	Old hot Jup (Count)	Young cool Jup (Count)	Old Cool Jup (Count)	Hot Jup (Gyr)	Cool Jup (Gyr)
MESA	207	60	115	46	2.43	3.50
Yonsei Y	191	76	97	67	3.08	4.35
PARSEC	289	48	132	56	2.15	3.38

Note: The standard error of the mean is typically 0.01 Gyr for all the cases. The p-value is obtained in the same way as in table 5.2. Note the p-values are significant in all the cases.

stellar ages obtained from PARSEC models when comparing the ages with MESA and YY.

5.4 Results

5.4.1 Ages of the planet-hosting stars

We compute the ages of the planet-hosting stars from isochrone fitting methods using different models and input parameters. Figure 5.5 shows the distribution of stars hosting small planets and giant planets. It is interesting to note that, even though the stellar ages are computed using different models and input parameters that vary, and there are noticeable differences in the distribution of their ages, the final statistical interpretation from the stellar ages remains unaffected. We find that the median ages of the stars hosting small planets are higher compared to stars hosting giant planets in all cases (Table 5.3). We also find that the median ages obtained from PARSEC models are slightly lower when compared with the ages from MESA and YY isochrone models, and this is due to the systematics of the stellar ages as obtained in Section 5.3.3.

Further, the cumulative age fraction shown in figure 5.6 implies that stars hosting small and giant planets belong to different populations. We also performed a Kolmogorov Smirnov test (k-s) test on the sample and found that the sample of stars hosting small and giant planets fall into distinct age groups (table 5.2). This result suggests that small planets are common around both young and older stars, whereas giant planets are more prevalent around younger stars.

It is important to note that, around young stars, detection of small planets is challenging when compared to giant planets due to high stellar activity and RV jitters[¶]. It is possible that some small planets' detection might have been missed for younger stars due to these effects. However, the lack of giant planets around older stars is not due to any detection or selection bias, as it is easier to detect giant planets compared to small planets, irrespective of the detection technique or stellar age.

5.4.2 Planet mass as a function of stellar age

Figure 5.7 shows the planet mass distribution as a function of stellar age with $\sim$ 70%-85% of stars in the sample having an age below 7 Gyr. We also note that the population of giant planets began to increase approximately 4-5 Gyr ago, indicating that the formation of giant planets is a relatively recent phenomenon when compared to the population of small planets, with the onset occurring as late as approximately 7-8 Gyr ago. Moreover, the color bar (which represents stellar metallicity) from the figure 5.7, we infer that the young planet-hosting stars are

---

[¶] RV jitter is the intrinsic noise in radial velocity measurements of a star, caused by factors such as stellar activity, granulation, oscillations, and instrumental limitations. It poses challenges in detecting planets, raising the detection threshold, and introducing false positives/negatives.

statistically metal-rich, and a stellar gradient exists with increasing ages. This is also in line with the previous studies that have shown giant planet-hosting stars are metal-rich (Fischer & Valenti 2005; Sousa et al. 2019; Narang et al. 2018; Swastik et al. 2022), which supports the core-accretion model for planet formation.

5.4.3 Planet fraction vs stellar age

In order to understand the fact that giant planets started forming late in the universe, we investigated the ratio of stars hosting giant planets to the stars hosting small planets as a function of the stellar age. In all the cases that are analyzed in this chapter, the ratio falls as a function of stellar age, with the majority of the old stars $\geq$ 5 Gyr hosting small planets (figure 5.8). However, It is possible that the ratio of stars hosting giant planets to stars hosting small planets is higher for younger stars ($<$ 5 Gyrs) due to detection biases as many more small planets that are present in these systems might have been missed out when compared to giant planets. However, for stars $>$ 5 Gyrs, the finding is not due to any selection or observation bias, as giant planets would have been easier to detect compared to small planets for any type of star, regardless of its age or detection technique. This finding suggests that it is more likely that young stars have a higher ratio of giant planets to small planets, while older stars host mostly small planets. Although we find a small scatter at the age bin 10-12 Gyr, this is due to the lower number of planet-hosting stars in that bin.

5.4.4 Hot Jupiters are younger

We investigated the stellar ages of the giant planet-hosting stars as a function of their orbital period. For this, we choose the stellar ages from three different

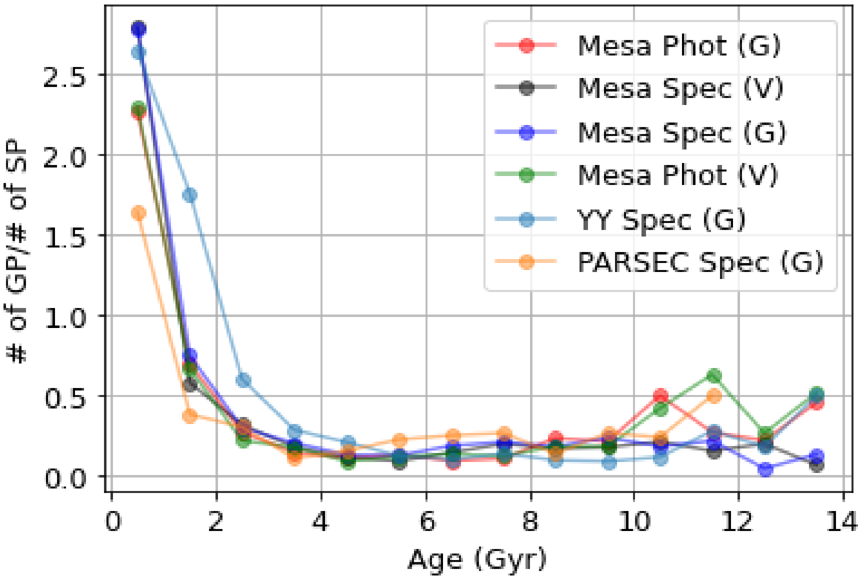

FIGURE 5.8: Fraction of stars hosting giant planets to small planets as a function of stellar age using different models and input parameters. The data is binned at an interval of 1 Gyr.

models whose ages were obtained using spectroscopic T_{eff} and V-band magnitude. A closer look at figure 5.9 shows that most of the giant planet hosts are young ($\leq$ 5 Gyrs) and are hot Jupiter's having an orbital period of fewer than 10 days. The table 5.3 lists the median age of hot (orbital period $\leq$ 10 days) and cool Jupiter's (orbital period $>$ 10 days). On average, the hot Jupiter hosting stars are $\sim$ 1.2 Gyr younger than the cool Jupiter hosting stars.

We also find that around $\sim$ 70 percent of giant planets lie in the age range $\leq$ 5 Gyr, indicating that the overall giant planet population is younger. Although the high number of young hot-Jupiter's can be possibly due to detection bias as hot-Jupiters are easy to detect (Kipping & Sandford 2016), we find that the number of young cool Jupiters is notably higher than old hot-Jupiters, which is not due to observational bias but points towards the scenario that Jupiters started forming at the later stages of GCE.

5.4.5 Isochrone, asteroseismology and chemical clocks

We compared the stellar ages derived from MIST-MESA isochrone models with those obtained using Asteroseismology and from α abundances (also known as chemical clocks). For Asteroseismology we used the ages from Silva Aguirre et al. (2015) and our analysis reveals that isochrone-based ages are slightly overestimated when compared to asteroseismology-derived ages as shown in Figure 5.10. Conversely, when comparing the ages obtained using the α abundances using the relationship in Delgado Mena et al. (2019), we find that the ages are over-estimated for the younger stars ($\leq$ 4 Gyrs) while they slightly underestimated for the older stars ($>$ 4 Gyrs) as shown in Figure 5.10. The comparison primarily focused on FGK type stars. Asteroseismology included 23 stars, while the analysis involving alpha abundances encompassed 220 stars.

The discrepancies observed between the ages derived from MIST-MESA isochrone models, asteroseismology, and α abundances underscore the need for methodological refinement across age-determination techniques. Specifically, the tendency of asteroseismology to underestimate ages, compared to isochrone models, and the accuracy of chemical clocks for stars of different ages highlights the importance of cross-validating stellar ages to identify and correct systematic biases.

5.5 Discussion

The results from section 4 indicate that the ages for the majority ($\sim$75-85 %) of stars hosting planets are around $\sim$ 6 to 7 Gyrs depending on the model. Further, within the planet's population, the giant planet-hosting stars are younger when compared to the stars hosting small planets. The reason why younger stars host more giant planets compared to older stars can be explained by peeping into the

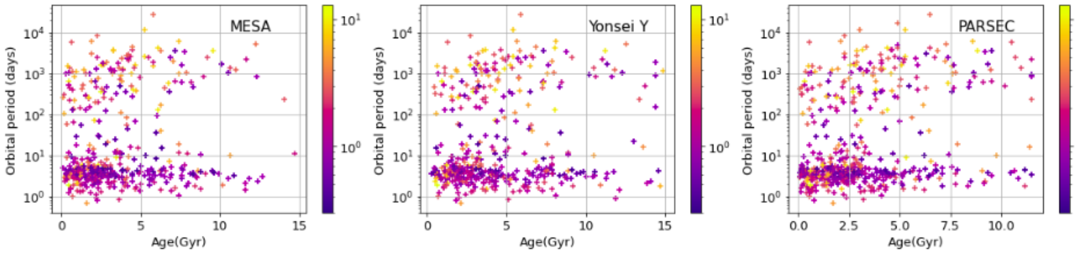

Figure 5.9: Distribution of giant planets as a function of stellar age. The color-bar on the right represents the planetary mass of the companion. The label represents the stellar models used, while for input parameters, we used spectroscopic T_{eff} and G magnitude for all three cases.

dust-to-gas ratio of their circumstellar environment. A higher dust-to-gas ratio favors the formation of giant planets (Kama et al. 2015) as a) the solid dust grains act as the building blocks for planetesimals and planetary cores. When the dust-to-gas ratio is higher, it means there is a larger amount of solid material available compared to the surrounding gas. This increased availability of material provides a larger reservoir for the growth and accumulation of solid cores. b) In a higher dust-to-gas ratio environment, collisions between dust grains become more frequent. These collisions can lead to sticking and aggregation, allowing the particles to grow in size. With a greater number of collisions occurring, the growth process can proceed more rapidly, enabling the formation of larger planetesimals and planetary cores over shorter timescales ($\sim$ 5-10 Myrs). c) Larger solid cores have stronger gravitational forces, enabling them to attract and capture more surrounding gas. When the dust-to-gas ratio is higher, there is a denser population of dust grains that can coalesce into larger planetesimals and cores. These more massive cores can then more effectively accrete gas from the protoplanetary disk, rapidly increasing their size and leading to the formation of gas giant planets (Emsenhuber et al. 2021; Drazkowska et al. 2022).

Together with the dust-to-gas ratio, the grain composition also plays a key role in the formation of the planetary core (Dorschner et al. 1995; Fabian et al. 2001; Draine 2003). During the early stages of galaxy evolution, the circumstellar disk is devoid of sufficient grains as the ISM is mostly enriched with Type II supernovae. The dust grains consisted of mostly silicates, magnesium, and other α but lacked iron or other heavier elements and thus resulting in a lower dust-to-gas ratio (<<0.01). As the galaxy evolved, the ISM was enriched with Fe-peak elements from Type Ia supernovae, which in turn increased the dust-to-gas ratio and thus favoring the formation of both small and giant planets (Nissen 2015; Bedell et al. 2018; Anders et al. 2018; Feuillet et al. 2018; Buder et al. 2019; Delgado Mena et al. 2019). The presence of giant planets around metal-rich and young stars also correlates with higher dust-to-gas ratio ($\sim$ 0.01) in young and metal-rich protoplanetary disks which makes them conducive to the formation of giant planets. This is also consistent with the core-accretion process (Pollack et al. 1996; Matsuo et al. 2007) leading to the formation of giant planet, where a solid core of $\sim$ 10-15 $M_{\oplus}$ needs to form quickly ($\sim$ 10 Myr) before the gas in the disk dissipates (Haisch et al. 2001; Kraus et al. 2012), otherwise the resulting planet would end up rocky in nature. The presence of a higher dust-to-gas ratio, thus promotes faster core formation, thereby facilitating the formation of giant planets.

5.6 Summary and Conclusions

The characteristics of exoplanets and their host stars exhibit a close interdependence. In the present study, we focused on estimating the stellar ages of planets orbiting main-sequence stars. To accomplish this, we used the isochrone fitting technique to estimate the stellar ages of the planet-hosting stars. Furthermore, we conducted an extensive analysis, exploring possible correlations between stellar and planetary properties to gain insights into their formation mechanisms. Our analysis encompassed a substantial sample of over 2336 stars known to host planets, detected through both transit and radial velocity (RV) methods. In conclusions:

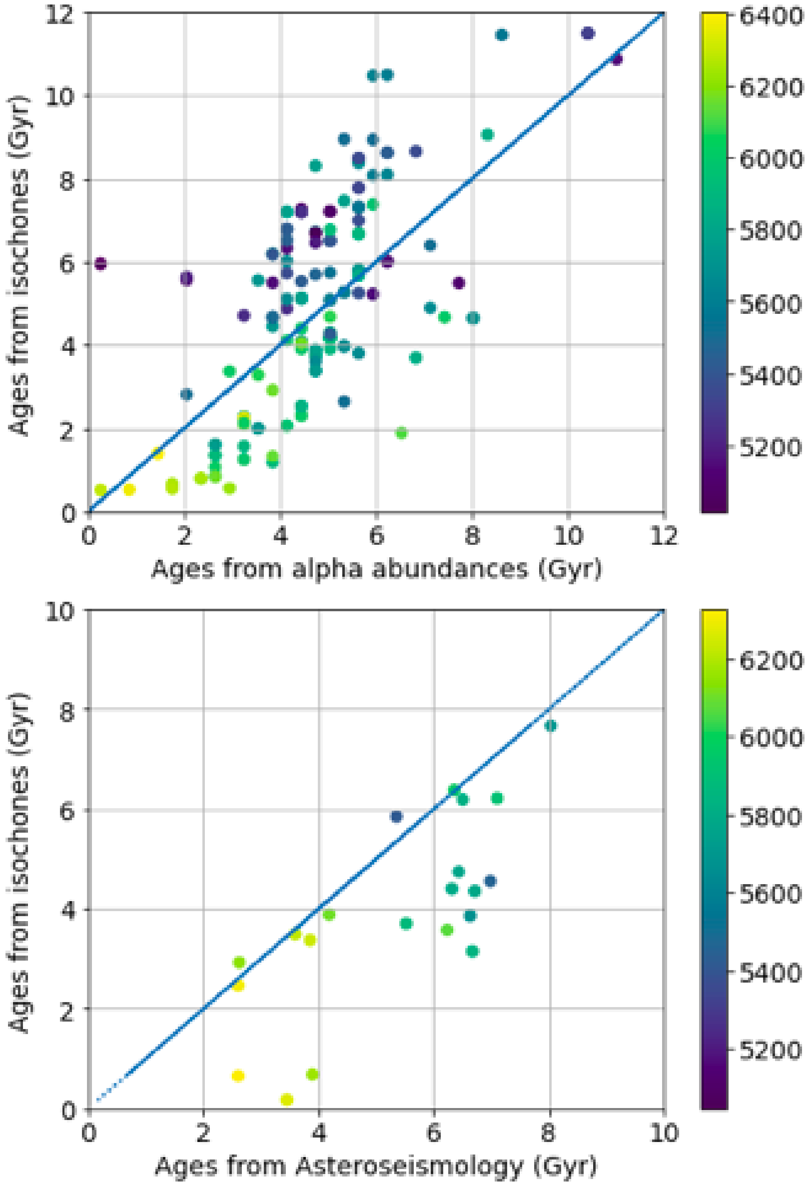

FIGURE 5.10: **Top:** Comparison of ages obtained from stellar isochrones and from [α/Fe] abundances. **Bottom:** Comparison of ages obtained from stellar isochrones and from Asteroseismology. The colorbar represents the effective temperature of the star.

1. We computed the stellar ages for the main sequence planets hosting stars using the isochrone fitting technique. Since isochrone ages are highly model- and input-parameter-dependent, we used several models and input parameters in order to minimise the uncertainties in the model dependency and input parameters.

2. We find that, even though individual age estimates and their distributions vary depending on the choice of model or input parameters, the statistical correlations and implications remain unaffected.

3. Our findings suggest that 70% to 85% of planets have stellar ages < 7Gyrs and most of the planets started forming after the ISM was enriched sufficiently to form the cores of the planets.

4. Our analysis reveals a distinct divergence in the ages of stars hosting small planets compared to those hosting giant planets. Specifically, we observe a statistically significant age difference, with stars hosting giant planets being notably younger than those hosting small planets. This disparity suggests that the formation of Jupiter-sized planets occurred at a later stage in the galaxy's evolution, specifically when the necessary dust-to-gas ratio had reached a threshold enabling the formation of a significant number of giant planets. These findings corroborate the core-accretion theory of planet formation.

5. Among the giant-planet population, we find that the hot Jupiters are the youngest, and they are the most recently formed systems in the context of planet formation.

In conclusion, we have analysed the stellar ages for the largest number of exoplanet-hosting stars, connecting the planet formation process to the ages of their hosts. The fact that stars hosting giant planets are younger is largely consistent with the GCE. From the observed trends between stellar ages and planet masses, we conclude that the small planet formation started to peak after the ISM was sufficiently enriched ($\sim$ 6-7 Gyr), while the giant planet formation is much younger and has started to form in large numbers only in the past ($\sim$ 4-5 Gyr).

The major challenge in estimating the ages of the stars using the isochrone method is the large uncertainties in its measurements. To strengthen the findings that are presented in this chapter, future astroseismology observations on a larger sample of exoplanet-hosting stars might shed some light, though astroseismology has its own limitations and is only applicable to specific groups of stars. Future indirect stellar age estimates from various techniques such as stellar kinematics and chemical cartography might also shed some light on the correlations between stellar ages and planet masses.

Chapter 6

Planet Formation in LkCa 15 Proto-planetary Disk [*]

6.1 Introduction

Protoplanetary disks, the dense circumstellar gas and dust of $\sim$ 1 to 100 M_J encircling young stars are widely recognized as the birthplaces of planetary systems (Trapman et al. 2017; Baillié et al. 2019). The direct imaging of these disks and sometimes planets within them offers an unparalleled window into the dynamic processes of planets in formation. So far, in scattered light, we have imaged one such system, PDS 70, the host of two such protoplanets (Keppler et al. 2018; Müller et al. 2018; Haffert et al. 2019; Wang et al. 2021). Further, we have detected a circumplanetary disk around PDS70 c using ALMA observations (Benisty et al. 2021). Observations of several proto-planetary disk systems, such as TWA Hya (Andrews et al. 2016; van Boekel et al. 2017), HD 97048 (Ginski et al. 2016; van der Plas et al. 2017), and HD 142527 (Casassus et al. 2012; Avenhaus et al.

---

[*] This work has been submitted for publication in A&A

2017), have revealed intricate patterns of dust rings. These structures have been captured both in scattered light, using Adaptive Optics (AO) systems like GPI and SPHERE, and in the sub-millimeter range, using interferometers such as ALMA. Hydrodynamical simulations, when integrated with sophisticated radiative transfer models, suggest that planets ranging from sub-Jovian to Jovian mass are capable of producing such substructures within their disks (e.g. Montesinos et al. 2016; Price et al. 2018; Dong et al. 2015; Dipierro et al. 2015; Pinte et al. 2016; Bae et al. 2017). Consequently, the analysis of disk features like gaps, rings, and spirals not only sheds light on the mass and properties of the associated proto-planets but also offers insights into the evolutionary mechanisms at play. In this context, the LkCa 15 protoplanetary disk presents a compelling case study, offering a unique perspective on the early stages of planet formation and disk evolution.

The young LkCa 15 (K5, $0.97M_{\odot}$, [Fe/H]=0.26 dex; (Simon et al. 2000; Swastik et al. 2021) system is a T-Tauri star located in the Taurus-Auriga star-forming region which is 1-3 Myr old (Currie et al. 2019) and is about 157.185±0.652 pc away (Gaia Collaboration et al. 2023). LkCa 15 is also suspected to host multiple Jupiter-sized planets (Kraus & Ireland 2012; Isella et al. 2012; Sallum et al. 2015). Besides the planets, it has a proto-planetary disk with a gap around 45 to 50 au and also several substructures observed in scattered light as well as in ALMA images (e.g. Piétu et al. 2006; Espaillat et al. 2007, 2008; Isella et al. 2014; Oh et al. 2016; Ren et al. 2023).

Until the advent of ALMA, optical and near-infrared (NIR) scattered light observations were the best methods to image the protoplanetary disk in high resolution in order to resolve the disk features. Sparse aperture masking interferometry (SAM; Tuthill et al. 2006) and AO-assisted angular differential imaging (ADI; Marois et al. 2006) are two complementary techniques used for obtaining diffraction-limited images from ground-based telescopes. The first proto-planet candidate around LkCa 15 was detected by Kraus & Ireland (2012). Further, using SAM,

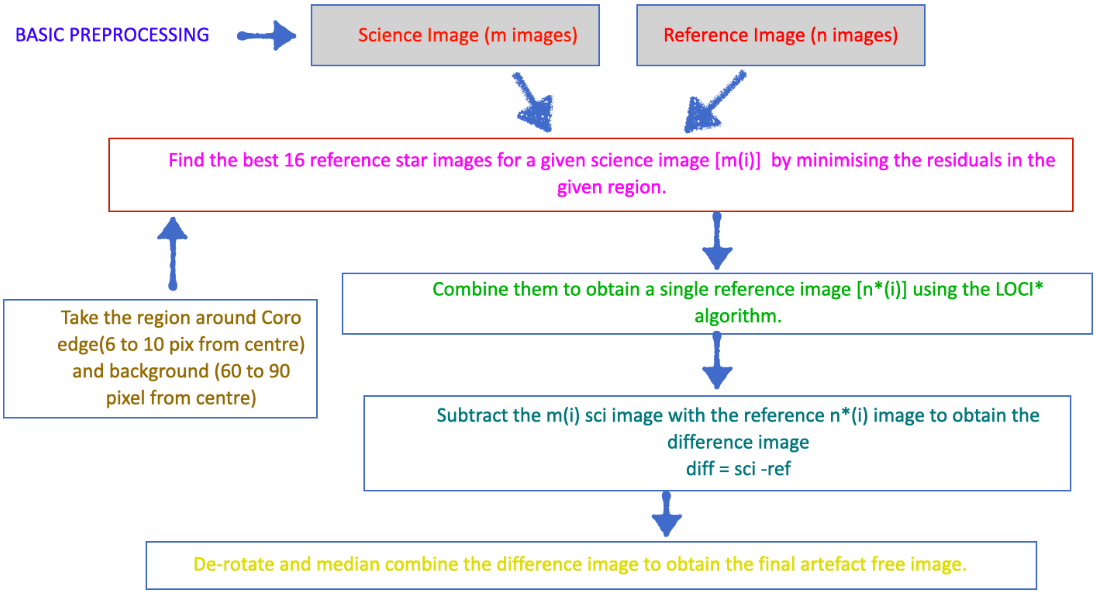

FIGURE 6.1: Schematic diagram explaining the steps in the star-hopping RDI pipeline in order to obtain the artefact-free LkCa 15 disk images.

the proto-planet candidate was confirmed by Isella et al. (2012). Subsequent investigations by Sallum et al. (2015) using SAM also reported the presence of three possible protoplanets on Keplerian orbits within 25 au, one of which was recovered in H_α (LkCa 15b). However, studies such as Currie et al. (2019) used high-contrast imaging and suggested that proto-planetary signals detection with SAM are likely inner disk signals. Further, using SAM, Blakely et al. (2022) report the detections of two previously observed asymmetric rings at ∼17 and ∼45 au but no clear evidence for candidate planets. Recently, Sallum et al. (2023) have also found that the three companion planet model falls shot to explain the positional evolution of the infrared sources as the longer time baseline images lack the coherent orbital motion that would be expected for companions.

Polarimetric studies in optical and NIR have also been done for LkCa 15. Using ZIMPOL, Thalmann et al. (2015) detected the previously unseen far side of the disk gap. Subsequent polarimetric observations by Thalmann et al. (2016) using J-band IRDIS have reported the presence of persistent asymmetric structures at the location of the planetary candidates. Oh et al. (2016) used H-band polarized intensity images from Subaru/HiCIAO and reported the existence of a bright inner disk offset by 13±4°. The grain size and polarized intensity fractions were not estimated in these studies.

With the advent of ALMA, the scattered light images of the LkCa 15 system have been complimented by mm and sub-millimeter images. ALMA images mainly probe the larger grains which were previously not probed by the scattered light images. These ALMA images have reconfirmed the existence of a gap at 45 to 50 au which was seen in scattered light images (Piétu et al. 2006; Espaillat et al. 2007, 2008; Isella et al. 2014; Oh et al. 2016). Additionally Jin et al. (2019) used the disk density profile to fit the ^{12}CO observed radial profile obtained using ALMA and found the total disk mass to be 0.1$M_\odot$. Although there is no direct evidence for protoplanets detected in ALMA, recent studies in the ALMA 1.3 mm images show multiple gaps and rings. It can be shown using hydrodynamic simulations that the existence of sub-Jovian planets can explain such morphology.

Even though the presence of companions in LkCa 15 is yet to be established

TABLE 6.1: Basic stellar parameters for the LkCa 15 system.

Parameters	Value	Units
RA (J2000)	04 39 17.79	(h m s)
Dec (J2000)	+ 22 21 03.39	(deg)
Distance [a]	157±0.06	(pc)
K-Band magnitude	8.16±0.018	(mag)
T_{eff} [b]	4210^{+185}_{-199}	(K)
$R_\star$	1.65	$R_\odot$
$M_\star$	1.01	$M_\odot$
Age	∼1	(Myr)

Note: [a] Gaia Collaboration et al. (2021) [b]Swastik et al. (2021)

Table 6.2: Observation modes used for LkCa 15 imaging.

Arm	UT Date	Mode	DIT (s)	NDIT		Sci. time(s)	Ref. time(s)
				Sci.	Ref.		
IRDIS	Nov 27, 2020	`DP_0_BB_Ks`	16	122	20	1952	320
IRDIS	Dec 8, 2020	`DP_0_BB_Ks`	16	312	56	4992	896

firmly, studies in scattered light and sub-millimeter wavelengths have predicted the likely mass of the proto-planet to be around $6M_J$ (Kraus & Ireland 2012). Other studies such as Isella et al. (2014) using the very large array (VLA) have estimated the mass of the protoplanetary candidate LkCa 15b from the accretion rate and found it to be greater than $5M_J$. Similarly, using observations from VLT/SPHERE, Gemini/NICI and Subaru/HiCIAO, Dong & Fung (2017) used hydrodynamical simulations in combination with 3D radiative transfer modeling to estimate the mass of the simulated planet in the gap of LkCa 15 to be 0.15 to 1.5 M_J depending on the value of viscosity (α) in the gap. Facchini et al. (2020) using the ALMA 1.3 mm images also performed hydrodynamical simulation and showed that the presence of sub-Jovian planet could explain the observed multi-ringed substructure. Nonetheless, there is a general agreement that the substructures in the LkCa 15 system might have been caused by the presence of a giant planet which is in the process of formation.

I obtained the new K_s-band star-hopping data from SPHERE/VLT which provides the first artifact free images of the proto-planetary disk. Although LkCa 15 have been studied previously in both scattered light and sub-millimeter wavelength, it is important to revisit the LkCa 15 protoplanetary disk because a)Previous LkCa 15 observations were carried out using ADI where self-subtraction was a major limitation, b) detect new planets beyond separations of $\sim$ 100 mas ($\sim$ 15.7 au) and c) obtain a self-consistent model that satisfactorily explains the total intensity, polarimetric, and sub-millimeter disk observations. In this chapter, we present the first self-subtraction free K_s-band imaging observations of the LkCa 15

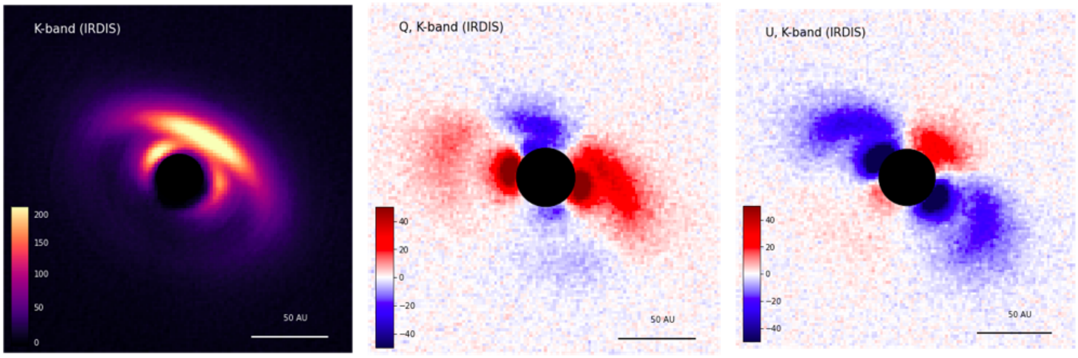

Figure 6.2: Left to right: IRDIS total intensity K-band, Stokes Q-K-band and Stokes U-K-band images as observed from VLT-SPHERE.

protoplanetary disk using the star-hopping technique (Wahhaj et al. 2021). For the first time, the inner 30 au of the disk is clearly visible. We use this observation together with ALMA observations from Jin et al. (2019) and Facchini et al. (2020) to create a consistent radiative transfer model of the disk using `RADMC-3D`. In section 6.2, we provide a brief description of the star-hopping technique and our observations of LkCa 15. In section 6.3, we present the analysis of the radiative transfer modeling of our proto-planetary disk using `RADMC-3D`. In section 6.4, we discuss the possible implications of our disk models and finally, we summarise our results in section 6.5.

6.2 Observation and Data Reduction

6.2.1 LkCa 15 observations

The new observations of LkCa 15, which is the main focus of this chapter, were obtained using the VLT SPHERE instrument (Fusco et al. 2006; Bonnefoy et al. 2016; Zurlo et al. 2016; Beuzit et al. 2019). The SPHERE is a state-of-the-art instrument that incorporates an advanced adaptive optics (AO) system (Fusco

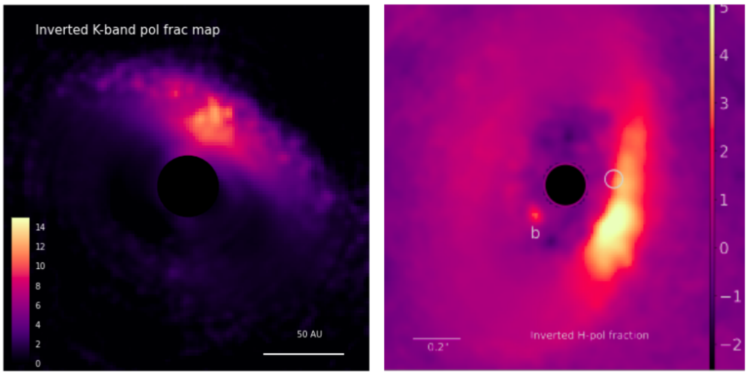

FIGURE 6.3: Left: Inverted K-band polarization fraction ($I_{\text{tot}}/\sqrt{Q^2+U^2}$) map of LkCa 15 system. Planets with low polarization, if exist, overlay on a backdrop of highly polarized light coming from the disk, resulting in a robust discrimination caused by a high signal-to-noise ratio (SNR). However, there is no unambiguous planetary signature in this image. Right: The PDS 70b planet detected using inverse polarization mapping by Wahhaj et al. (2024)

et al. 2006, 2014) and has three distinct science sub-instruments (1) IRDIS (InfraRed Dual-band Imaging and Spectroscopy) which captures wide field images and performs differential imaging (Dohlen et al. 2008), (2) IFS (Integral Field Spectrograph) designed for low-resolution spectroscopy, enabling the characterization of exoplanetary atmospheres (Claudi et al. 2008), and (3) ZIMPOL (Zurich IMaging POLarimeter), a polarimetric device to detect and study the polarized light scattered by planetary atmospheres and circumstellar disks (Schmid et al. 2018). SPHERE can deliver a high K-band Strehl ratio (>90%) for stars with R<11 for median seeing conditions (0.8”- 1.2”) [†] which makes it an ideal instrument to detect young planets and study proto-planetary disks.

LkCa 15 was imaged in K_s-band in IRDIS-Dual polarization (IRDIS-DPI) mode on two nights, 27 November and 8 December 2020, as part of a larger survey of 29 proto-planetary disks in the nearby star-forming regions (Ren et al. 2023), aiming to study the disk morphology and detect planets using the star-hopping technique (Wahhaj et al. 2021). The data collected on 27 November was partial due to poor sky conditions with 122 science frames but only 20 reference frames.

[†] http://bit.ly/3Fpwazj

Fortunately, the data collected on 8th December, had a sufficient number of both science frames (312) and reference frames (56) to obtain the artefact free disk images of LkCa 15. For the reference star PSF subtraction, we chose TYC 1279-203-1 which is separated by $621''(0.172^\circ)$ from LkCa 15. Moreover, the magnitudes (in K- and V-band) for TYC 1279-203-1 are 8.03 and 12.10 vs 8.16 and 12.03 for LkCa 15, thus making it an ideal reference star for PSF subtraction. The science frames were observed in a sequence of ~ 6 minutes followed by a hopping overhead time of ~ 1 minute, following which the reference star was observed for ~ 2 minutes. In order to block the star-light, we used the `N_ALC_Ks` chronograph which is suitable for observations in the K_s-band. The LkCa 15 observations in K_s-band IRDIS-DPI mode are summarized in Table 6.2.

6.2.2 The star-hopping pipeline

The basic reduction for the LkCa 15 was done using the standard star-hopping pipeline as discussed in Wahhaj et al. (2021). This includes the flat-fielding, removing bad-pixels, and centering the raw image files to get the science and reference image frames. After obtaining the science and reference frames, we subtracted the background from each image by computing the median in the region between 90 and 120 pixels. Now, for each science frame, the most suitable reference images for subtraction were determined by assessing the standard deviation in two zones. The first region is inside the coronagraphic mask, spanning 6 to 10 pixels, while the other region encompasses the speckle ring, ranging between 90 to 120 pixels. These selected regions are not dominated by the disk and ensure optimal PSF matching.

Based on the residuals in the above two zones between the individual pairs of science and reference images, we selected the top 16 reference images for each science frame with the lowest residuals, ensuring that they are from the same side of the detector. We then applied the `LOCI` algorithm (Lafrenière et al. 2007) to obtain the best linear combination of reference frames by minimizing the standard deviation in the previously defined PSF matching region. We chose the best 16 images from our analysis which we found optimal during our post-processing analysis as increasing the number of reference images for each science image results in flux loss in the final `LOCI` combined reference image. On the other hand, choosing lower number of reference images tend to miss significant features in the `LOCI` combined image (for more details see (Wahhaj et al. 2021). After obtaining the best reference image using `LOCI`, we obtained the difference frame by subtracting the science frame from the `LOCI` obtained reference frame. We apply this procedure to all the science frames. Subsequently, all the resultant difference images are derotated and median combined. While speckle subtraction in some individual difference images was not optimal, the derotation followed by median combination effectively suppressed the remaining speckles, yielding an artifact-free image of the LkCa 15 disk. A visual representation of the steps involved in star-hopping pipeline is given in Figure 6.1.

6.3 Analysis

6.3.1 IRDIS: Simultaneous polarimetry and total-intensity in K-band

The IRDIS system, a component of SPHERE, has the ability to capture total-intensity and polarimetric images in the Y, J, K, and K_s bands. While the H-band offers superior resolution compared to the K_s-band, the latter demonstrates a markedly ∼10% higher Strehl ratio, especially for faint objects like LkCa 15 (R = 11.61). Consequently, we chose to image the LkCa 15 protoplanetary disk in the

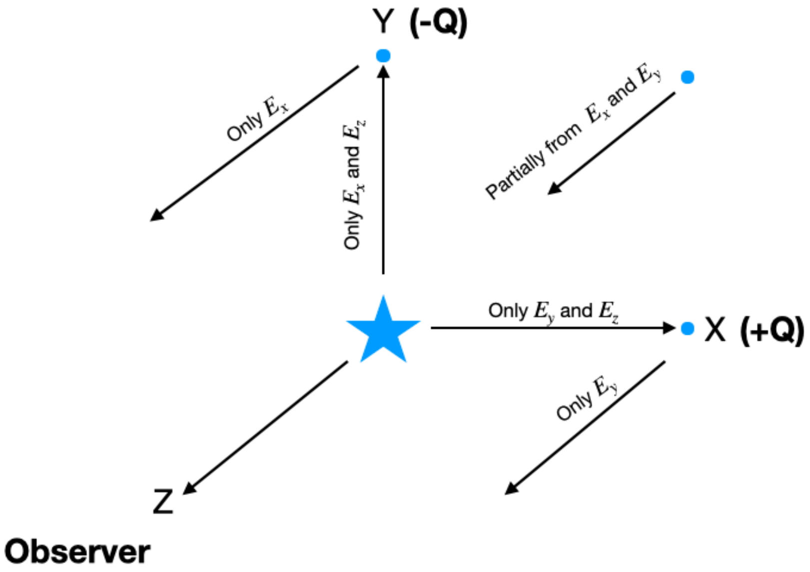

FIGURE 6.4: Schematic diagram showing the axis orientation for the E-field chosen in this chapter. The +Q is aligned along the X-direction and -Q is aligned along the Y-direction. The blue points represent the dust grains while the arrows indicate the vector of light towards the observer.

K_s-band. Figure 6.2 shows the total intensity image together with the polarimetric Q and U images.

From the total intensity and polarization images, we proceeded to estimate the polarimetric fraction map, $I_{\mathrm{tot}}/\sqrt{Q^2+U^2}$), which could potentially reveal planets with low polarization signal. Planetary atmospheres usually scatter light with much lower polarization fraction than disks (also see (van Holstein et al. 2021)). Therefore, in a polarization fraction map, planets would normally appear as intensity dips. Here, we use inverse maps so that planets show up as bright spots on the dark background. However, we do not find any planetary signatures in the LkCa 15 image shown in Figure 6.3. Note that our method can only detect planets if a low-polarization planet is superimposed on a high-polarization disk and detected with a robust SNR.

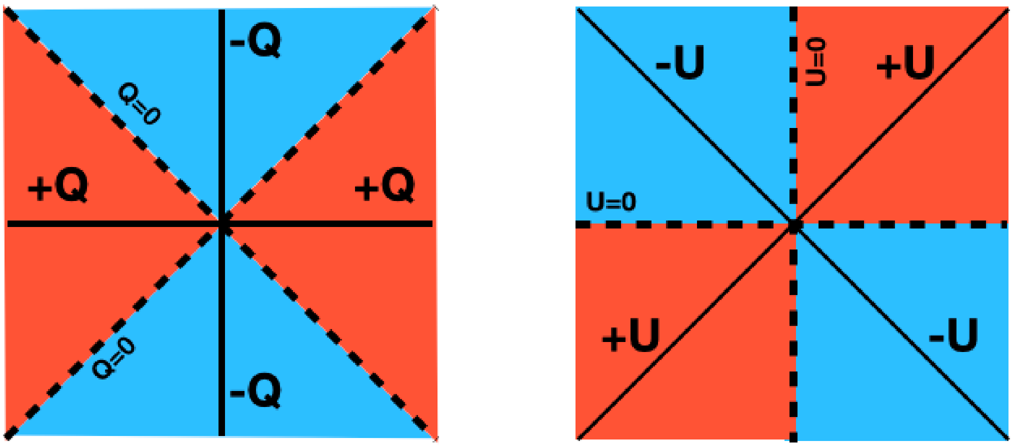

FIGURE 6.5: The signs of Stokes parameters taken in this chapter indicate the positive and negative regions in Q and U images.

6.3.2 Radiative transfer modeling of the LkCa 15 disk

In order to understand the dust grain properties and reproduce the observed morphology of our protoplanetary disk, we used the radiative transfer modeling code `RADMC-3D` (Dullemond et al. 2012) to model our protoplanetary disk. `RADMC-3D` is a software package written in Fortran 90, that can perform radiative transfer calculations for a given geometrical distribution of gas and dust in a system. `RADMC-3D` can produce scattered light, thermal, and polarimetric images at any position angle (posang) and inclination, which makes it easy to compare with the observational data. By integrating the fluxes from images at different wavelengths, it can also create a model spectral energy distribution (SED) for a given input combination. Since `RADMC-3D` uses the Monte Carlo method for photon scattering, it is computationally intensive. It takes around $\sim$ 30 sec to 2 minutes to create a model, depending on the resolution of the model. For the models presented in this chapter, it takes around one minute to generate each case.

6.3.2.1 Setting up the model

In order to model our protoplanetary disk using `RADMC-3D`, we need to specify the input parameters to match the observations. Some of the key parameters used by `RADMC-3D` are listed below:

- Disk geometry: It includes the disk shape and extent (*rin*, *rout*), size, gaps (*gap-rin*, *gap-rout*) and orientation (*inc*, *posang*).

- Surface density distribution: It includes how the surface density varies as a function of the radial distance of the disk (*plsig*).

- Pressure scale height: The pressure scale height (H_P) in a protoplanetary disk is a critical parameter representing how rapidly pressure decreases with vertical distance from the mid-plane of the disk. The ratio of H_P over radius at a reference radius (*hrpivot*), termed as *hrdisk* is also one of the key parameters in the `RADMC-3D` modeling.

- Flaring of disk: Many proto-planetary disks show flaring (*plh*), a phenomenon where the disk scale height changes with the radial distance. In `RADMC-3D` modeling, it is necessary to account for the flaring, if any.
- Dust grain properties: Protoplanetary disks are mainly composed of gas and dust grains, and it is necessary to specify parameters such as dust grain composition, grain sizes (*gs*), opacity, and other scattering properties in order to perform the radiative transfer calculations.

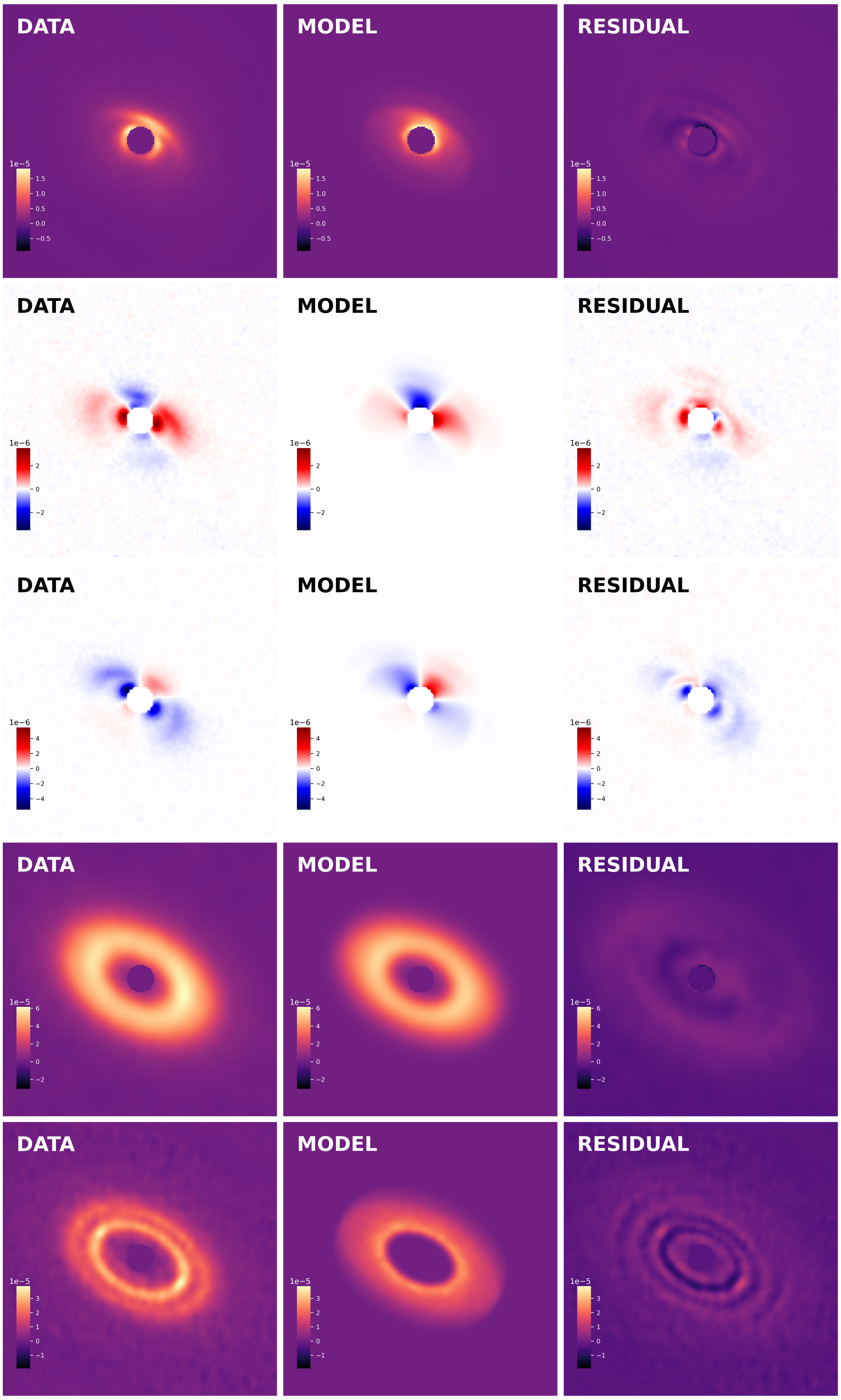

FIGURE 6.6: Comparison of `RADMC-3D` two-Zone model with Olivine grains and observed data. The sequence from left to right shows the data, the simulated model, and the residuals. The top row is the K-band total intensity image, followed by the K-band Stokes Q, and the Stokes U. The fourth and fifth rows at the bottom correspond to ALMA 870 μm and 1300 μm images, respectively.

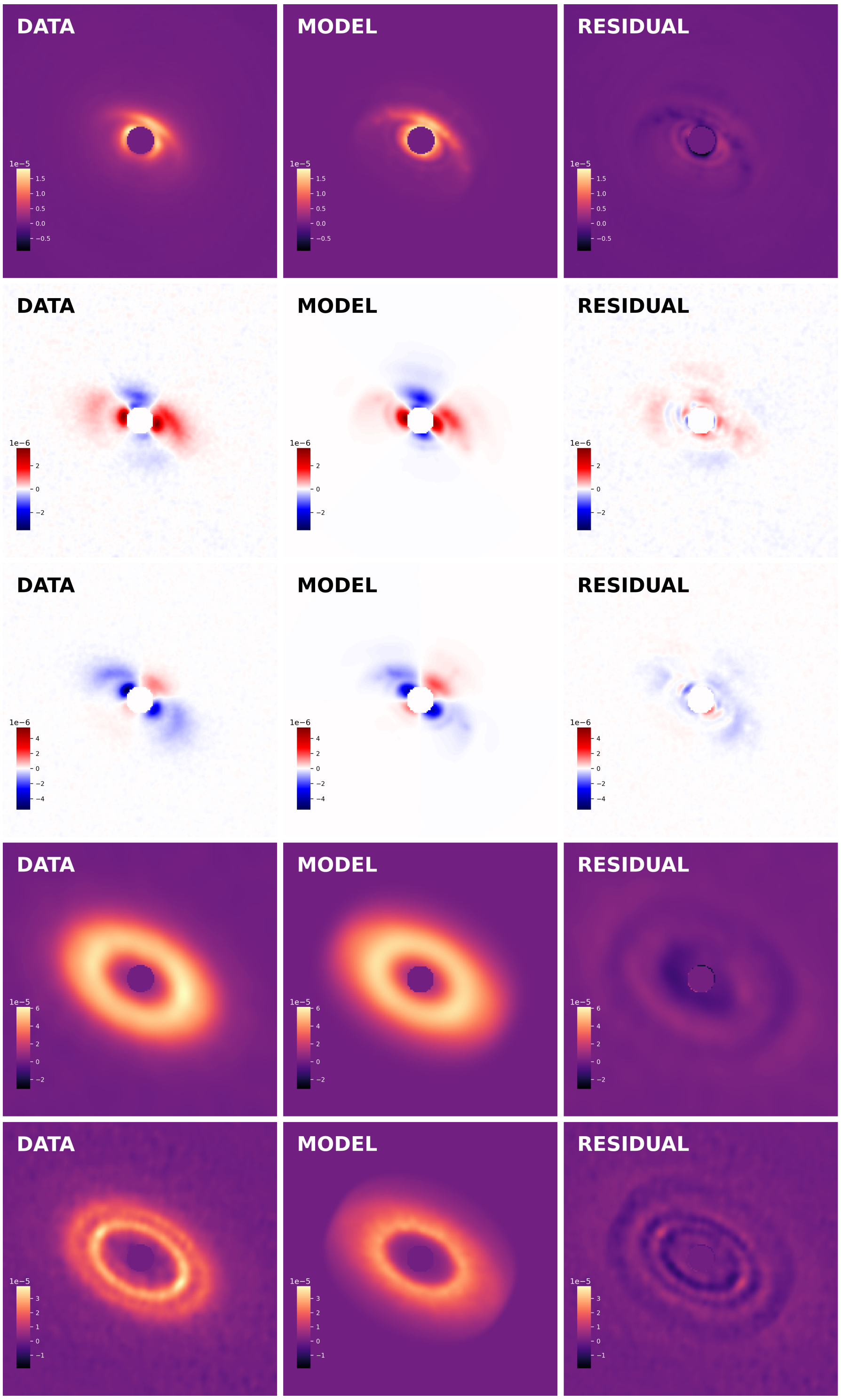

FIGURE 6.7: Comparison of data and the three-zone model with Olivine grains. From left to right columns: actual data, model simulation, and residuals. Top to bottom rows: K-band total intensity, K-band Stokes Q, Stokes U, and ALMA 870 μm and 1300 μm images

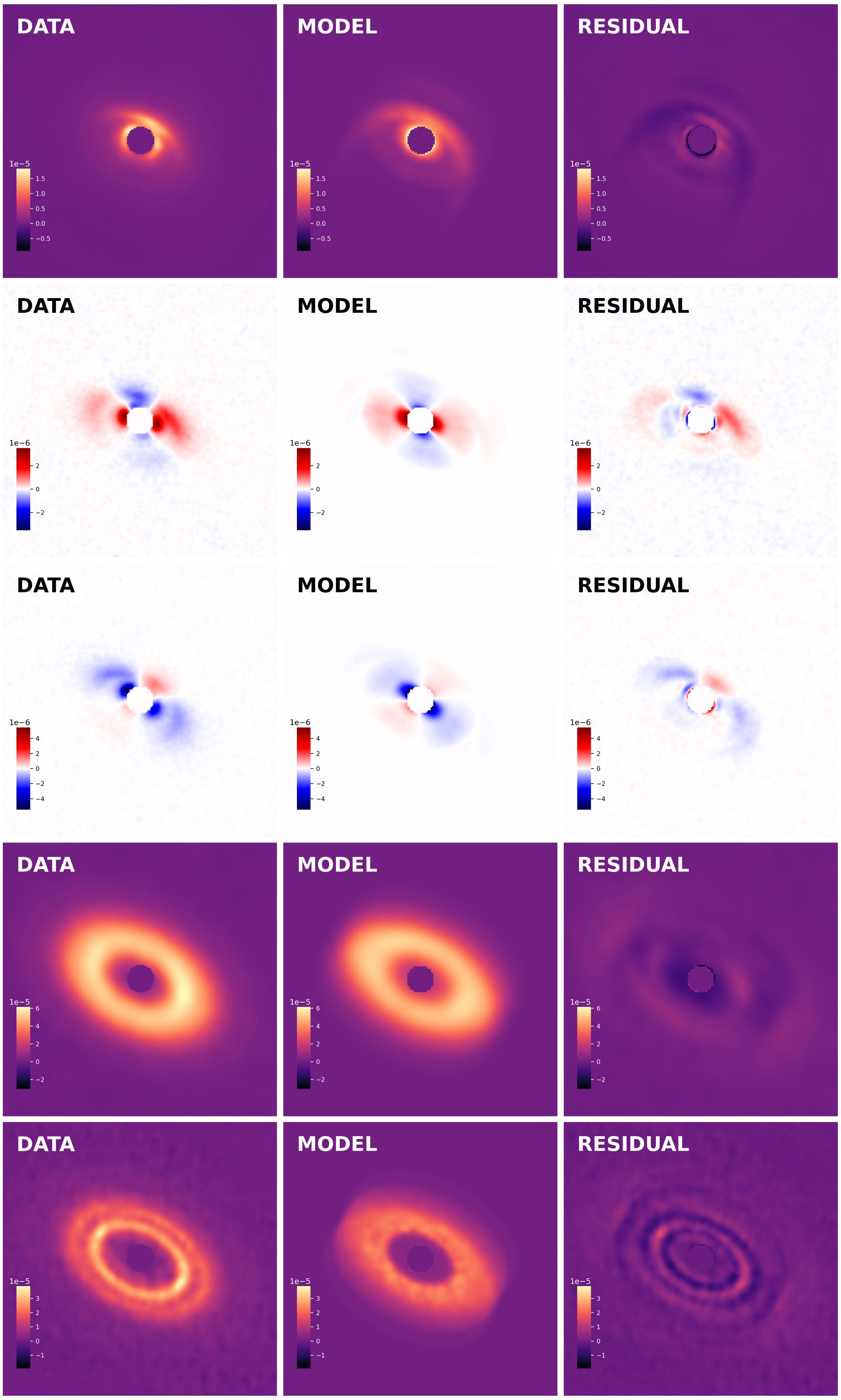

FIGURE 6.8: Comparison of data and the three-zone model similar to Figure 6.7 but with Pyroxene grains.

6.3.2.2 The polarimetric images

`RADMC-3D` offers the capability to generate polarimetric images (Stokes: I, Q, U) along with intensity images. Our polarimetric images for LkCa 15 obtained from IRDIS SPHERE are processed using `IRDAP` pipeline (van Holstein et al. 2020). Because the axes used to define the components of the electric field vectors are arbitrary, the appearance of the Q and U images also varies depending on the chosen convention. To make the images obtained from `IRDAP` and `RADMC-3D` consistent with each other, for both images we define the axis of E-field relative to the North as shown in Figure 6.4. The positive Q (+Q) is oriented along the X-direction, whereas the negative Q (-Q) is aligned along the Y-direction. As a photon is emitted from the star, by definition in an electromagnetic wave, the component of the electric field along its direction of motion is zero, resulting in the presence of only the two orthogonal components. If a photon hits the particle from the E$_y$ direction, then after scattering only the E$_x$ will survive as there can be no contribution from the component that is towards the line of sight of the observer. Similarly, if the photon hits the particle from the E$_x$ direction, then only E$_y$ will survive. At intermediate angles, both E$_x$ and E$_y$ components contribute, with Q>0 if E$_x$¿E$_y$, and Q<0 if E$_x$¡E$_y$. For an inclined disk, the orientations of the E$_x$ and E$_y$ components vary, resulting in uneven positive regions (red) in the east-west direction and negative regions (blue) in the north-south direction. Similar to the Q images, the U images also exhibit positive and negative regions, which are represented in a similar manner as illustrated in Figure 6.5. Since the orientation of the +Q and -Q is arbitrary, different models and reduction tools may use different directions to represent +Q and -Q. Therefore, it is necessary to apply a suitable corrections before comparing the images. For example, the orientation of the images obtained from `IRDAP` pipeline and `RADMC-3D` has an offset of +90^o clockwise, and thus a proper alignment is necessary before comparison. The second row in Figure 6.6, 6.7 and 6.8 shows both the observed and modeled polarimetric images for the LkCa 15. We find that the orientation of the positive and negative regions of the

Q and U image and the model (after applying the offset correction) are correct though there is a considerable residual for both cases. The detailed description of how these models are created is given in section 6.3.2.5 and section 6.3.2.6.

6.3.2.3 Converting the images to Jansky

Images obtained using IRDIS are initially in Analog-to-Digital Units (ADU). It is necessary to convert ADU to flux density in Jansky (Jy) as `RADMC-3D` image units are in Jy. For the conversion, we need the flux density of LkCa 15 in Jy which is obtained from its K-band magnitude, and also the total flux of the LkCa 15 which is obtained using aperture photometry from the non-coro flux frames taken for LkCa 15. Let's assign the flux density of LkCa 15 to be F_{flux}, which is known to be 0.369 Jy. If we acquire images with a certain flux (f_{flux}) in ADU, we need to convert it to Jy as our model images which are generated using `RADMC-3D` are in Jy. This conversion is facilitated by a Conversion Factor (CF), which is expressed in units of Jy/ADU. The CF essentially translates the flux values from ADU into the standard Jy unit as,

$$CF = \frac{F_{\text{flux}}}{\text{CPS}_{flux}}$$

where CPS_{flux} represents the effective counts per second in ADU for the images. Given that a neutral density filter (NDF) and a filter bandwidth (fw) are used, and for an exposure time of t_{expsci}, the effective CPS can be expressed as,

$$\text{CPS}_{flux} = \frac{f_{flux}}{\text{t}_{expflux}} \times \frac{\text{NDF}}{\text{fw}}$$

As our science frames are taken with coronagraphs, to convert the protoplanetary disk image from ADU to Jy, we first calculate the effective counts per second for our protoplanetary disk image (CPS_{pp}) by taking into account for the Nd filter and its bandwidth, similar to CPS_{flux}. Thus, the conversion of our protoplanetary disk image from ADU per second to Jy can be given by:

$$\text{Flux Density} = \text{ADU per second } \times CF$$

6.3.2.4 Calculations of $\overline{\chi}_R^2$

To obtain the best-fit solution, we need to compute the mean of the reduced chi-square ($\overline{\chi}_R^2$) for our images. The ($\overline{\chi}_R^2$) in turn consists of both the mean image reduced chi-square ($\overline{\chi}_{R,Img}^2$) and the mean flux chi-square ($\overline{\chi}_f^2$) which can also be expressed as,

$$\overline{\chi}_R^2 = \overline{\chi}_{R,Img}^2 + \overline{\chi}_f^2 \tag{6.1}$$

To calculate $\overline{\chi}_{R,Img}^2$, we first calculate the image chi-square (χ_{Img}^2) in the region (rgn) from 10 to 75 pixels, considering the pixels with counts above 2 times the standard deviation in the background region (2σ). The σ is determined by calculating the robust sigma in the background region between 75 to 100 pixels. Thus the χ_{Img}^2 is given as,

$$\chi_{Img}^2 = \sum \frac{(data - model)^2}{\sigma^2} * \frac{nsig}{tp} \tag{6.2}$$

where, the $nsig$ is the number of effective data-points in the rgn. The $nsig$ is obtained by dividing the total number of pixels in the rgn with counts greater than $2\sigma_{data}$ by the resolution area of each pixel and tp is the total number of pixels in the rgn. Thus, to get the $\chi_{R,Img}^2$, we need to divide χ_{Img}^2 by $nsig$ for all our images as given by,

$$\chi_{R,Img}^2 = \frac{1}{nsig} * \chi_{Img}^2 \tag{6.3}$$

In order to account for the flux mismatch between the science and model images, we also need to consider the χ^2_f for each of the images. We computed the χ^2_f using,

$$\chi^2_f = \left(\frac{f_{data} - f_{model}}{0.5 * f_{data}}\right)^2 \tag{6.4}$$

where the uncertainties in science fluxes are taken to be around 50%. Since the polarimetric images contain both positive and negative fluxes, we needed to use the absolute values of the fluxes to calculate the χ^2_f for the Q and U images. Thus our final chi-square ($\overline{\chi^2_R}$) which we used for the minimization can be expanded as,

$$\begin{aligned}\overline{\chi^2_R} = (&\chi^2_{R,I} + \chi^2_{R,Q} + \chi^2_{R,U} + \chi^2_{R,880} + \chi^2_{R,1300} \\ &+\chi^2_{f,I} + \chi^2_{f,Q} + \chi^2_{f,U} + \chi^2_{f,880} + \chi^2_{f,1300})/10\end{aligned} \tag{6.5}$$

where the subscript R and f represent the reduced and flux chi-squares and the I, Q, U, 880, and 1300 represent the I, Q, and U images in the K_s-band, while 880 and 1300 represent the ALMA images in 880μm and 1300μm.

To obtain the best-fit model, we begin with the initial parameters from the literature (Jin et al. 2019; Swastik et al. 2021) and used the *Nelder-Mead* minimization algorithm from the Scipy.optimise[‡] Python package, minimizing the $\overline{\chi^2_R}$ calculated in equation 6.5 to derive the optimal solution for our data. Due to the computational demands of the minimization search process in `RADMC-3D`, it takes approximately 8 hours to complete approximately 500 iterations, making it impractical to find an exact best-fit solution for the data within these constraints. Instead, the solution obtained after 10000 iterations represents the closest approximation achievable.

[‡] https://docs.scipy.org/doc/scipy/reference/generated/scipy.optimize.minimize.html

6.3.2.5 Two-zone disk

To model the proto-planetary disk in scattered light and sub-millimeter wavelengths, we initially used two-grain sizes, with micron-sized grains and sub-millimeter grains. In ALMA observations, the disk appeared mainly two-dimensional (2D), while in the NIR, it exhibited a flared and three-dimensional (3D) structure. ALMA observations mainly probe the large grains that are expected to settle vertically in the disk mid-plane and produce almost all of the thermal emissions. On the other hand, in the NIR, micron-sized grains are needed to reproduce the observed scattering features such as flaring. Therefore, at least two-grain species are necessary to model the protoplanetary disk accurately. For the two-zone model, the flared zone consisted of micron-sized particles ($\sim 1\ \mu$m), while the 2D flat zone consisted of millimeter ($\sim$ 1 mm) sized grains. Additionally, from the SPHERE and ALMA images, we can infer the radial segregation of the micron and millimeter-sized grains. The micron-sized grains were found to be closer to the star (within $\sim$ 50 au), while the millimeter-sized grains were located farther from the host star (beyond $\sim$ 50 au). This kind of segregation can happen due to the radial drift process occurring within the disk which we will discuss in section 6.5.

As discussed in section 6.2, we are modeling the LkCa 15 proto-planetary disk in K_s-band (2.2 μm), I, Q, and U images observed using SPHERE and the 880 μm and 1300 μm images observed using ALMA. We are using the chi-square (χ^2) minimization technique to find the best-fit solutions for our images. The mean of the reduced chi-square ($\overline{\chi}^2_R$) consists of both the image chi-square ($\overline{\chi}^2_{R,Img}$) and the flux chi-square ($\overline{\chi}^2_f$). For the calculation of the $\overline{\chi}^2_{R,Img}$ we only cared about the matching the structure and morphology of the protoplanetary disk. We don't want the $\overline{\chi}^2_R$ to be influenced by the image and model fluxes as the flux uncertainties are much higher due to the absolute photometric calibration uncertainties. The model images are artificially scaled to the observed images by minimising the rms in a given region from 10 pixels to 75 pixels. Since, for the $\overline{\chi}^2_{R,Img}$, the penalty for flux mismatch is not taken into account, we need an additional flux chi-square ($\overline{\chi}_f^2$) which accounts for the flux mismatch between the data and the image. For the initial analysis, we used the $\overline{\chi}_{R,Img}^2$ to search for a good fit as $\overline{\chi}_{R,Img}^2$ takes a shorter path towards an optimal model solution. On the other hand, if we used the ($\overline{\chi}_R^2$), it would take much longer to reach the optimal solution as the algorithm would put equal weight to minimizing both the flux and image simultaneously. The details of the calculation of $\overline{\chi}_R^2$, $\overline{\chi}_{R,Img}^2$ and $\overline{\chi}_f^2$ as well as the minimization procedure are presented in section 6.3.2.4. We find that the fluxes for the K_s-band images are not well constrained for all I, Q, and U images, while for the ALMA images, the fluxes are well-constrained within ~ 10 %.

Our best-fit model, as shown in Figure 6.6, consists of micron-sized grains spanning from 23.5 au to 80 au. Conversely, the sub-millimeter disk begins slightly far from the host star, ranging from 28.5 au to 93 au. Based on prior chemical analysis of protoplanetary disks from Dorschner et al. (1995), we chose the primary composition of the grains in both disks as Olivine, with a composition of 50% iron (Fe) and 50% magnesium (Mg). Table 6.3 presents the best-fit model parameters with two-grain zones. Our models can reproduce some of the main observed features, mainly the disk geometry as seen in LkCa 15. An in-depth examination of Figure 6.6, particularly focusing on the residuals column, reveals several inadequacies in the modeling of crucial disk morphology. Notably, in the K_s-band total intensity image, the inner disk as seen in the model is less forward scattered compared to observed images, resulting in a discernible negative region in the residual map. Likewise, in the polarimetric image, the positive and negative regions overlap in the science and model images. We find that the backward scattering seen in polarimetric data is much less than in our models. Backward scattering (like typical reflection) occurs when light is reflected in a direction roughly opposite to its original path. The micron-sized grains in the model mainly forward scatter so they cannot create sufficient backward scattering for the polarimetric image models. For the ALMA images, our model is successful in reproducing the 880 μm images,

Table 6.3: The best-fit parameters for the two-zone models using Olivine grains.

Parameters	Values
inc [deg]	-47.76
posang [deg]	61.47
Inner zone	
gs [in μm]	16
M_{dust} [$M_{\odot}$]	0.036
R_{in} [au]	23.5
R_{out} [au]	80.17
plh	0.96
$hrdisk^{a}$	0.05
plsig	0.52
Outer zone	
gs [in μm]	2280
M_{dust} [$M_{\odot}$]	0.15
R_{in} [au]	28.23
R_{out} [au]	94.89
plh	1.11
$hrdisk^{a}$	0.08
plsig	-0.49

Note: [a] hrpivot = 50 au

but only the inner ring of the disk could be modeled for the 1300 μm images. The ALMA images are 2D, with distinct inner and outer rings. To compensate for having only a single ring, our models were made to portray a flared appearance, using a simple power law. It delineates the inner ring with a pronounced surface density distribution (*plsig*) in a small and nearly consistent scale height, forming a bright inner edge and a gap. On the other hand, the outer rim is produced by the abrupt pivot of the disk angle due to high flaring.

To improve our two-zone model, we explored the role of composition of the dust grains. This is important because the way the grains scatter light, particularly in micron and sub-micron regions, depends on their chemical composition and albedo. The albedo of the grains affects the overall brightness and reflectivity in the NIR spectrum and can lead to discrepancies in the observed versus modeled flux, particularly in the NIR range. Additionally, a flux mismatch in the sub-millimeter range might occur due to the model's inability to accurately represent the thermal emission properties of the dust grains. Other than Olivine, we also modeled our protoplanetary disk using Pyroxene grains (made up of 30% Fe and 70% Mg). However, the Pyroxene grains produced significant residuals in the polarimetric images and did not produce sufficient backscatter. Though it is important to note that the exact composition of the protoplanetary disk is difficult to determine from SPHERE and ALMA images alone, it appears that the protoplanetary disk is Fe-rich, which is also consistent with the high Fe-rich composition of the host star (Swastik et al. 2021). Interestingly, when we examined the sub-millimeter models, changing the grain composition did not significantly affect the results. The grain size compensated the thermal emission needed to produce the models and thus we were able to obtain good models for both Olivine and Pyroxene grains. While our two-disk model successfully accounted for certain observed features such as inclination and position angle, it fell short of reproducing most of the observed disk morphologies. To address key discrepancies, such as the underrepresented forward and back-scattering produced in our models and flux mismatch, we used an additional zone comprising submicron-sized grains in order to match our models with observations.

6.3.2.6 Three-zone disk

Although the two-zone disk model seems visually adequate, there are still features that are missing in the two-disk zone model. In order to improve our model,

Table 6.4: The best-fit parameters for the three-zone models using Olivine grains.

Parameters	Values
inc [deg]	-47.5
posang [deg]	61.5
Inner zone	
gs [in μm]	0.15
M_{dust} [M$_\odot$]	0.06
R_{in} [au]	21
R_{out} [au]	52
plh	0.34
hrdisk[a]	0.02
plsig	3.06
Middle zone	
gs [in μm]	10
M_{dust} [M$_\odot$]	0.0008
R_{in} [au]	26
R_{out} [au]	90
plh	2.90
hrdisk[a]	0.06
plsig	0.61
Outer zone	
gs [in μm]	1200
M_{dust} [M$_\odot$]	0.15
R_{in} [au]	46
R_{out} [au]	131
plh	3.70
hrdisk[a]	0.005
plsig	-0.97

Note: [a] hrpivot = 50 au

Table 6.5: The best-fit parameters for the three-zone models using Pyroxene grains.

Parameters	Values
inc [deg]	-47.56
$posang$ [deg]	61.67
Inner zone	
gs [in μm]	0.1
M_{dust} [M$_\odot$]	0.16
R_{in} [au]	9.5
R_{out} [au]	82
plh	0.28
$hrdisk^a$ [hs]	0.025
$plsig$	1.25
Middle zone	
gs [in μm]	18
M_{dust} [M$_\odot$]	0.0003
R_{in} [au]	27
R_{out} [au]	98
plh	3.9667
$hrdisk^a$	0.08
$plsig$	3.79
Outer zone	
gs [in μm]	1489
M_{dust} [M$_\odot$]	0.13
R_{in} [au]	46
R_{out} [au]	127
plh	4.14
$hrdisk^a$	0.004
$plsig$	-1.82

Note: ^{a} hrpivot = 50 au

particularly in the inner part of the disk in the scattered light, we decided to introduce an additional zone consisting of submicron-sized grains ($\sim 0.1\ \mu$m) in the inner regions of the protoplanetary disk, closer to the central star. After the addition of an inner zone, our revised model now encompasses three distinct zones within the disk, each characterized by grains of different sizes. Similar to the two disk zone model, we used Olivine grains to model our disk. Our best-fit model solution obtained using the Nelder-Mead minimization algorithm includes an inner zone with submicron-sized grains from 21 au to 52 au, an intermediate zone consisting of micron-sized grains from 26 au to 90 au, and an outer zone consisting of millimeter-sized grains from 46 au to 131 au. The obtained best-fit solution using the three-zone model is illustrated in Figure 6.7 and the parameters are listed in Table 6.5.

A closer look at the residual column in Figure 6.7 reveals that with the addition of the submicron zone, our three-zone model incorporates a significant portion of the observed morphologies of LkCa 15. Despite these, some discrepancies between the models and observations persist. For example, in the K_s-band total intensity images, the forward scattering observed in the data is somewhat less pronounced than in the model. We also used Pyroxene grains to see if there are any substantial improvements in this regard, but we found that the forward scattering is even less for Pyroxene grains. The degree of forward scattering in total-intensity images increases with the number of micron-sized grains (~ 1 to $2\ \mu$m); however, the relative forward scattering decreases as the sub-micron-sized grains increases ($\leq 0.5\ \mu$m). Thus, to increase the forward scattering one may increase the micron-sized grains but that makes the back-scattering insufficient. Several factors could account for these discrepancies. First, the grain size distribution in our model, which comprises a sub-micron and a micron component, may not fully capture the range of sizes present in the actual disk. Second, differences in grain composition and shape between the model and the real disk can lead to different scattering behaviors. For instance, the scattering efficiency changes notably when the size of the grains is close to the wavelength of observation, possibly leading to Mie scattering phenomena. Third, disk properties such as geometry and optical depth could further contribute to the difference in forward scattering between the model and observations. In particular, the real disk's potentially complex geometry and optical depth could induce multiple scattering events that amplify forward scattering.

In the polarimetric Q and U images, our observational data suggest a modest level of backscattering in both the inner and outer regions of the disk, separated by a gap. However, both our Olivine and Pyroxene grain models, exhibit more backscattering in the disk's inner regions and relatively little backscattering in the outer regions. This discrepancy may be partly attributed to the grain size distribution used in our model. In our model, an under-representation of these smaller grains in the outer disk regions could explain the lack of observed backscattering. However, similar to the total intensity images, an increase in sub-micron grains would decrease the forward scattering phenomenon that is seen in total intensity images. Additionally, other structural features like the observed gap and variations in disk density could also be influencing the scattering behavior, but to a much lesser extent.

Our protoplanetary disk model, both in total intensity and polarimetric images, shows more flaring than the observed data. This is because the model is unable to simultaneously fit for forward scattering (for total intensity images) and backscattering (for polarimetric images) in the observed data. To compensate for the forward scattering, the model produces a disk that is slightly more flared in the models than in the data. This flaring is also due to the *plsig* (related to the surface density distribution) which falls off steeply in the disk. Additionally, the optical thickness of the disk in our model is also affecting the detectibility of the flaring. A higher optical thickness enhances the scattering effects, particularly for sub-micron grains, thereby exaggerating the flaring in both total intensity and

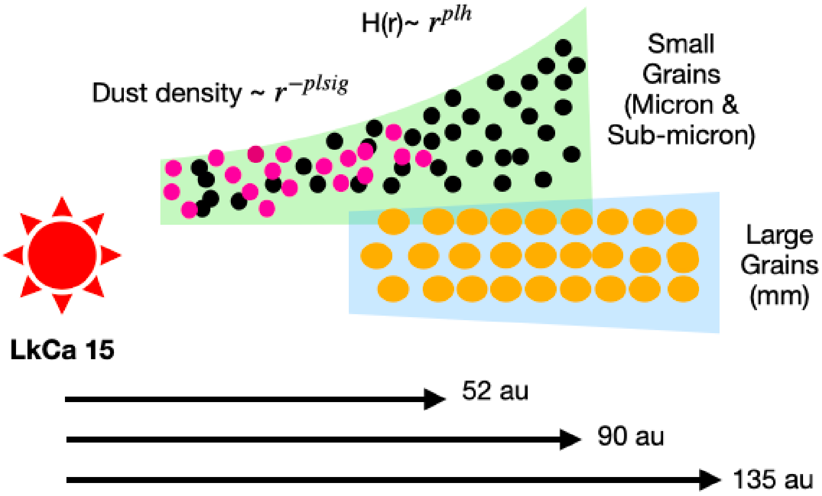

Figure 6.9: Schematic diagram of our LkCa 15 protoplanetary disk with Olivine grains. The purple, black and orange represents the sub-micron, micron and millimeter sized grains.

polarimetric model images. A more detailed model considering variations in optical thickness along with a different grain size distribution might provide a more accurate representation of the observed features.

The ALMA images appear to be 2D with inner and outer rings. In order to replicate this, the model images are forced to be flared. The model uses a simple power law to simulate the disk's structure. It forms the inner ring with a steep surface density distribution ($plsig$) over a small, consistent scale height, resulting in a bright inner rim and a gap. The outer rim is shaped by a sudden pivot in the disk angle due to a high flaring. However, the ALMA images suggest the disk's internal structure is not continuous, hinting at a gap possibly caused by a planetary body, an exo-Kuiper belt, or a planetesimal belt. This leads to the model inaccurately representing the outer ring. Adding another ring might make small improvement, though only at the cost of increasing the number of parameters.

In the K_s-band images, the disk is optically thick as seen in observed dataset and the model. In the Near-Infrared (NIR), the scattering is mainly dominated by the micron and submicron-sized grains, and these smaller grains substantially increase the disk's overall surface area with very little disk mass, leading to optical thickness. Consequently, in the NIR images, the disk's far side remains obscured, imparting a more three-dimensional appearance rather than a transparent one. Conversely, our ALMA images are dominated by thermal emission due to larger millimeter-grain sizes. The larger grains, although contributing more to the disk's total mass when compared to micron grains, are fewer in number, and thus the effective scattering surface is smaller, which results in an optically thin disk. This allows us to look through the disk, rendering a 2-D appearance, especially evident in the 1300 μm image. Overall, our model is fairly consistent with the optical thickness of images in K_s-Band and are also optically thin the ALMA images as seen in the observational data. A rough sketch of the LkCa protoplanetary disk model with three zones using Olivine grains is shown in Figure 6.9.

Additionally, it is crucial to address the issue of parameter degeneracy in our model, particularly the pressure scale height ($hrdisk$), the flaring index (plh), and the surface density distribution ($plsig$). These parameters are not independent and modifications to one often change the best-fit solutions. For example, in our ALMA images an increase in $hrdisk$ can be balanced by either a reduction in plh or an increase in $plsig$, resulting in comparable disk morphologies. Likewise, changes in plh and $plsig$ can be mutually adjusted to achieve similar disk structures. Such degeneracies pose a challenge in isolating the distinct impact of each parameter. Nevertheless, despite these overlapping parameters, our model successfully constrains the key parameters such as the disk's mass and overall geometry.

6.3.3 Companion detection limit

For the LkCa 15, we didn't detect any planets either in the total intensity or inverted polarimetric images. Detecting planets is challenging especially when the

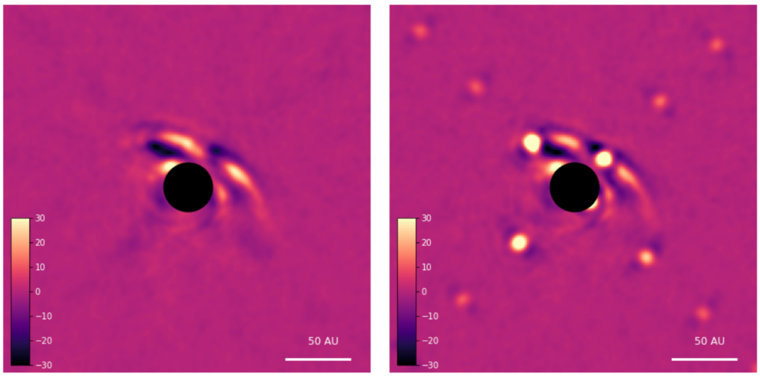

Figure 6.10: **Left:** IRDIS K-band reduction with `LOCI` algorithm after removing most of the disk in order to detect obscured planets. **Right:** IRDIS K-band reduction to recover simulated planets and to estimate the contrast limit

protoplanetary disk is very bright as in the case of LkCa 15. Nonetheless, we try in this section to detect planets that might be hidden in the disk by removing the disk. This involved creating a median-smoothed version of the disk using an 8-pixel box size, which we then subtracted from the original image along with the reference star PSF, as detailed in Section 6.2. Although we successfully suppressed a significant part of the disk, some residuals could still be seen as evident in Figure 6.10. Despite this partial removal, no new planet was detected.

In spite of the visual non-detection of planets, we could place an upper mass limit for any unseen planets in the disk using the 5σ contrast curve derived from the disk-removed image as shown in Figure 6.10. The 5σ contrast estimates were obtained by calculating the standard deviation within a 4-pixel moving box, using peak stellar fluxes measured from 2-second exposure flux images of LkCa 15. The contrast curve as a function of angular separation is shown in Figure6.11. Using `DUSTY` models and assuming the age of the system $\sim$ 1 Myrs (Swastik et al. 2021) we estimated the upper mass limits for the planets based on the contrast magnitude as shown on the right side of Y-axis of Figure 6.11. We can detect planets more massive than 2.5 M_J outside of $\sim$ 20 au and 1.5 M_J outside of 50 au. The deepest contrast is achieved from $\sim$ 200 au to 250 au where the detection limit is $\sim$ 1.36 M_J. However, the disk around LkCa 15 is very bright and the detection limit on

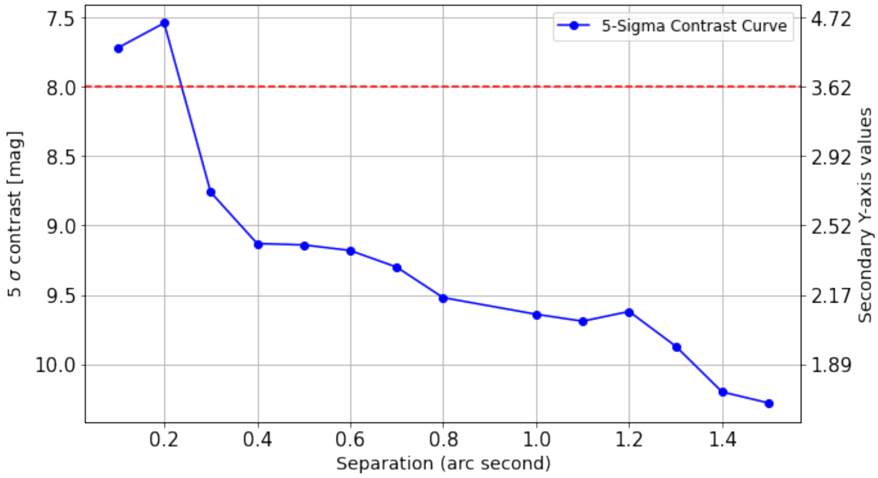

FIGURE 6.11: The 5σ contrast curve in K-band obtained by removing the LkCa 15 protoplanetary disk as shown in Figure 6.10. The blue dashed line represents the detection limit at the brightest part of the disks. The mass estimates for the companions were obtained using `DUSTY` models assuming the stellar age to be 1 Myrs for LkCa 15. See the text for more details.

the brightest part of the disk is around 3.62 M_J, and planets might be hidden where the disk emission is very strong. It's important to note the considerable uncertainty ($\sim$ 5 Myrs) in age estimates for such young systems, which in turn affects the reliability of mass limit calculations for companion detection. We also compared SCExAO/CHARIS contrast in K-band with the contrast obtained in this work. Cheetham et al. (2018) reported a contrast range of $\sim$ 5.75 to 6.15 mag within the inner regions of the disk ($\sim$18 AU), while noting a contrast ratio $\sim$ 10 in the outer regions. In fact, our observations yielded a higher contrast of $\sim$ 7.5 to 8 magnitudes in the inner regions and $\sim$ 10.5 in the outer regions.

6.4 Discussion

We have found a good model for our protoplanetary disk LkCa 15 which can simultaneously satisfy the total intensity, polarimetric, and sub-millimeter images. Our best-fit model encompasses three distinct regions with three distinct grain sizes. The smaller submicron-sized grains are mainly in the inner region of the disk (within ~ 50 au). The micron-sized grains extend from inner ~ 26 au till ~ 90 au, while the millimeter-sized grains mainly populate the outer part of the disk from ~ 46 au extending till ~ 131 au. Thus, the radial segregation of the grains is clearly evident for our proto-planetary disk which is quite unusual as larger grains are expected to lie closer to the central star (Birnstiel & Andrews 2014). This radial segregation of grain sizes in the disk could be attributed to several key mechanisms a) In the outer regions of our disk, where the temperature is low, the grain growth is much efficient as there is less kinetic energy, in contrast to the inner parts of the disk, b) the smaller, submicron-sized grains in the disk are more influenced by gas drag, migrating towards the central star (Taki et al. 2021), c) the segregation of small and large dust grains is significantly influenced by gas pressure gradients (de Juan Ovelar et al. 2012). These gradients arise from variations in the disk's gas density and temperature. Larger grains, being less coupled to the gas, drift towards regions of higher pressure where they get trapped. This occurs because, in high-pressure zones, the gas moves slower, causing a 'headwind' that reduces the grains' momentum and halts their inward drift. On the other hand, smaller grains, which are more tightly bound to the gas, continue to follow its motion without being significantly affected by these pressure variations. This differential behavior leads to the observed segregation, with larger grains accumulating in high-pressure areas, a key factor in planetesimal formation (Birnstiel et al. 2010; Meheut et al. 2012; Swastik et al. 2022).

The Dohnanyi (1969) model, a fundamental study of asteroidal and dust collisional evolution, proposes a specific distribution of particle sizes resulting from such processes. According to this model, when particles collide and break apart in a dynamically evolving system, such as a protoplanetary disk, they tend to follow a power-law distribution. This distribution is mathematically expressed as

$$\frac{dN}{da} = a^{\zeta} \tag{6.6}$$

where dN/da represents the number of particles per unit size interval, a is the particle size, and ζ is the power-law exponent. Dohnanyi found that, in an equilibrium state where collisional fragmentation and coagulation balance each other, ζ would be -3.5. For our optimal three-zone Olivine model, characterized by grain sizes of $0.15\,\mu$m, $10\,\mu$m, and $1200\,\mu$m, the calculated number ratio of grains, as derived from Equation 6.6, between zones 1 and 2 is approximately 3.6×10^4, and between zones 2 and 3, it is about 1.06×10^5. However, these computed ratios do not align with the actual number ratios in our computed models, which are roughly 495 for zones 1 and 2, and approximately 0.06 for zones 2 and 3, respectively. To reconcile these discrepancies and satisfy Equation 6.6, an adjustment of the ζ value is required. Specifically, ζ needs to be adjusted to -2.99 to correspond with the observed number ratio between zones 1 and 2. Similarly, for the calculated ratio between zones 2 and 3, ζ should be set to -1.95.

Our unusual estimated ζ could be attributed to several factors. The original model proposed by Dohnanyi (1969) might not fully apply to protoplanetary disks. Further, the material properties of asteroids, which are chosen to be 2-part stony (silicates and nickel) and one part iron while for our case we have taken it to be Olivine or Pyroxene, could significantly influence the collision outcomes and debris size distribution. However, A recent analysis of PDS 70 by Wahhaj et. al 2023 has also found similar results (zone1/zone2 $\sim$ -2.67 and zone2/zone3 $\sim$ -2.13) suggesting that our estimates of number ratios from total intensity, polarimetric, and sub-millimeter images might be a correct measurement for the power-law distribution seen for protoplanetary disk, as opposed to the -3.5 typically observed in debris disks. However, to substantiate our conclusions, it is necessary to extend this modeling and analysis to a broader range of protoplanetary disks.

While we successfully acquired an artefact-free image of LkCa 15, previous marginal detection of proto-planets within this system remains unconfirmed (Currie et al. 2019). This observation leads to a pivotal question: Are the planets hidden, or is the system too young or not massive enough for the formation of massive giant planets? The brightness of our disk also limits our detection capabilities in the disk-dominated regions as can be seen from the contrast curve in Figure 6.11. In comparison to systems like PDS 70, LkCa 15 is considerably younger, with an estimated age of approximately $1 - 2$ Myrs. Since both PDS 70 and LkCa 15 are pre-main sequence stars and have protoplanetary disks and are thus in a similar evolutionary stage, by assuming a mass accretion rate for LkCa 15 equal to that of PDS 70 (Wagner et al. 2018), ranges from $10^{-8} M_J/yr$ to $10^{-7} M_J/yr$, we infer that the maximum mass of a forming planet in this system would be around $0.2 M_J$. Although this method of estimating planetary mass is somewhat oversimplified, it suggests that planets within LkCa 15 could be in the early stages of formation and may still be too small to be detected by high-contrast imaging techniques.

6.5 Summary and Conclusions

In this work, we obtain K_s-band total intensity and polarimetric images of the LkCa 15 protoplanetary disk using the star-hopping RDI technique. Our observations capture the true disk intensities for the first time without any artefact that were present in previous observations mainly conducted using ADI. Our primary goal for this work was a) to detect new planets in the regions ($\sim$ 20-30 au) both using total-intensity images and fractional polarization maps and b) to understand the disk morphology and the probable composition of the disk. Using the radiative transfer modeling tool `RADMC-3D`, we attempted to model the total-intensity, polarimetric, and millimeter images in order to get a complete picture of the disk spanning from small sub-micron sized grains, all the way to large millimeter-sized grains. We were able to constrain most of the observed morphology for the protoplanetary disk. Here we summarise the key findings of this study,

- Initially, we used micron and millimeter-sized Olivine grains to model our protoplanetary disk. We were able to reasonably constrain the total intensity and sub-millimeter images.

- With an additional submicron-sized grain in the inner part of the disk, our model successfully incorporated all of the key observed morphology for the LkCa 15 protoplanetary disk with small residuals.

- Our best-fit model consists of submicron grains in the innermost zone spanning from 21 au to 52 au. The micron-sized grains span the disk from 26 au to 90 au followed by millimeter-sized grains from 46 au to 131 au.

- The LkCa 15 disk is considerably flared in the micron regime with a scale height of ∼6%. In the millimeter regime, we also find the disk to be flared with a very small scale height ∼2%.

- There may be a radial drift in the dust grains, with the small grains lying mainly in the inner 50 au of the disk, while the outer part of the disk is mainly composed of larger millimeter-sized grains. This can be because there is more thermal energy close to the star which hinders the formation of larger-sized grains.

- We find that the number ratio for small-to-micron, and micron-to-submicron-sized grains indicate a shallow grain-size index of -2.99 and -1.95, instead of -3.5 as expected from collisonal models. This indicates that our models are under-abundant in small-sized grains.

- We analyzed the inverted polarized intensity map but didn't find any discernible planetary signatures in the high SNR regions of the disk.

- We couldn't detect any planets in the total intensity images either. Despite not detecting new planets within the disk, we were able to estimate the upper mass limit for potential planets, finding that planets more massive than 1.36 M_J are unlikely to exist beyond 200 au, whereas the inner brighter disk regions may conceal planets up to 3.62 M_J.

In conclusion, our three-grain zone model can explain the observed morphology of the LkCa 15 protoplanetary disk. However, we acknowledge the non-uniqueness of these solutions, given the degenerate nature and interplay of various parameters such as flaring, surface density distribution, and pressure scale height. Furthermore, it is difficult to exactly determine the dust grain composition of these protoplanetary disks from imaging observations alone. Therefore, future endeavors should aim for spectroscopic observations, providing a more thorough understanding of grain composition.

It is also crucial to recognize the computational limitations present in the determination of the optimal solution. The long model computation times pose a challenge, confining us to the discovery of the best solution around serendipitous local minima, rather than the true global best-fit solution. Furthermore, accurate modeling and prediction of a protoplanetary disk morphology are impaired by large uncertainty in the knowledge of specific physical conditions. However, our study using a simple radiative transfer model is able to account for the main features observed in LkCa 15.

Chapter 7

Conclusion and Future Plans

7.1 Conclusion

My thesis has provided a comprehensive analysis of the metallicity, chemical composition, and age distribution of exoplanet-hosting stars and a detailed study of the LkCa 15 proto-planetary disk system. Using these, I investigated the host star's and the circumstellar environment's role in planet formation from nascent stages till its main sequence. Below, I summarise my thesis chapters,

Chapter 2: Spectroscopic analysis of host stars of directly imaged planets: This study analysed the high-resolution spectra of 22 young stars hosting planets detected by direct imaging. I used spectroscopic archival data from HARPS, FEROS, UVES, and HIRES. Using iSpec and combining it with the Bayesian Monte Calo Markov Chain technique (MCMC), I estimated the stellar atmospheric parameters and metallicity. My findings indicate that metal-rich stars host Jupiter-type planets ($M_P \leq 5\ M_J$), supporting the core accretion model of planet formation. While in the case of super-Jupiters ($M_P > 5\ M_J$), we see a more scattered distribution with no dependence on metallicity, suggesting gravitational instability is a likely formation mechanism.

Chapter 3: Galactic chemical evolution of exoplanet hosting stars: This study investigates the chemical compositions of 968 exoplanet hosts by analyzing the chemical abundance of 17 elements to understand their role in planet formation. I used data from HARPS-GTO, CKS, and CPS surveys. My key findings include a negative correlation between α-elements wrt Fe and planet mass, indicating stars with smaller planets are α-rich compared to those with giant planets. For Fe-peak elements, we don't see any such correlations. These results imply that systems with smaller planets formed earlier in the galaxy's history, while high-mass planetary systems formed later as α elements enriched the ISM at much earlier stages of the galaxy when compared with Fe-peak elements. Multi-planetary systems with both low and high-mass planets showed no specific trends, suggesting a younger age. Overall, the study connects planetary formation to the chemical evolution of the interstellar medium, indicating low-mass planets formed across various epochs, while giant planets formed around chemically enriched, younger stars.

Chapter 4: Kinematics age analysis of planet-hosting stars from GAIA DR3: This study uses GAIA DR3 data to study the chemical abundances, kinematics, and ages of stars hosting exoplanets. My key findings include that giant planet-hosting stars are typically metal-rich and α-poor, suggesting they belong to a younger population formed later in the galaxy's history after the Interstellar Medium (ISM) was enriched with Fe-peak elements. Most planet-hosting stars are part of the thin disk population, indicating a younger generation. The study also finds differences in galactic space velocities and orbital parameters between stars hosting small and Jupiter-like planets. Small planet-hosting stars exhibit higher Z_{max} and eccentricities, trends of older stars, compared to their giant planet-hosting counterparts. The findings support the idea that giant planets formed later in the context of the galactic chemical evolution (GCE) when the ISM had sufficient Fe-peak elements necessary for the core-accretion theory of planet formation.

Chapter 5: Age analysis of extra-solar planets from stellar isochrone models: In this study, the ages of over 2336 stars hosting exoplanets were estimated using isochrone fitting techniques, revealing a close relationship between the mass of exoplanets and their host stars. Despite model dependence and variations in individual age estimates, the findings consistently showed that most (70% to 85%) of planets orbit stars younger than 7 billion years, indicating that planet formation predominantly occurred after the ISM was sufficiently enriched. A notable age difference was observed between stars hosting small planets and those with giant planets, with the latter being significantly younger. This trend also supports the core-accretion theory of planet formation, suggesting that Jupiter-sized planets formed later in the galaxy's evolution. The study highlights that while small planets began forming around 6-7 Gyrs ago, the formation of giant planets is a more recent phenomenon, occurring predominantly in the last 4-5 Gyrs from now.

Chapter 7: Understanding planet formation in LkCa 15 proto-planetary disk: In this work, the LkCa 15 protoplanetary disk was imaged using Ks-band total intensity and polarimetric techniques, specifically the star-hopping RDI method, to overcome self-subtraction common in previous ADI observations. The study aimed to detect new planets and analyze the disk's morphology and composition. Using RADMC-3D modelling, I successfully replicated the disk's morphology with a mix of grain sizes, finding submicron grains in the inner zone (21-52 au), micron-sized grains (26-90 au), and millimetre-sized grains (46-131 au). The disk showed considerable flaring and radial distribution of dust grains, with smaller grains closer to the star and larger grains in the outer regions. Despite not detecting new planets, I am able to place upper mass limits for potential planets within the disk. The findings suggest a complex structure of the LkCa 15 disk, influenced by various factors like grain size distribution and disk flaring. However, the exact determination of dust composition and the disk's physical history remain challenging, highlighting the need for future spectroscopic studies.

In conclusion, this thesis represents a significant contribution to exoplanetary science. The combination of detailed spectroscopic, photometric, polarimetric, and kinematic analyses across multiple chapters has advanced our understanding of the complex interplay between host stars and the planets they host. The insights gained from this thesis are crucial for future studies in the field, particularly those focusing on the formation, evolution, and dynamics of exoplanetary systems.

7.2 Future Plans

My future research proposals aim to deepen our understanding of planetary formation and evolution by integrating observational data from state-of-the-art space missions with advanced theoretical modelling. The proposed studies will focus on the a) direct imaging of protoplanetary disks using JWST/SCALES-KECK/VLT-ERIS/VLT-SPHERE+/ALMA etc, b) studying the accretion rates and morphological features of these disks, c) Radiative transfer modelling of these disks to explain the observed morphology of these disks. Below I list some of my research ideas that I plan to work on in the future,

1. Unveiling the Dynamics of Protoplanetary Disks

I am excited to propose a research project to expand our understanding of protoplanetary disks using high contrast imaging (HCI) from the James Webb Space Telescope (JWST), ERIS, and SPHERE+. Below I discuss my tentative research plans,

- The central focus of my future research will be on analyzing the morphology and chemical composition of protoplanetary disks in young star-forming regions, such as Lupus and Ophiuchus, and also search for new planets using NIRCAM and MIRI. A critical aspect of the study involves focusing on specific planetary spectral features in the L (3-4 µm) and M (4-5 µm) bands, which indicate various chemical compositions and physical processes in these disks. Features associated with CO_2($\sim$ 4.3 µm), Hydrocarbons ($\sim$ 3.3 µm), Methane ($\sim$7 µm), water ice, or silicate dust, for instance, can provide valuable insights into the conditions and materials important for planet formation. The L and M bands are particularly adept at studying warm dust and gas close to stars, often obscured at other wavelengths, and can penetrate dust that obscures shorter wavelengths for a clearer view of the inner regions of protoplanetary disks. Unlike ground-based telescopes facing challenges in these bands due to atmospheric absorption and thermal emission, space-based observatories like JWST (using NIRCAM and MIRI) offer significant advantages. They can observe these wavelengths without atmospheric interference, giving clearer and more detailed images. Additionally, the contrast ratio in the L and M bands is more favorable for detecting young, warm planets that are still radiating heat from their formation process, making them relatively brighter in these bands.

- The NIRCAM is the most capable instrument to date for detecting the fainter objects where it reaches S/N $\sim$ 10 for point sources as faint as AB mag $\sim$ 28.9 in some wide filters and thus is ideal for detecting planets was not possible to detect before due to contrast limitations.

- The major challenge using JWST's NIRCAM and MIRI is the Inner working angle (IWA) which is quite large (0.23 to 0.88" for NIRCAM and 0.33 to 2.16" for MIRI) and thus only the outer disk/planets can be observed. In contrast, we can use ERIS/VLT to probe the inner regions of the disk and detect new planets, as it has a much smaller IWA than JWST. Further, ERIS/VLT can reach up to $\sim$ 9 mag at 0.9" for a 12-minute exposure time on an L=2.2 star.

Our objective is to achieve high-resolution and high-sensitivity imaging to detail the morphology of these disks, focusing on aspects such as disk mass, temperature profile, and grain size distributions. Based on these measurements, I will formulate specific hypotheses. For instance, certain morphological features, like gaps or spirals within the disks, may correlate with the presence of forming planets. Additionally, one can anticipate that variations in the chemical composition across different disk regions could indicate varying stages of planetesimal formation. These hypotheses will be tested against existing theories of planet formation and disk evolution, providing a critical assessment of current models of disk accretion and planet-disk interactions. Furthermore, my research aims to pose new questions that challenge existing paradigms, such as investigating if the chemical diversity observed in different disk regions can indicate the types of planets that will form.

2. Accretion Dynamics and its connection to the disk morphology

The accretion of material from the disks onto their central stars is a fundamental aspect that influences their evolution and eventual dispersal of the gas and dust in the disk. By analyzing accretion rates, we can gain significant insights into the lifetimes of these disks, the efficiency of planet formation, and the impact on the eventual architecture of the planetary system. Below I propose my research ideas that I plan to investigate in the future,

Hypothesis 1: Correlation between gap size in disks and accretion Rates

- Using high-resolution imaging (from VLT-SPHERE/JWST/VLT-ERIS/ALMA) and spectroscopy, I will analyze the gaps in various protoplanetary disks. The RADMC-3D radiative transfer modeling tool will be used to model the disk structures and compare them with observational data. This comparison will help in understanding how gap sizes correlate with accretion rates. Further, I will also investigate if the disk morphology is also related to the accretion rate, for instance, comparing the accretion rate for disks with and without planets.

Hypothesis 2: Relationship between gas content and accretion dynamics.

- Using spectroscopic observations to analyze CO emission lines, which serve as proxies for the overall gas content. The focus will be on high-resolution spectra from instruments like JWST-NIRSPEC/MIRI and ALMA. I will then implement chemical models of protoplanetary disks to understand the relationship between CO abundance and the overall gas mass. This will involve using chemical codes (for example, ProDiMo) that simulate the conditions in protoplanetary disks. Further, I will also examine the gas content and relate it to disk features like gaps, rings, and spirals, and their potential impact on accretion processes.

This future research trajectory is designed to enhance our understanding of planetary systems, offering vital insights into the processes that govern planet formation, evolution, and the fate of planetary systems. The interdisciplinary approach, blending observational data with theoretical models, resonates with the overarching vision of exploring fundamental questions about our universe and contributes to the broader field of astrophysics and exoplanetary science.

"Science is a way to call the bluff of those who only pretend to knowledge. It is a bulwark against mysticism, against superstition, against religion misapplied to where it has no business being."

- *Carl Sagan, The Demon-Haunted World: Science as a Candle in the Dark.*

Bibliography

Abdurro'uf et al., 2022, *Astrophys. J. Suppl.*, 259, 35

Adibekyan V., 2019, Geosciences, 9, 105

Adibekyan V. Z., Santos N. C., Sousa S. G., Israelian G., 2011, *Astron. Astrophys.*, 535, L11

Adibekyan V. Z., et al., 2012a, *Astron. Astrophys.*, 543, A89

Adibekyan V. Z., Sousa S. G., Santos N. C., Delgado Mena E., González Hernández J. I., Israelian G., Mayor M., Khachatryan G., 2012b, *Astron. Astrophys.*, 545, A32

Akeson R. L., et al., 2013, *Pub. Astron. Soc. Pac.*, 125, 989

Alibert Y., Mordasini C., Benz W., Winisdoerffer C., 2005, *Astron. Astrophys.*, 434, 343

Alibés A., Labay J., Canal R., 2001, *Astron. Astrophys.*, 370, 1103

Anders F., Chiappini C., Santiago B. X., Matijevič G., Queiroz A. B., Steinmetz M., Guiglion G., 2018, *Astron. Astrophys.*, 619, A125

Andreasen D. T., et al., 2017, *Astron. Astrophys.*, 600, A69

Andrews S. M., et al., 2016, *Astrophys. J. Lett.*, 820, L40

Andrews S. M., et al., 2018, *Astrophys. J. Lett.*, 869, L41

Arlandini C., Käppeler F., Wisshak K., Gallino R., Lugaro M., Busso M., Straniero O., 1999, *Astrophys. J.*, 525, 886

Armstrong D. J., Meru F., Bayliss D., Kennedy G. M., Veras D., 2019, *Astrophys. J. Lett.*, 880, L1

Asplund M., Grevesse N., Sauval A. J., Scott P., 2009, *Ann. Rev. Astron. Astrophys.*, 47, 481

Avenhaus H., et al., 2017, *Astron. J.*, 154, 33

Avenhaus H., et al., 2018, *Astrophys. J.*, 863, 44

Ayliffe B. A., Bate M. R., 2012, *Mon. Not. Roy. Astron. Soc.*, 427, 2597

Bae J., Zhu Z., Hartmann L., 2017, *Astrophys. J.*, 850, 201

Baillié K., Marques J., Piau L., 2019, *Astron. Astrophys.*, 624, A93

Banerjee B., Narang M., Manoj P., Henning T., Tyagi H., Surya A., Nayak P. K., Tripathi M., 2024, *Astron. J.*, 168, 7

Baraffe I., El Eid M. F., Prantzos N., 1992, *Astron. Astrophys.*, 258, 357

Baraffe I., Chabrier G., Barman T. S., Allard F., Hauschildt P. H., 2003, *Astron. Astrophys.*, 402, 701

Baraffe I., Chabrier G., Barman T., 2010, Reports on Progress in Physics, 73, 016901

Barker A. J., Ogilvie G. I., 2009, *Mon. Not. Roy. Astron. Soc.*, 395, 2268

Baron F., Lafrenière D., Artigau É., Gagné J., Rameau J., Delorme P., Naud M.-E., 2019, *Astron. J.*, 158, 187

Bashi D., Zucker S., 2022, *Mon. Not. Roy. Astron. Soc.*, 510, 3449

Batalha N. M., 2014, Proceedings of the National Academy of Science, 111, 12647

Battistini C., Bensby T., 2016, *Astron. Astrophys.*, 586, A49

Beaulieu J. P., et al., 2006, *Nature*, 439, 437

Bedell M., et al., 2018, *Astrophys. J.*, 865, 68

Bellinger E. P., Hekker S., Angelou G. C., Stokholm A., Basu S., 2019, *Astron. Astrophys.*, 622, A130

Benedict G. F., McArthur B. E., Nelan E. P., Harrison T. E., 2017, *Pub. Astron. Soc. Pac.*, 129, 012001

Benisty M., et al., 2021, *Astrophys. J. Lett.*, 916, L2

Bergemann M., Lind K., Collet R., Asplund M., 2011, in Journal of Physics Conference Series. p. 012002 (`arXiv:1109.2601`), doi:10.1088/1742-6596/328/1/012002

Berger T. A., Huber D., Gaidos E., van Saders J. L., 2018, *Astrophys. J.*, 866, 99

Berger T. A., Huber D., van Saders J. L., Gaidos E., Tayar J., Kraus A. L., 2020a, *Astron. J.*, 159, 280

Berger T. A., Huber D., Gaidos E., van Saders J. L., Weiss L. M., 2020b, *Astron. J.*, 160, 108

Bertran de Lis S., Delgado Mena E., Adibekyan V. Z., Santos N. C., Sousa S. G., 2015, *Astron. Astrophys.*, 576, A89

Beuzit J. L., et al., 2019, *Astron. Astrophys.*, 631, A155

Binney J., Merrifield M., Wegner G. A., 2000, American Journal of Physics, 68, 95

Birnstiel T., Andrews S. M., 2014, *Astrophys. J.*, 780, 153

Birnstiel T., Dullemond C. P., Brauer F., 2010, *Astron. Astrophys.*, 513, A79

Birnstiel T., Fang M., Johansen A., 2016, *Space Sci. Rev.*, 205, 41

Bisterzo S., Gallino R., Pignatari M., Pompeia L., Cunha K., Smith V., 2004, *Memorie della Societa Astronomica Italiana*, 75, 741

Bisterzo S., et al., 2016, Journal of Physics: Conference Series, 665, 012023

Blakely D., et al., 2022, *Astrophys. J.*, 931, 3

Blanco-Cuaresma S., 2019, *Mon. Not. Roy. Astron. Soc.*, 486, 2075

Blanco-Cuaresma S., Soubiran C., Jofré P., Heiter U., 2014a, *Astron. Astrophys.*, 566, A98

Blanco-Cuaresma S., Soubiran C., Heiter U., Jofré P., 2014b, *Astron. Astrophys.*, 569, A111

Bodenheimer P., Pollack J. B., 1986, , 67, 391

Bohn A. J., et al., 2020, *Astrophys. J. Lett.*, 898, L16

Bond I. A., et al., 2004, *Astrophys. J. Lett.*, 606, L155

Bonfanti A., Ortolani S., Piotto G., Nascimbeni V., 2015, *Astron. Astrophys.*, 575, A18

Bonfanti A., Ortolani S., Nascimbeni V., 2016, *Astron. Astrophys.*, 585, A5

Bonnefoy M., et al., 2016, *Astron. Astrophys.*, 587, A58

Borucki W. J., et al., 2011a, *Astrophys. J.*, 728, 117

Borucki W. J., et al., 2011b, *Astrophys. J.*, 736, 19

Boss A. P., 1997, Science, 276, 1836

Boss A. P., 2002, *Astrophys. J. Lett.*, 567, L149

Boss A. P., 2010, in Cunha K., Spite M., Barbuy B., eds, IAU Symposium Vol. 265, Chemical Abundances in the Universe: Connecting First Stars to Planets. pp 391–398, doi:10.1017/S1743921310001067

Bovy J., 2015, *Astrophys. J. Suppl.*, 216, 29

Bowler B. P., 2016, *Pub. Astron. Soc. Pac.*, 128, 102001

Bressan A., Marigo P., Girardi L., Salasnich B., Dal Cero C., Rubele S., Nanni A., 2012, *Mon. Not. Roy. Astron. Soc.*, 427, 127

Brewer J. M., Fischer D. A., 2018, *Astrophys. J. Suppl.*, 237, 38

Brewer J. M., Fischer D. A., Valenti J. A., Piskunov N., 2016, *Astrophys. J. Suppl.*, 225, 32

Brugamyer E., Dodson-Robinson S. E., Cochran W. D., Sneden C., 2011, The Astrophysical Journal, 738, 97

Bruntt H., et al., 2012, *Mon. Not. Roy. Astron. Soc.*, 423, 122

Buchhave L. A., et al., 2012, *Nature*, 486, 375

Buchhave L. A., et al., 2014, *Nature*, 509, 593

Buchhave L. A., Bitsch B., Johansen A., Latham D. W., Bizzarro M., Bieryla A., Kipping D. M., 2018, The Astrophysical Journal, 856, 37

Buder S., et al., 2019, *Astron. Astrophys.*, 624, A19

Buder S., et al., 2021, *Mon. Not. Roy. Astron. Soc.*, 506, 150

Burrows A., et al., 1997, The Astrophysical Journal, 491, 856

Butler R. P., Marcy G. W., 1996, *Astrophys. J. Lett.*, 464, L153

Butler R. P., Vogt S. S., Marcy G. W., Fischer D. A., Henry G. W., Apps K., 2000, *Astrophys. J.*, 545, 504

Butler R. P., Vogt S. S., Marcy G. W., Fischer D. A., Wright J. T., Henry G. W., Laughlin G., Lissauer J. J., 2004, *Astrophys. J.*, 617, 580

Cai K., Durisen R. H., Michael S., Boley A. C., Mejía A. C., Pickett M. K., D'Alessio P., 2006, *Astrophys. J. Lett.*, 636, L149

Calvet N., Gullbring E., 1998, *Astrophys. J.*, 509, 802

Carrera R., et al., 2019, *Astron. Astrophys.*, 623, A80

Casagrande L., Schönrich R., Asplund M., Cassisi S., Ramírez I., Meléndez J., Bensby T., Feltzing S., 2011, *Astron. Astrophys.*, 530, A138

Casassus S., Perez M. S., Jordán A., Ménard F., Cuadra J., Schreiber M. R., Hales A. S., Ercolano B., 2012, *Astrophys. J. Lett.*, 754, L31

Castelli F., Kurucz R. L., 2003, in Piskunov N., Weiss W. W., Gray D. F., eds, IAU Symposium Vol. 210, Modelling of Stellar Atmospheres. p. A20 (`arXiv:astro-ph/0405087`)

Charbonneau D., Brown T. M., Latham D. W., Mayor M., 2000, *Astrophys. J. Lett.*, 529, L45

Chauvin G., Lagrange A. M., Dumas C., Zuckerman B., Mouillet D., Song I., Beuzit J. L., Lowrance P., 2004, *Astron. Astrophys.*, 425, L29

Cheetham A., et al., 2018, *Astron. Astrophys.*, 615, A160

Chen C., 2003, Science in China A: Mathematics, 46, 1

Chen J., Kipping D., 2017, *Astrophys. J.*, 834, 17

Choi J., Dotter A., Conroy C., Cantiello M., Paxton B., Johnson B. D., 2016, *Astrophys. J.*, 823, 102

Christensen-Dalsgaard J., Aguirre V. S., 2018, in Deeg H. J., Belmonte J. A., eds, , Handbook of Exoplanets. p. 184, doi:10.1007/978-3-319-55333-7_184

Claudi R. U., et al., 2008, in McLean I. S., Casali M. M., eds, Society of Photo-Optical Instrumentation Engineers (SPIE) Conference Series Vol. 7014, Ground-based and Airborne Instrumentation for Astronomy II. p. 70143E, doi:10.1117/12.788366

Costa Silva A. R., Delgado Mena E., Tsantaki M., 2020, *Astron. Astrophys.*, 634, A136

Côté B., et al., 2018, *Astrophys. J.*, 855, 99

Cowan J. J., Sneden C., Lawler J. E., Aprahamian A., Wiescher M., Langanke K., Martínez-Pinedo G., Thielemann F.-K., 2021, Reviews of Modern Physics, 93, 015002

Cropper M., et al., 2018, *Astron. Astrophys.*, 616, A5

Cumming A., 2004, Monthly Notices of the Royal Astronomical Society, 354, 1165

Currie T., et al., 2019, *Astrophys. J. Lett.*, 877, L3

D'Angelo G., Lissauer J. J., 2018, Formation of Giant Planets. p. 140, doi:10.1007/978-3-319-55333-7˙140

Davies R., et al., 2018, in Evans C. J., Simard L., Takami H., eds, Society of Photo-Optical Instrumentation Engineers (SPIE) Conference Series Vol. 10702, Ground-based and Airborne Instrumentation for Astronomy VII. p. 1070209 (`arXiv:1807.05089`), doi:10.1117/12.2311480

Delgado Mena E., Tsantaki M., Adibekyan V. Z., Sousa S. G., Santos N. C., González Hernández J. I., Israelian G., 2017, *Astron. Astrophys.*, 606, A94

Delgado Mena E., et al., 2018, *Pub. Astron. Soc. Pac.*, 130, 094202

Delgado Mena E., et al., 2019, *Astron. Astrophys.*, 624, A78

Delgado Mena E., Adibekyan V., Santos N. C., Tsantaki M., González Hernández J. I., Sousa S. G., Bertrán de Lis S., 2021, arXiv e-prints, p. arXiv:2109.04844

Demarque P., Woo J.-H., Kim Y.-C., Yi S. K., 2004, *Astrophys. J. Suppl.*, 155, 667

Desrochers M.-E., Artigau É., Gagné J., Doyon R., Malo L., Faherty J. K., Lafrenière D., 2018, *Astrophys. J.*, 852, 55

Dipierro G., Price D., Laibe G., Hirsh K., Cerioli A., Lodato G., 2015, *Mon. Not. Roy. Astron. Soc.*, 453, L73

Dohlen K., et al., 2008, in McLean I. S., Casali M. M., eds, Society of Photo-Optical Instrumentation Engineers (SPIE) Conference Series Vol. 7014, Ground-based and Airborne Instrumentation for Astronomy II. p. 70143L, doi:10.1117/12.789786

Dohnanyi J. S., 1969, *J. Geophys. Res.*, 74, 2531

Dong R., Fung J., 2017, *Astrophys. J.*, 835, 146

Dong S., et al., 2014, *Astrophys. J. Lett.*, 789, L3

Dong R., Hall C., Rice K., Chiang E., 2015, *Astrophys. J. Lett.*, 812, L32

Dorschner J., Begemann B., Henning T., Jaeger C., Mutschke H., 1995, *Astron. Astrophys.*, 300, 503

Dotter A., Chaboyer B., Jevremović D., Kostov V., Baron E., Ferguson J. W., 2008, *Astrophys. J. Suppl.*, 178, 89

Draine B. T., 2003, *Astrophys. J.*, 598, 1017

Drazkowska J., et al., 2022, arXiv e-prints, p. arXiv:2203.09759

Drout M. R., et al., 2017, Science, 358, 1570

Dullemond C. P., Juhasz A., Pohl A., Sereshti F., Shetty R., Peters T., Commercon B., Flock M., 2012, RADMC-3D: A multi-purpose radiative transfer tool, Astrophysics Source Code Library, record ascl:1202.015 (ascl:1202.015)

Ecuvillon A., Israelian G., Santos N. C., Mayor M., Villar V., Bihain G., 2004, *Astron. Astrophys.*, 426, 619

Edvardsson B., Andersen J., Gustafsson B., Lambert D. L., Nissen P. E., Tomkin J., 1993, *Astron. Astrophys.*, 500, 391

Emsenhuber A., Mordasini C., Burn R., Alibert Y., Benz W., Asphaug E., 2021, *Astron. Astrophys.*, 656, A70

Erspamer D., North P., 2002, *Astron. Astrophys.*, 383, 227

Espaillat C., Calvet N., D'Alessio P., Hernández J., Qi C., Hartmann L., Furlan E., Watson D. M., 2007, *Astrophys. J. Lett.*, 670, L135

Espaillat C., Calvet N., Luhman K. L., Muzerolle J., D'Alessio P., 2008, *Astrophys. J. Lett.*, 682, L125

Everett M. E., Howell S. B., Silva D. R., Szkody P., 2013, *Astrophys. J.*, 771, 107

Fabian D., Henning T., Jäger C., Mutschke H., Dorschner J., Wehrhan O., 2001, *Astron. Astrophys.*, 378, 228

Facchini S., et al., 2020, *Astron. Astrophys.*, 639, A121

Feuillet D. K., et al., 2018, *Mon. Not. Roy. Astron. Soc.*, 477, 2326

Fischer D. A., Valenti J., 2005, *Astrophys. J.*, 622, 1102

Fischer D. A., et al., 2002, *Astrophys. J.*, 564, 1010

Fischer D. A., Howard A. W., Laughlin G. P., Macintosh B., Mahadevan S., Sahlmann J., Yee J. C., 2014, in Beuther H., Klessen R. S., Dullemond C. P., Henning T., eds, Protostars and Planets VI. p. 715 (`arXiv:1505.06869`), doi:10.2458/azu˙uapress˙9780816531240-ch031

Fleming S. W., et al., 2015, *Astron. J.*, 149, 143

Frebel A., 2018, Annual Review of Nuclear and Particle Science, 68, 237

Fulton B. J., Petigura E. A., 2018, *Astron. J.*, 156, 264

Fulton B. J., et al., 2017, *Astron. J.*, 154, 109

Fulton B. J., et al., 2021, *Astrophys. J. Suppl.*, 255, 14

Fusco T., et al., 2006, in Ellerbroek B. L., Bonaccini Calia D., eds, Society of Photo-Optical Instrumentation Engineers (SPIE) Conference Series Vol. 6272, Society of Photo-Optical Instrumentation Engineers (SPIE) Conference Series. p. 62720K, doi:10.1117/12.670794

Fusco T., et al., 2014, in Marchetti E., Close L. M., Vran J.-P., eds, Society of Photo-Optical Instrumentation Engineers (SPIE) Conference Series Vol. 9148, Adaptive Optics Systems IV. p. 91481U, doi:10.1117/12.2055423

Gaia Collaboration et al., 2018, *Astron. Astrophys.*, 616, A1

Gaia Collaboration et al., 2021, *Astron. Astrophys.*, 649, A1

Gaia Collaboration et al., 2022, arXiv e-prints, p. arXiv:2208.00211

Gaia Collaboration et al., 2023, *Astron. Astrophys.*, 674, A1

Ghezzi L., Cunha K., Smith V. V., de Araújo F. X., Schuler S. C., de la Reza R., 2010, *Astrophys. J.*, 720, 1290

Ginski C., et al., 2016, *Astron. Astrophys.*, 595, A112

Goda S., Matsuo T., 2019, The Astrophysical Journal, 876, 23

Gonzalez G., 1997, *Mon. Not. Roy. Astron. Soc.*, 285, 403

Goswami P. P., Goswami A., 2022, *Astron. Astrophys.*, 657, A50

Goswami P. P., Rathour R. S., Goswami A., 2021, *Astron. Astrophys.*, 649, A49

Gray R. O., Corbally C. J., 1994, *Astron. J.*, 107, 742

Grevesse N., Sauval A. J., 1998, *Space Sci. Rev.*, 85, 161

Haffert S. Y., Bohn A. J., de Boer J., Snellen I. A. G., Brinchmann J., Girard J. H., Keller C. U., Bacon R., 2019, Nature Astronomy, 3, 749

Haisch Karl E. J., Lada E. A., Lada C. J., 2001, *Astrophys. J. Lett.*, 553, L153

Hamer J. H., Schlaufman K. C., 2019, *Astron. J.*, 158, 190

Han S. I., Kim Y. C., Lee Y. W., Yi S. K., Kim D. G., Demarque P., 2009, in Richtler T., Larsen S., eds, , Globular Clusters - Guides to Galaxies. p. 33, doi:10.1007/978-3-540-76961-3˙9

Hayashi C., Nakazawa K., Nakagawa Y., 1985, in Black D. C., Matthews M. S., eds, Protostars and Planets II. pp 1100–1153

Haywood M., Di Matteo P., Lehnert M. D., Katz D., Gómez A., 2013, *Astron. Astrophys.*, 560, A109

Henry G. W., Marcy G. W., Butler R. P., Vogt S. S., 2000, *Astrophys. J. Lett.*, 529, L41

Herwig F., 2005, Annual Review of Astronomy and Astrophysics, 43, 435

Hinkel N. R., Timmes F. X., Young P. A., Pagano M. D., Turnbull M. C., 2014, *Astron. J.*, 148, 54

Hinkley S., et al., 2023, *Astron. Astrophys.*, 671, L5

Hogg D. W., Foreman-Mackey D., 2018, The Astrophysical Journal Supplement Series, 236, 11

Howard A. W., et al., 2010, *Astrophys. J.*, 721, 1467

Howard A. W., et al., 2012, *Astrophys. J. Suppl.*, 201, 15

Huber D., et al., 2017, *Astrophys. J.*, 844, 102

Ida S., Lin D. N. C., 2004, *Astrophys. J.*, 616, 567

Iglesias C. A., Rogers F. J., 1996, *Astrophys. J.*, 464, 943

Ikoma M., Emori H., Nakazawa K., 2001, *Astrophys. J.*, 553, 999

Isella A., Pérez L. M., Carpenter J. M., 2012, *Astrophys. J.*, 747, 136

Isella A., Chandler C. J., Carpenter J. M., Pérez L. M., Ricci L., 2014, *Astrophys. J.*, 788, 129

Jin S., Isella A., Huang P., Li S., Li H., Ji J., 2019, *Astrophys. J.*, 881, 108

Jofré P., et al., 2014, *Astron. Astrophys.*, 564, A133

Jofré P., Heiter U., Soubiran C., 2019, *Ann. Rev. Astron. Astrophys.*, 57, 571

Johnson D. R. H., Soderblom D. R., 1987, *Astron. J.*, 93, 864

Johnson J. A., et al., 2010a, *Pub. Astron. Soc. Pac.*, 122, 149

Johnson J. A., Aller K. M., Howard A. W., Crepp J. R., 2010b, *Pub. Astron. Soc. Pac.*, 122, 905

Johnson J. A., et al., 2017, *Astron. J.*, 154, 108

Jovanovic N., et al., 2015, *Pub. Astron. Soc. Pac.*, 127, 890

Kains N., et al., 2013, *Astron. Astrophys.*, 552, A70

Kama M., Folsom C. P., Pinilla P., 2015, *Astron. Astrophys.*, 582, L10

Karakas A. I., Lattanzio J. C., 2014, Publications of the Astronomical Society of Australia, 31, e030

Keppler M., et al., 2018, *Astron. Astrophys.*, 617, A44

Kipping D. M., Sandford E., 2016, Monthly Notices of the Royal Astronomical Society, 463, 1323

Kobayashi C., Umeda H., Nomoto K., Tominaga N., Ohkubo T., 2006, *Astrophys. J.*, 653, 1145

Kobayashi C., Karakas A. I., Lugaro M., 2020, *Astrophys. J.*, 900, 179

Kornet K., Bodenheimer P., Różyczka M., Stepinski T. F., 2005, *Astron. Astrophys.*, 430, 1133

Kratter K. M., Matzner C. D., Krumholz M. R., Klein R. I., 2010, *Astrophys. J.*, 708, 1585

Kraus A. L., Ireland M. J., 2012, *Astrophys. J.*, 745, 5

Kraus A. L., Ireland M. J., Hillenbrand L. A., Martinache F., 2012, *Astrophys. J.*, 745, 19

Lafrenière D., Marois C., Doyon R., Nadeau D., Artigau É., 2007, *Astrophys. J.*, 660, 770

Lagrange A. M., 2014, Philosophical Transactions of the Royal Society of London Series A, 372, 20130090

Lagrange A. M., et al., 2010, Science, 329, 57

Laughlin G., Adams F. C., 1997, *Astrophys. J. Lett.*, 491, L51

Laughlin G., Chambers J. E., 2002, The Astronomical Journal, 124, 592

Lin D. N. C., Bodenheimer P., Richardson D. C., 1996, *Nature*, 380, 606

Lindegren L., et al., 2021, *Astron. Astrophys.*, 649, A4

Lo Curto G., et al., 2010, *Astron. Astrophys.*, 512, A48

Luhman K. L., et al., 2006, *Astrophys. J.*, 649, 894

Ma B., Ge J., 2014, Monthly Notices of the Royal Astronomical Society, 439, 2781

Macintosh B. A., et al., 2008, in Hubin N., Max C. E., Wizinowich P. L., eds, Society of Photo-Optical Instrumentation Engineers (SPIE) Conference Series Vol. 7015, Adaptive Optics Systems. p. 701518, doi:10.1117/12.788083

Maldonado J., Villaver E., Eiroa C., Micela G., 2019, *Astron. Astrophys.*, 624, A94

Malhotra R., 2015, The Astrophysical Journal, 808, 71

Marois C., Lafrenière D., Doyon R., Macintosh B., Nadeau D., 2006, *Astrophys. J.*, 641, 556

Marois C., et al., 2008a, , 322, 1348

Marois C., Macintosh B., Barman T., Zuckerman B., Song I., Patience J., Lafrenière D., Doyon R., 2008b, Science, 322, 1348

Matsuo T., Shibai H., Ootsubo T., Tamura M., 2007, *Astrophys. J.*, 662, 1282

Matteucci F., Francois P., 1989, *Mon. Not. Roy. Astron. Soc.*, 239, 885

Matteucci F., Spitoni E., Recchi S., Valiante R., 2009, *Astron. Astrophys.*, 501, 531

Mayer L., Quinn T., Wadsley J., Stadel J., 2002, Science, 298, 1756

Mayor M., Queloz D., 1995, *Nature*, 378, 355

Mayor M., et al., 2003, The Messenger, 114, 20

Mayor M., et al., 2011, arXiv e-prints, p. arXiv:1109.2497

Meheut H., Meliani Z., Varniere P., Benz W., 2012, *Astron. Astrophys.*, 545, A134

Meléndez J., Asplund M., Gustafsson B., Yong D., 2009, *Astrophys. J. Lett.*, 704, L66

Meshkat T., et al., 2017, *Astron. J.*, 154, 245

Mikolaitis Š., de Laverny P., Recio-Blanco A., Hill V., Worley C. C., de Pascale M., 2017, *Astron. Astrophys.*, 600, A22

Mizuno H., 1980, Progress of Theoretical Physics, 64, 544

Montesinos M., Perez S., Casassus S., Marino S., Cuadra J., Christiaens V., 2016, *Astrophys. J. Lett.*, 823, L8

Mordasini C., Alibert Y., Benz W., Klahr H., Henning T., 2012, *Astron. Astrophys.*, 541, A97

Mulders G. D., 2018, Planet Populations as a Function of Stellar Properties. p. 153, doi:10.1007/978-3-319-55333-7˙153

Mulders G. D., Pascucci I., Apai D., Frasca A., Molenda-Żakowicz J., 2016, The Astronomical Journal, 152, 187

Müller A., et al., 2018, *Astron. Astrophys.*, 617, L2

Murray N., Chaboyer B., Arras P., Hansen B., Noyes R. W., 2001, *Astrophys. J.*, 555, 801

NASA Exoplanet Science Institute 2024, Planetary Systems Table, doi:10.26133/NEA12, `https://catcopy.ipac.caltech.edu/dois/doi.php?id=10.26133/NEA12`

Narang M., Manoj P., Furlan E., Mordasini C., Henning T., Mathew B., Banyal R. K., Sivarani T., 2018, *Astron. J.*, 156, 221

Ness M. K., Johnston K. V., Blancato K., Rix H. W., Beane A., Bird J. C., Hawkins K., 2019, *Astrophys. J.*, 883, 177

Neuhäuser R., Schmidt T. O. B., 2012, arXiv e-prints, p. arXiv:1201.3537

Nielsen E. L., et al., 2019, The Astronomical Journal, 158, 13

Nissen P. E., 2015, *Astron. Astrophys.*, 579, A52

Nissen P. E., Gustafsson B., 2018, *Astron. Astrophys. Rev.*, 26, 6

Nomoto K., Iwamoto K., Nakasato N., Thielemann F. K., Brachwitz F., Tsujimoto T., Kubo Y., Kishimoto N., 1997, *Nuclear Physics A*, 621, 467

Nomoto K., Kobayashi C., Tominaga N., 2013, *Ann. Rev. Astron. Astrophys.*, 51, 457

Oh D., et al., 2016, *Pub. Astron. Soc. Japan*, 68, L3

Owen J. E., Murray-Clay R., 2018, *Mon. Not. Roy. Astron. Soc.*, 480, 2206

Pätzold M., Carone L., Rauer H., 2004, *Astron. Astrophys.*, 427, 1075

Pedregosa F., et al., 2011, Journal of Machine Learning Research, 12, 2825

Perryman M., Hartman J., Bakos G. Á., Lindegren L., 2014, *Astrophys. J.*, 797, 14

Petigura E. A., et al., 2017, *Astron. J.*, 154, 107

Petigura E. A., et al., 2018, The Astronomical Journal, 155, 89

Petigura E. A., et al., 2022, *Astron. J.*, 163, 179

Piétu V., Dutrey A., Guilloteau S., Chapillon E., Pety J., 2006, *Astron. Astrophys.*, 460, L43

Pinsonneault M. H., DePoy D. L., Coffee M., 2001, *Astrophys. J. Lett.*, 556, L59

Pinte C., Dent W. R. F., Ménard F., Hales A., Hill T., Cortes P., de Gregorio-Monsalvo I., 2016, *Astrophys. J.*, 816, 25

Piskunov N., Valenti J. A., 2017, *Astron. Astrophys.*, 597, A16

Piskunov N. E., Kupka F., Ryabchikova T. A., Weiss W. W., Jeffery C. S., 1995, *Astron. Astrophys. Suppl.*, 112, 525

Piso A.-M. A., Youdin A. N., 2014, *Astrophys. J.*, 786, 21

Piso A.-M. A., Youdin A. N., Murray-Clay R. A., 2015, *Astrophys. J.*, 800, 82

Pollack J. B., Hubickyj O., Bodenheimer P., Lissauer J. J., Podolak M., Greenzweig Y., 1996, , 124, 62

Pont F., Eyer L., 2004, *Mon. Not. Roy. Astron. Soc.*, 351, 487

Price D. J., et al., 2018, *Mon. Not. Roy. Astron. Soc.*, 477, 1270

Ramírez I., et al., 2014, *Astron. Astrophys.*, 572, A48

Recio-Blanco A., et al., 2016, *Astron. Astrophys.*, 585, A93

Recio-Blanco A., et al., 2022, arXiv e-prints, p. arXiv:2206.05541

Reddy B. E., Lambert D. L., Allende Prieto C., 2006, *Mon. Not. Roy. Astron. Soc.*, 367, 1329

Reggiani H., Schlaufman K. C., Casey A. R., Simon J. D., Ji A. P., 2021, *Astron. J.*, 162, 229

Ren B. B., et al., 2023, arXiv e-prints, p. arXiv:2310.08589

Ribas I., et al., 2023, *Astron. Astrophys.*, 670, A139

Rice W. K. M., Armitage P. J., 2003, *Astrophys. J. Lett.*, 598, L55

Rodrigo C., Bayo A., Solano E., 2017, in Arribas S., Alonso-Herrero A., Figueras F., Hernández-Monteagudo C., Sánchez-Lavega A., Pérez-Hoyos S., eds, Highlights on Spanish Astrophysics IX. pp 447–452

Sabotta S., et al., 2021, *Astron. Astrophys.*, 653, A114

Saffe C., Gómez M., Chavero C., 2005, *Astron. Astrophys.*, 443, 609

Sahlmann J., et al., 2011, *Astron. Astrophys.*, 535, A66

Sahlmann J., Lazorenko P. F., Ségransan D., Martín E. L., Queloz D., Mayor M., Udry S., 2013, *Astron. Astrophys.*, 556, A133

Sallum S., et al., 2015, *Nature*, 527, 342

Sallum S., Eisner J., Skemer A., Murray-Clay R., 2023, *Astrophys. J.*, 953, 55

Santos N. C., Israelian G., Mayor M., 2000, *Astron. Astrophys.*, 363, 228

Santos N. C., Israelian G., Mayor M., 2001, *Astron. Astrophys.*, 373, 1019

Santos N. C., Israelian G., Mayor M., 2004, *Astron. Astrophys.*, 415, 1153

Santos N. C., et al., 2011, *Astron. Astrophys.*, 526, A112

Santos N. C., et al., 2013, *Astron. Astrophys.*, 556, A150

Santos N. C., et al., 2017, *Astron. Astrophys.*, 603, A30

Saraf P., Sivarani T., 2023, arXiv e-prints, p. arXiv:2308.05097

Saraf P., Sivarani T., 2024, Bulletin de la Societe Royale des Sciences de Liege, 93, 381

Saraf P., Allende Prieto C., Sivarani T., Bandyopadhyay A., Beers T. C., Susmitha A., 2023, *Mon. Not. Roy. Astron. Soc.*, 524, 5607

Saumon D., Marley M. S., 2008, The Astrophysical Journal, 689, 1327

Saumon D., Chabrier G., van Horn H. M., 1995, *Astrophys. J. Suppl.*, 99, 713

Schlaufman K. C., 2018, *Astrophys. J.*, 853, 37

Schmid H. M., et al., 2018, *Astron. Astrophys.*, 619, A9

Schneider J., Dedieu C., Le Sidaner P., Savalle R., Zolotukhin I., 2011, *Astron. Astrophys.*, 532, A79

Schönrich R., Binney J., Dehnen W., 2010, *Mon. Not. Roy. Astron. Soc.*, 403, 1829

Shkedy Z., Decin L., Molenberghs G., Aerts C., 2007, *Mon. Not. Roy. Astron. Soc.*, 377, 120

Silva Aguirre V., et al., 2015, *Mon. Not. Roy. Astron. Soc.*, 452, 2127

Simon M., Dutrey A., Guilloteau S., 2000, *Astrophys. J.*, 545, 1034

Skúladóttir Á., Salvadori S., 2020, *Astron. Astrophys.*, 634, L2

Snaith O., Haywood M., Di Matteo P., Lehnert M. D., Combes F., Katz D., Gómez A., 2015, *Astron. Astrophys.*, 578, A87

Sneden C., 1973, *Astrophys. J.*, 184, 839

Snellen I. A. G., Brown A. G. A., 2018, Nature Astronomy, 2, 883

Sousa S. G., et al., 2018, *Astron. Astrophys.*, 620, A58

Sousa S. G., et al., 2019, Monthly Notices of the Royal Astronomical Society, 485, 3981

Sousa S. G., et al., 2021, *Astron. Astrophys.*, 656, A53

Spiegel D. S., Burrows A., Milsom J. A., 2011, *Astrophys. J.*, 727, 57

Steinmetz M., et al., 2020, The Astronomical Journal, 160, 82

Stempels H. C., Piskunov N., 2002, *Astron. Astrophys.*, 391, 595

Stempels H. C., Piskunov N., 2003, *Astron. Astrophys.*, 408, 693

Stempels H. C., Collier Cameron A., Hebb L., Smalley B., Frandsen S., 2007, *Mon. Not. Roy. Astron. Soc.*, 379, 773

Suárez-Andrés L., Israelian G., González Hernández J. I., Adibekyan V. Z., Delgado Mena E., Santos N. C., Sousa S. G., 2016, *Astron. Astrophys.*, 591, A69

Suárez-Andrés L., Israelian G., González Hernández J. I., Adibekyan V. Z., Delgado Mena E., Santos N. C., Sousa S. G., 2017, *Astron. Astrophys.*, 599, A96

Swastik C., Suresh P. K., Maity B., 2019, arXiv e-prints, p. arXiv:1903.04725

Swastik C., Banyal R. K., Narang M., Manoj P., Sivarani T., Reddy B. E., Rajaguru S. P., 2021, *Astron. J.*, 161, 114

Swastik C., Banyal R. K., Narang M., Manoj P., Sivarani T., Rajaguru S. P., Unni A., Banerjee B., 2022, *Astron. J.*, 164, 60

Swastik C., Banyal R. K., Narang M., Unni A., Banerjee B., Manoj P., Sivarani T., 2023, *Astron. J.*, 166, 91

Taki T., Kuwabara K., Kobayashi H., Suzuki T. K., 2021, *Astrophys. J.*, 909, 75

Tautvaišienė G., et al., 2022, arXiv e-prints, p. arXiv:2202.10102

Thalmann C., et al., 2015, *Astrophys. J. Lett.*, 808, L41

Thalmann C., et al., 2016, *Astrophys. J. Lett.*, 828, L17

Trapman L., Miotello A., Kama M., van Dishoeck E. F., Bruderer S., 2017, *Astron. Astrophys.*, 605, A69

Traub W. A., Oppenheimer B. R., 2010, Direct Imaging of Exoplanets. pp 111–156

Tuthill P., et al., 2006, in Ellerbroek B. L., Bonaccini Calia D., eds, Society of Photo-Optical Instrumentation Engineers (SPIE) Conference Series Vol. 6272, Society of Photo-Optical Instrumentation Engineers (SPIE) Conference Series. p. 62723A, doi:10.1117/12.672342

Udry S., Santos N. C., 2007, *Ann. Rev. Astron. Astrophys.*, 45, 397

Ujjwal K., Kartha S. S., Mathew B., Manoj P., Narang M., 2020, *Astron. J.*, 159, 166

Unni A., Narang M., Sivarani T., Puravankara M., Banyal R. K., Surya A., Rajaguru S. P., Swastik C., 2022, *Astron. J.*, 164, 181

Valenti J., Fischer D., 2008, in van Belle G., ed., Astronomical Society of the Pacific Conference Series Vol. 384, 14th Cambridge Workshop on Cool Stars, Stellar Systems, and the Sun. p. 292

Valls-Gabaud D., 2014, in EAS Publications Series. pp 225–265 (`arXiv:1607.03000`), doi:10.1051/eas/1465006

Vanderburg A., Plavchan P., Johnson J. A., Ciardi D. R., Swift J., Kane S. R., 2016, *Mon. Not. Roy. Astron. Soc.*, 459, 3565

Vigan A., et al., 2017, *Astron. Astrophys.*, 603, A3

Viswanath G., Narang M., Manoj P., Mathew B., Kartha S. S., 2020, *Astron. J.*, 159, 194

Wagner K., et al., 2018, *Astrophys. J. Lett.*, 863, L8

Wagner K., Apai D., Kratter K. M., 2019, The Astrophysical Journal, 877, 46

Wahhaj Z., et al., 2021, *Astron. Astrophys.*, 648, A26

Wahhaj Z., et al., 2024, arXiv e-prints, p. arXiv:2404.11641

Wang J., Fischer D. A., 2015, *Astron. J.*, 149, 14

Wang J. J., et al., 2018, The Astronomical Journal, 156, 192

Wang J. J., et al., 2021, *Astron. J.*, 161, 148

Wilson R. F., et al., 2021, arXiv e-prints, p. arXiv:2111.01753

Wing R. F., Yorka S. B., 1979, in IAU Colloq. 47: Spectral Classification of the Future. p. 519

Winn J. N., Fabrycky D. C., 2015, *Ann. Rev. Astron. Astrophys.*, 53, 409

Wojno J., et al., 2018, *Mon. Not. Roy. Astron. Soc.*, 477, 5612

Wolszczan A., Frail D. A., 1992, *Nature*, 355, 145

Wright J. T., et al., 2011, *Astrophys. J.*, 730, 93

Wu Y., Xiang M., Chen Y., Zhao G., Bi S., Li C., Li Y., Huang Y., 2021, *Mon. Not. Roy. Astron. Soc.*, 501, 4917

Wyatt M. C., Clarke C. J., Greaves J. S., 2007, *Mon. Not. Roy. Astron. Soc.*, 380, 1737

Zakamska N. L., Pan M., Ford E. B., 2011, Monthly Notices of the Royal Astronomical Society, 410, 1895

Zhao H., Schultheis M., Rojas-Arriagada A., Recio-Blanco A., de Laverny P., Kordopatis G., Surot F., 2021, *Astron. Astrophys.*, 654, A116

Zurlo A., et al., 2016, *Astron. Astrophys.*, 587, A57

de Juan Ovelar M., Kruijssen J. M. D., Bressert E., Testi L., Bastian N., Cánovas H., 2012, *Astron. Astrophys.*, 546, L1

van Boekel R., et al., 2017, *Astrophys. J.*, 837, 132

van Holstein R. G., et al., 2020, IRDAP: SPHERE-IRDIS polarimetric data reduction pipeline, Astrophysics Source Code Library, record ascl:2004.015 (ascl:2004.015)

van Holstein R. G., et al., 2021, *Astron. Astrophys.*, 647, A21

van Leeuwen F., 1997, *Space Sci. Rev.*, 81, 201

van Oirschot P., Nelemans G., Pols O., Starkenburg E., 2019, *Mon. Not. Roy. Astron. Soc.*, 483, 4397

van der Plas G., et al., 2017, *Astron. Astrophys.*, 597, A32